

UNIVERSITY OF COPENHAGEN
NIELS BOHR INSTITUTE
FACULTY OF SCIENCE



SODIUM, IODINE AND BROMINE IN POLAR ICE CORES

PhD THESIS

Niccolò Maffezzoli

A DISSERTATION PRESENTED TO
THE CENTER FOR ICE AND CLIMATE

IN PARTIAL FULFILLMENT OF THE REQUIREMENTS
FOR THE DEGREE OF
DOCTOR PHILOSOPHIÆ
IN THE SUBJECT OF
PHYSICS

THESIS ADVISOR: PAUL VALLELONGA

COPENHAGEN UNIVERSITY
NIELS BOHR INSTITUTE
COPENHAGEN
SEPTEMBER 2017

This thesis has been submitted to the PhD School of The Faculty of Science, University of Copenhagen

FATEMI PASSARE, HO IL CANCRO.
« ANDREI »

SORRY, FROM ITALY.
« GIOVANNI »

NOOICE.
« ROSS »

!@#\$%•
« SPOLI »

LA NEVE, CHE BELLA LA NEVE. DANI, L'ABBIAMO RIBECCATO.
« IL MAFFE »

LA BARCA SI CHIAMERA DAWN WIND.
« L'ALTRO MAFFE »

IL BUSINESS NON DORME, MAI.
« NIZZO »

ERO IO QUELLA MATTINA A PARTICELLE II.
« GIGI »

MA CHE VUOI ?
« LA DANI »

SODIUM, IODINE AND BROMINE IN POLAR ICE CORES

ENGLISH ABSTRACT

This research focuses on sodium, bromine and iodine in polar ice cores, with the aim of reviewing and advancing their current understanding with additional measurements and records, and investigating the connections of these tracers with sea ice and their feasibility as sea ice indicators. Modern Arctic sea ice decline clearly yields further motivation in this direction, as the reconstruction of past sea ice conditions could provide clues to the mechanisms in play nowadays and in the future projections. Inductively Coupled Plasma Mass Spectroscopy (ICP-MS) has been applied for the determination of Na, Br and I in firn records retrieved at Law Dome and Talos Dome (Antarctica) and in the NEEM and Renland ice cores (Greenland).

The dissertation is presented as a monograph. It is structured in a way that would logically bring the reader from the broad perspective of sea ice and ice cores into the details of the physical and chemical transformations of these impurities from their emission to their deposition and finally to their determination in ice cores and interpretation of their climatic significance. This view reflects, to some extent, the thread of understanding that led to the research activities.

Chapter 2 briefly introduces sea ice, with particular focus on its salinity as a source of sea salt aerosols. Some features regarding the role of sea ice in the climate system and the differences between sea ice in the two hemispheres are described. The chapter ends with a brief summary of the state-of-the-art of the chemical tracers that are used in ice cores and marine sediment cores to reconstruct past sea ice. Chapter 3 introduces ice cores with a geochemical perspective. The historically measured ions and compounds are described, together with their climatic relevance. The chapter ends with a description of the main analytical techniques used to measure ionic and elemental species in ice cores.

Chapter 4 introduces sodium, bromine and iodine with a theoretical perspective and a particular focus on their connections with sea ice. Some of the physical and chemical properties that are believed to affect the sea salt aerosol signature in ice cores are described. Halogen chemistry is presented, with a particular focus on the halogen sources and radical chemistry in the polar boundary layer. The chapter continues with a historical review of the relevant atmospheric studies that have demonstrated the activation of halogen compounds

and the importance of halogen chemistry at high latitudes. Finally, the use of sodium and bromine as sea ice tracers is introduced.

Chapter 5 describes the Renland ice core, drilled in coastal East Greenland in 2015 as part of "Ice2Ice", a project which aims at understanding the causes of past abrupt climate changes in Greenland. The study of the timescale and other glaciological parameters led to the calculation of the annual accumulation rate for the past 4000 years. Finally, a study of the potential sea salt aerosol sources arriving at the ice core site is presented, using back trajectory analyses of the past 17 years. The results identify the aerosol source area influencing the Renland ice cap, a result necessary for the interpretation of impurity records obtained from the ice core.

Chapter 6 reviews the published ice/snow measurements of bromine and iodine at polar latitudes. Where available they are compared to atmospheric halogen measurements. A selection of sodium records from the same locations is included to provide a more complete picture. The additional measurements performed during the research activities are also displayed. With the goal of presenting and extending the state-of-the-art of knowledge of bromine and iodine in polar snow, a critical comparison between the proxies is adopted, trying to elucidate the established and the unknown features and their potential as sea ice indicators. The last section is dedicated to the measurements of sodium and bromine in the Renland core, which could provide the first ice core-based reconstruction of Arctic sea ice in the Greenland Sea for the last 125 kyr.

SODIUM, IODINE AND BROMINE IN POLAR ICE CORES

DANISH ABSTRACT

Dette projekt omhandler natrium, brom og iod i polare iskerner, og har til formål at gennemgå den nuværende forståelse og videreudvikle denne på baggrund af nye målinger og data, samt at undersøge sammenhænge mellem disse tre sporstoffer og deres potentiale som havis-indikatorer. De seneste årtiers reduktion af den Arktiske havis er en stærk motivation til at efterforske disse sammenhænge, da fortidens havisændringer kan bidrage til forståelsen af de mekanismer, der er afgørende for nutidens og fremtidens klima. Natrium, brom og iod er blevet målt i firn-prøver fra Law Dome og Talos Dome (på Antarktis) og fra NEEM og Renland iskernerne (fra Grønland) ved hjælp af massespektroskopi (Inductively Coupled Plasma Mass Spectroscopy, ICP-MS).

Denne afhandling er skrevet som en monografi. Den er struktureret således at læseren først gives et bredt overblik over havis og iskerner. Derefter følger en detaljeret gennemgang af de fysiske og kemiske processer der påvirker de tre sporstoffer fra de emitteres til de deponeres, før det til sidst beskrives hvordan iskerne-analyserne udføres og hvordan resultaterne fortolkes i en klimamæssig sammenhæng. Denne struktur afspejler, i nogen grad, det samme forløb som forskningen i dette projekt har gennemgået.

Kapitel 2 introducerer havis, med særlig fokus på isens salinitet, der er afgørende for dannelsen af havsalt-aerosoler. Herefter præsenteres havisens rolle i klimasystemet og forskellen mellem havisen på den nordlige og sydlige halvkugle i hovedtræk. Kapitlet afsluttes med et overblik over den nuværende forståelse af de kemiske sporstoffer fra is- og havbundssedimentskerner, der kan benyttes til at rekonstruere fortidens havisudbredelse. Kapitel 3 beskriver iskerner fra et geo-kemisk perspektiv. De relevante kemiske forbindelser og ioner, der traditionelt måles, præsenteres, med særlig fokus på deres relevans for forståelsen af klimasystemet. Kapitlet afsluttes med en beskrivelse af de grundlæggende analysemetoder, der benyttes til måling af ioner og grundstoffer i iskerner.

Kapitel 4 beskriver natrium, brom og iod fra et teoretisk perspektiv, med særlig fokus på deres forbindelse til havis. Udvalgte fysiske og kemiske egenskaber, der er afgørende for havsalt-aerosoler og deres signatur i iskerner, beskrives. Halogenernes kemi præsenteres, og specielt gennemgås kilder til halogener og frie radikaler samt de kemiske processer der foregår i atmosfærens grænselag i de polare egne. Kapitlet fortsætter med en historisk gennemgang af tidligere studier, der har undersøgt halogenernes rolle i atmosfærekemiske

processer på høje breddegrader. Til sidst introduceres det hvordan natrium og brom kan benyttes som havis-indikatorer.

Kapitel 5 beskriver Renland-iskernen, der blev boret nær kysten i Østgrønland i 2015 som en del af ice2ice-projektet, som har til formål at forbedre forståelsen af fortidens bratte klimaændringer i Grønland. På baggrund af iskernens tidsskala og en række andre glaciologiske parametre er den årlige akkumulationsrate blevet udregnet for de seneste 4000 år. Afslutningsvis benyttes beregninger af den atmosfæriske cirkulation ("back trajectories") over de seneste 17 år til at identificere kildeområderne for de havsalt-aerosoler der deponeres på iskerne-lokationen. Kortlægningen af kildeområdet, der har indflydelse på snefaldet på iskapen på Renland, er et vigtigt og nødvendigt element i den klimamæssige fortolkning af de sporstoffer der kan måles i iskernen.

Kapitel 6 resumerer publicerede målinger af brom og iod fra polare egne. I de områder, hvor der er tilgængelige målinger, sammenholdes disse med atmosfæriske halogen-målinger. For at give et samlet overblik, præsenteres natrium-målinger og andre udførte målinger også fra udvalgte lokationer. For at udbygge den nuværende viden om brom og iod i polar sne, præsenteres herefter en kritisk gennemgang af sporstofferne som klimatisk proxydata, og de etablerede og de stadig ukendte aspekter af sporstoffernes potentiale som havis-indikatorer diskuteres. Den sidste del af afhandlingen præsenterer målinger af natrium og brom fra Renland-iskernen, der kan benyttes som grundlag for den første iskerne-baserede havis-rekonstruktion for Grønlandshavet over de sidste 125,000 år.

Contents

1	MOTIVATION AND OUTLINE	1
2	SEA ICE	3
2.1	Salinity and brine drainage	3
2.2	Sea ice in the climate system	6
2.3	Arctic and Antarctic sea ice	8
2.4	Sea ice proxies	11
3	ICE CORES	13
3.1	A record of the past climate	13
3.2	Glaciochemistry	16
3.3	Analytical techniques for impurity detection	21
4	SODIUM AND HALOGENS IN THE POLAR BOUNDARY LAYER	29
4.1	Sea salt aerosols	29
4.2	Halogens in the polar boundary layer	38
5	THE RENLAND ICE CORE	57
5.1	The ice core site	57
5.2	The density profile	59
5.3	The thinning function	60
5.4	The ReCAP V ₄ and the annual layer counted timescales	62
5.5	Annual accumulation rate of the last 4k years	65
5.6	Back trajectories	66
6	SODIUM, BROMINE AND IODINE MEASUREMENTS IN POLAR ICE CORES	75
6.1	Seasonal timescales	78
6.2	Decadal to centennial timescales	88
6.3	From millennial to glacial – interglacial timescales	93
6.4	Antarctica: Talos Dome	94
6.5	Greenland: NEEM	100

6.6	Greenland: Renland	103
7	CONCLUSIONS AND OUTLOOK	122
	APPENDIX A BROMINE, IODINE AND SODIUM IN SURFACE SNOW ALONG THE 2013 TALOS DOME–GV7 TRA- VERSE (NORTHERN VICTORIA LAND, EAST ANTARCTICA)	125
A.1	Introduction	125
A.2	Sampling and analyses	127
A.3	Results and discussion	130
A.4	Conclusions	135
	REFERENCES	137

1

Motivation and outline

Impurities in ice cores have now been measured for half a decade to retrieve information regarding the past atmospheric composition, in order to reconstruct valuable parameters of the Earth past climate. Sea ice constitutes the boundary between the ocean and the atmosphere; as such it plays an active role within the climate system, showing at the same time to be an extremely sensitive indicator of climate change in the northern hemisphere. Since sea ice has proved to be a very elusive climatic property from a paleorecord perspective, reconstruction of past sea ice extents has been a very challenging task. In ice cores, sodium, emitted from brine and other saline substrates has historically been used as an indicator of sea ice, yet some features have proved to undermine its use. Competing inputs from open water and the influence of atmospheric circulation on the transport and production of sea salt aerosols challenge the interpretation of sodium records, for which different controlling variables modulate sodium signals. Although bromine and iodine have initially drawn attention for their importance as ozone depletion substances, their use in glaciochemistry as sea ice indicators has recently shown some potential. Iodine is related to biological production under sea ice at polar latitudes, while bromine is involved in a sequence of multiphase reactions over fresh sea ice surfaces that lead to the exponential increase of radical species in the atmosphere. To what extent can we rely on the signatures of these tracers and what are the variables controlling their concentrations as found in ice cores ?

This work addresses the topic from a dual perspective. From one side, it aims at reviewing the published measurements and records of bromine and iodine in snow/ice in order to deepen our knowledge and understanding of these impurities. The review is divided into ranges of timescales covered by the different records; ice cores from both the northern and southern hemispheres are presented throughout the comparisons to infer, from the spatial variability, which different mechanisms are in play in the two polar environments. The sec-

ond aim is to expand the still very limited dataset of halogen measurements and integrate them with new data. During this project, snow and ice from snowpits, firn cores and ice cores were measured for sodium, bromine and iodine at Talos Dome and Law Dome in Antarctica and at NEEM and Renland in Greenland. Each study addresses different features: mechanisms acting at seasonal timescales are inferred from snowpits, larger-scale effects becoming dominant at decadal and centennial timescales. Multimillennial records are aimed at paleoreconstructions. The last part of this work investigates the Arctic sea ice signature in the 125 kyr Renland ice core.

The research activities led to a first-author ([Maffezzoli et al. 2017](#)) and two co-authored publications ([Spolaor et al. 2016b](#); [Vallelonga et al. 2017](#)). A second first-author manuscript is in preparation and an additional co-authored manuscript has been submitted (Cuevas et al., submitted).

All the figures have been produced by the author, unless specified in the caption. Data analyses have been carried out in the Python, and using the ROOT analysis framework for statistics, natively in C++, adapted to Python. All the codes are available to the public upon request, but are not attached here.

2

Sea ice

This chapter provides an introduction to the basic concepts of sea ice. The salt content of sea ice is briefly described, followed by a description of the water circulation patterns in the Arctic and Antarctic environments and the role of sea ice. The major differences between Arctic and Antarctic sea ice and the techniques used to reconstruct past sea ice extents are described and give introduction to the following chapters. Some basic concepts related to sea ice biology will be given in the discussion related to Iodine (see Sec 4.2.1).

2.1 SALINITY AND BRINE DRAINAGE

The salinity of seawater ranges from 31 to 38 g kg⁻¹ (or parts per thousand or ‰), with an average of 35 g kg⁻¹. Due to the presence of dissolved ions (Table 2.1), the freezing point of sea water is lower than that of fresh water. Thermodynamically it is described by the equation:

$$\frac{d\Theta_k}{dS_M} = -\frac{k_B N_A \Theta_K^2}{\eta_w - \eta}, \quad (2.1)$$

where Θ_K is the freezing point in K, $k_B = 1.38 \cdot 10^{-23} \text{ J K}^{-1}$ is the Boltzmann constant, $N_A = 6.023 \cdot 10^{23} \text{ mol}^{-1}$ is Avogadro's Number, $\eta_w - \eta = 6.01 \text{ kJ mol}^{-1}$ is the molar heat of solidification and S_M is the molar concentration. Due to the difficulties in determining the molar concentrations of all the dissolved species, the equation is empirically solved by making use of the salinity S with Krümmel's formula (at 1 atm):

$$\Theta = -10^{-3}(3 + 52.7S + 0.04S^2 + 0.0004S^3), \quad (2.2)$$

where Θ is the freezing point in °C.

In the polar regions the atmospheric temperature at sea level is low enough for the ocean surface water to start freezing, approximately at $-1.8\text{ }^{\circ}\text{C}$ (Eq. 2.2, $S=35\text{ g kg}^{-1}$). The floating frozen layer of sea water found at high latitudes is known as sea ice. While sea ice grows, salts are expelled from the ice matrix and become concentrated in the liquid phase (brine) inside inclusions within the ice lattice. As temperature decreases, the ice fraction and hence the brine salinity increases. At equilibrium, if the ice matrix salinity is assumed as zero (only trace amounts of salts remain trapped within the ice lattice), the bulk salinity S is given by

$$S = (1 - \varphi)S_{br}(T), \quad (2.3)$$

where φ is the ice to brine mass fraction of solid ice and $S_{br}(T)$ is the brine salinity (Hunke et al., 2011). Phase equilibrium between brine pockets and the ice matrix is always maintained: as temperature continues to drop, the brine mass fraction $(1-\varphi)$ decreases as its salinity S_{br} increases. In addition, selective crystallization of several salts takes place. Salts within sea ice are found both in the liquid and solid phases when precipitation occurs. Different ionic species have a different crystallization temperature: at $-8.2\text{ }^{\circ}\text{C}$ the brine becomes oversaturated with respect to sodium sulphate, and mirabilite ($\text{Na}_2\text{SO}_4 \cdot 10\text{ H}_2\text{O}$) starts to precipitate. By the time a temperature of $\sim -30\text{ }^{\circ}\text{C}$ is reached and hydrohalite ($\text{NaCl} \cdot 2\text{ H}_2\text{O}$) starts to precipitate, 90% of the mass of salts is in the solid phase. Overall, any change in temperature will affect the size, mass and salinity of the brine pockets, as well as the amount of precipitated salts.

Sea ice bulk salinity ranges from $\sim 10\text{-}15\text{‰}$ for newly formed (fresh) sea ice to $\sim 1\text{-}2\text{‰}$ for multi-year sea ice. As sea ice ages, its bulk salinity decreases, mostly via three mechanisms: gravitational drainage, pressure stress and temperature gradients.

Gravitational drainage is the most efficient process. It is observed that salinity decreases faster when sea ice is relatively young. Young sea ice is relatively warm and porous, and it allows brine channels to open and widen, thus facilitating its removal by gravity. Especially in the Arctic, summertime surface melting enhances salt loss, explaining why Antarctic sea ice is generally slightly more saline. In wintertime, the capillaries shrink and the discharge is weakened. This mechanism is also slowed down by hydrostatic forces and by the surface tension. By filling the inclusions within the sea ice structure, sea water opposes the discharge. Gravitational drainage can also happen in wintertime, created by density stratification.

Pressure stresses facilitate brine expulsion: as the pressure within the brine pockets increases, due to the freezing or thermal expansion of the ice matrix, brine migration and loss occurs through such cracks.

During periods of colder temperatures, such as in wintertime, brine channels shrink, eventually close and become separated by bulk ice. When a temperature gradient is applied

across the cell, a salinity gradient is also established: brine at lower temperature becoming more concentrated. Thanks to free movement of salt within the cell, equilibrium in concentration is reached if melting of ice occurs at the 'high' temperature pole of the cell; similarly, freezing occurs at the 'cold' pole. The net result is a thermal migration of the cell downwards towards the heat source (ocean below the sea ice). In explaining the observed salinity profiles, however, the temperature gradient mechanism is thought to be of little significance.

Salt loss from sea ice continues as it ages and thickens (Fig. 2.1). The combination of sea ice growth, consolidation and desalination is responsible for the observed salinity profiles. First-year-sea ice salinity profiles often display a 'C-shaped' curve, with higher salinity values both at the surface and the bottom, likely because of the freezing of brine drainage cavities at the sea ice - atmosphere interface (Malmgren and Institut. 1927; Tucker et al. 1992 and references therein).

Table 2.1: Atlantic surface seawater Reference Composition* .

Solute, i	W_i
Na^+	0.307
Mg^{2+}	0.037
Ca^{2+}	0.012
K^+	0.011
Sr^{2+}	0.00023
Cl^-	0.55
SO_4^{2-}	0.077
HCO_3^-	0.0030
Br^-	0.0019
CO_3^{2-}	0.0004
$B(OH)_4^-$	0.0002
F^-	0.00004
OH^-	0.000004
$B(OH)_3$	0.0006
CO_2	0.00001
SUM	1

W_i - mass fractions of sea salt (grams of a particular solute/grams of total solute).

* $S_R = 35.165 \text{ g kg}^{-1}$

From [Millero et al. 2008](#)

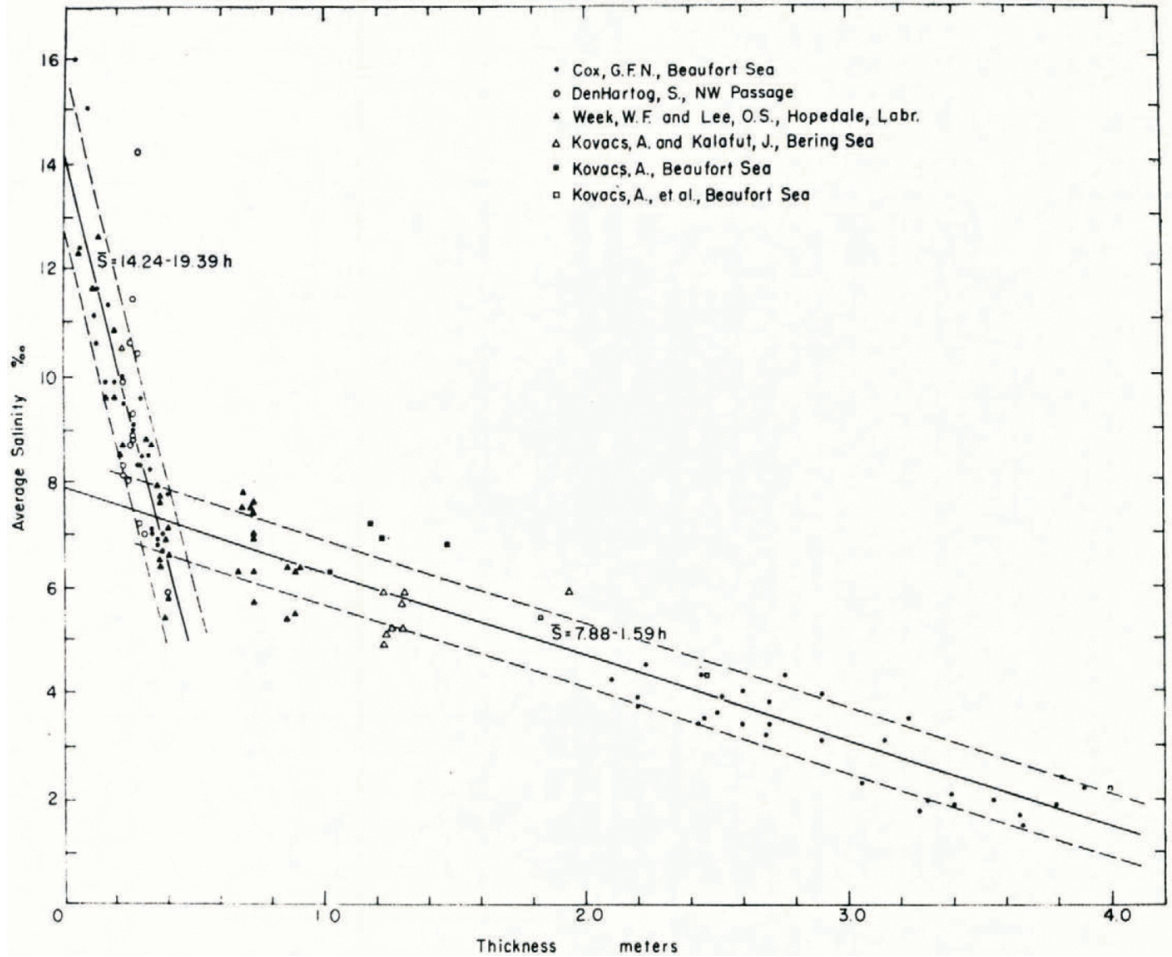


Figure 2.1: Average salinity of sea ice as a function of ice thickness for cold sea ice sampled during the growth season. From Cox and Weeks 1974.

2.2 SEA ICE IN THE CLIMATE SYSTEM

Sea ice is an important component of the climate system. Intrinsically bound to the ocean and the atmosphere, sea ice provides a highly dynamic interface for the exchange of energy, mass, and momentum between the two, thus affecting, and being affected by the Earth climate. Salt rejection processes have a profound effect on the stratification of the ocean water masses. With an increased density, the surface water layers at polar latitudes start to sink and initiate deep water formation while participating in the ocean convection. This process is particularly efficient in Antarctica, especially in the Weddel Sea, where cold katabatic winds and a higher sea ice salinity form dense water masses known as Antarctic Bottom Wa-

ter.

Deep water formation takes place also in the northern hemisphere. Warm and salty water masses carried northwards from the subtropics by the North Atlantic Current (NAC) sink in the Greenland and Labrador Seas, creating the North Atlantic deep water, which fills the Atlantic ocean between 2 - 4 km depth. The flow of surface warm water to the northern latitudes and southwards flow of deep water, known as Atlantic Meridional Overturning Circulation (AMOC), is responsible for the heat transport from the tropics and the southern hemisphere to the North Atlantic. The water columns in the Arctic ocean are strongly stratified (Fig. 2.3): cold atmospheric temperatures and high salinity provided during sea ice formation contribute to densify surface waters. Deep waters fill the ocean water column below 900 m. Water masses originated from the NAC enter the Arctic basin filling the depth range between 150 - 900 m: they are warmer than deep waters but with a similar salinity. Arctic surface waters fill the upper 150 m and result from the cooling of NAC waters and the mixing with Arctic freshwater inputs. They have a temperature of -1.5 to -1.9 °C and a salinity of 28-33.5 ‰.

The Arctic water masses, including the bottom waters, are partially separated from the Atlantic and Pacific oceans by high-rising ridges (the 600-800 m Greenland-Scotland Ridge and the Bering Strait in the Atlantic and Pacific respectively). Such topography of the sea bed limits the water outflow, which exits the Arctic ocean from Fram Strait (between Greenland and the Svalbard islands) and continues to the Greenland-Scotland Ridge through the East Greenland Current.

Although open ocean convection in the North Atlantic is supposed to be influenced mainly by atmospheric circulation, brine rejection mechanisms and anomalous sea ice extents play a key role in the stratification of the water columns in present times and may have played a similar role in the past (Dickson et al. 1996; Howe et al. 2016; Dokken and Jansen 1999).

Sea ice provides an effective insulating cover that limits the release of heat from the underlying ocean to the atmosphere. Moreover, it decreases the incoming short wave radiative flux, by providing a reflective surface (top-of-atmosphere TOA albedo of sea ice is 0.5-0.9



Figure 2.2: The Arctic seas. Picture from NSIDC

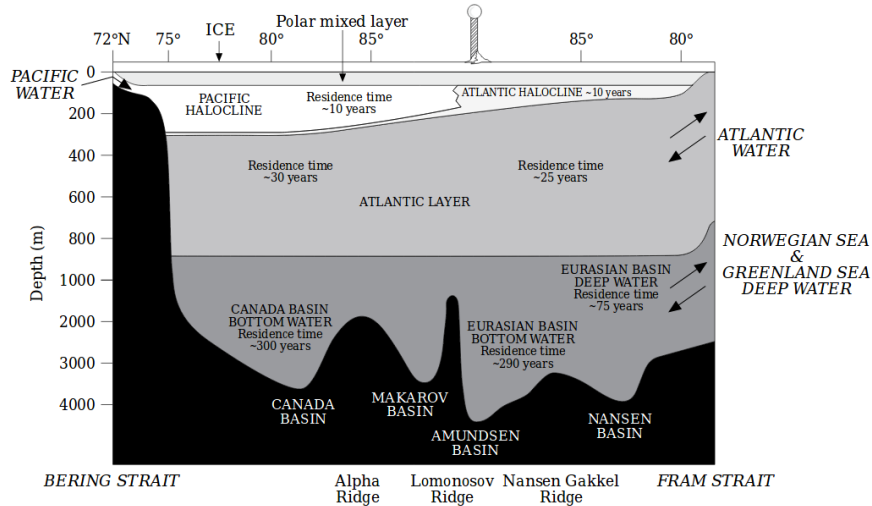


Figure 2.3: The vertical structure of the Arctic Ocean showing the polar mixed layer (approximately the top 50 m), the regions of density gradients between 50 m and 150 m (the haloclines and Pacific layer), the Atlantic Layer (approximately 150 - 900 m), and the deep and bottom waters. Adapted from [Macdonald and Bowers 1996](#).

under clear sky compared to 0.06 for ocean albedo), at the same time limiting the outgoing longwave radiation (OLR) by a smaller amount. Overall, sea ice is a strong cooling factor in the polar environment ([Yamanouchi and Charlock, 1995](#)). A series of positive feedbacks could contribute to a climate warming in response to an initial sea ice reduction. This mechanism is known as polar amplification.

Sea ice extent and thickness are controlled by the growth/decay and drift of the ice cover. They are therefore linked to combined thermodynamic and dynamic processes in the ocean and the atmosphere. While atmospheric forcing is likely to play the biggest role on annual timescales, the ocean heat flux provides the major contribution to sea ice variability at longer timescales. However, the complexity that exists between these climate players makes it difficult to understand the net of causes and the effects. The fact that climate models are generally not able to reproduce the recent Arctic sea ice decline is one example of such difficulties.

2.3 ARCTIC AND ANTARCTIC SEA ICE

The main differences between the Arctic ($90^{\circ}\text{N} - 40^{\circ}\text{N}$) and the Antarctic ($75^{\circ}\text{S} - 55^{\circ}\text{S}$) sea ice is that the former is surrounded and constrained by land, with only the Fram Strait allowing a significant exchange of water masses between the Arctic basin and the other oceans. The Arctic basin has a shallow shelf (the mean depth of the Arctic ocean is 1361 m),

while Antarctic sea ice grows on very steep shelves which reach 4000 – 6500 m depth and no land masses constrain the movement and expansion of Antarctic sea ice.

The movement of Arctic sea ice depends primarily on two wind-driven ocean currents: the Beaufort Gyre (BG) and the Transpolar Drift (TPD). The former spins clockwise in the Beaufort sea (north Canada), following the prevailing winds of the high-pressure system of the Polar Hadley cell. Sea ice that forms and becomes trapped in the BG may circulate in the Arctic basin for several years (up to 5-6). During this time, sea ice ages and deforms reaching a thickness up to 5 m (the present mean thickness being 2-3 m). The Transpolar Drift is the second major near-surface current in the Arctic. It starts in the East Siberian Sea and transports water and sea ice across the Arctic basin and along the coasts of East Greenland through the Fram Strait before exiting into the North Atlantic. The average TPD speed is 2.4 km day^{-1} , resulting in a drifting time of 1-2 years. Overall, the Arctic sea ice residence time is $\lesssim 1-7$ years.

Following autumn and wintertime growth, Arctic sea ice is at its maximum in March (Fig. 2.4), with an average extent (area with $>15\%$ sea ice concentration) of $\sim 15.5 \text{ M km}^2$ ($\text{M} = 10^6$, average 1980-2010). The minimum extent is around mid-September ($\sim 6.3 \text{ M km}^2$), following the summertime melting season. Due to a warming climate, Arctic sea ice extent is steadily decreasing (the record minimum extent of 3.4 M km^2 was observed in September 2012), with first-year fraction becoming $> 70\%$ of the total Arctic sea ice cover (was $\sim 35-40\%$ in the 1980s). Over the last 3 decades, the minimum summertime Arctic sea ice has suffered from a reduction between -12% and -13% decade $^{-1}$ relative to the 1980-2010 average (Comiso 2012).

Antarctic sea ice displays approximately a radial circumpolar symmetry, and average (1980-2010) maximum and minimum extents of 18.5 M km^2 and 2.8 M km^2 , the maximum and minimum being in September-October and February respectively (Fig. 2.4). The greater seasonal variation in extent, up to $\sim 80\%$, is also reflected by the lower thickness, on average $0.5-0.6 \text{ m}$. Antarctic sea ice drifts faster, $>20 \text{ km day}^{-1}$, and moves freely towards the ice edge pushed by katabatic winds, where it is melted by warm waters. Overall sea ice in this hemisphere is younger, $\approx 1-2$ years, and more saline. Unlike the Arctic, Antarctic sea ice has showed a slight increase since the 1970s. Although the reasons are yet to be fully understood, it appears that Antarctic sea ice edge may be controlled by the southern Antarctic Circumpolar Current (ACC) front which may be in turn constrained by seafloor features (Nghiem et al. 2016).

Major other differences exist between Arctic and Antarctic sea ice, including texture, impurity level, sediment inclusions, biology and fauna.

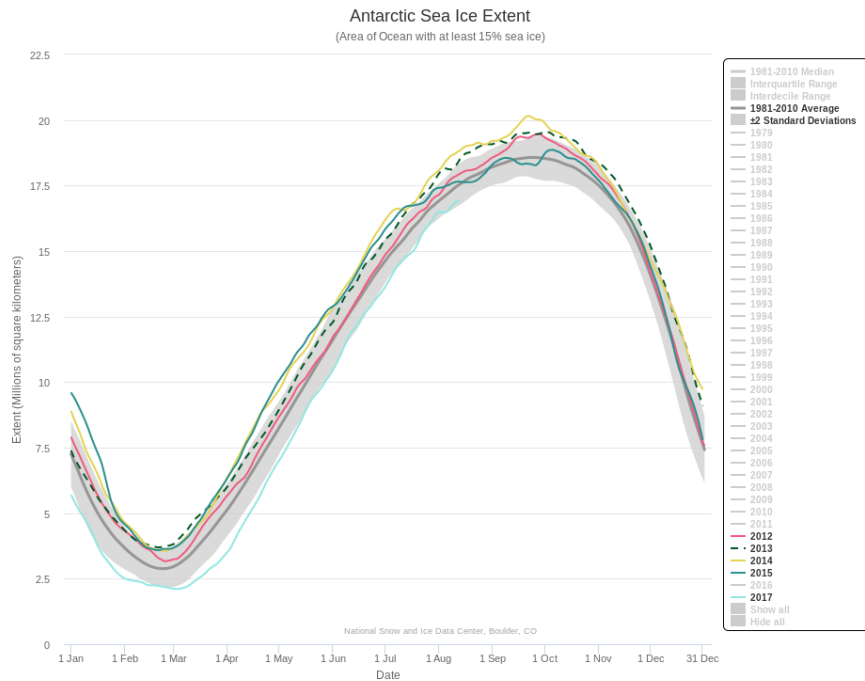
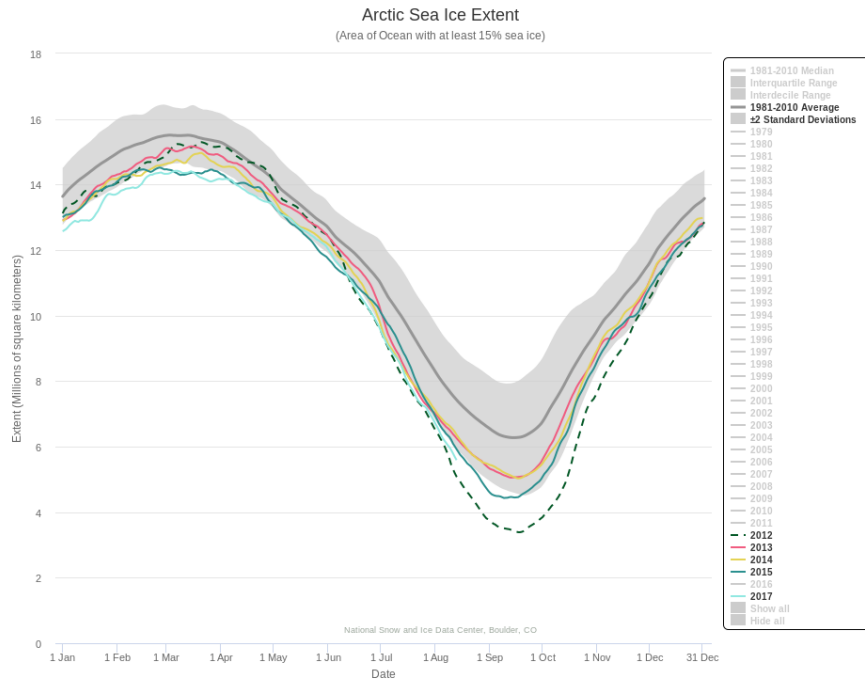


Figure 2.4: Arctic and Antarctic sea ice extent (sea ice concentration > 15%) annual cycles from 1980 to 2010 (grey line; $\pm 2\sigma$ band is grey shaded). Some single years are indicated: 2012, 2013, 2014, 2015 and 2017 (up to August). Arctic sea ice maximum (minimum) occurs in March (September). The Antarctic timing is in opposite phase. In the Arctic, 2012 was registered as the minimum sea ice extent (September) since satellite observations. From [NSIDC](#).

2.4 SEA ICE PROXIES

Especially in the a perspective of a warming climate, the knowledge of past sea ice extent is of primary importance, to better understand its links with the other components of the climate system. Past sea ice reconstructions are based on geochemical parameters or compounds linked to sea ice which can therefore record its signature in time. Several proxies have been established for such purposes: each one of them is typically linked to some sea ice parameters (for example seasonal or multi year sea ice), is more or less interfered by other variables, it has detection challenges, provides high or coarse resolution depending on proxy preservation and on the archive it is contained in. In general, therefore, a multi proxy approach is required for accurate and reliable reconstructions.

Information of past sea ice can be extracted from observations of raised beaches (St-Hilaire-Gravel et al. 2010), drifted material such as wood (e.g. Häggblom 1982; Funder et al. 2011) or from other land-based indicators. Among core records, sea ice proxies can be extracted primarily from two different matrixes: marine sediments from the ocean sea beds and from ice cores, the latter being retrieved on ice sheets or glaciers. Marine cores have been drilled in the Arctic Ocean and in the North Atlantic, as well as in the Southern Ocean. Several marine species, some of which only live in one of the two hemispheres, have been attributed to the presence of sea ice.

Diatoms are a major group of photosynthetic unicellular algae that group into colonies and range in size between 2-200 μm . They are characterized by opal silica frustules and more than 731 species have been identified living in Arctic sea ice and in the Southern Ocean. Despite silica dissolution processes affecting the transport and the preservation of diatoms fossils in the sediment floor, diatoms have been used for sea ice reconstructions in both the northern (Justwan and Koç 2008) and southern hemispheres (Crosta et al. 2004).

Several taxa of benthic and planthic foraminifera, eukaryotic organisms that typically produce a CaCO_3 shell, have been associated to seasonal and perennial sea ice covers (Scott et al. 2009), although it should be noticed that these species are indirectly related to sea ice because no true sea ice species have yet been identified (Seidenkrantz 2013). The use of such organisms as a sea ice proxies shares common limitations as for diatoms, especially if corrosive bottom-waters dissolve the calcium carbonate shell.

IP_{25} (Ice Proxy 25) has been introduced 10 years ago as a new sea ice proxy. It is an organic biomarker, a highly branched isoprenoid (HBI) alkene containing a 25 atom Carbon chain (C_{25}) which is biosynthesised by sea ice related diatoms in the Arctic during the spring algal bloom (Volkman et al. 1994; Belt et al. 2007). IP_{25} is largely limited within sea ice to interstitial brine channels with sufficient networks for diatom growth (Brown et al. 2011), which makes it a proxy of seasonal rather than multi year sea ice or open water conditions (Belt and Müller 2013). To discriminate between the three situations (seasonal and multi year sea

ice, open water), another proxy can be included, namely brassicasterol or dinosterol, two phytoplankton biomarkers considered indicators of open water conditions. The PIP_{25} index is defined as

$$PIP_{25} = \frac{IP_{25}}{IP_{25} + N \cdot OW} \quad (2.4)$$

where OW refers to the open water proxy, brassicasterol or dinosterol, and N is a normalization factor that accounts for the very different scales in concentration between IP_{25} and the open water proxy. The PIP_{25} index now ranges from 0 to 1. High PIP_{25} values (high IP_{25} and low OW) correspond to multi year sea ice conditions. Low PIP_{25} values (low IP_{25} and high OW) are associated to open water conditions, while intermediate PIP_{25} values indicate marginal sea ice conditions. The PIP_{25} has been successfully deployed to reconstruct Arctic sea ice at time scales of tens of thousands of years (Müller et al. 2009; Hoff et al. 2016).

Among the two established sea ice proxies that can be extracted from ice cores are: sea salts, particularly sodium (Na), and methane sulfonic acid (MSA). A growing literature is pointing at two halogen elements, bromine (Br) and iodine (I) as potential proxies. Sodium has traditionally been recognized as linked to sea ice. This validation is based on the fact that it is more concentrated in the glacial periods, when the open ocean was further away. However, sodium signals are particularly sensitive to the extra contribution of open water and to the transport (e.g. Levine et al. 2014), which modulates the sea ice and open water relative contributions to the overall budget. Sodium, bromine and iodine will be addressed in more detail in Chapter 4. Methane sulfonic acid (MSA, $CH_3SO_3^-$) is an end product of the oxidation of dimethylsulfide (DMS, CH_3SCH_3 , see for e.g. Read et al. 2008), which is produced by phytoplankton synthesis of DMSP (dimethylsulfonium propionate, an osmoregulator in plankton cells) and is therefore indicator of ocean productivity (Legrand et al. 1991). High salinity in sea ice brine pockets may involve an increase in DMSP production and an increased sea-ice extent may cause higher DMS (and thus MSA) emissions in the atmosphere (Legrand et al. 1997b). MSA deposition has been linked to Antarctic winter sea ice extent (Curran et al. 2003; Abram et al. 2010) and Arctic sea ice conditions (Maselli et al. 2017) on decadal to centennial scales, although some studies reported that the correlation between MSA and satellite sea ice observations is strongly site dependent (Abram et al. 2013). Several atmospheric studies reported no evidence of such link (e.g. Weller et al. 2011). Postdepositional processes causing loss and migration in the ice layers have also been widely reported to affect MSA, limiting its use to recent periods and high accumulation sites (Curran et al. 2002; Abram et al. 2008).

3

Ice cores

This chapter introduces some concepts of ice cores as climate archives. A selection of chemical impurities found in the liquid phase (ions and dust particles) is discussed, with some of the major results. Then, the traditional measurements techniques for impurity detection in ice cores are introduced, with a particular focus on inductively coupled plasma mass spectroscopy (ICP-MS). [Thomas 2013](#) was used as a guide for the ICP-MS description. Some key components of the instrument are addressed, to give the reader a basic knowledge of this analytical technique which was used thoroughly during the research activities. In particular, the two major designs of mass analyzers are now discussed, the quadrupole (ICP-QMS) and the sector field (ICP-SFMS). Both ICP-QMS and ICP-SFMS techniques have been used for the determination of sodium, bromine and sodium in Renland ice core. The measurements will be discussed in Section 6.6.2, while the results will be presented in Sections 6.2.1 (Iodine) and 6.6 (sodium and bromine).

3.1 A RECORD OF THE PAST CLIMATE

Ice cores are some of the better detailed archives of the Earth past climate. They are drilled on mountain glaciers or ice sheets, where year-round below freezing temperatures allow undisturbed solid deposition and preservation of the original stratigraphy. Ice cores recovered from the Antarctica and Greenland provide the oldest records, covering respectively the last 800 000 and 125 000 years ([EPICA Community Members, 2004](#); [North Greenland Ice Core Project members, 2004](#)). Among the climatic information ice core analyses can give insight to are: past temperatures, volcanism, winds, precipitation, aridity, solar activity and atmospheric composition. The understanding of the forces driving changes in climate through analyses of paleo proxies allows the possibility to improve and better constrain cli-

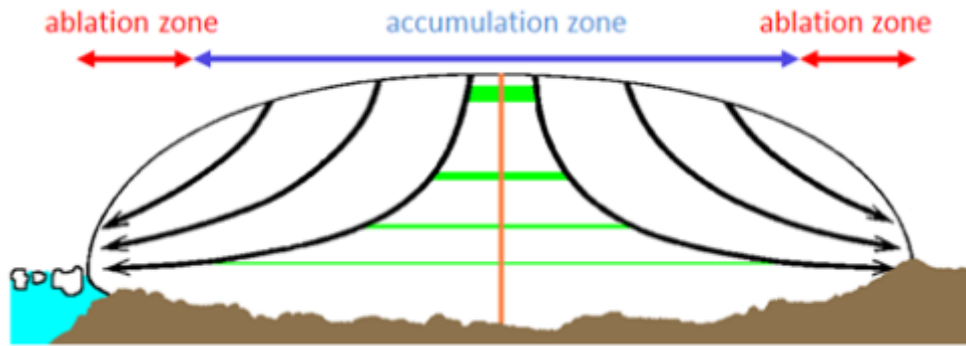


Figure 3.1: A sketch of an ice sheet (Antarctica or Greenland), showing the processes of ice accumulation and ablation, the thinning and flow of ice layers within the ice sheet.

mate models, lowering uncertainties on future climate projections. As an example, ice cores have shown the tight coupling between climate and greenhouse gases, demonstrating that the abrupt recent increase in CO_2 and CH_4 is unprecedented in the last 8 glacial cycles and mankind is playing an active role in modifying the climate (Petit et al. 1999). The analysis of the isotopic composition of water in Greenlandic and Antarctic cores revealed important perturbations in climate, still today being investigated, known as Dansgaard-Oeschger events (Johnsen et al. 1972; Wolff et al. 2010).

A timescale is the function mapping depth of an ice layer to its age since deposition. The timescale depends on several factors like the amount of precipitation at the time of deposition (accumulation rate) and the ice flow, which is in turn depending on the local properties of the site. As a layer of snow is deposited through precipitation, it is progressively pushed down as it compacts and thins. The deformation is due to compaction of snow which progressively increases in density, to become firn and ice. Since ice is incompressible, when density of ice is reached ($\rho_{\text{ice}} \simeq 917 \text{ kg m}^{-3}$), any further deformation takes place in the form of vertical plastic deformation and horizontal spreading. Several methods can be used to derive the timescale, the primary being counting the annual layers of snow, by identifying annual cycles of impurities having a seasonal signature. Below a certain depth, however, this method is challenged by thinning of the ice layers, which become so thin that the diffusion of the water isotopes (for $\delta^{18}\text{O}$ detection) and the finite instrumental resolution (for ionic species and dust particle detection) make this method ineffective. The identification of horizons of known age, like volcanic eruptions or other climatic events, or radiocarbon dating of CO_2 trapped in air bubbles allow an absolute dating of the records. Once an absolute dating is obtained, it is possible to synchronize (convert a depth serie into a time serie) a new record to such established timescale. The most efficient way to achieve such goal is to match methane (CH_4) records, a well mixed gas in the atmo-

sphere whose variations in the atmosphere are therefore expected to be synchronous. Ice cores from Greenland and Antarctica have been "aligned" in time with such technique. A model approach is also used to date an ice core. The flow model is used to describe how the deformation develops with depth: it predicts, for the present-day value of layer thickness, and temperature, how much the deformation would be at a given depth. The comparison between the predicted and the measured thickness at a certain depth gives an indication on how the accumulation rate has changed over time, assuming the other input variables of the model have remained constant.

The annual accumulation rate A , defined as the amount of (solid) precipitation falling in one year per square meter ($\text{kg m}^{-2} \text{yr}^{-1}$), is an important glaciological parameter. It is higher at coastal sites, where humid maritime air masses are forced to rise up to elevated continental cliffs, where condensation and precipitation occur, and lower at inland locations. For example the present day accumulation value at Law Dome,

coastal Antarctica, is $\sim 700 \text{ kg m}^{-2} \text{yr}^{-1}$ (Roberts et al. 2015). At Dome C, further inland in the Antarctic plateau, the accumulation is reduced to $\sim 30 \text{ kg m}^{-2} \text{yr}^{-1}$ (Cavitte et al. 2017). Ice mass losses occur through ablation mechanisms (sublimation and melting) as well as iceberg calving at coastal ice sheets. Generally, in most glaciers and ice sheets both accumulation and ablation zones are present. The difference between accumulation and ablation defines the surface mass balance, SMB, which is responsible for the mass gain ($\text{SMB} > 0$) or loss ($\text{SMB} < 0$) of ice sheets and glaciers. Past accumulation rates can be inferred by calculating the annual layer thicknesses (therefore knowing the timescale) and correcting for the deformation (mostly thinning) they experienced since the original deposition at the surface.

Ice cores are particularly valuable paleoarchives for the past atmospheric composition of the Earth. A major differentiation that is usually made is to distinguish between the chemical compounds that are found in the ice/snow matrix and the gases that are trapped as air bubbles become sealed during the snow densification. Information can also be extracted by analyzing the gases which are undergoing the sealing process as snow is compacted (so called firn air analysis). Firn air studies provide information on the chemical behavior and transport mechanisms of the different gas species during the trapping process. Physical

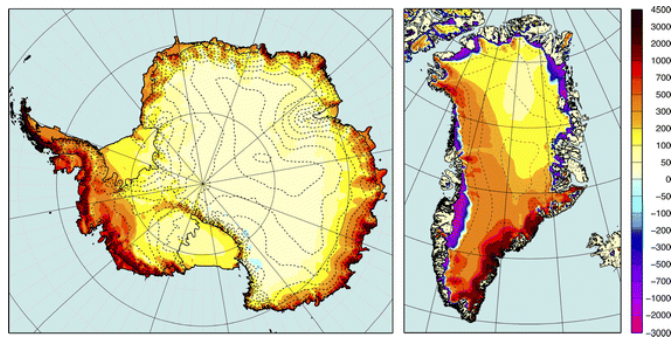


Figure 3.2: Modelled (RACMO2) surface mass balance (SMB, 1989–2009) of Antarctica (left) and the Greenland (right) in $\text{kg m}^{-2} \text{yr}^{-1}$. From Van den Broeke et al. 2011.

properties of the ice layers can also be studied and provide a history of the dynamics of the ice sheet.

3.2 GLACIOCHEMISTRY

The interpretation of the time variability of a chemical impurity record (usually expressed in concentration or depositional flux) depends on a combination of processes, which may be in turn time dependent: emission, transport and deposition. For example, atmospheric circulation patterns that are driving the transport of impurities to Greenland and Antarctica in present times might have not been the same in the past glacial cycles, when climate was colder and the atmosphere drier. As a consequence, the main source areas which are active today might have been different in the past. Additionally, the atmospheric circulation patterns affect the loss of the impurities during their transport and therefore, via the residence time, affect the depositional flux. The "air-snow" transfer function incorporates information on how the impurity is transferred from the atmosphere to the precipitation. Such processes depend on the phase (liquid, gas, solid) and on the chemical reactions involved. For example, a highly soluble gas phase impurity (e.g. HBr) is more likely to be incorporated into water droplets and thus have an additional wet deposition component. Conversely, less soluble gases (e.g. SO₂) will be mostly dry deposited. The relative importance of wet/dry deposition depends also on the accumulation at the specific site. The stability of the impurity in the snow layers after deposition must be addressed to evaluate how robust the stratigraphy is. For example, hydrogen peroxide (H₂O₂), formaldehyde (HCHO), nitrate (as HNO₃), chloride (as HCl) and methane sulfonic acid (MSA) are some of the compounds whose concentration in snow layers has been observed not to be constant after deposition. Among the involved mechanisms: volatilization, photolysis, migration towards neighbor snow layers due to gradients in concentrations. These mechanisms are in turn dependent on properties of the ice core site, such as temperature, impurity load, accumulation rate, wind. Overall, in interpreting the time series of any chemical proxies, these variables have to be taken into consideration.

Measurements of impurities are usually expressed in mass of a specific element or compound per mass unit of water (ice), i.e. concentration C_{ice} . This quantity depends on the concentration of the impurity in the atmosphere C_{air} but also on other variables. In general, the air-to-snow flux J is given by:

$$J = v_d \cdot C_{air} + k \cdot A \cdot C_{air}, \quad (3.1)$$

where C_{air} is the atmospheric concentration of the impurity, A is the accumulation rate, v_d is the dry deposition velocity and k is the scavenging coefficient. The value of deposition

velocity v_d depends on the nature of the species (gaseous or particle), and to its properties like solubility, reactivity, size, and to the nature of the deposition surface. Typical deposition velocities range from $O(10^{-2})$ to $O(10)$ cm s^{-1} * (e.g. see Fig. 9 in [Slinn et al. 1978](#)). The scavenging coefficient k accounts for the rate of transfer of the species into the precipitation. The flux contains a dry ($v_d \cdot C_{air}$) and wet ($k \cdot A \cdot C_{air}$) component. The concentration in the ice is given by:

$$C_{ice} = \frac{J}{A} = \frac{v_d \cdot C_{air}}{A} + k \cdot C_{air} \quad (3.2)$$

From Eq. 3.1 and 3.2 it follows that at sites where wet deposition dominates ($k \cdot A \cdot C_{air} \gg v_d \cdot C_{air}$), the concentration in the ice is proportional to the concentration in the atmosphere, $C_{ice} \propto C_{air}$. Conversely, at low accumulation sites, $J \propto C_{air}$. Therefore for sites dominated by wet deposition, like coastal locations, the time series of concentrations provides the better estimate of atmospheric loading. Fluxes will provide a better representation at dry sites like central Greenland or Antarctica. The question concerning what is the threshold value of accumulation rate above which it is more appropriate to use concentration rather than the flux can be answered by analyzing fluxes in different locations which are believed to experience the same atmospheric loading. Such tests have indicated that wet deposition dominates at site with an accumulation rate above $A \approx 100 \text{ kg m}^{-2} \text{ yr}^{-1}$ ([Legrand 1987](#); [Alley et al. 1995](#); [Wolff et al. 2006](#)).

The water of the oceans has a nearly uniform isotopic composition:

$$\text{H}^{16}\text{O} : \text{HD}^{16}\text{O} : \text{H}_2^{18}\text{O} = 0.99768 : 0.00032 : 0.002. \quad (3.3)$$

A minor percentage is represented by water molecules containing ^{17}O . Due to a higher binding energy the molecules containing the heavy isotopes (D and ^{18}O) have a lower vapor pressure and are preferentially condensed, while light component (H and ^{16}O) molecules are preferentially evaporated from the liquid phase ([Mook and Rozanski 2000](#)). As a result, the isotopic composition of water vapor changes from the moment it evaporates to the moment it precipitates on the ice sheet in the form of snow. The relative fractionations of the isotopic species of oxygen and hydrogen take place at every phase change (kinetic fractionation) but also during the transport from the vapor source to the deposition sites. By defining the isotopic ratio as the ratio of abundances of 'rare' to the 'abundant' isotopes:

$${}^2R = \frac{D}{H}; \quad {}^{18}R = \frac{{}^{18}\text{O}}{{}^{16}\text{O}}; \quad {}^{17}R = \frac{{}^{17}\text{O}}{{}^{16}\text{O}} \quad (3.4)$$

*Let's define: $y = O(10^i) \Leftrightarrow 10^i < y < 10^{i+1}$.

the δ notation is usually used to express the isotopic composition of a water sample:

$$\delta D = \frac{{}^2R - {}^2R_{vsmow}}{{}^2R_{vsmow}}; \quad \delta^{18}O = \frac{{}^{18}R - {}^{18}R_{vsmow}}{{}^{18}R_{vsmow}}; \quad \delta^{17}O = \frac{{}^{17}R - {}^{17}R_{vsmow}}{{}^{17}R_{vsmow}}, \quad (3.5)$$

where iR is the ratio of the isotope under consideration i , as in Eq. 3.4 and ${}^iR_{vsmow}$ is the reference value as in the Vienna Standard Mean Ocean Water (VSMOW), the internationally accepted water with reference values defined by the International Atomic Energy Agency (IAEA). The values in Eq. 3.5 incorporate all the fractionations that occurred since ocean water evaporation (in the liquid phase, $\delta x = 0 \forall x$) and the final precipitation. Precipitation that occurs at ice coring sites originates from evaporation sources at lower latitudes. Water vapor is enriched in the light isotopes and as the water vapor in the atmosphere cools and becomes condensed into water as it travels to higher latitudes, it gets more enriched in the light isotopes (or depleted in the heavy ones). The process is called Rayleigh fractionation. To first order, the processes leading to isotopic fractionation are a function of the amount of cooling that takes place (Dansgaard 1973). Since sea surface temperatures are much more stable than air temperatures at high latitudes, the δ values in polar ice cores strongly correlate with the local atmospheric temperatures. Moreover, the relation between ${}^{18}\delta O$ and mean annual values of local temperature is linear both in Greenland and Antarctica (Johnsen et al. 1989; Lorius and Merlivat 1975). The conversion to absolute temperature using this functional form, yet, is challenged by isotopic modifications that occur in the ice and features at the ice core site that may have changed over time (like elevation, ice flow patterns, differences in the seasonality of the precipitation, change in circulation patterns). Recent studies have used a combination of the δ values, to give information about the conditions at the evaporation site. Landais et al. 2008 used $\delta^{17}O_{excess} = \delta^{17}O - 0.528\delta^{18}O$ from Vostok (Antarctica) in connection to wind speed and humidity in the glacial times. Such proxies are currently under study.

In the liquid phase, the main ionic species found in polar precipitation are Na^+ , NH_4^+ , K^+ , Ca^{++} , Mg^{++} , Cl^- , NO_3^- and SO_4^{--} . Other ions like Br^- , I^- are also found in sub- $ng\ g^{-1}$ range. Together with ionic species, insoluble particulates (dust, ash, pollen) are also found. The relative contributions of these two types of impurities depends on the location of the site, as well as on the climate period. Sea salt contributions are greater at coastal locations; biogenic species are found at greater concentrations in the Greenland, due to closer continental land in comparison to Antarctica. Pollen is found on alpine glaciers; dust is found at different concentrations and size distributions depending on the distance of the source areas (thus the transport) and other climatic variables. Acid species are also present, in the form of HNO_3 , H_2SO_4 and HCl .

Sulfate (SO_4^{2-}) originates from multiple sources. Among these are volcanic emissions, recent anthropogenic inputs (coal, oil burning), sea salts, and as an oxidation product of

DMS, in turn produced by marine biogenic activity. To a first approximation, the non-sea-salt (nss-) contribution to sulfate can be calculated by subtracting the sea salt component from the total sulfate concentration, calculated from sodium (e.g. in Greenland (De Angelis et al. 1997 and Antarctica (Legrand et al. 1988)). The excess sulfate mainly originates from sulfur dioxide (SO_2), converted into sulfuric acid (H_2SO_4). The latter is produced by oxidation of SO_2 in the atmosphere. SO_2 and H_2SO_4 undergo a number of reactions which result in sulfate containing species (Legrand 1997). Among primary SO_2 sources: volcanic emissions, recent anthropogenic inputs and human-related activities, or a product of DMS oxidation. In Antarctica, the sulfur budget was found to be dominated, both in warm and cold periods, by marine biological emissions. Unlike Antarctica, Greenland records show that sulfate has increased four times since the 1850 in response to SO_2 fossil fuel combustion in the northern hemisphere (Mayewski et al. 1990; Legrand et al. 1997a). The recent decrease (since the early 1970s) in sulfate concentrations measured at the Col Du Dome ice core (French Alps) has been attributed to stricter air quality standards (Preunkert et al. 2001). Marine biota and background volcanic emissions equally dominate the sulfur budget in Greenland. Lower MSA and higher SO_4^{2-} concentrations in Greenland ice cores during the last glacial era suggest reduced biological activity and higher terrestrial sulfur inputs in this period (as gypsum mineral, $\text{CaSO}_4 \cdot 2\text{H}_2\text{O}$, or by the reaction between calcium carbonate and sulfuric acid: $\text{CaCO}_3 + \text{H}_2\text{SO}_4 \rightarrow \text{H}_2\text{O} + \text{CO}_2 + \text{CaSO}_4$, Legrand 1997). Several records of methane sulfonic acid (MSA), another oxidation product of DMS, have been produced from ice cores. The reader is referred to section 2.4.

Spikes of ammonium (NH_4^+) in Greenland have been associated to summertime biomass burning events (Whitlow et al. 1994; Legrand et al. 1992; Legrand et al. 1995; Legrand et al. 2016a). This has been confirmed by the presence of black carbon and other species that are characteristic of biomass burning plumes (Wolff et al. 2012). Such events are point-like in time and therefore the signature in a particular location is strongly dependent on the transport conditions at the time of the event. The order-of-magnitude lower concentration of ammonium in Antarctica and the summer time peaks in Greenland support the continental biogenic origin of this compound, ruling out an oceanic source (Legrand and Mayewski 1997).

The electrical conductivity (ECM) of the ice is a non destructive mm-range resolution technique: it is based on the measurement of electric current which flows between two electrodes placed in contact with the ice, at a potential of $\sim 1200\text{V}$. The ECM method provides an indication of the DC conductivity, which is believed to be controlled primarily by the acidity of the ice, $[\text{H}^+]$ (Hammer 1980). A direct calibration between the DC current and the acidity $[\text{H}^+]$ was suggested, although a number of issues exist. The proportionality factor first suggested depends on the geometry of the instruments, on the ice core quality and therefore seems to be an effect of other anionic species associated with H^+ . Although a pre-

cise acidity quantification with ECM is less accurate than direct acidity measurements, the ECM technique is useful to identify very acid volcanic layers, and to help developing age models thanks to the seasonality of its signal (Taylor et al. 1992).

Aeolian particulate matter (dust) consists of insoluble mineral particles, originating from the continental crust. Dust represents an essential supply of nutrients in many ecosystems. In the Southern Ocean, the distance from wind exposed land masses represents a limiting factor for the marine biosphere (Martin et al. 1990). The Amazon forest is greatly fertilized by Saharan dust, transported from Africa to South America over the Atlantic ocean. Dust has also an effect on the albedo of high reflective surfaces, like glaciers, by lowering their albedo and hence changing the heat balance. Dust plays different roles in the clouds, by creating cloud condensation nuclei and by absorbing or scattering sunlight. Dust concentration (or flux) time series reflect a number of variables: area of exposed land masses, wind strength, soil moisture and vegetation cover. The comparison between the geochemical composition of dust in the ice and in areas of the Earth gives indications on its provenance. High concentrations of dust are found in Greenland during the glacial part of the records: such increases have been associated to a low precipitation rate and changes in atmospheric circulation patterns, to include dust source areas which were previously excluded from the circulation (De Angelis et al. 1997). Among these, arid regions of east Asia were recognized to be the main source areas, by studies on the Strontium (Sr) and Neodymium (Nd) isotopes (Biscaye et al. 1997; Bory et al. 2003). The long range transport from Asia appears to be mixed to other sources in the Holocene, possibly of Saharan origin (Lupker et al. 2010). During the LGM, Patagonia was clearly defined to be the source of dust to Dome C (Antarctica). Similarly to Greenland, more proximal sources may contribute in the Holocene (Delmonte et al. 2010). Overall, in both hemispheres the increase of dust fluxes in glacial periods ($J_{dust,LGM}/J_{dust,Hol}=80, 15$ in Greenland and Antarctica respectively) is related to a combination of increased source strength, atmospheric residence time and transport (Fischer et al. 2007b), as a result of a drier climate. Calcium (Ca^{++}) has a crustal origin as well as a marine contribution. The former is dominant in central Greenland, because of closer continental land masses, and shows seasonal maxima in spring (Legrand and Mayewski 1997; Whitlow et al. 1992; Steffensen 1988). In Antarctica, especially at coastal sites, the relative strength of the two sources is more similar (Sommer et al. 2000). Discrepancies in the seasonality in different locations are then found because the marine emissions are stronger in winter while dust has a summer behavior.

Nitrate (NO_3^-) is an oxidation product of several reactions involving NO_x ($= NO + NO_2$). Nitrate concentrations in the snow are therefore linked with past atmospheric concentrations of NO_x . From a South Greenland ice core (Dye 3) Neftel et al. 1985 reported a factor 2 increase of NO_3^- from ~ 1940 because of rising fossil fuel combustion. No such increase is observed in Antarctic records. Multiple sources of NO_3^- exist before the anthro-

pogenic emission period: the reader is referred for example to [Wolff 1995](#). Different factors also challenge nitrate preservation in the snow. Loss of nitrate after deposition has been reported, the suggested mechanisms being the evaporation of HNO_3 ([Röthlisberger et al. 2000b](#)) or photolysis of nitrate itself ([Honrath et al. 2000](#)). Temperature and accumulation are key factors for the preservation of nitrate. Post depositional displacement of NO_3^- has also been found in correspondence to very acid snow layers ([Röthlisberger et al. 2000b](#)). Overall, the interpretation of nitrate in polar ice cores remains a challenge.

Sodium cations (Na^+) and chloride (Cl^-) have a marine origin (the mass of NaCl constitutes 86% of salts in sea water, Table 2.1). From a seasonal perspective, sodium winter maxima have been reported both in Greenland and in Antarctica, a consequence of more frequent advection of marine air masses in winter over ice sheets ([Herron 1982](#); [Legrand and Delmas 1984](#)). Chloride is deposited onto the snow as Cl^- and HCl. The latter is formed during the sea salt 'dechlorination' processes: the reaction of sea salt aerosol with nitric acid (HNO_3) or sulfuric acid (H_2SO_4) leading to HCl. A different fractionation of sodium and chlorine within the SSA (sea salt aerosol) and gas phase HCl then takes place during the transport. Therefore, a Cl/Na ratio higher than in sea water is observed due to longer residence time of the HCl species. The ratio is then lowered below the sea water reference since chlorine is reemitted from the surface snow ([Röthlisberger et al. 2003](#)). Sodium will be described in more detailed in Chapter 4.

3.3 ANALYTICAL TECHNIQUES FOR IMPURITY DETECTION

Different analytical techniques are used to measure impurities in ice cores (soluble and insoluble).

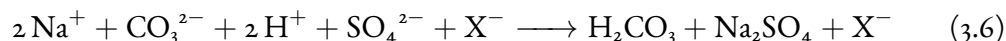
Insoluble particulate matter (dust) concentration is measured by Coulter Counter ([Coulter and Hogg 1971](#)). Information about the number and size of the particles is extracted by measuring the drop of voltage between two electrodes, as the water sample is allowed to flow between them. The 'Abakus' is an alternative laser-based dust concentration detector.

Water soluble ionic species have been traditionally detected by Ion Chromatography. The detection of ionic species with ion-exchange chromatography is based on a stoichiometric chemical reaction between ions in the solution and a substance (usually a solid resin) contained inside a column where the solution is forced to flow into. The resin carries functional groups which can retain the sample ions as a result of electrostatic forces (the sample ions and the functional groups are opposite in charge). Since each ionic specie has a different affinity with the functional group, it is eluted from the column at a different time (called retention time), and is hereafter detected (usually with a conductivity detector).

A solution, called eluent, is used to carry the sample solution along the ion chromatograph. Prior to the sample injection, the eluent anions (in case anions are to be measured)

are retained by the resin functional groups (cations). While moving through the column, the eluent anions continuously compete with each other (a process known as ion exchange). Once injected, the sample anions displace the eluent anions and are retained by the functional groups. Moving through the column, the sample anions compete with the eluent anions and are eventually eluted from the column. An ion with a larger charge and smaller hydrate ionic radii experiences stronger retention by the ion exchange resin and is therefore eluted at a greater time. Elution times are on the order of minutes.

The chromatogram is the graph showing the electrical conductivity signal as a function of time. Each ionic group appears in the chromatogram as a (\sim gaussian) peak whose area is proportional to its concentration in the solution. Since the eluent itself also exhibits electrical conductivity, a suppressor solution is used to lower the background conductivity of the eluent and therefore increase the sensitivity of the analyte ions. As an example, in the Copenhagen IC setup for anion (X^-) detection, the eluent is a Na_2CO_3 solution, and the suppressor is sulfuric acid, H_2SO_4 . The H^+ liberated by the suppressor neutralize the carbonate ion, to form H_2CO_3 , a weak acid. Similarly, the Na^+ eluent cations react with sulfate ions to form Na_2SO_4 :



Since anions and cations in ice cores are often in the $\mu g L^{-1}$ (ppb) or or sub- $\mu g L^{-1}$ levels, ultra-clean handling and decontamination procedures need to be adopted to avoid the measurements of contaminants. Additionally, traditional IC measurements have been done on discrete ice samples which were manually cut and decontaminated from the cores. Order of tens of samples per day were measured until the introduction of Continuous Flow Analysis setups.

Continuous Flow Analysis (CFA) systems have been developed since the 1990s (Sigg et al. 1994). With a CFA setup the ice core is melted and the water flux is extracted, split and delivered to several instruments for online measurements. The main advantage of the CFA is that the core is efficiently decontaminated by saving only the central portion of the core section: the outer layers are usually discarded. Among the instruments that are usually attached to the CFA setup: the water conductivity detector, the Abakus, and several absorption and fluorescence instruments for the detection of anionic (NO_3^- , SO_4^{2-}) and cationic (Ca^{2+} , Na^+ , NH_4^+ , H^+) species, as well as H_2O_2 . Other compounds like total organic carbon (TOC), formaldehyde (HCHO) and black carbon (BC) are sometimes measured. For the description of CFA setups in the framework of ice core measurement campaigns, the reader is referred to Sigg et al. 1994; Röthlisberger et al. 2000a; Kaufmann et al. 2008; Bigler et al. 2011.

Water samples can also be extracted from the CFA water stream and saved for instru-

ments that cannot work in a continuous fashion. Among these, the ion chromatograph and the mass spectrometers. In recent years, however, a considerable experimental effort has been addressed to the implementation of such traditionally-discrete-measuring instruments to CFA setups, thus allowing continuous or semi continuous detection of a wide variety of elements and compounds. Regarding such possibility for ion chromatography (so-called fast ion chromatography), the reader is referred to [Traversi et al. 2002](#); [Cole-Dai et al. 2006](#); [Severi et al. 2015](#). For continuous ICP-MS detection of elemental species, the reader is referred to [McConnell et al. 2002](#); [Knüsel et al. 2003](#). It is worth mentioning that traditional absorption and fluorescence devices (and ion chromatographs) measure the ionic concentration, while ICP-MS instrument detect the total elemental concentration, in spite of their ionic form. An additional contribution in an ICP-MS signal derives from dissolution of particulate matter through plasma interaction or through acid dissolution in case of sample acidification (in such case, the acid recovery is to be quantified prior to the measurement campaign).

During the 2015/2016 Renland ice core measurement campaign, the following water properties and soluble and insoluble species, were detected continuously (Fig. 3.3): electrical conductivity, dust, Na^+ , NH_4^+ , Ca^{2+} , pH, Fe, H_2O_2 , black carbon (BC), methane (CH_4) and water isotopes (oxygen: ^{16}O , ^{17}O , ^{18}O and hydrogen: H, D). During the ice melting, discrete water samples to be measured by offline instruments were continuously collected. The ICP-MS measurements (particularly sodium, bromine and iodine) from the Renland ice core which lead to the results described in Sections 6.2.1 and 6.6 have been performed on such discrete samples.

3.3.1 INDUCTIVELY COUPLED PLASMA - MASS SPECTROSCOPY (ICP-MS)

Inductively coupled plasma mass spectrometry (ICP-MS) is a major analytical technique used to carry out rapid multielement determinations down to the parts-per-trillion level. Among the advantages of ICP-MS instruments: the speed of analysis (in terms of analytical detection, \sim ms, and automation of the experimental routine), low detection limits and isotopic capabilities. Since in the ICP-MS all the species are atomized by the mean of a plasma and single atoms (precisely the mass-to-charge ratio) are detected, the ICP-MS yields the total concentration of each chemical species, irrespective of the several possible ionic forms.

The sample introduction consists of two stages: the generation of aerosol with a nebulizer followed by a droplet selection in the spray chamber. A peristaltic pump is usually used to pump the sample into the nebulizer at a flow rate of $\sim 0.1\text{-}1 \text{ mL min}^{-1}$. Different types of nebulizers are available. The pneumatic nebulizer is the most common and uses a co-introduced argon gas (flux $\sim 1 \text{ L min}^{-1}$) to generate the aerosol. Such devices exist in different designs. In the concentric nebulizer, the sample enters through a capillary tube to a low pressure region, created by gas flowing alongside, next to the capillary. The low

Renland CFA setup
 Holocene ice (0-530m)
 3.0 cm/minute melt rate
 Updated: 1 Nov 2015

Pump values refer to flow speed (mL/min)
 W is waste
 BD is bubble detector
 D is triangular debubbler (Bigler et al, ES&T 2011)
 Injection valves V1 (6 port) and V2 (4 port)
 Red text is Peripump lines used

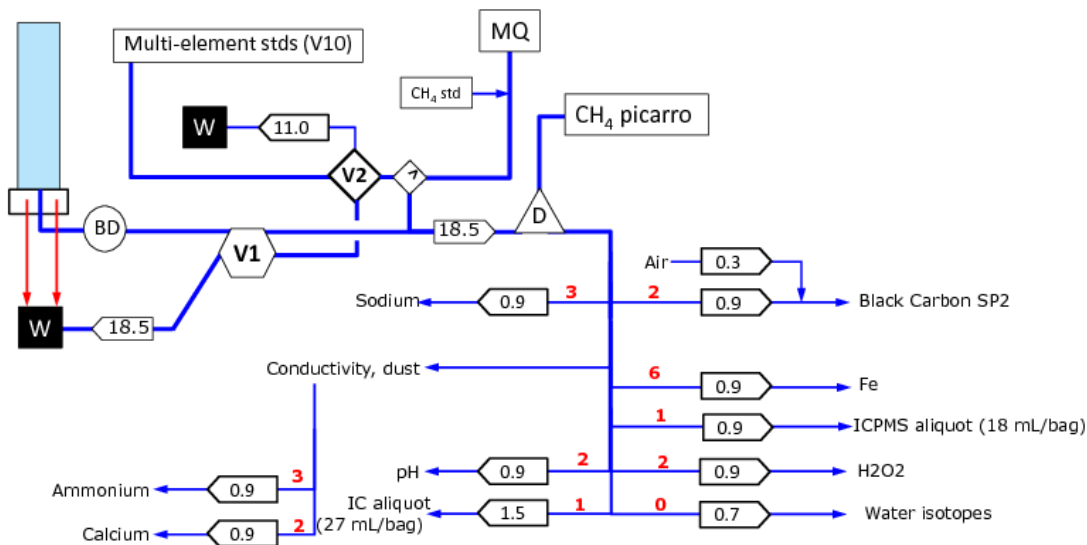


Figure 3.3: Diagram of the Copenhagen CFA setup used for the 2015/2016 Renland ice core measurement campaign. Discrete water samples collected at the ICP-MS line have been used for Na, Br and I measurements (Sec. 6.2.1 and 6.6).

pressure combined with the high speed of the gas combine to break up the liquid solution at the end of the capillary tip. In the crossflow design, the stream of gas is directed orthogonally to the capillary. Crossflow nebulizers are not as efficient as concentric nebulizers in creating very small droplets. Designed to operate at lower ($<0.1 \text{ mL min}^{-1}$) sample rates and higher gas pressures, microflow nebulizers are based on the concentric principle and create a finer aerosol. Since they are more efficient and more sample is allowed to reach the plasma, problems can arise if the samples contain high concentrations of dissolved solids. They are therefore more suited for cleaner sample solutions.

The function of the spray chamber is to select only the small fraction of droplets ($<10 \mu\text{m}$) of the aerosol and to create a uniform flow at the outlet of the nebulizer from the pulses produced by the peristaltic pump. As for nebulizers, different designs are available for spray chambers. External cooling is sometimes applied to some spray chambers for thermal stability and to reduce the amount of solvent reaching the ICP-MS. In the Double pass spray chambers, the large droplets are removed gravitationally. The Cyclonic designs uses the cen-

trifugal force of a vortex created by the tangential flow of aerosol and argon gas. Cyclonic spray chambers offer higher efficiency and therefore higher S/N ratio. Overall, the aerosol which is formed represents $\sim 2\%$ of the sample which is introduced. The larger fraction is discarded.

The plasma torch is composed of three concentric tubes, usually made of quartz. The source gas for the plasma, usually argon, flows between the outer and the middle tube, at a flow of $\sim 15 \text{ L min}^{-1}$. A second gas stream (auxiliary gas) flows between the middle and the inner (sample) tubes, at a reduced flow of $\sim 1 \text{ L min}^{-1}$. In the sample injector inner tube, the nebulizer gas at $\sim 1 \text{ L min}^{-1}$ carries the sample in the form of aerosol. The plasma torch is mounted horizontally and

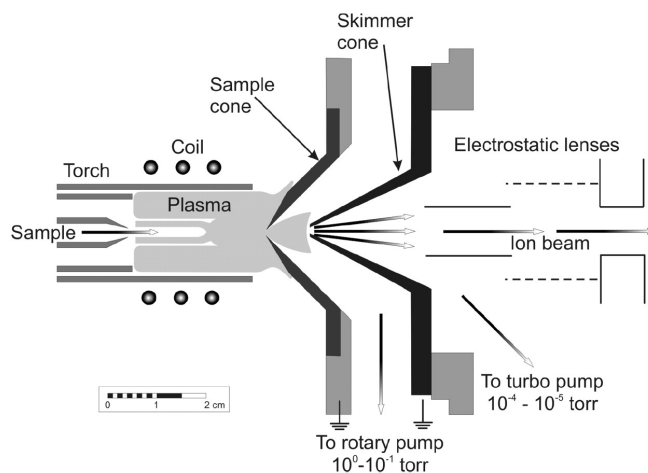


Figure 3.4: The ICP-MS torch. From Košler and Sylvester 2003

centered with respect to the RF coil, at a distance of 1-2 cm from the interface of the instrument. When RF power (27-40 MHz; 750-1500 W) is applied to the coil, alternate current creates an electromagnetic field in the proximity of the end of the tubes. Some initial argon gas molecules Ar_2 are atomized and ionized by a high-voltage spark. A chain reaction induced by accelerated free electrons then continues the ionizing process. The ICP discharge is sustained by the energy transferred by the RF.

The aerosol that emerges from the spray chamber is injected into the argon plasma through the sample injector. As it travels through the plasma, the sample is progressively desolvated, brought into gas-phase and atomized. When it reaches the analytical zone of the plasma, at $\sim 6000\text{-}7000 \text{ K}$, the sample is constituted of ground state atoms, which are finally ionized mainly by argon electrons and to a lesser extent by argon ions. The first ionization potential of argon is 15.8 eV, enough to ionize the majority of the elements in the periodic table ($E_i = 4\text{-}12 \text{ eV}$).

The interface region, which is maintained at 10^{-3} atm by a mechanical pump, consists of two introduction plates, the sampler and skimmer cones, whose role is to introduce and transport the ions from the plasma to the ion optics part of the instrument. The diameter of the sampler cone orifice is 0.8-1.2 mm, while it is reduced to 0.4-0.8 mm in the skimmer cone. Possible dissolved solid deposition can occur on the cones, reducing the flow through

the orifices. To prevent the formation of the so-called "secondary discharge", between the plasma and the sampler cone (in turn created by a potential difference between the RF coil and the plasma of 100-200 V), several methods have been developed, the main one being grounding the RF coil. In fact, if the RF coil is grounded, the plasma will be neutral and the energy spread of the ion beam will be minimal (~ 10 -20 eV). The secondary discharge (or pinch effect) has the following potential negative effects: creation of doubly charged interfering species, production of a wide kinetic energy spread of sampled ions, the formation of ions generated from the sampler cone, and a decreased orifice lifetime. Following the skimmer cone, the ion beam is directed to the 'ion optics' part of the instrument.

The role of the ion focusing system is to transport as many analyte ions as possible to the mass separation component, at the same time rejecting matrix ions and other non analyte-based species. The ion optics consist of several lenses (metallic electrodes of different shape, set at some potential difference) maintained at $\sim 10^{-6}$ atm vacuum by a turbomolecular pump. Different designs are implemented to stop non-analyte species: they are all based on deflection of the charged ion beam into the mass analyzer, while blocking or non-deflecting neutral particles. "Extraction" lenses are placed in modern instruments after the skimmer cone to "pull" ions, in order to reduce the loss of low mass elements, which tend to be pushed off axis by the heavy ions. Because of the drop in pressure after the interface region, the expansion that takes place results in a major diffusion of electrons out of the ion beam. This is the first "natural" charge separation that creates a positive charged ion beam. The drift of light positive ions off axis (repelled by heavier species) is then controlled by a series of lenses. Different ion optics designs exist, all having the function of "steering" and focusing the ions in a narrow beam.

QUADRUPOLE MASS ANALYZER: ICP-QMS

The quadrupole mass analyzer consists of four metallic rods (15-20 cm in length, 1 cm in diameter, in stainless steel or molybdenum) which are set at different potentials. One pair is set at a positive DC and RF voltage; the second pair is set to a negative DC and RF voltage (180° out of phase with the other pair). The quadrupole operates at a pressure of $\sim 10^{-9}$ atm. Without an AC potential, the ions would be attracted to the negative DC rod and be lost. Instead, they are repelled as soon as the positive AC value exceeds the negative DC. The potentials are set so that only ions with specific mass-to-charge ratios are kept and move through the rods to the detector, while all the others are dispersed. The potentials are then changed to allow the detection of a different ionic species. The ions move inside the quadrupole rods in a spiral motion. The scan of all the analyte ions is then achieved progressively, by changing the potential values on the rods.

The resolving power R is defined as $m/\Delta m$, where m is the mass of the analyte and Δm is the FWHM. For a quadrupole, the width of the peak at 10% the maximum height is often

used instead (often called resolution). The resolving power gives a measure of how well two adjacent peaks can be resolved in the final mass spectrum. The ability to separate different masses is determined by different factors, which include the geometry (length, shape, diameter) of the rods, the applied RF/DC voltages, the vacuum pressure and the initial spread in kinetic energy of the ions entering the quadrupole from the ion optics part. The resolution of a quadrupole is on the order of 0.7 - 1.0 amu. When the resolution is increased (by changing instrumental parameters), in general the area of the peak will decrease (therefore a cleaner but smaller signature is obtained). A compromise between resolution and signal strength has to be reached. If the resolution is decreased, a bigger peak will result. However, problems of overlaps with adjacent peaks may arise (the abundance sensitivity is defined as the signal contribution of the tail of an adjacent peak).

When the ions hit the detector, the energy is converted into an electric signal. The typical detector is a SEM (Secondary Electron Multiplier): the first active part of the detector is a a dynode, where the ion impact results in an emission of electrons. The electron signal is multiplied by other dynodes in sequence set at increasing potential. The amplified electric signal is then recorded (as cps, counts per second), and translated to analyte concentration by calibration with standard solutions (i.e. solutions in which the concentrations of each analyte is known).

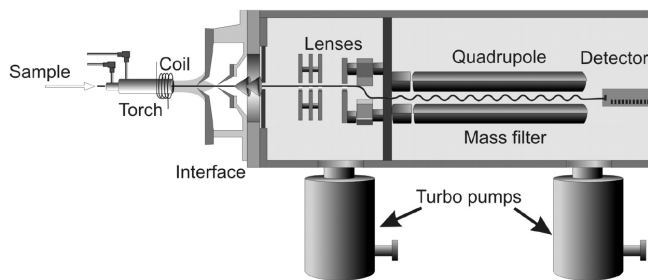


Figure 3.5: Diagram of a quadrupole ICP-MS. From Košler and Sylvester 2003

SECTOR-FIELD MASS SPECTROMETER: ICP-SFMS

Interferences in mass spectroscopy are divided into three categories: isobaric, polyatomic, and doubly-charged species. Isobaric are species having the same mass, e.g. $^{40}\text{Ar}^+$ and $^{40}\text{Ca}^+$. Polyatomic interferences are formed in the plasma when molecular species have the same mass-to-charge ratio as the analyte of interest, e.g. $^{79}\text{Br}^+$ and $^{40}\text{Ar}^{39}\text{K}^+$. The final type of interference occurs with doubly charged species which are not distinguished by the mass analyzer, e.g. $^{136}\text{Ba}^{2+}$ and $^{68}\text{Zn}^{2+}$. To resolve interferences which may occur in quadrupole instruments, higher resolution mass spectrometers have been introduced. Sector field mass spectrometers, ICP-SFMS (or double sector, or double focusing) have a resolving power up to 10000 (compared ~ 300 for a quadrupole-based ICP-MS).

In this setup, ions are accelerated in the ion optics region to a few kV and enter an entrance slit. Here they are bended according to their m/q ratio and velocity v , according to

$$r = \frac{mv}{qB}, \quad (3.7)$$

where q is the charge of the ion (for single ionized ions = $+e$), m its mass, r the radius of the circular trajectory, B the magnetic field of the magnet. For a specific value of B , ions with a specific m/q are selected at the end of the magnet by constraining the radius r with slits. However,

the resolution achievable with a magnetic sector alone is ~ 5000 , due to the ions having a spread in their energy distribution, affecting v . The energy distribution is in turn caused by thermal energy distribution out of the plasma, spatial inhomogeneity of the electric field and spatial distributions of the ions. The dispersion in energy can be avoided by using an electric sector with a radial symmetry (electrostatic analyzer, ESA), which consists of two curved plates with applied DC voltage. The ESA bends and focuses all particles according (only) to their kinetic energy K :

$$qE = m \frac{v^2}{r} = \frac{2K}{r} \rightarrow r = \frac{2K}{qE} \quad (3.8)$$

where q is the ion charge, E is the electric sector field, v is the ion velocity, r the radius of the trajectory. The ESA and the magnetic sectors can be combined together to focus species with a certain m/q and different energies in a narrow point (the exit slit), before the detector. Sector field mass analyzers are differentiated between 'standard' and 'reversed' Nier-Johnson geometry according to the relative positions of the ESA and the magnet. In the standard geometry the ESA is placed before the magnet, and viceversa for a reversed geometry instrument.

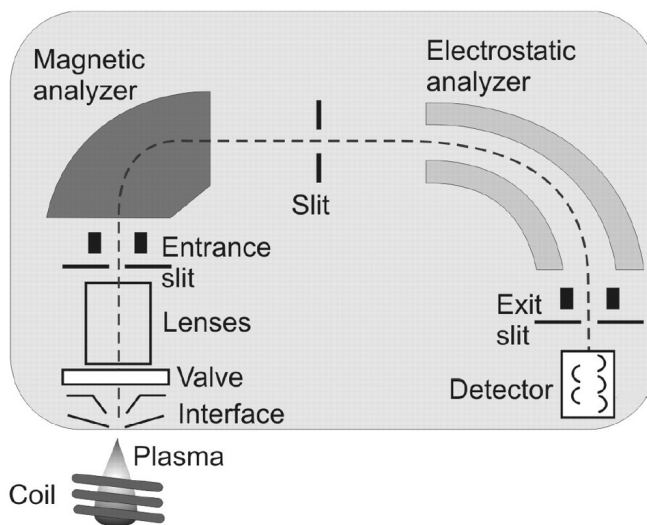


Figure 3.6: Diagram of a sector field ICP-MS. From Košler and Sylvester 2003

4

Sodium and halogens in the polar boundary layer

This chapter investigates some aspects of sea salt aerosols and the halogen chemistry (bromine, chlorine and iodine) which are relevant to the marine and polar boundary layer. It provides the knowledge framework to interpret the measurements of these impurities in ice cores. Particular emphasis is given to the connection of their properties and their chemistry to sea ice, in order to investigate their signature as a sea ice indicator. Chapter 6 will review the already-published measurements on such impurities, and new results performed on the Renland ice core, drilled in 2015.

4.1 SEA SALT AEROSOLS

Sea salt aerosol (SSA) consists of liquid droplets emitted from the ocean and sea ice surfaces. The radii of SSA range from $0.1 \mu\text{m}$ to $1000 \mu\text{m}$, although only those with radii $< O(100) \mu\text{m}$ make it to the marine boundary layer (MBL). SSA contributes to tropospheric aerosols, together with wind-blown mineral dust, sulfate, black carbon and organic carbon (Haywood et al. 1999). The annual global emission of sea salt from the oceans is estimated 10^{12} - 10^{14} kg (Textor et al. 2006). In the polar regions, where anthropogenic contribution is relatively low, SSA dominate the atmospheric mass budget.

SSA affects the Earth's radiative balance, directly by scattering, absorbing and transmitting electromagnetic radiation (shortwave and longwave), and indirectly, by providing cloud condensation nuclei (CCN) and affecting cloud formation. Model studies estimate the annual mean direct radiative forcing induced by sea salt scattering to be -1.52 and -0.6 W m^{-2} for clear sky and all sky respectively (Ma et al. 2008; Ayash et al. 2008).

4.1.1 SOURCES AND PRODUCTION OF SSA

Two main mechanisms are responsible for the production of sea salt aerosols from the ocean surface: bubble bursting and wave crest tearing. The first mechanism originates from the stress of wind on the sea surface. The breaking of waves entrain air into the water in a cloud of bubbles (Thorpe 1992), having diameters of $O(1)$ mm. Following the rise up to the surface, the bubbles burst, releasing $O(10-100)$ nm "film" drops from the bubble cap, which are ejected in the overlaying atmosphere. Following the collapse of the mother bubble bursting, the cavity left behind is filled with liquid. The vertical column of liquid (jet drop) which is then shot vertically,

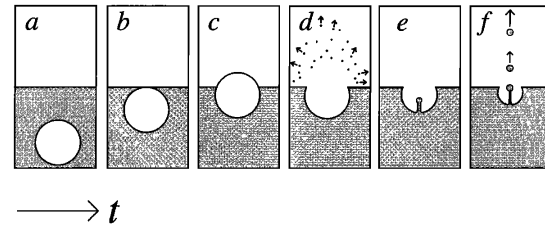


Figure 4.1: Drop formation from bubble bursting. a-c) Rise of bubble to the surface and formation of the bubble film or cap. d) Production of film drops from the bursting of the bubble film. e) Shrinkage of the cavity left by the bubble and formation of a jet rising from the center of this cavity. f) Further decrease in size of the cavity as it is filled by the surrounding liquid, and formation of several jet drops from breakup of the jet. From Lewis and Schwartz 2004.

breaks in turn into 1-10 "jet" drops (Fig. 4.1). Film drop radii are less than $1 \mu\text{m}$, while jet drops span in the range of $2-500 \mu\text{m}$ (e.g. De Leeuw et al. 2011). The white area visible on the ocean, called 'whitecap', is the result of scattering of visible light from the air-water film interfaces. "Spume" drops (Monahan et al. 1983) are produced directly from mechanical disruption of wave crests if the wind strength is above a certain threshold ($5-10 \text{ m s}^{-1}$). These drops are projected nearly horizontally, and have generally bigger size than film or jet drops, with radii up to several $O(100) \mu\text{m}$; they typically fall back to the sea surface within seconds to minutes (Andreas 1992).

Sea spray droplets that are produced from the sea surface are entrained upwards the lower atmosphere (the marine boundary layer, MBL). Here, the motion is provided by the mechanical turbulence caused by wind shear and by the convective turbulence associated with the thermodynamic stability of the atmosphere. Measurements of various trace substances have shown that the MBL is generally well mixed and is isolated from the overlying atmosphere by a thermal inversion. The thickness of the MBL is on the order of $H_{mbl} \sim O(100-1000)$ meters.

Several variables and mechanisms affect the surface properties of the ocean and the overlying atmosphere, which affect in turn the production flux of SSA and its properties (e.g. size distribution, concentration). Wind strength plays a dual role in influencing SSA production flux: it controls the amount of bubbles and drops generated by waves breaking and drives the upwards entrainment of the created droplets by turbulent transport. U_{10} , the wind speed at 10 m height, is usually used to parametrize wind speed in SSA production

flux models. Other variables influencing SSA production are fetch (the ocean area of nearly constant wind velocity), atmospheric stability (often parameterized by the air-sea temperature difference - affecting the vertical transport) and sea water temperature (De Leeuw et al. 2011).

At high latitudes other sources of sea salt aerosols are present: they are connected with the presence of sea ice. As explained in Ch. 2, fresh sea ice has a salinity up to 15‰ (decreasing to 2‰ for aged sea ice).

Frost flowers are crystalline structures that form on new "young" sea ice in cold temperature and low wind conditions. During sea ice formation, brine is moved upwards through brine channels to the colder ice surface by thermomolecular pressure gradient (Wettlaufer and Worster 1995), forming a 2-4 mm liquid brine layer. Brine evaporation creates an overlying water vapor layer that is supersaturated with respect to ice. The growth of frost crystals from the vapor phase and the draw up of surface brine onto the frost crystals by surface tension yield salinities about three times that of bulk seawater, ~ 100 PSU (Rankin et al. 2002). Frost flowers typically last a few days (Xu et al. 2016), before they are buried under snow, sublimated or lifted and transported by wind. The snow cover on fresh sea ice that becomes enriched in salts by contact with frost flowers or with the brine layer can be in turn lifted by the wind, becoming another potential SSA source, as suggested by Obbard et al. 2009. The relative contribution of ocean emissions, frost flowers and salty blowing snow to the SSA budget is not precisely known, although a growing number of studies indicate that salty blowing snow provides the major contribution of sea salt aerosol to polar regions in wintertime (e.g. Huang and Jaeglé 2017).

4.1.2 PHYSICAL PROPERTIES OF SSA

As sea spray droplets leave the sea surface and enter the atmosphere, their size changes since sea salts are hygroscopic. The relative humidity is the major variable affecting the droplet size. At the moment of formation, a drop has a water vapor pressure that corresponds to air RH of 98%; its radius r_{98} is the radius of film, jet or spume drops at the moment of formation. At RH=80%, the radius of the drops shrinks by approximately a factor 2. If the RH is below the efflorescence point of NaCl (45% at 20°C), the particle starts to shrink considerably. The inverse phase transformation, occurring for increasing RH values, is called deliquescence; it is the process by which a supersaturated substance, therefore mostly NaCl, absorbs moisture from the atmosphere until it dissolves in the absorbed water. The deliquescence point of NaCl is 75%. The radius of a 'dry' SSA particle, r_{dry} is half of r_{80} . Overall, for a 35‰ sea water droplet:

$$r_{98} : r_{80} : r_{dry} = 4 : 2 : 1 \quad (4.1)$$

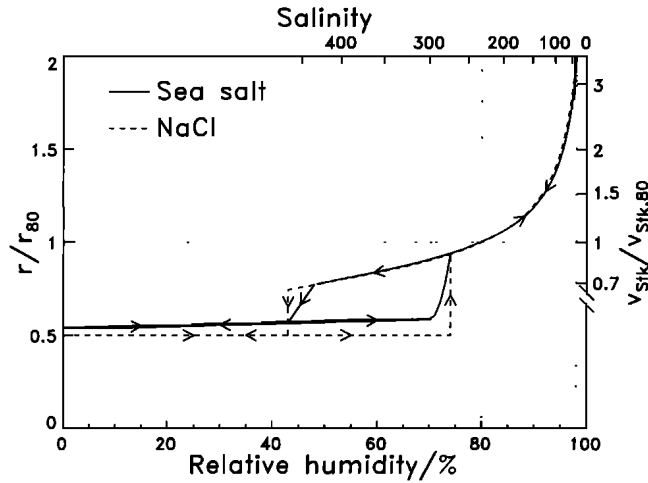


Figure 4.2: Left axis: dependence of the equilibrium radii of SSA (thick) and NaCl (dotted) particles on relative humidity RH. As RH is increased, the size of a dry particle remains constant until the deliquescence point is reached ($\sim 75\%$). Conversely, when the RH is decreased, the particle remains as a supersaturated (with respect to the solute) solution until the efflorescence point is reached. The radius of SSA is always slightly above $r_{\text{dry}}=0.5r_{80}$. From [Lewis and Schwartz 2004](#).

Because of the low deliquescence point of MgCl_2 , which forms some percent of the sea salt mass, sea spray particles are never completely dry ($r_{\text{RH}=0\%} > r_{\text{dry}}$, see Fig. 4.2). Relative humidity values over the Arctic ocean span in the 70-95% range, depending on the season (e.g. [Przybylak et al. 2003](#), Fig. 6.5). A decrease in RH values is observed for increasing elevation, with values around 40% at the top of the MBL.

SSA particles can be characterized by their size, which is assumed spherical. According to their radius or diameter (usually the radius at 80% RH, r_{80} is used) they are classified in the nuclei, accumulation and coarse mode. Aerosols ranging from 0.1 to about $2.5 \mu\text{m}$ in diameter belong to the 'accumulation' mode. It accounts for most of the aerosol surface area and substantial aerosol mass. Particles in this size range originate from the coagulation of smaller particles (which belong to the 'nuclei' mode) and from condensation of vapors onto existing particles, causing them to grow. Gravitational sedimentation has a lower effect on these particles, which tend to accumulate; they have therefore the longest residence time in the atmosphere. The 'coarse' mode accounts for particles with diameter $> 2.5 \mu\text{m}$. Gravitational sedimentation is efficient in this size range, reducing their residence time. The size distribution of the number concentration of SSA particles is defined as the distribution of $n(r_{80}) = dN(r_{80})/d\log r_{80}$, the number of SSA particles per unit volume at a given location and time in a unit logarithmic interval of r_{80} . $N(r_{80})$ denotes the number concentration of SSA particles having $r_{80} < r_{80}$ of the argument. The number distribution $n(r_{80})$

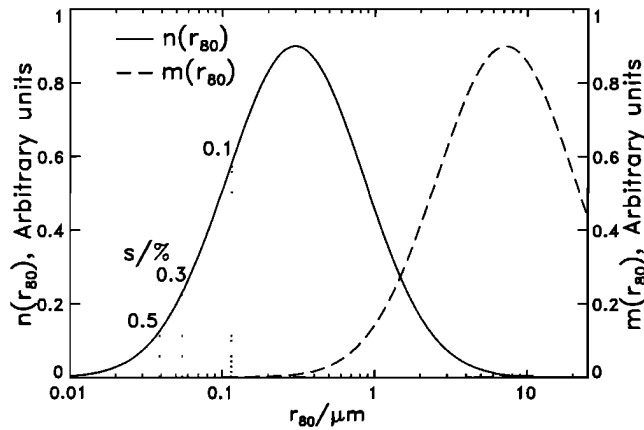


Figure 4.3: Size distribution of SSA number concentration, $n(r_{80})$: a lognormal distribution with $r_{80}=0.3\mu\text{m}$ and $\sigma=2.8$. The dashed curve shows the size distribution of SSA mass concentration, $m(r_{80})=dM(r_{80})/d\log r_{80}$. From [Lewis and Schwartz 2004](#).

describes the relative abundance of SSA particles as a function of r_{80} . It is a relevant parameter to quantify the emission fluxes of SSA and to describe any parameter which depends on the number and the size of SSA particles. The distribution of $n(r_{80})$ is usually found to be a lognormal distribution, with r_{80} parametrizing the geometric mean and σ the geometric standard deviation. An example of the shape of such distribution is displayed in Fig. 4.3. Typical marine SSA size distributions are reported in the sub μm – $20\mu\text{m}$ range ([Warneck 1999](#)).

4.1.3 WET, DRY DEPOSITION AND ATMOSPHERIC RESIDENCE TIME

The removal of SSA particles from the atmosphere occurs through the mechanisms of dry and wet depositions. Such removal mechanisms will affect the amount of SSA in the atmosphere and thus the amount of salts that are deposited at the ice core location. Wet deposition refers to the removal by precipitation. In-cloud or below-cloud scavenging occurs when SSA particles form cloud drops that are directly removed by gravity or by intercepting and merging with other falling liquid or solid water particles. Among the factors that influence the efficiency (rate) of wet deposition are the particle size, shape, hygroscopicity, the concentration and the properties of other particles which can provide CCN, temperature and properties of rainfall (frequency, phase and size of precipitation). Generally, wet deposition processes are efficient in removing SSA in the whole size range (one order of magnitude drop in number concentration is expected for a precipitation event lasting a few hours). In-cloud scavenging is particularly effective in removing small SSA particles (since

they can reach the top of the MBL), while below-cloud removes preferentially larger drops. The mean residence time of SSA in the atmosphere against wet deposition, τ_{80} , can be quantified as the mean time elapsing between precipitation events (which is on the order of a day to a week). On the hypothesis that wet deposition is an effective removal mechanism for all particles, $\tau_{80} \simeq 3$ d, independent of size. This value is expected to be accurate within a factor of 2-3.

Dry deposition (particles and gases) mechanisms include gravitational sedimentation, turbulent transfer, Brownian diffusion, impaction, interception by waves, and scavenging by other particles. Over snow, the filtration of aerosol by the firn layer ("wind pumping effect", [Cunningham and Waddington 1993](#)) is an additional mechanism. The SSA size and the wind speed are the key variables that affect the rate of dry deposition. The vertical downwards flux of SSA particle of size r_{80} intercepting a plane at a given height z can be calculated by:

$$f_d(z) = v_{dry}(z) \cdot n(z) \quad (4.2)$$

usually the reference z taken to be 10 m, since v_d has a weak dependence on z ([Slinn 1983](#)); this altitude is where measurements are usually performed. The dry deposition velocity v_{dry} is an increasing function with respect to particle size, r_{80} , because of increased influence of gravitational sedimentation. The number concentration $n(z)$ also depends on particle size (Fig. 4.3) and on meteorological conditions.

The mean residence time of a particle of size r_{80} against dry deposition, $\tau_d(r_{80})$ is inversely proportional to the deposition velocity and directly proportional to the height over which particles of given size are well mixed, H_{mix} . For a marine boundary layer of height 500 m and wind speed $U_{10} = 10 \text{ m s}^{-1}$, estimates of τ_d for particles of size $r_{80} = 1, 5, 15$ and $25 \mu\text{m}$ are 1.5 weeks, 10 h, 1.5 h and 5 min, respectively (see Table 8 in [Lewis and Schwartz 2004](#)). For particles with $r_{80} \leq 1 \mu\text{m}$, wet deposition is more important than dry deposition ($\tau_{wet} \sim 3$ days independently of size, while $\tau_{dry} = 1.5$ weeks). For a particle size of $2.5 \mu\text{m}$, τ_{dry} and τ_{wet} are nearly the same. Already at $3 \mu\text{m}$, however, dry deposition becomes the dominant mechanism ($\tau_{dry} \ll \tau_{wet}$).

4.1.4 VERTICAL DISTRIBUTION OF SSA PARTICLES

The net vertical SSA flux of a given particle size r_{80} at height z above the water surface, j_z , consists of the sum of several contributions: the vertical transport by mean vertical flow, vertical transport by turbulent diffusion (parametrized by the Eddy turbulent diffusion D_{eddy}), transport by slip-flow (which contains the gravitational sedimentation component and some components linked to the correlation between the fluctuating part of the vertical flow and the SSA number concentration) and the contribution by Brownian diffusion.

The gravitational terminal velocity, v_{term} depends among other variables on the density, viscosity of air (in turn depending on temperature) and on RH. The relative importance of these contributions depends on the height above the surface: in the surface layer gravitational sedimentation and turbulent flux are the dominant terms. Thus, in the surface layer (above the viscous sublayer), if the vertical component of the wind speed is assumed zero (i.e. if convection is neglected), the mean vertical flux can be expressed by:

$$j_z = j_{z,turb} - nv_{term} \quad (4.3)$$

where $j_{z,turb}$ is the turbulent flux, which is proportional to the vertical gradient of the size-dependent number concentration:

$$j_{z,turb} = -D_{eddy} \frac{\partial n}{\partial z} \quad (4.4)$$

The steady state vertical concentration profile can be obtained by imposing $j_z = 0$:

$$D_{eddy} \frac{\partial n}{\partial z} = -v_{term}n \quad (4.5)$$

Equation 4.5 (known as the Rouse equation) yields, for a given height z_1 :

$$\frac{n(z)}{n(z_1)} = \exp\left(-\int_{z_1}^z \frac{v_{term}}{D_{eddy}} dz\right) \quad (4.6)$$

If RH (thus will be v_{term}) and D_{eddy} are independent of height, an exponential dependence of $n(z)$ with height z results. However, for a neutral atmosphere, D_{eddy} is proportional to z :

$$D_{eddy} = \kappa u_* z \quad (4.7)$$

where u_* is the wind friction velocity, κ is the von Karman constant (a dimensionless constant describing the logarithmic velocity profile of a turbulent fluid flow near a boundary with a no-slip condition, ≈ 0.4). The resulting number concentration profile follows a power law:

$$\frac{n(z)}{n(z_1)} = \left(\frac{z}{z_1}\right)^{\left(\frac{-v_{term}}{\kappa u_*}\right)} \quad (4.8)$$

The relative importance of the gravitational term v_{term} and the turbulent diffusion κu_* determines the shape of the concentration profile. Small particles, less affected by gravitational deposition ($v_{term} < \kappa u_*$), become well mixed up to considerable heights; viceversa concentrations of bigger particles will decrease rapidly.

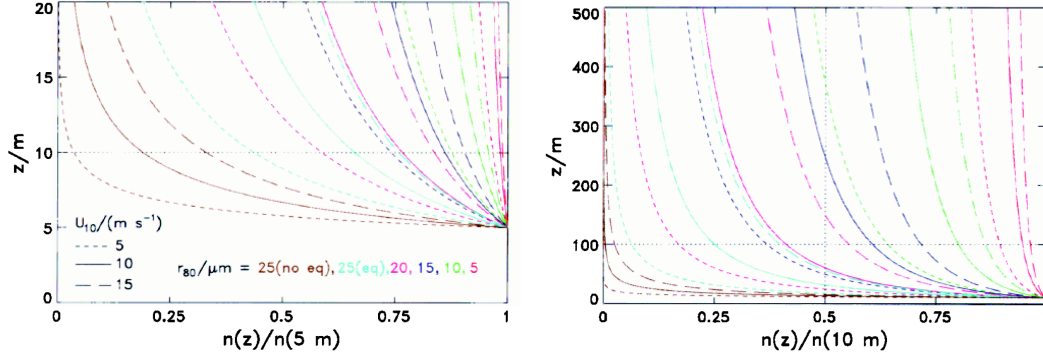


Figure 4.4: Dependence of the steady state number concentration on height from the sea surface, expressed with respect to the concentration at 5 m (right) and 10 m (left), for different particle size and wind speed U_{10} . From [Lewis and Schwartz 2004](#).

The height dependence of the number concentration of SSA in the MBL affects the extent to which air masses can transport a SSA signal to high elevation ice sheets (Greenland and Antarctica). The steady state number concentration in Fig. 4.4 is calculated from Eq. 4.8 under the assumption of neutrally stable atmospheric conditions. The curves can be characterized by z_{50} , the height at which the concentration is 50% of the concentration at 10 m. It can be observed that z_{50} for particles of size $r_{80} = 10, 15, 20$ and $25 \mu\text{m}$ is $z_{50} = 1.2 \cdot 10^4, 230, 60$ and 30 m. Therefore, it can be concluded that particles of size $< 10 \mu\text{m}$ are nearly uniformly mixed throughout the MBL.

Observations from aircraft surveys on SSA concentration profiles roughly confirm these theoretical distributions (references in [Lewis and Schwartz 2004](#)): SSA of size up to $r_{80} \approx 5\text{-}10 \mu\text{m}$ are uniformly distributed up to heights of $\sim 1000\text{-}1500$ m a.s.l. These considerations are used in Chapter 5.6 to estimate the potential SSA sources arriving at the Renland ice cap (East Greenland).

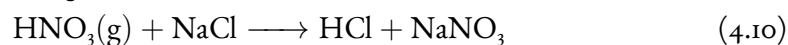
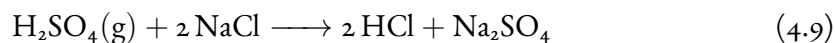
4.1.5 CHEMICAL COMPOSITION OF SSA

At the moment of injection into the atmosphere, sea spray retains the same chemical composition and pH of surface sea water (7.6-8.1). Aerosols rapidly evaporate and equilibrate with ambient RH. SSA contain several types of salts: among those, NaCl (85% of the total salt mass), sulfates ($\text{CaSO}_4, \text{MgSO}_4$) and chlorides ($\text{MgCl}_2, \text{KCl}$). Since the RH in the MBL

is usually greater than the deliquescent point of NaCl (75%, [Warneck 1999](#)), sea salt aerosol exists as hygroscopic liquid solutions of salt species (see Table 2.1). Additional enrichment of organic species, iodine, organisms and bacteria can occur for aged aerosols, especially particles with $r_{80} < 0.25 \mu\text{m}$ ([De Leeuw et al. 2011](#)). Fresh aerosols experience a number of homogeneous and heterogeneous chemical reactions between the components of the bulk liquid aerosol and gases scavenged from the atmosphere or volatilization products from precursor reactions. The rates of the reactions are strongly pH and temperature dependent, and are therefore influenced by the environment to which aerosols are exposed between emission and removal ([Keene et al. 1998](#)).

SSA are able to scavenge gas phase acids (H_2SO_4 , HNO_3 , HCl , HBr) from the atmosphere, for which the aqueous solubility and dissociation rates are sufficiently high. The released H^+ ions can then combine with dissolved anions with the SSA, bicarbonate (HCO_3^-), carbonate (CO_3^{2-}), borate (H_2BO_3^-) and hydroxyl (OH^-). Excess H^+ ions decrease alkalinity of SSA (reaching $\text{pH} < 5$ within 15 min, [Keene et al. 1998](#)). The uptake of acid impacts the nucleation ability of creating CCN. It has often been assumed that the main parameter controlling the uptake of trace gases is the aerosols concentration surface area (e.g. [Covert et al. 1992](#)). pH also controls scavenging rates, which decrease as the aerosol is acidified.

Dehalogenation processes from SSA are important atmospheric processes in the MBL. As anticipated in Section 3.2, chlorine can be removed from SSA via acid displacement reactions:



Loss of chloride occurs via HCl volatilization, especially at low pH (< 4). Other mechanisms for chloride loss via acid displacement involve N_2O_5 , free radicals in SSA or interaction with mineral dust particles. Chlorine can also be degassed via HOCl , Cl_2 , ClNO_2 , BrCl . Halogen chemistry will be further examined in Section 4.2.

As SSA incorporates sulphate and nitrate ions by acid scavenging (R4.1-4.2), the concentration of sodium cations remains constant. The concentration of sodium can therefore be used as a reference for sea water composition.

4.2 HALOGENS IN THE POLAR BOUNDARY LAYER

Halogen chemistry in the PBL received increasing attention since it was observed that ozone depletion events (ODEs) were associated with high levels of brominated compounds (Barrie et al. 1988). Since ozone is the precursor for most atmospheric oxidizers, the removal of ozone changes the oxidizing capacity of the atmosphere, increasing the relative importance of halogen oxidation pathways. Some relevant topics connected to halogens, like the connections with atmospheric mercury (Schroeder et al. 1998) and DMS will not be covered here. The reader is referred to Simpson et al. 2007b and references therein.

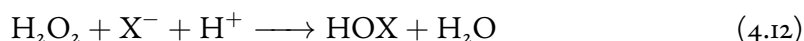
4.2.1 SOURCES OF HALOGENS IN THE PBL

Here, the sources of halogens (Br, I, Cl) in the PBL are described. The role of these sources will appear more clear in Section 4.2.2, where the main reactions of halogen chemistry are described, in association with Ozone Depletion Events (ODEs).

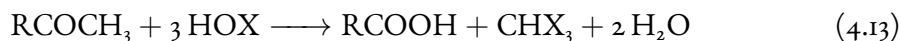
ORGANOHALOGENS

Despite the extreme cold temperatures at polar latitudes, with lows of -40°C in coastal Arctic and -70°C in coastal Antarctica, sea ice gives habitat to both microorganisms (bacteria and micro algae) and macro aggregates. Microbial cells are concentrated in the liquid brine network within the sea ice structure, while ice algae are mostly found beneath the sea ice cover Boetius et al. (2015). Although iodine release mechanisms in polar environments are not fully understood when compared to the observed atmospheric iodine concentrations, organohalogenes from micro and macro algae are believed to be the dominant source for iodine (Carpenter et al. 2003).

The suggested mechanism for organohalogen release (Moore et al. 1996) involves enzymatic processes that convert O_2^- to H_2O_2 , catalyzed by the Superoxide dismutase enzyme (SOD), followed by the reduction of H_2O_2 by halides:



where $\text{X} = \text{Br}, \text{Cl}, \text{I}$. The last reaction has a higher branching ratio for $\text{X}=\text{Cl}$. HOCl quickly reacts with bromide and iodide, forming HOBr and/or HOI. Halocarbons (one or more carbon atoms linked by covalent bonds with one or more halogen atoms) are formed mainly by the reaction of HOX with organic matter (RCOCH₃ compounds):



The "Haloform" reaction (4.13), in combination with halogenation reactions (single substitution reactions in which one or more halogens are added to a organic substrate) lead to the production of all halocarbons, except CH_3I . Bromoform (CH_3Br) is the main brominated organohalogen, while methyl iodide (CH_3I) is believed to be the main organo-iodine in open ocean waters and in the MBL (Moore and Groszko 1999; Cicerone 1981). Sea water measurements of organohalogens in the polar regions have shown that maximum concentrations of several species are higher from the start of the sunlight period throughout summer, in association to algae blooms, and especially near the sea ice edge. Halocarbons can also be produced by algae living within the sea ice matrix and in brine channels: emission in the atmosphere could occur during the sea ice melt season or through diffusion and percolation up to the sea ice surface.

High daytime concentrations of I_2 , precursor of IO, were first measured by Atkinson et al. 2012 in the Antarctic MBL. Some sources of iodine appear to be missing in the Antarctic boundary layer, to correctly reproduce the observed IO concentrations: such concentrations cannot be explained by iodocarbon emissions alone. In Antarctica, Saiz-Lopez et al. 2015 suggested that emissions of inorganic iodine (I_2 and HOI), biologically produced by sea ice micro-algae and diffused and accumulated in the surface brine layer, is the main source of iodine. Follow up studies have suggested that the photolysis of iodate (IO_3^-) in frozen salts can potentially provide a pathway for the release of active iodine to the polar atmosphere (Gálvez et al. 2016), and the production of triiodide (I_3^-) via iodide oxidation, can lead to production and release of molecular iodine, I_2 (Kim et al. 2016). Recently, it was established that emissions of inorganic iodine in the MBL are related to the deposition of ozone and reaction with iodide in surface sea water (Carpenter et al. 2013; MacDonald et al. 2014), thus possibly explaining the missing contribution of iodine in the MBL.

For the atmospheric lifetimes of organohalogens, the reader is referred to Law et al. 2007. In particular, Bromoform (CHBr_3) can be an important bromine source in general but not under bromine explosion conditions (Abbatt et al. 2012), owing to slow photolysis lifetime (≈ 100 days, Simpson et al. 2002). Increased photolysis rates and hence reduced photolysis lifetimes in the upper troposphere and lower stratosphere (see Papanastasiou et al. 2014) make biogenic halogen chemistry relevant at these altitudes (Yang et al. 2005; Salawitch 2006).

HALIDE ACTIVATION IN SEA ICE: FROST FLOWERS, SALINE SNOW, BRINE

The link between frost flowers (FF) as a source of SSA (FF are depleted in sulfate, see Sect 4.2.6) and enhanced tropospheric halogen chemistry was pointed out by Kaleschke et al. 2004 and Rankin et al. 2002. Frost flowers are formed in cold and low wind speed conditions when supersaturated water vapor condenses on the sea ice surfaces. Pickup of brine from the underlying liquid brine layer raises salinity values of frost flowers, observed up to

≈ 100 PSU (Rankin et al. 2002, Fig. 4.5). Different precipitation temperatures of different salts may lead to fractionation of ionic species on the FF, depending on the temperature of formation. Fractionations may occur, for example, during the precipitation of mirabilite ($\text{Na}_2\text{SO}_4 \cdot 10 \text{H}_2\text{O}$) at -8.2°C , $\text{NaBr} \cdot 5 \text{H}_2\text{O}$ at -28°C , hydrohalite ($\text{NaCl} \cdot 2 \text{H}_2\text{O}$) at -30°C . A growing literature, however, is pointing at other sea ice formations as likely main sources of reactive halogens in the PBL, namely salty snow in contact with first year sea ice, FYSI (e.g. Simpson et al. 2007a), limiting the role of FF in bromide activation and as the main source of SSA (Obbard et al. 2009; Domine et al. 2005).

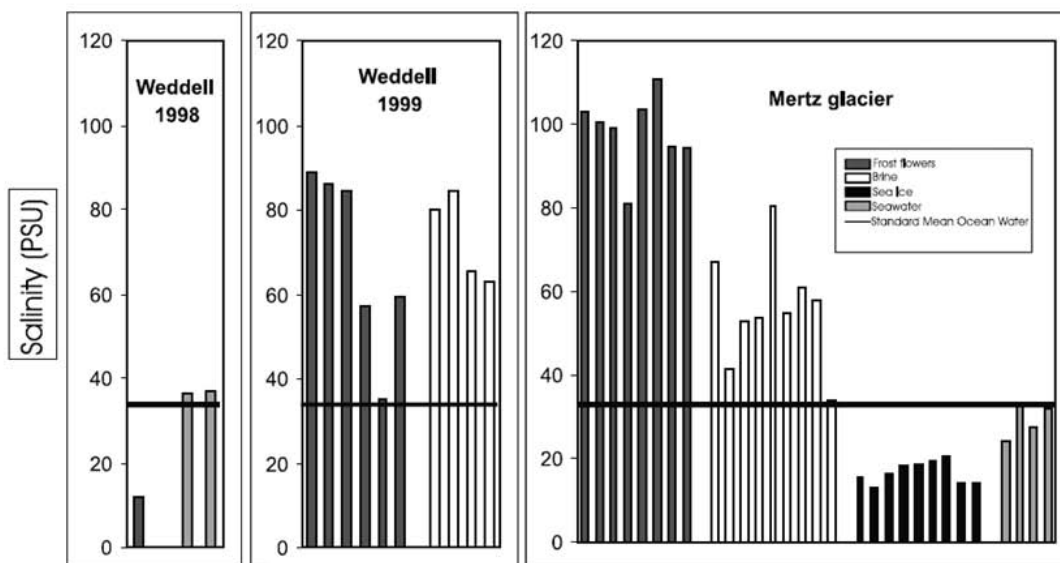


Figure 4.5: Salinities of frost flowers (darker grey), brine (white), ice (black) and sea water (light grey) in Antarctica (Rankin et al. 2002).

Salty snow, blowing from sea ice surfaces, was proposed as a source of SSA and reactive bromine and chlorine (Yang et al. 2008; Jones et al. 2009). The snow cover can be enriched in salts through sea water percolation in fresh sea ice brine channels and through upward migration of salts from the liquid brine layer. An additional mechanism which could be of importance as brine reservoir particularly in thin sea ice in Antarctica is seawater flooding (Sturm and Massom 2009). Measurements have shown that the basal snow has the highest salinity, while snow at the top of the snowpack is more diluted (Toyota et al. 2011). However, sea spray inputs can raise the surface snow salinity, which can be further increased by blowing wind across sea ice, re-exposing the basal layers (Simpson et al. 2007a). Model studies (Yang et al. 2010) and observations (Lieb-Lappen and Obbard 2015) have linked blowing

snow to halogen chemistry. Open ocean SSA can also provide a significant amount of reactive halogens (Yang et al. 2005; Sander et al. 2003).

4.2.2 OZONE DEPLETION AND RADICAL HALOGEN CHEMISTRY

The depletion of stratospheric ozone in the Antarctic environment was related to anthropogenic emissions of Chlorofluorocarbons (CFCs) and other halogenated ozone depleting substances (ODS) in the 1970s (Molina and Rowland 1974). Particularly, the main sink of CF_2Cl_2 and CFCl_3 is UV photodissociation at stratospheric altitudes ($\approx 20\text{-}40$ km), leading to the creation of chlorine radicals (Cl and ClO) while destroying ozone (O_3). Springtime losses of stratospheric ozone were found in Antarctica by Farman et al. 1985.

Ozone depletion events (ODEs) at polar latitudes were also reported within the polar boundary layer (at ground level or in the lower troposphere). Following the Arctic discoveries (e.g. Barrie et al. 1988), similar results found in Antarctica (Kreher et al. 1997) suggested that a similar halogen catalyzed chemistry was occurring at in the PBL in both hemispheres.

Since CFC molecules are extremely stable (the photodissociation occurs only at stratospheric altitudes), while stratospheric ozone depletion is dominated by chlorine and (less importantly) bromine chemistry, bromine cycles play the major role in the troposphere. Ozone depletion events are most commonly observed during springtime, March to May in the Arctic and August to October in Antarctica (since sunlight is necessary to activate photochemistry reactions), and in associations with sea ice, as supported by airborne, ground based, ship-borne and satellite observations (Simpson et al. 2007b and references therein). Low temperatures (≈ -20 °C) seem to enhance halogen activation in polar environments (Tarasick and Bottenheim 2002), although such conditions are not a prerequisite in other environments, like salt lakes and lake beds, where ODEs are observed.

Ozone destruction occurs through the reaction between ozone (O_3) and highly reactive halogen atoms:



where X = Br, Cl or I. Typical conversion times (at 40 ppb O_3) are on the order of 0.1 s for Cl and 1 s for Br and I atoms (Simpson et al. 2007b). Halogen monoxides can be photolyzed to recreate X and ozone, therefore with no net effect on ozone concentration:



The above reaction is often the fastest decay for halogen oxides, taking place on the order of minutes to seconds for BrO and IO (Kanaya et al. 2003). ClO has a much longer photolytic lifetime (Platt and Hönniger 2003), and therefore plays a minor role in the ozone "null"

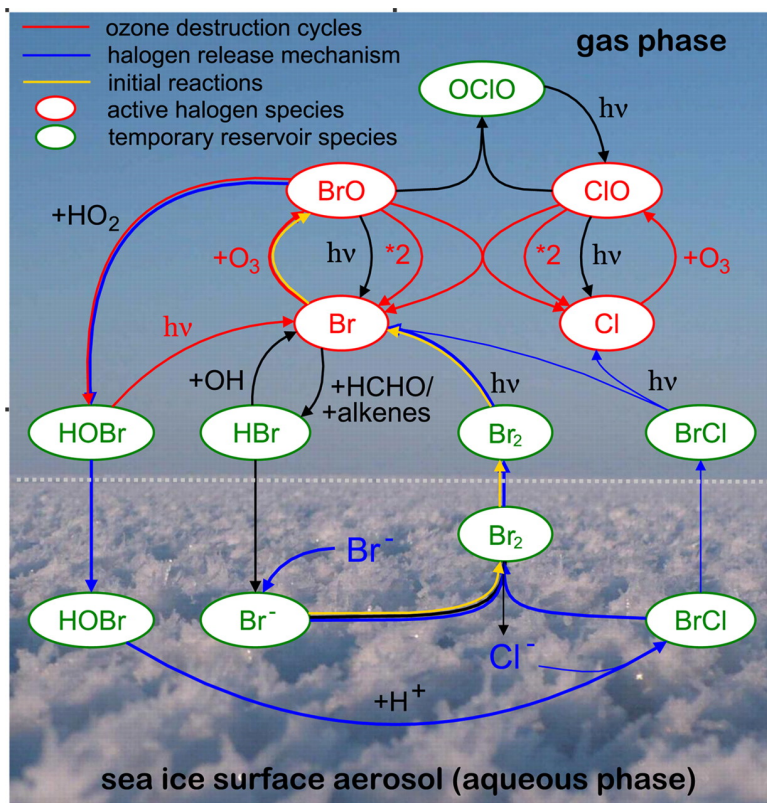
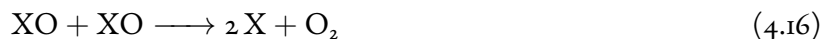


Figure 4.6: A simplified scheme of bromine and chlorine ozone destruction and explosion cycles (chlorine undergoes similar release mechanisms as bromine) from sea ice reservoirs of halides. The picture shows frost flowers in the Amundsen Gulf (Arctic), although liquid brine and salty blowing snow are now believed to play a larger contribution for RHS release. From Pöhler et al. 2010

cycle (R4.15). Since at typical ozone concentrations the halogen oxides exceed the atomic species, which are more reactive, the net effect is to increase the overall lifetime of the X + OX family. The partitioning between X and OX is controlled by R4.14 and R4.15.

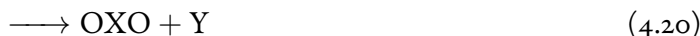
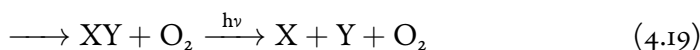
For catalytic destruction of ozone to occur, the halogen oxides must be recycled to their atomic forms without the production of ozone. Several pathways has been shown to occur, but the main ones are self reactions between XO, cross reactions between two different halogen oxides (XO and OY) and reactions between XO and HO₂. The self reaction of XO produces two halogen atoms or a dihalogen, which is readily photolyzed:



For BrO, the branching ratios for the two channels are (at $T = 298$ K) two bromine atoms (85%) and a molecular bromine (15%). The self reaction can also have other products. In the case of ClO, for example, Cl_2O_2 is produced and thermally decomposed back to $\text{ClO} + \text{ClO}$ (Platt and Janssen 1995) or photolyzed in the upper troposphere.

The net combination of ozone destruction (R4.14) and the recycling of XO to the atomic species (R4.16) is: $2 \text{O}_3 \longrightarrow 3 \text{O}_2$. Barrie et al. 1988 suggested the above mechanism to explain ozone depletion in the Arctic, with $X = \text{Br}$.

Ozone depletion (R4.14) can also occur by cross reactions between different halogen oxides:



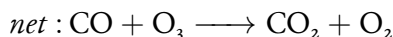
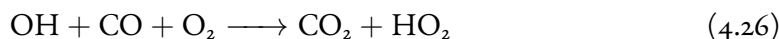
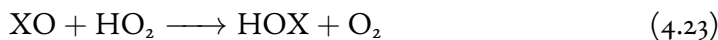
The efficiency and the products of the cross reactions depend on the halogen species involved. For example, the products of the reaction between BrO and IO are OIO + Br (80%) and $\text{I} + \text{Br} + \text{O}_2$ (20%, Atkinson et al. 2008). The reactions between ClO or IO with BrO are about one order of magnitude faster than the self reaction of BrO (Le Bras and Platt 1995; Solomon et al. 1994). The ClO + BrO reaction is believed to be important in the stratosphere, but there is no evidence of significant amounts of ClO in the polar boundary layer (Simpson et al. 2007b). The cross reaction between BrO and IO plays a bigger role in the Antarctic PBL compared to the Arctic, since in the former IO concentrations are higher. In the dioxide halogen channel (R4.20), the photolysis of OXO can mitigate ozone destruction:



For $X = \text{I}$, OIO photolysis (R4.21) can have different products (see Saiz-Lopez and von Glasow 2012 and references therein).

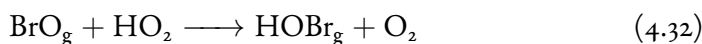
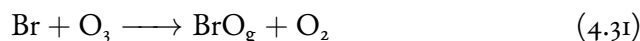
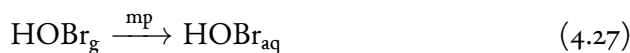
Cross reactions are the dominant pathway for ozone destruction when BrO and IO mixing ratios are ≈ 3 ppt. At lower concentrations, the reaction between the oxide and the

HO₂ radical becomes important:



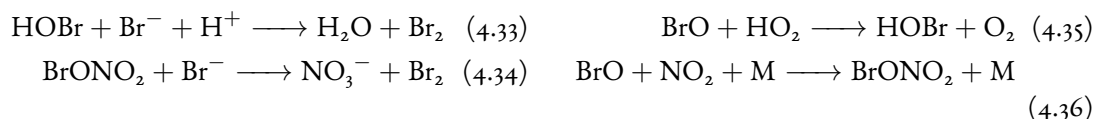
The oxidation of CO to CO₂ may proceed in a similar fashion involving hydrocarbons.

In summary, the reactions that destroy ozone are self reactions (XO+XO R4.16), cross reactions between different halogen oxides (XO+YO, R4.18) and the reaction between an oxide and the HO₂ radical (XO+HO₂, R4.23). In all these reactions, the halogen cycles between the atomic and the oxide form, but the reservoir of radicals eventually decreases by conversion to non radical species like HBr or HOBr. A sequence of multiphase (mp) reactions known as "bromine explosion", which can convert non radicals species back to Br and BrO through scavenging by several kinds of substrates, was postulated to sustain radical chemistry during ozone depletion events (Fan and Jacob 1992; McConnell et al. 1992; Tang and McConnell 1996; Wennberg 1999). For X = Br (Fig. 4.6):

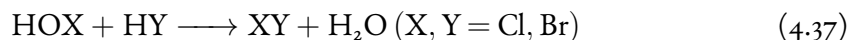


The first of this set of reactions takes place in the liquid brine layer or on the snowpack over sea ice, or in wind-blown sea salt aerosols, where bromide is removed from the saline reservoir and emitted in the gas phase (see Abbatt et al. 2012 for the mechanisms related to the different substrates). The reaction displays therefore a multiphase feature: HOBr gas up-

take by the brine solution, where the reaction occurs in the liquid phase, producing Br₂ which is then degassed from the reservoir. The cycle is autocatalytic since it produces halogen atoms which accelerate ozone depletion. During the reactions, H⁺, HO₂ and Br⁻ are consumed, therefore acidic sources of salts are the favored substrates for bromine explosions to occur. Bromine explosions lead to an exponential increase of gas-phase bromine in the atmosphere, which has been clearly observed by recent satellite measurements of BrO (e.g. [Begoïn et al. 2010](#)). Similar cycles involve BrONO₂ in triggering halogen release from halide reservoirs (like HOBr):



Laboratory studies ([Abbatt and Molina 1992](#); [Abbatt 1994](#); [Adams et al. 2002](#)) have shown that these reactions could also take place in frozen salt matrixes, between the hypohalous acid (HOBr, HOCl) and hydrogen halides (HBr, HCl):



Especially, by studying these reactions on NaCl/NaBr surfaces, [Adams et al. 2002](#) has shown that if the surface becomes bromine-to-chlorine depleted, the preferential product is BrCl rather than Br₂. For HOX = HOI, IBr is the main product until bromine is depleted, followed by release of ICl. Acidity, [H⁺], is therefore an important variable for bromine explosions if the halogen release takes place in liquid surfaces ([Huff and Abbatt 2002](#), R4.28), while in icy substrates it is not as important (R4.37).

Chlorine atoms typically react with hydrocarbons (e.g. methane):



The high probability of R4.38 ($\approx 50\%$ at present day CH₄ mixing ratios) reduce the potential of ozone depletion by chlorine radicals (e.g. [Jobson et al. 1994](#)). For this reason, chlorine explosions are not observed, although in sea salts Cl⁻/Br⁻ is about 650. Molecular chlorine Cl₂ has not been reported in significant amount, BrCl being the dominant source of chlorine during polar sunrise ([Foster et al. 2001](#)).

Similarly to chlorine, no "iodine explosions" are observed, since there is considerable loss of I-atoms by the reaction I+HO₂. This can be due to the high I/IO ratio (modelled value ~ 0.2 , Fig. 7B of [Saiz-Lopez et al. 2014](#)) during the day (in contrast: Br/BrO < 0.01; Cl/ClO < 0.001).

4.2.3 SPECTROSCOPIC DETECTION OF HALOGEN GAS SPECIES

Reactive halogen species (RHS) in the troposphere can be detected by different analytical techniques. Among them, spectroscopic detection of several halogen gas species (ClO, OClO, BrO, IO, OIO, I₂) from satellites, airborne or ground based instruments has played an important role to increase the understanding of the sources and the mechanisms involved in halogen chemistry. For a detailed description of the other techniques, the reader is referred to [Platt and Stutz 2008](#). Recently, cavity enhanced absorption spectroscopy (CEAS) instruments have been introduced (e.g. mode-locked ML-CEAS - [Grilli et al. 2012](#)).

Briefly, the principle of absorption spectrometer trace gas measurements is based on is the *Lambert-Beer* law, which links the absorption cross section at a certain wavelength by a material to its chemical nature, concentration and properties. The transmitted radiative flux I_t of a monochromatic incident flux I_o traveling through an absorber of length l is given by:

$$I_t = I_o \exp\left(-\sum_{i=1}^N \sigma_i \int_0^l \rho_i(z) dz\right) \quad (4.39)$$

where σ_i , ρ_i are the attenuation cross section and the number concentration of the i -th specie in the material sample, respectively. Often the spectral intervals of the target species span in the UV - Visible region (300 - 700 nm). Equation 4.39 is not directly applicable since the absorption spectra of several atmospheric compounds overlap in different λ ranges. Rayleigh and Mie scattering of light by gases and particles in the atmosphere must also be evaluated to extract absorption information of the compounds of interest. To overcome these difficulties, the Differential Optical Absorption Spectroscopy (DOAS) technique was introduced in the '70.

The absorption contribution by the gases are separated from the Rayleigh σ_{Ray} and Mie σ_{Mie} scattering contributions in the Lambert-Beer law:

$$I(\lambda, \vartheta) = I_o(\lambda) \exp\left(-\int \left(\sum_{i=1}^N \sigma_i(\lambda) \rho_i(s) + \sigma_{Mie}(\lambda) \rho_{Mie}(s) + \sigma_{Ray}(\lambda) \rho_{Ray}(s)\right) ds\right) \quad (4.40)$$

where the integral is taken over the light path. If the cross sections do not vary along the light path, and by introducing the slant column as $SC_i = \int \rho_i(s) ds$, one obtains:

$$I(\lambda, \vartheta) = I_o(\lambda) \exp\left(\sum_{i=1}^N \sigma_i(\lambda) SC_i + \sigma_{Mie}(\lambda) SC_{Mie} + \sigma_{Ray}(\lambda) SC_{Ray}\right) \quad (4.41)$$

The Rayleigh and Mie contribution can be approximated by low order polynomials, since $\sigma_{Ray} \sim \lambda^{-4}$ and $\sigma_{Mie} \sim \lambda^{-K}$. The absorption cross sections can also be approximated by a high ("differential") and a low frequency component: $\sigma = \sigma_{low} + \sigma'$. The Lambert-Beer law is then given by:

$$I(\lambda, \vartheta) \simeq I_o(\lambda) \exp\left(-\sum_{i=1}^N \sigma'_i(\lambda) SC_i + \sum_{p \in polys} c_p \lambda^p\right) \quad (4.42)$$

Finally, if the logarithm is taken:

$$\ln(I(\lambda, \vartheta)/I_o(\lambda)) = -\sum_{i=1}^N \sigma'_i(\lambda) SC_i + \sum_{p \in polys} c_p \lambda^p \quad (4.43)$$

In this equation $I(\lambda, \vartheta)$ is measured, $I_o(\lambda)$ is a reference measurement, $\sigma'_i(\lambda)$ is measured in lab-experiments, while the polynomials are fitted to the spectra. The slant columns of the several gas species can be determined by solving the equation at different wavelengths (the least squares approximation). The slant columns given by the DOAS equation indicate the concentrations of absorbers along the actual light path. To get the vertical column, i.e. the absorber amounts in a virtual vertical column above the instrument, it is necessary to convert the slant columns using a so called air mass factor: $AMF = SC / VC$. The AMF can be calculated (numerically) with a radiative transfer model simulating the light path of the observed photons for different viewing modes.

DOAS instruments can be ground-based or air-borne (including satellites). The sun or artificial light sources are used for ground based instruments, while sunlight (or either the moon or star light) is detected in the case of satellite devices. Long-Path DOAS instruments make use of an artificial light source (high-pressure Xenon arc lamp or LEDs), placed at a telescope that acts as a transmitter and receiver unit at the same time. The collimated light beam is reflected by a reflector placed some km away from the light source. The reflected light beam is analyzed by the spectrometer-detector system.

Multi AXis DOAS systems (MAX-DOAS) are a development to the DOAS setup: with the addition of several off-axis viewing directions, varying lightpaths measurements are used to separate the tropospheric and stratospheric absorptions, thus extracting vertical distribution information ([Wittrock et al. 2004](#)).

Several absorption spectrometers have been mounted on satellites, providing global mapping of atmospheric trace gases, including BrO and IO. BrO measurements are available from [GOME](#) (Global Ozone Monitoring Instrument), [GOME-2](#), [SCIAMACHY](#) (SCanning Imaging Absorption SpectroMeter for Atmospheric CHartography) and [OMI](#)

(Ozone Monitoring Instrument) devices, while IO has been detected from [SCIAMACHY](#).

4.2.4 EVIDENCE OF HALOGEN ACTIVATION IN THE PBL

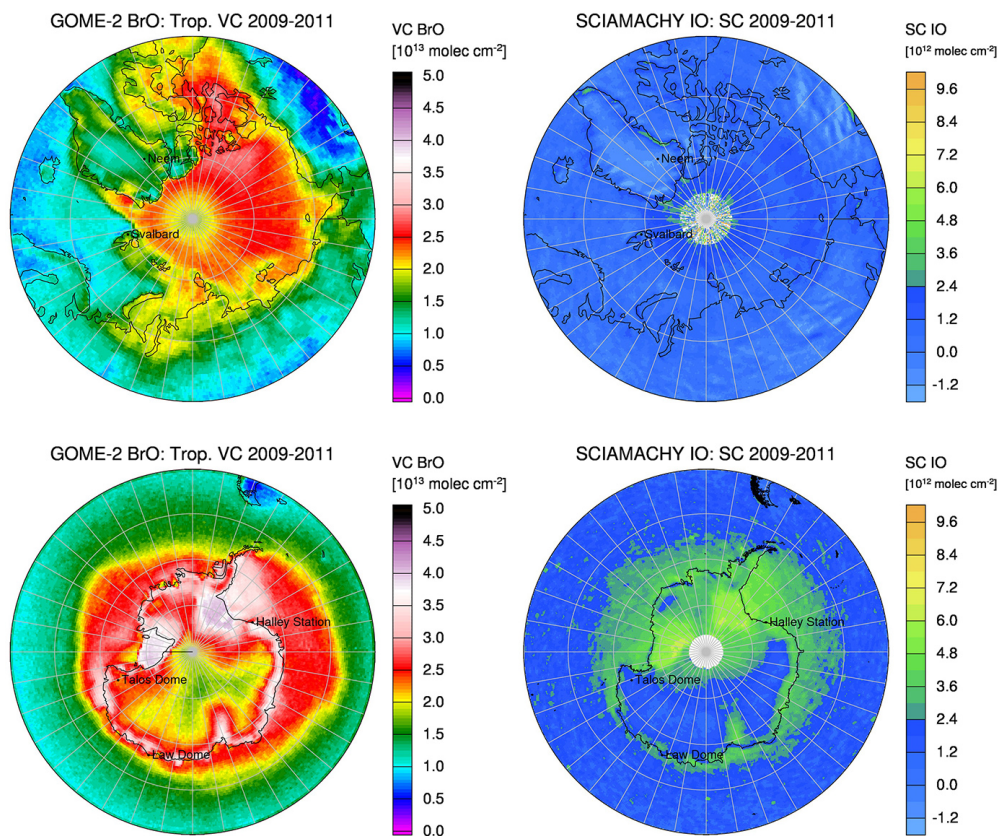


Figure 4.7: Average atmospheric column amounts of BrO and IO in Antarctica and the Arctic between 2009 and 2011. Bromine and iodine concentrations are greatest above the Antarctic ice shelves and along the coast. In the Arctic, iodine concentrations are near detection limit. From [Spolaor et al. 2014](#).

The role of bromine in ozone depletion in the polar troposphere has been demonstrated since [Barrie et al. 1988](#) showed that ozone concentrations were anticorrelated with filterable bromide during the Arctic spring. The discovery was confirmed when simultaneous LP-DOAS measurements of BrO and O₃ were performed by [Hausmann and Platt 1994](#) in Alert (Canada) in April 1992. Subsequently, DOAS measurements in other regions of the Arctic ([Tuckermann et al. 1997](#)) found that high BrO and ClO concentrations (~ 30 ppt) were found to coincide with low ozone events. High BrO concentrations were also detected in the free troposphere by high-altitude aircrafts, the suggested transport mechanisms be-

ing convective transport over large Arctic ice leads, providing surfaces like ice crystals and SSA for heterogeneous reactions (McElroy et al. 1999). The role of chlorine chemistry was investigated in the Polar Sunrise 1992 Experiment (Jobson et al. 1994) in connection with hydrocarbons. The study concluded that chlorine atom concentrations were too low to account for the ozone destruction in a significant way. Halogen-catalyzed boundary layer ozone depletion events were also found in August-September in Antarctica, when BrO concentrations at the same order of magnitude as in the Arctic and low ozone concentrations were detected from ground-based measurements (Kreher et al. 1997; Hönninger and Platt 2002) and satellites (Wagner and Platt 1998). Almost all of the studies that report elevated BrO concentrations over sea ice surfaces also reveal a characteristic daily cycle with the concentration profile following sunlight. For example, springtime LP-DOAS measurements of BrO on sea ice surfaces in the Amundsen Gulf (Arctic) have revealed highest BrO concentrations during sunlight hours, with morning and evening maxima and a minimum at noon (Pöhler et al. 2010).

Halogen measurements since the 1990s went in hand with modelling studies, trying to elucidate the pathways of the involved reactions and the sources of halogens in the PBL. Mozurkewich 1995 suggested that sea salt aerosol is a source of gas phase bromine and Vogt et al. 1996 proposed an autocatalytic mechanism for halogen release from SSA. Reactive iodine (IO) was detected in Antarctica near the Weddell Sea (Saiz-Lopez et al. 2007b), with concentrations up to 20 ppt and diurnal cycles with noon maxima, in spring. Iodocarbons from phytoplankton colonizing sea ice were speculated to be the source of iodine. A follow up study (Saiz-Lopez et al. 2015) has also shown that biological emissions of inorganic iodine from sub-ice algae also contribute to atmospheric iodine budget, in Antarctica. Unlike Antarctica, below detection limit IO concentrations (~ 1 ppt) have been reported in the Arctic environment (Tuckermann et al. 1997; Hönninger et al. 2004; Pöhler et al. 2010). The pole-to-pole "iodine asymmetry" may be explained by the different thickness of sea ice (in Antarctica, the average thickness is 50 cm, compared to 3 m in the Arctic) or by different algae colonies living in the two polar environments. Recent enhanced sub-ice biological production and sea ice thinning experienced by Arctic sea ice are potentially increasing iodine fluxes since few decades (see Sect. 6.2.1).

Since the availability of spectroscopic measurements from the Global Ozone Monitoring Experiment (GOME), launched on the ESA ERS-2 satellite in April 1995, measurements of vertical column density of BrO plumes over sea ice surfaces have been widely reported at both poles (Richter et al. 1998; Wagner and Platt 1998; Chance 1998).

Recent studies have investigated the properties of snow/ice samples in relation to their ability to produce halogen compounds. During field experiments in Alert (Canada), Br₂ and BrCl were detected at concentrations up to ~ 25 and 35 ppt, while Cl₂ was not detected above the 2 ppt detection limit (Foster et al. 2001). Snow chamber experiments with various

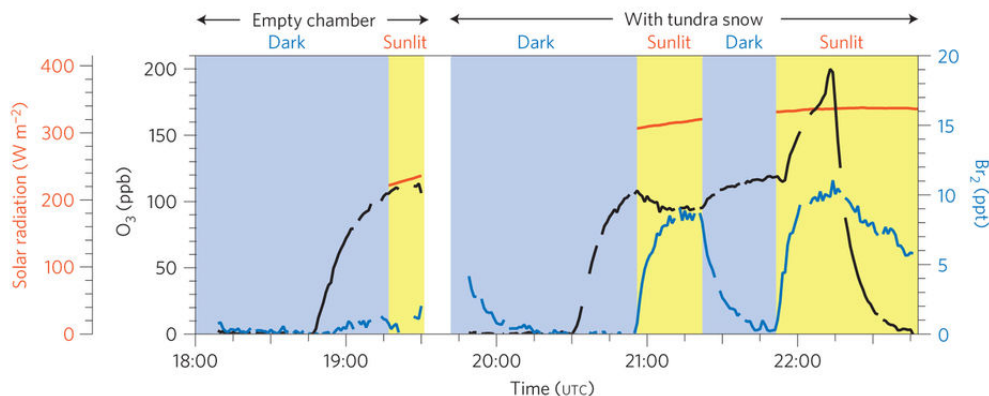


Figure 4.8: Br₂ production during a snow chamber experiment. From Pratt et al. 2013.

saline snow and sea ice samples were carried out to investigate molecular bromine production when exposed to ambient radiation and ozone: molecular bromine, Br₂, was detected only on exposure of surface snow (collected above tundra and first-year sea ice) to sunlight (Pratt et al. 2013). This suggests that the oxidation of bromide is facilitated by a photochemical mechanism (Pratt et al. 2013). The authors also found that such a mechanism is most efficient for acidic samples (pH 4.6-6.3), and characterized by enhanced bromide to chloride ratios (molar ratio Br⁻/Cl⁻ \gtrsim 1/200). The study suggested that snow covered first-year sea ice was therefore the most efficient halogen activation source, since Arctic first-year sea ice is covered on average by \sim 29 cm of snow in the springtime (Kwok et al. 2011), and frost flowers and brine on the new sea-ice surface are characterized by high pH and low Br⁻/Cl⁻ ratio. Moreover, the study also suggested that bromine explosions occurred most rapidly in the interstitial air of the snowpack with Br₂ release to the atmosphere primarily through wind pumping (Abbatt et al. 2012). Similar results for photochemical bromine and chlorine activation within (artificial) saline snow were obtained by Wren et al. 2013. The correlation between elevated BrO concentrations and contact with first year sea ice (Simpson et al. 2007a) is therefore consistent with snowpack photochemistry. Considering the short lifetime of BrO, observed BrO plumes lasting several days also suggest that blowing snow and SSA provide a reservoir for halogen recycling within the plume. The model studies (Yang et al. 2008; Yang et al. 2010) suggesting the role of blowing snow as a source of SSA and bromine are therefore being supported now with an increasing number of observations both in the Arctic and Antarctica (e.g. Zhao et al. 2016; Liao et al. 2006; Jones et al. 2009; Frieß et al. 2011). In a recent study, Peterson et al. 2017 measured a BrO plume, at 1-2 km altitude (Barrow, Alaska). Concurrent aerosol particle measurements suggest that this lofted reactive bromine plume was transported and maintained at elevated levels through heterogeneous reactions in collocated supermicron aerosol particles, independent of surface snowpack

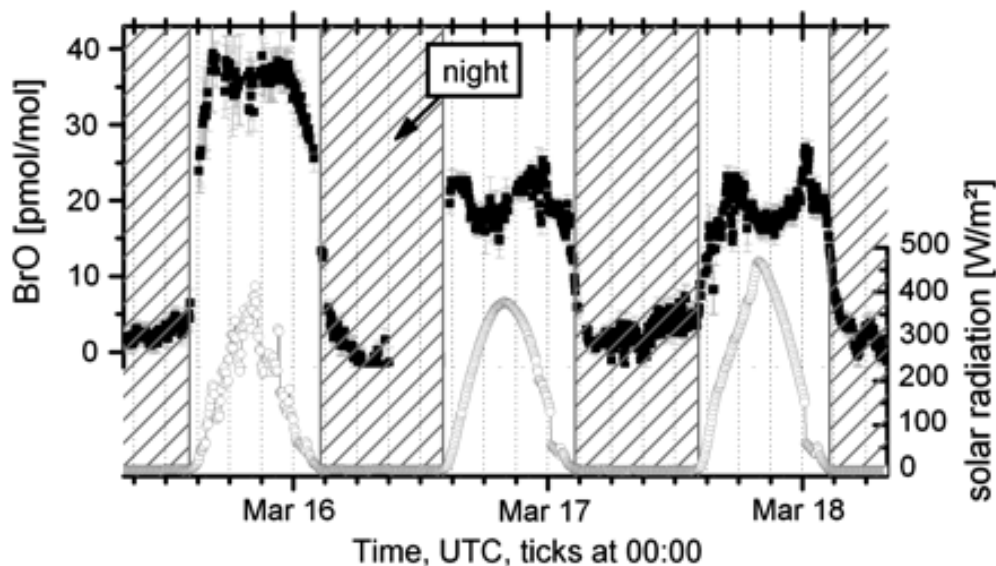


Figure 4.9: LP-DOAS BrO measurements over sea ice in the Amundsen Gulf (Arctic). From Pöhler et al. 2010.

bromine chemistry. Hence, high tropospheric bromine concentrations are also sustained by recycling in SSA particles during the air mass transport.

Although high BrO concentrations extend to some hundreds of metre within the PBL (Frieß et al. 2011), some studies have reported that both in the Arctic and Antarctica, large amounts of BrO frequently extend to several km altitude in the free troposphere, when high winds cause increased vertical transport above the convective boundary layer up to 1-2 km (Koo et al. 2012; Choi et al. 2012; Frieß et al. 2011; Roscoe et al. 2014). Stratospheric contributions can also affect the vertical column density of BrO (Salawitch et al. 2010). The relative importance of the stratospheric contribution to the total BrO vertical column density at polar latitudes, the BrO hotspots being at present mainly at tropospheric altitudes, are not believed to have played the major contribution in the past, since stratospheric sources of bromine are long-lived organic bromine compounds mostly of anthropogenic origin (CBrClF₂, CBrF₃, CBrF₂CBrF₂) (Theys et al. 2011).

4.2.5 HALOGEN ACTIVATION FROM CONTINENTAL SNOWPACK

The activation mechanism of halogen compounds from continental snowpacks on ice sheets or other locations far from source regions is particularly relevant in order to investigate their preservation after deposition and therefore for the correct interpretation of halogen timeseries in ice cores.

At Summit, Greenland, Dibb et al. 2010 measured gas-phase soluble bromine mixing

ratios of up ~ 0.6 - 0.7 ppt, with mean Br^- concentrations in the snow between 8 and 15 nM. The authors suggest that the photochemical activation of Br^- in the snow sustains active Br chemical cycling above the snow. Consistent with [Dibb et al. 2010](#), at the same site [Stutz et al. 2011](#) reported mixing ratios of BrO up to 5 ppt in May and June (average 1-3 ppt), photoactivated and released from the snow. [Thomas et al. 2011](#) developed a coupled snow-atmosphere chemistry model, the chemical interaction of interstitial air with snow grains simulated by assuming chemistry in a liquid-like layer (LLL) on the grain surface. The authors managed to reproduce the observed BrO and NO mixing ratios, sustained by photoactivated bromine in the snow. In Antarctica, an investigation combining model and measurements (denuder tubes/snow sampling) was carried out by [Legrand et al. 2016b](#) both on the coast (Dumont d'Urville station, DDU) and inland (Concordia station). In summer, the estimated gaseous inorganic bromine mixing ratios derived from bromide measurements made on denuder tube extracts (10 and 4 ng m^{-3} at DDU and Concordia, respectively) are consistent with model simulations, suggesting sea salt as the main source of gaseous inorganic bromine species. In addition, in summer, it is shown that the observed bromide content of snow (~ 0.1 ppb) is not large enough to serve as a source able to maintain the observed gaseous inorganic bromine mixing ratios at Concordia ([Legrand et al. 2016b](#)).

In light of the above considerations, it is still clear that some doubts persist in quantifying the fraction of bromine that is reactivated and lost from the snowpack, and not further redeposited, and how much of the loss depends on the absolute snow concentration.

Laboratory experiments have shown that iodine activation from the snowpack may proceed via:

- $\text{O}_2(\text{aq}) + 4 \text{H}^+ + 6 \text{I}^- \longrightarrow 2 \text{H}_2\text{O} + 2 \text{I}_3^-$. Iodide can be oxidized to triiodide slowly in the aqueous phase in the presence of O_2 , in acidic conditions. The reaction is accelerated in frozen solutions in both dark and irradiated conditions. In the equilibrium between iodide and triiodide, $\text{I}^- + \text{I}_2 \rightleftharpoons \text{I}_3^-$, I_2 may be lost in the gas-phase ([Kim et al. 2016](#)). It should be noticed that in the experimental setup, the authors have added 1 mM of iodate (several orders of magnitude above the concentration of I^- found in polar snow). It would be interesting to know how much of I_3^- originated in the above reaction depends on the original I^- concentration, in order to quantify the loss of I^- via this mechanism.
- $\text{NO}_2^- + \text{IO}_3^- \longrightarrow \text{NO}_3^- + \text{I}^-$, followed by I_2 release in the atmosphere. This reaction is shown to occur within bulk ice even in dark conditions ([Kitae et al.](#), in prep.).

In-situ observations of iodine loss from continental snowpack have been reported in Antarctica and are described in more detail in Sec. 6.1.3.

4.2.6 SEA ICE PROXIES IN ICE CORES: SODIUM AND BROMINE ENRICHMENT FACTOR

From the observational perspective, two lines of evidence support a predominant source of sodium from sea ice compared to open ocean, in coastal Antarctica. A first connection between SSA and sea ice was suggested, in connection to measurements of snow samples with depleted sulfate (relative to sodium, in sea water). At $-8\text{ }^{\circ}\text{C}$, sodium and sulfate precipitate out as mirabilite ($\text{Na}_2\text{SO}_4 \cdot 10\text{ H}_2\text{O}$). Thus, preferential removal of sulfate compared to sodium (which precipitates as NaCl at $-30\text{ }^{\circ}\text{C}$) will reduce the $\text{SO}_4^{2-}/\text{Na}^+$ ratio in liquid brine. Alternatively, a negative non-sea-salt sulfate will result: $\text{nssSO}_4^{-2} = \text{SO}_4^{-2} - \text{ssSO}_4^{-2}$, where ssSO_4^{-2} is sulfate in seawater (estimated to be 0.25Na^+) (Rankin et al. 2002). Observed sulfate-depleted snow samples have therefore been associated to fractionated salt on sea ice surfaces. Secondly, concentrations of sodium have been reported with summer minima and winter-spring maxima in coastal Antarctica (e.g. Wagenbach et al. 1998; Weller et al. 2011). Such seasonality suggests that the signal originates from sea ice, since greater winter wind speeds do not seem sufficient to explain such observations (Wolff et al. 2003). Additionally, concentrations (and fluxes) of sodium during glacial times are higher than interglacial periods, models not being able to explain such a difference just by stronger circulation during such cold periods (Mahowald et al. 2006). A sea ice source appears to be necessary to explain the observed sodium concentrations. In inland Antarctica, the sea ice signature is weaker, and sulfate fractionation is not so strongly observed, although some evidence exists (Hara et al. 2004). Sodium was indeed related to past sea ice extent at multi-millennial timescales (Wolff et al. 2006).

In Greenland, authors have generally identified connections between sodium and particular atmospheric circulation patterns rather than with sea ice conditions (Fischer 2001; Hutterli et al. 2007), despite a similar seasonal pattern of high winter sodium concentrations.

Overall, although some features link sodium with sea ice, lacking quantitative calibration and a coupled open water and meteorology influences (Rhodes et al. 2017) make sodium a qualitative proxy for past sea ice reconstructions.

In recent years, bromine excess (or non-sea-salt bromine, nssBr) beyond the expected concentration in sea water (assumed from sodium as $0.0062 \cdot \text{Na}$, Millero et al. 2008) was used as an indicator for the bromine recycling mechanisms over fresh sea ice surfaces that exponentially increase atmospheric bromine, as described in Sec. 4.2.2:

$$\text{nssBr} = \text{Br} - 0.0062 \cdot \text{Na} \quad (4.44)$$

Equivalently, the bromine enrichment is defined as:

$$Br_{enr} = \frac{Br}{0.0062 \cdot Na} \quad (4.45)$$

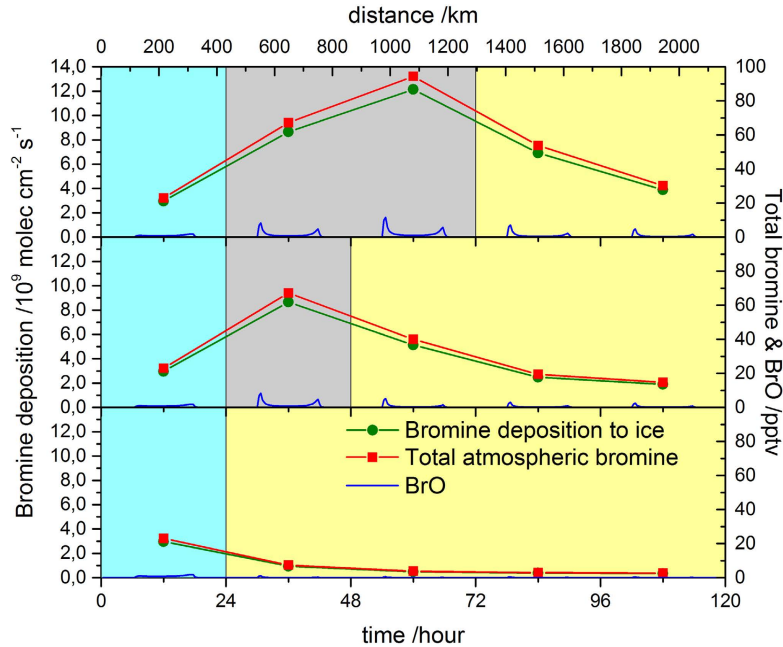


Figure 4.10: Simulated diurnal averages of total atmospheric bromine and deposited bromine, along with gas phase BrO mixing ratios. Three simulations were run to illustrate the sensitivity of bromine deposition at NEEM to distant “bromine explosion” events. In each case, the air mass initially spends 24 hours over open ocean (blue). (a) Upper panel shows 48 hours over FYSI(grey) with active bromine recycling on the surface, and 48 hours over MYSI/Greenland (yellow). (b) Middle panel shows 24 hours over FYSI (grey) with active bromine recycling on the surface, and 72 hours over MYSI/Greenland (yellow). (c) Lower panel shows the simulated air mass without encountering FYSI. From Spolaor et al. 2016b.

Let us first assume SSA originates from open water and the air mass does not contact any fresh sea ice surfaces during its path from source to deposition areas. Sodium concentration within the SSA would not change much. Bromine, on the other hand, would be activated within the SSA and emitted in the gas-phase as Br_2 . Loss of bromine is therefore expected from the liquid phase, as gas phase bromine accumulates in the atmosphere. The mechanisms, already described above, were suggested by Vogt et al. 1996 and have been observed by, for example, Peterson et al. 2017. Thus, it is to be expected that, although some bromine could go back into the aerosol phase as HBr, the loss of gas-phase bromine would lead to $Br_{enr} < 1$ in the liquid phase. Dry deposition of gas-phase bromine at the deposition

site could further reduce the Br_{enr} depletion. Overall, if no excess of bromine from sea ice occurs, Br_{enr} from an open water source is expected to be low ($Br_{enr} \simeq 1$; $nssBr \simeq 0$). The interpretation is based on the hypothesis that the relative transport of sodium and bromine is similar: this point is further discussed in Sec. 6.1.4.

Conversely, the influence of fresh sea ice would exponentially increase gas-phase bromine, as observed from ground-based and satellite BrO measurements. The net mechanisms of bromine loss from the liquid phase and increase in the gas-phase is expected to lead to $Br_{enr} > 1$ ($nssBr > 0$) at the deposition site. Although the absolute Br_{enr} value is not particularly meaningful (and would be site-dependent), it is expected to be an increasing function of the extent of the fresh sea ice area that has contributed to the increase of atmospheric bromine. Similar to the case of an open water source, multi-year sea ice (MYSI) would contribute to low Br_{enr} values, since this type of substrate is more depleted in halides than FYSI on an absolute scale, and thus would not provide efficient bromine activation.

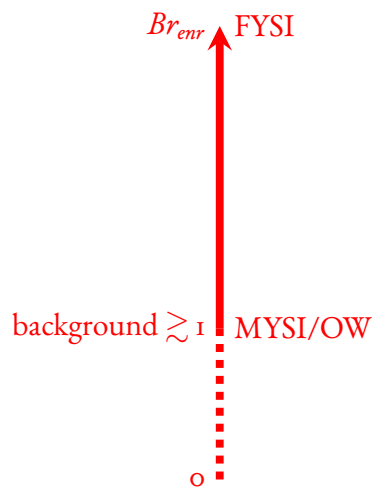


Figure 4.11: Br_{enr} as proxy for first-year sea ice (FYSI). Low values are associated with either open water (OW) or multi-year sea ice (MYSI) conditions.

The atmospheric bromine yield in three scenarios has been investigated in a one-dimensional model study (Fig. 4.10). Briefly, the model simulations suggest that the total bromine atmospheric concentration (gas-phase + SSA) increases over FYSI, compared to open water (OW) or MYSI scenarios. Both spectroscopic observations of BrO in springtime and laboratory studies on the different types of surfaces are consistent with this model simulation. Moreover, Br_{enr} variability on a seasonal timescale from ice cores also reflects springtime bromine activation from FYSI surfaces (6.1.2).

A complication can also arise from the fact that any source of salts from sea ice surfaces (and not from OW, where $Br_{enr}=1$ by definition) could be already fractionated at the source. Precipitation of mirabilite ($Na_2SO_4 \cdot H_2O$) and hydrohalite ($NaCl \cdot H_2O$) could in fact lead to bromide enrichment in the liquid brine. Therefore, if the source of SSA is sea ice, the use of bromine enrichment is based on the assumption that both the precipitated salts and the liquid brine are transported and contribute to the signal, which will then not be fractionated at the moment of emission. In other words, at the sea ice source $Br_{enr} = 1$. Based on

the above considerations, while increasing values of Br_{enr} indicate greater bromine recycling over fresh sea ice (first-year sea ice, FYSI hereafter), low values could either indicate open water conditions or an extended area of aged sea ice (multi-year sea ice, MYSI hereafter). For the correct interpretation between the two minimum states, other climatic parameters, such as $\delta^{18}\text{O}$, should be taken into consideration. A representation of the relation of Br_{enr} to different sea ice conditions is presented in Fig. 4.II.

Some differences exist between chlorine and bromine. Within sea salt aerosol, chlorine interacts with HNO_3 and H_2SO_4 to produce HCl , which is partially lost from the SSA in the gas-phase. This process, known as dechlorination, leads to sodium-to-chlorine fractionation as the SSA travels from the source to deposition areas. During halogen recycling cycles, unlike bromine, chlorine efficiently reacts with hydrocarbons to produce HCl (Eq. 4.38), limiting the role of chlorine in the ozone destruction and halogen release from sea ice surfaces (no "chlorine explosions" have been reported). Chlorine, like sodium, is expected to have, in terms of absolute concentration, a very dominant contribution from open water SSA. These considerations weaken the role of chlorine as a sea ice tracer. Similarly, no iodine explosions are observed, and very low IO are measured in the Arctic environment. The use of iodine as a sea ice proxy is therefore limited to the areas under the Antarctic sea ice where algal blooms dominate the iodine emissions.

5

The Renland ice core

This chapter introduces the Renland ice core, drilled in 2015. It will focus on the timescale, density profile and vertical strain which have been used to compute the accumulation history of the site for the last 4000 years. The timescale is necessary to translate depth series into time series, while the accumulation is necessary to compute air-to-snow fluxes of any impurity measured in an ice core. Finally, a back trajectory study is presented, to infer the potential marine aerosol source areas arriving to the Renland ice cap.

5.1 THE ICE CORE SITE

As part of the RENland ice CAP project (RECAP) project, the Renland ice core was drilled in 2015 on the Renland peninsula of the Scoresbysund fjord, in coastal East Greenland ($71^{\circ} 18' 18''$ N, $26^{\circ} 43' 24''$ W), at an altitude of 2315 m a.s.l. (Fig. 5.1). The Renland ice cap is located on the Hinkslund peninsula and is almost independent from the main ice sheet, constrained by the surrounding topography: high elevation cliffs separate the ice cap from the nearby fjords. The highest elevation of the ice cap is 2340 m. Thanks to its coastal location, the ice core record is believed to contain information about the marine-dominated climate of East Greenland. Hence, the ice core record is also expected to contain information about past sea ice. Sea ice in this area is currently linked to the East Greenland export channel, but different conditions and extent likely occurred in the past. The drilling started on May 13th 2015 and occurred in a dry borehole to 130 m depth and in drilling fluid for the remaining depth. A 98 mm diameter ice core was recovered to bedrock at 584 m, which was reached on June 12th, 2015. The core was stored frozen and shipped to Europe, where it was processed at the AWI (Germany) ice core facility. The core was here cut and sub sampled for different analyses. Among them, the continuous flow analysis 55 cm long ice pieces were

cut in a square section of ≈ 3 cm side, and shipped to Copenhagen for the continuous flow analysis campaign (see Sec. 6.6.1). The frozen conditions of the bedrock together with the almost absent brittle ice zone, provide a quality record which dates ~ 130 kyr back in time (Vinther et al., in prep).

A previous ice core was recovered at Renland in 1988 (Hansson 1994). The 324 m ice core was analyzed discretely for ions (IC) at 5 cm depth resolution and for $\delta^{18}\text{O}$ at 2.5 cm depth resolution. The new ice core aims to increase the knowledge of the atmospheric impurity content in the Northern hemisphere since the last interglacial, by adopting continuous flow techniques to reduce the ice contaminations introduced by discrete decontamination procedures and expanding the analytical techniques and types of detected impurities. Some of the results from the previous core (Hansson 1994) and the consistency of the new measurements with respect to the old ones are discussed in Sec. 6.6.

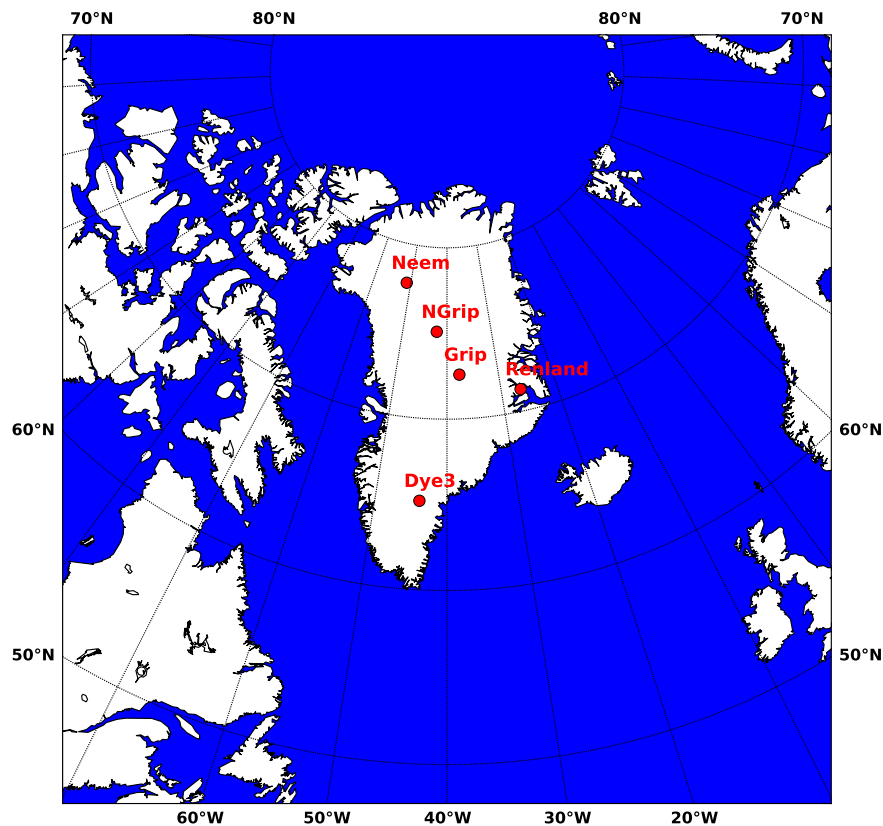


Figure 5.1: Location of Renland and some of the main Greenland ice cores.

5.2 THE DENSITY PROFILE

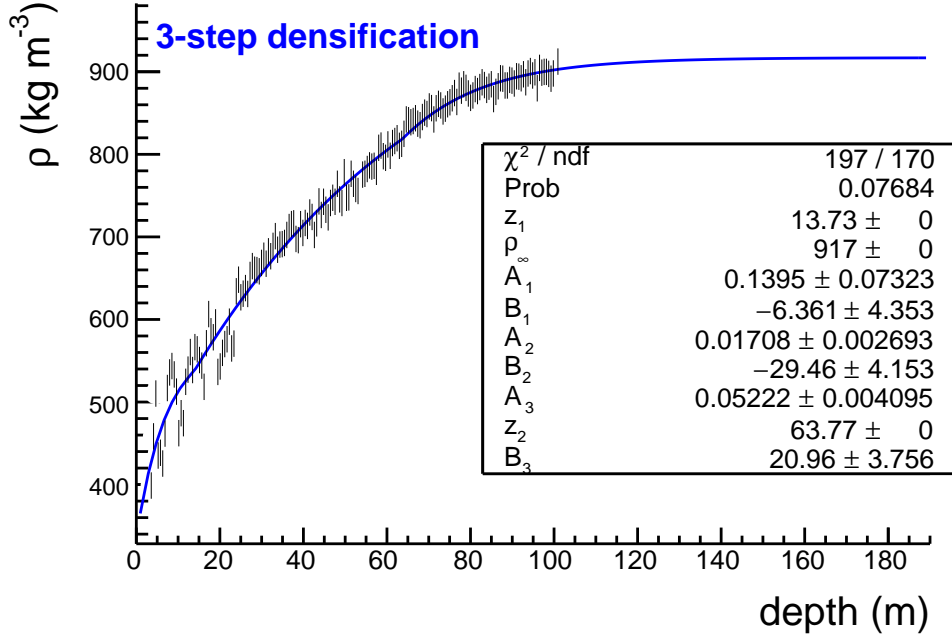


Figure 5.2: Density profile in the Renland ice core. Black points: measurements; blue: HL model fit.

Density measurements (1.0 m resolution) were performed from the surface to 102 m depth (Fig. 5.2). At this depth, the ice density reaches $\simeq 912 \text{ kg m}^{-3}$, being very close to ice density, $\rho_\infty = 917 \text{ kg m}^{-3}$. Below the depth corresponding to such value, all deformation of the layers occurs through ice flow. In order to describe the densification processes, a 3-step empirical model was tested (for the physical motivations related to the three steps, the reader is referred to [Herron and Langway 1980](#) and references therein). The three densification steps are here described by:

$$\varrho(x) = \begin{cases} \varrho_1 = \varrho_1^0 e^{-A_1(x-B_1)} & \varrho < 550 \text{ kg m}^{-3} \\ \varrho_2 = \varrho_2^0 e^{-A_2(x-B_2)} & 550 \text{ kg m}^{-3} < \varrho < 800 \text{ kg m}^{-3} \\ \varrho_3 = \varrho_\infty e^{-A_3(x-B_3)} & \varrho > 800 \text{ kg m}^{-3} \end{cases} \quad (5.1)$$

The model was tested on the experimental data (uncertainties $\sigma_\rho = 15 \text{ kg m}^{-3}$). A likelihood fit, was performed (using Minuit's minimization algorithm), leaving all the parameters freely floating (including the depth corresponding to 550 and 800 kg m^{-3} : z_1 and z_2).

The only fixed parameter was the asymptotic density of ice, $\rho_\infty = 917 \text{ kg m}^{-3}$. The associated χ^2 fit probability is 7.7%, therefore we accept the model hypothesis (3σ CL). Notably, the critical depths z_1, z_2 , associated with the change in densification rates are found by the fitting algorithm to be within 2m of the depths corresponding to 550 and 800 kg m^{-3} , inferred from the experimental data. By imposing the function to be the same at z_1 and z_2 , it is possible to constrain ρ_1° and ρ_2° , in order to avoid discontinuities in the density model.

$$\rho_1(z_1) = \rho_2(z_1) \quad (5.2)$$

$$\rho_2(z_2) = \rho_3(z_2) \quad (5.3)$$

A second fit was performed, fixing z_1 and z_2 to the values previously found, and by setting:

$$\rho_2^\circ = \rho_\infty \frac{I - e^{(-A_3(z_2 - B_3))}}{I - e^{(-A_2(z_2 - B_2))}}, \quad (5.4)$$

$$\rho_1^\circ = \rho_2^\circ \frac{I - e^{(-A_2(z_1 - B_2))}}{I - e^{(-A_1(z_1 - B_1))}}. \quad (5.5)$$

The new fit (Fig. 5.2) shows $p(\chi^2) = 7.7\%$. The absolute differences between the linear interpolation between data points and the HL model fit were considered as the ice density uncertainty, at each depth layer. Such uncertainties were propagated in the accumulation calculation.

Although the model is empirical, it is found to describe the density measurement reasonably well. A pure [Herron and Langway 1980](#) model (Eqs. 7 and 10), or more advanced models which may include ice lenses (the Renland summers may experience summer melting for few days), such as [Reeh et al. 2005](#), may be tested. These comparisons go beyond the aim of this work.

5.3 THE THINNING FUNCTION

The thinning function S describes the deformation of ice layers (strain) in response to the applied stress. The thinning function was calculated using a flow model with a constant vertical strain rate down to some distance above bedrock and from there decreasing linearly to zero at the bed ([Dansgaard and Johnsen 1969](#)). The model was implemented with the following parameters: $\lambda_H = 0.48 \text{ m yr}^{-1}$, $h = 310 \text{ m}$, $fb = 0.27$ (fraction of basal sliding, $fb = \frac{v_{x,bed}}{v_{x,surf}}$) and 47 m of dead ice above bed. This model choice was driven by several attempts to match the depth of well dated horizons in the core ([Vinther, personal comm., 2017](#)). The calculated thinning function (expressed in metre of ice equivalent, assuming the core material was ice throughout) was transformed into depth scale by finding consecutive depth layers z_i which

integrate to the ice density (917 kg m^{-3}). The following equation was solved for z_i :

$$\begin{aligned} \varrho_\infty &= \int_{\bar{z}_{i-1}}^{\bar{z}_i} \varrho(x) dx \\ &= P(\bar{z}_i) - P(\bar{z}_{i-1}), \\ \cap \bar{z}_0 &= 0, \end{aligned} \tag{5.6}$$

where $\varrho(x)$ is the density function from the model fit (5.2), $P(x)$ its integral function, $\varrho_\infty = 917 \text{ kg m}^{-3}$, z_i are the depth layers to be found.

The integral function, $P(x)$ was found analytically and checked by Von Neumann fashion (hit-miss) Monte Carlo simulations (see Fig. 5.3). The equation (Eq. 5.6) was solved numerically by finding its roots: the [Brent 1971](#) method was used for such purpose.

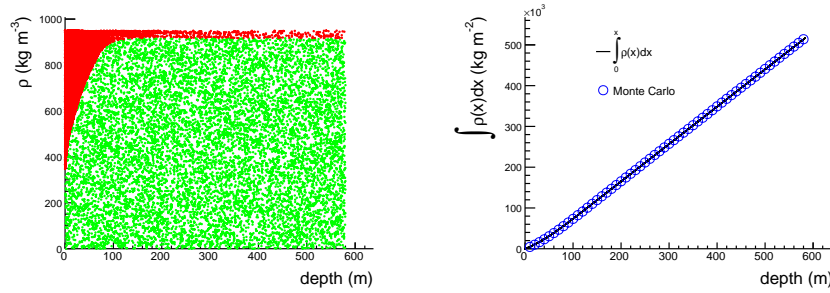


Figure 5.3: Left: MC simulations in the $[0, 590]$ m depth range. Right: $P(x)$ found by analytical integration of HL model (black) and by MC simulation (blue circles).

The resulting thinning function S (Fig. 5.4) on depth scale is shifted 20 m with respect to the ice equivalent depth scale, corresponding to 'squeezing' the firn layer into an ice equivalent layer.

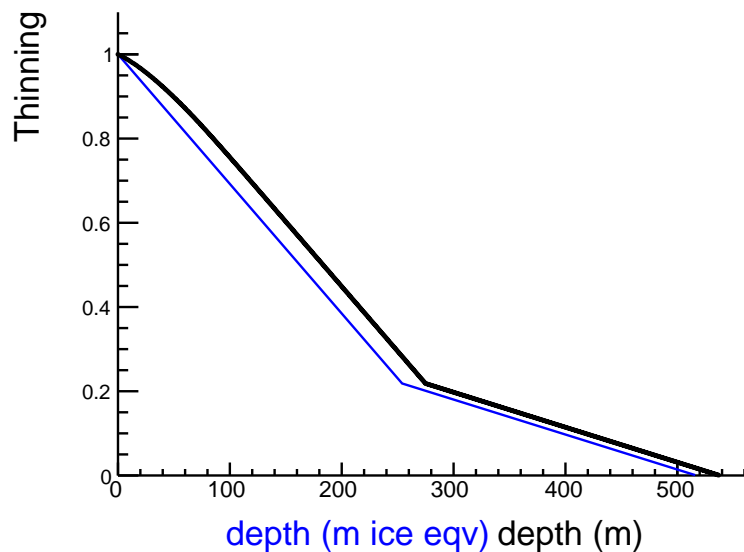


Figure 5.4: The thinning function in metre (black) and metre of ice equivalent (blue). The x-offset between the two curves is 20 metre.

5.4 THE RECAP V_4 AND THE ANNUAL LAYER COUNTED TIMESCALES

The timescale function maps the depth of an ice layer with its age (in terms of years AD/BC, years b2k or similar units). The timescale is usually constructed by multiple techniques (see also Sec. 3.1). Annual layer counting is the best choice technique in the top part of the core, where the annual layers ($\delta^{18}O$ or other annual signature indicators) can be clearly identified. In the deeper parts of the core well dated horizon markers such as volcanic eruptions are used, as well as synchronization with other 'known' chronologies. Methane (CH_4) matching is applied when a rapid transition in methane is found in several cores, since this gas is well mixed in the atmosphere and is therefore expected to be found synchronously within several cores. Flow modelling helps constraining the dating when other techniques cannot be applied.

At the time of writing, the timescale version 4 (V_4) has been produced. This timescale is based on the scaled 1988-drilled Renland ice core to 100 metre depth, on a linear interpolation between volcanic tiepoints (last 4.05 kyr), on the 8.2 kyr event to 521.5 meters and on scaling to the QSR_{2014} stratigraphy down to GS25 by CH_4 synchronization (Vinther et al., *in prep*).

A refined timescale, compared to the V_4 , has been produced by counting annual layers from different chemical impurity depth series, in an automated fashion (Winstrup et al.

2012). At the time of writing, this type of timescale dates the core from the surface down to 458m (2047 BC). Such timescale has a significant offset compared to the V₄ chronology: ~ 450 yr of difference is found at 370 m depth. The difference is expected to decrease in the early Holocene, as the 8.2 kyr event is a tiepoint.

The annual layer counted timescale has been used to calculate the accumulation rates for the last 4 kyr and to date the 1700-present iodine time series described in Sect. 6.2.1. The glacial/interglacial sodium and bromine variabilities (Sect. 6.6) are, on the other hand, on the V₄ timescale.

Based on the annual layer counted timescale, the annual layer thickness profile λ was calculated (Fig. 5.5), as the depth thickness between consecutive years. The annual layer profile exhibits a decreasing non-trivial shape, due to the multiple effects of densification, ice flow and annual snow accumulation.

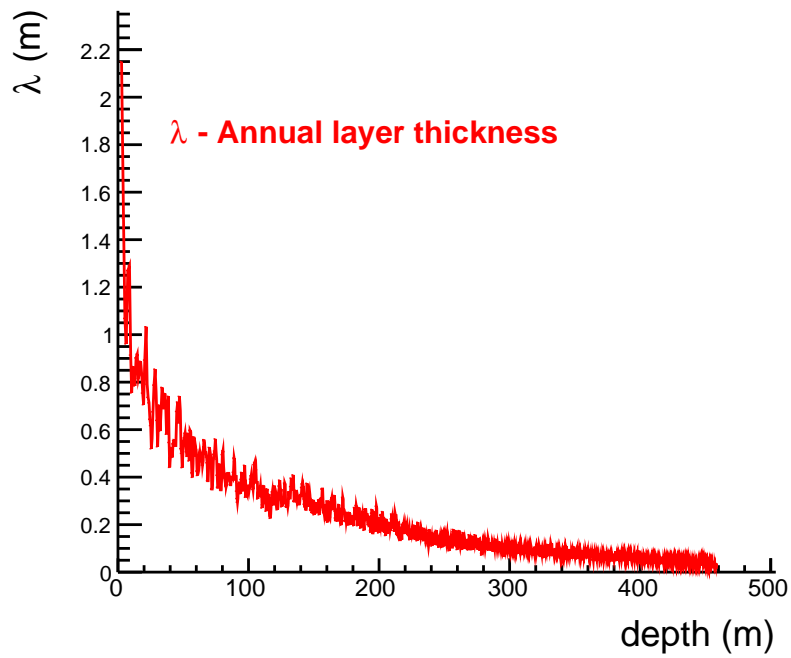
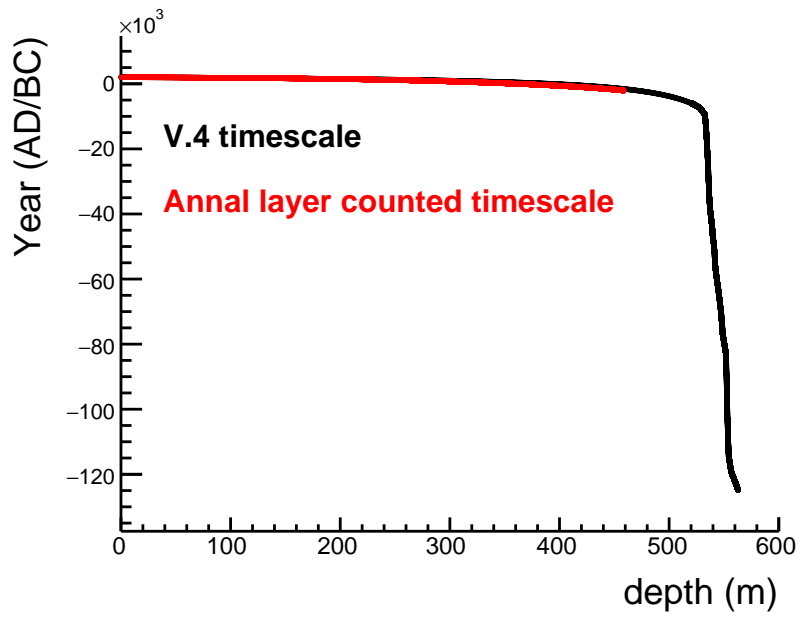


Figure 5.5: Upper panel: Timescale V4 (black) and the annual layer counted timescale (red, for the top 458 m, covering the 2015 AD - 2048 BC time period). Lower panel: calculated annual layer thicknesses, λ from the annual layer counted timescale.

5.5 ANNUAL ACCUMULATION RATE OF THE LAST 4K YEARS

Using the annual layer counted timescale, the annual accumulation rate A was calculated over the last ~ 4000 years (2015 BC - 2048 BC) by the following:

$$A(z) = \frac{\lambda(z) \cdot \rho(z)}{S(z)}, \quad (5.7)$$

where z [m] is depth, λ [m yr⁻¹] is the annual layer thickness (Fig. 5.5, bottom panel), ρ [kg m⁻³] is the density (Fig. 5.2) and S is the thinning function (Fig. 5.4). The timescale function allows the conversion from depth to age, and viceversa.

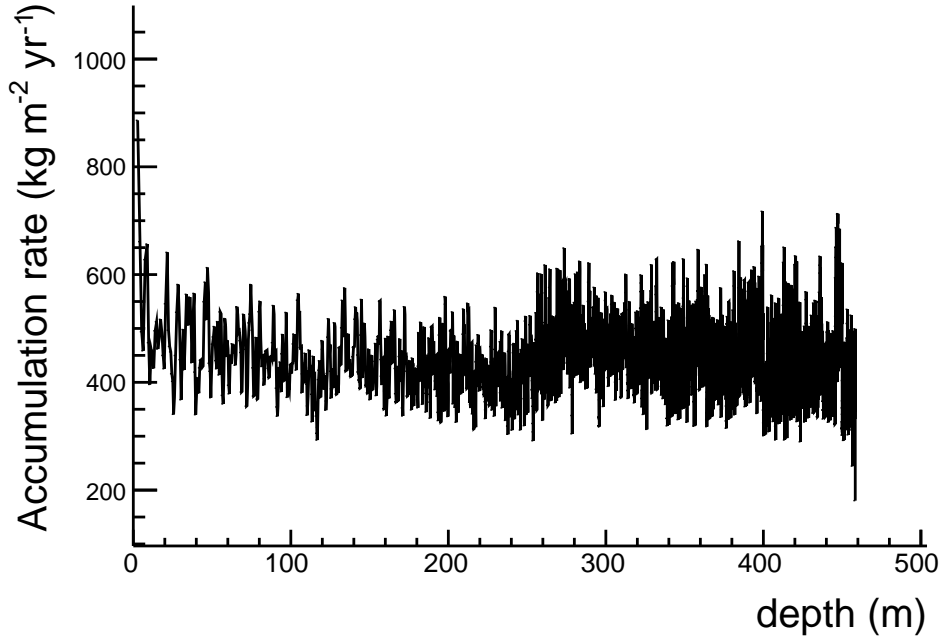


Figure 5.6: Accumulation rate reconstructed from the annual layer counted timescale in the top 458 m (~ 4 kyr).

The average value accumulation rate during the last 4000 years (Fig. 5.6) is $A_{\text{last4kyr}} = 436$ kg m⁻² yr⁻¹ (RMS = 64 kg m⁻² yr⁻¹). The value reported from the Renland 1988-drilled ice core (Hansson 1994) was estimated to be 50 cm ice equivalent per year during the Holocene (459 kg m⁻³). This value was calculated from the ice flow model that was used to date the core and it is consistent with our finding within 1σ . Overall, a high year to year accumulation variability is expected at the Renland site, due to its proximity to the ocean.

It is worth noticing that at the time of writing, uncertainties on the timescale (i.e. on the annual layer thicknesses λ) and on the thinning function S are not considered in the accumulation rate calculations. In addition, the real shape of the thinning function is unlikely to show a 'kink', as the one used in the model. A smooth transition between the two linear modes is more likely to be realistic.

5.6 BACK TRAJECTORIES

The interpretation of any impurity record in an ice core relies, among other variables, on the connection between the deposition at the site and the emission at the source. The identification of the sources of any impurity is therefore crucial. In order to access the potential sources of sea salt aerosol (SSA) arriving at Renland, a back trajectory approach was chosen, investigating the arrival of air parcels to the core location, in the recent past (see below for the model implementation). Such a study could be representative of the modern conditions, but might not be suitable for the distant past. A climatic model might be necessary to test the validity of the modern situation with respect to different time ranges.

Hysplit (HYbrid single-particle Lagrangian integrated trajectory), developed by the National Oceanic and Atmospheric Administration (NOAA) Air Resources Laboratory's (ARL) was used (Stein et al. 2015; Draxler et al. 1999; Draxler and Hess 1998; Draxler and Hess 1997). Hysplit is a widely used model in atmospheric sciences to perform several types of studies, from simple air mass trajectories to more complex models that include transport, dispersion, chemical transformations and deposition. Among the applications of Hysplit are: radionuclides projections from nuclear fallout, tracking of wildfires, dust, air pollutants, pollen and volcanic ash plumes.

The model concepts were initially developed in the 1950s and the first back trajectories were computed by hand using radiosonde balloon measurements data and assuming geostrophic conditions (the wind blowing along pressure isobars, the pressure gradient force being equal to the Coriolis force). Since the first ideas, different concepts have been incorporated. One of the oldest is the gaussian dispersion model, which tries to predict the diffusion of an air pollutant plume, assumed gaussianly distributed. The lagrangian approach follows a number of air parcels as they move in a random walk, and the dispersion is computed performing statistics on them. Unlike the lagrangian approach, which follows the air mass on a moving reference frame, the Eulerian approach makes use of a fixed reference frame. During the years, the hysplit modelizations of transport, dispersion and deposition became more sophisticated and new features were added, as well as the meteorological data, often a mixture of observations and meteorological models themselves. Nowadays, an array of model outputs can drive Hysplit for its calculations. The time and space resolution have been increased, the spatial coverage has been extended from hemispheric to local scales

(resolution of 1/10 degree).

5.6.1 IMPLEMENTATION OF HYSPLIT AT RENLAND - A STATISTICAL APPROACH TO INFER SSA POTENTIAL SOURCE AREAS

Daily back trajectory calculations were computed from 2000 to 2016, at an interval of 1 hour, starting at the Renland location (71.304 N; 26.713 W), each one for a duration of 6 days (144 h). The total number of trajectories was roughly $17 \times 365 \times 24 = 148920$. NCEP - NCAR reanalysis meteorological data were used. Such data have a grid resolution of 2.5° in both latitude and longitude, a global geographical coverage and a time domain of 1948 up to present (Kalnay et al. 1996). Since a single trajectory is unlikely to be representative, a statistical approach was adopted, making use of the large amount of computed trajectories. No dispersion model has been used at this time. As a future development, a dispersion implementation would be a good comparison as for the conclusions drawn from this current study. To "simulate" the dispersion approach, the single back trajectories are filtered out according to some criteria concerning the possibility of aerosol uptake, which will then be deposited at Renland. A way to visualize the results is to display snapshots of spatial distributions of the air parcel locations at a certain time t_o . For simplicity, $t_o = 24\text{h}, 48\text{h}, 72\text{h}$ spatial distributions will be presented. Note that the air parcels can follow any trajectories within these points in time.

Table 5.1: Hysplit setup parameters.

Parameter	Value	Unit
Meteo data	REANALISIS	-
Coverage	Global	-
Resolution	2.5×2.5	$^\circ$
Time step calc	1	h
Lat	71.305	$^\circ\text{N}$
Lon	26.726	$^\circ\text{W}$
Altitude	1700	m AGL
Duration	144	h
Start date	1 Jan 2000	-
End date	31 Dec 2016	-
Frequency	1	h^{-1}
TOT nr.	148920	-

The starting altitude was chosen to be 1700 m AGL. Due to the finite resolution of the meteorological data, 2.5° , the correct altitude of the core location, 2300 m ASL, was re-

solved to be 1100 m ASL. The core, in fact, is located in a coastal area where both high elevation terrain and marine pixels are both present, resulting in an average terrain height within the grids of the data domain. For this reason, the starting altitude was 'artificially' corrected, such that 1700m AGL + 1100m ASL = 2800m ASL. This altitude value is therefore 500 m AGL, an elevation within the atmospheric boundary layer (ABL) at which aerosol deposition onto the ground may potentially occur, and at the same time ground level turbulence is avoided. All spatial plots presented here (on a Mercator projection) represent on the z-axis the density of points per unit area of the lat-lon cell grid. The area of any cell grid has been calculated as $A = R^2 |\Delta\lambda| |\sin(\varphi_2) - \sin(\varphi_1)|$, R being the radius of the Earth, λ the longitude, φ the latitude of the cell boundaries.

A sensitivity test was carried out, to investigate how this correction could affect the representation of air masses arriving at Renland. Back trajectories were computed at Renland (71.304 N; 26.713 W; 1700 m AGL) and at 'Location3' (71.305N; 20W; 2800 m AGL). For the Location3, the terrain altitude is correctly resolved, being at sea level and without elevated terrain within the domain grid. The elevation is therefore set to be the same, being the resolved terrain at Renland 1100m ASL. The two sites are approximately 250 km apart and thus they are assumed to be subject to similar circulation patterns. Figure 5.7 shows the distribution of the endpoints of the trajectories at 1-day, 2-days, 3-days for 2009 (test case) in the two locations. The 3-day patterns look similar although noisy, with the 90% envelope up to $\sim 10^\circ$ wider for Location3, extending to 85-90°N, eastwards to the coasts of Norway and Svalbard, westwards the Baffin Bay and the Canadian arctic. The major difference however is the southern boundary, with the envelope extending as south as 50°N in the case of Location3. This difference could arise from generally southerly wind direction, partially blocked by the Greenland ice sheet on Renland, and not at Location3. Further comparisons on other years confirm this picture, the main difference being the extent of the 90% envelope in the south direction.

On the basis of the considerations on the atmospheric lifetime of sea salt aerosols (Sec. 4.1.3), the back trajectories were considered representative only up to 3 days. It should be noted however, that, since the results here presented are interpreted with respect to bromine (Sec. 6.6) and iodine (Sec. 6.2.1) records, as well as sodium (Sec. 6.6), halogen elements are likely to display greater atmospheric residence time than SSA, due to their transport in the form of a mixed gas and aerosol phase (e.g. up to ≈ 6 days for BrO). For bromine and iodine, therefore, 3 days should be considered as a lower inferior.

The spatial distribution of 1-2-3 day endpoints from 2000 to 2016 at Renland are represented in Fig. 5.8 (and in the animation 5.9). The 3-day 90% line extends from 50-90° N in latitude and 100° W- 40° E longitude. Higher density of endpoints are found along the eastern and to a lesser extent western Greenland coasts, again possibly due to low-altitude trajectories blocked by the high coastlines. This hypothesis should be, however, further

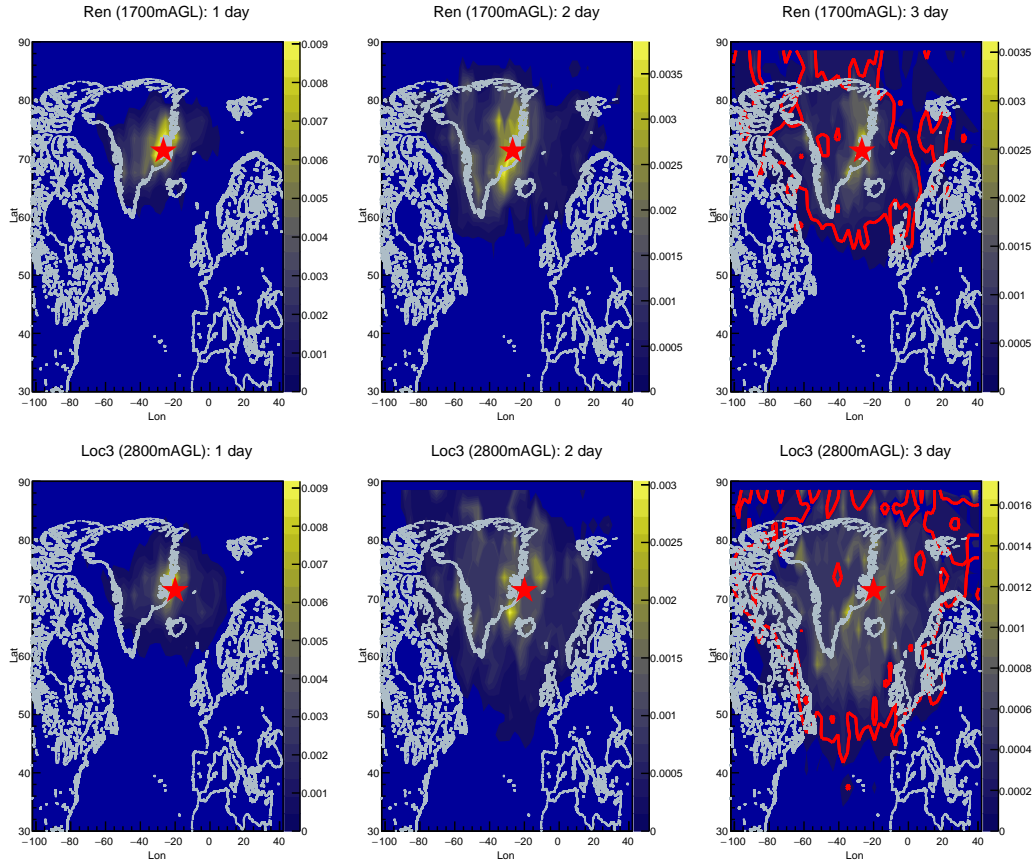


Figure 5.7: Distribution of endpoints per unit area ($\frac{\text{counts}}{\text{km}^2}$) for 2009 at Renland (top) and Location3 (bottom). Red contour lines corresponding to 90% of the maximum value. The 90% envelope extends south to 40-50° N lat.

tested.

To investigate the aerosol source areas to the Renland ice core, it is necessary to distinguish among the trajectories those which could potentially bring aerosol during their 3-day path. The vertical dependence of SSA concentrations varies widely according to SSA size, wind and atmospheric conditions. The size distribution of SSA arriving at Renland is not expected to exceed the $r_{80} \approx 10\text{-}20 \mu\text{m}$, given the altitude of the site (2315 m ASL). Studies of vertical mixing of SSA in the marine boundary layer have shown that SSA particles with r_{80} up to $10 \mu\text{m}$ are expected to be nearly uniformly mixed throughout the marine boundary layer (Lewis and Schwartz 2004 and references therein), with little fractionation up to $\sim 1000\text{-}1500$ m ASL. The concentration undergoes a rapid decrease in the upper troposphere, showing values two orders of magnitude lower.

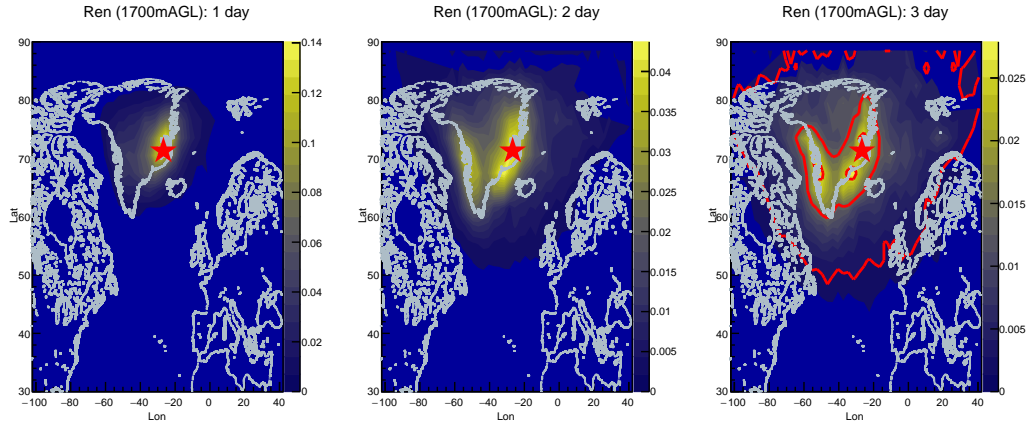


Figure 5.8: Distribution of 1, 2 and 3 day endpoints per unit area ($\frac{\text{counts}}{\text{km}^2}$) at Renland from 2000 to 2016 along with contour lines corresponding to 10%, 50% and 90% of the maximum value.

Figure 5.9: Animated distribution of endpoints up to 3 day back in time, at 1 h time step.

Based on these assumptions, a simple pressure criterion was implemented, to keep only the trajectories that cross the marine boundary layer (MBL) for at least some time, \bar{t} . The

height of the marine boundary layer H_{mbl} was here conservatively chosen to be the 900 hPa isosurface $p_{H_{mbl}}$, corresponding roughly to 1000 m ASL (Fig. 5.10).

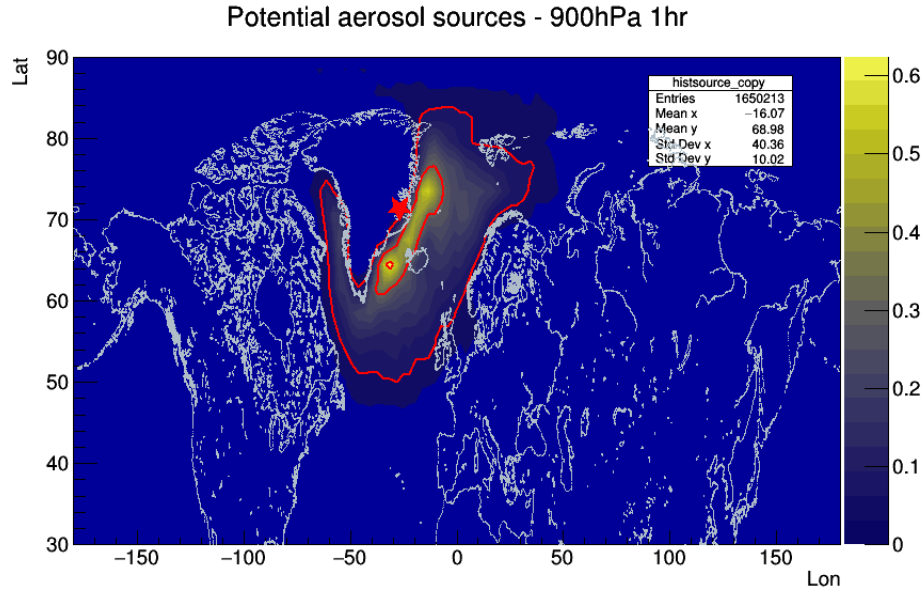


Figure 5.10: Potential aerosol areas from 2000 to 2016 along with contour lines corresponding to 10%, 50% and 90% of the maximum value. Approx 21% of the trajectories fulfill the aerosol criterion.

Sensitivity tests have been carried out to investigate how the potential source areas depend on the duration within the MBL, \bar{t} , as well as on the pressure cutoff $p_{H_{mbl}}$. The time distributions of the trajectories that cross the 900 and 950 hPa isosurface (1000 and 500 m ASL respectively), shown in Figs. 5.11 and 5.12, have means of 31 and 25 hours, and RMS of 18 and 16 hours respectively. Overall, compared to the total duration, 72 hours, the trajectories spend a significant amount of time below these altitudes. It is worth noticing that the MBL could be crossed multiple times during the total travel time. The 950 hPa distribution shows a faster drop for $\bar{t} > 20$ hr, since in this case the MBL is almost half in thickness, and the probability of being inside for a longer time becomes smaller. The atmospheric residence time of SSA depends on many variables, the main one being the size of the particles. Here again, by assuming \bar{t} on the order of hours, it is assumed that no SSA with $r_{80} \gtrsim 20 \mu\text{m}$ reach the site. Such a hypothesis should be valid since such SSA have a residence time of \sim seconds to minutes. Overall, the larger \bar{t} constraint, the fewer trajectories that trigger the filter, though the spatial pattern is similar. Similarly, the effect of 950 hPa threshold, compared to the 900 hPa, has a weak effect on the spatial distribution plot, the main visible difference being a higher southern importance for the former.

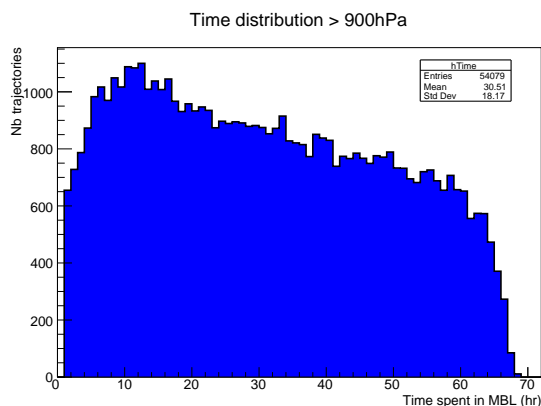


Figure 5.11: Distribution of the time spent within the MBL (900 hPa isosurface) within 3 day backtrajectories from 2000 to 2016.

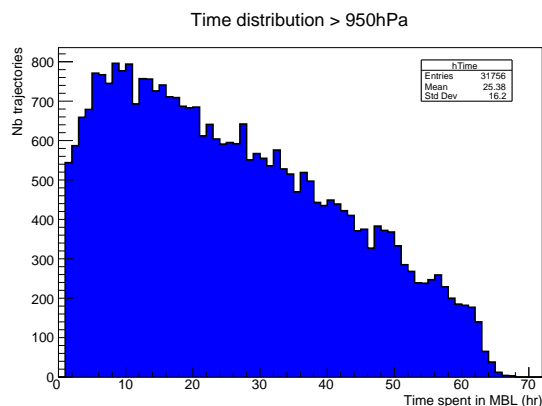


Figure 5.12: Distribution of the time spent within the MBL (950 hPa isosurface) within 3 day backtrajectories from 2000 to 2016.

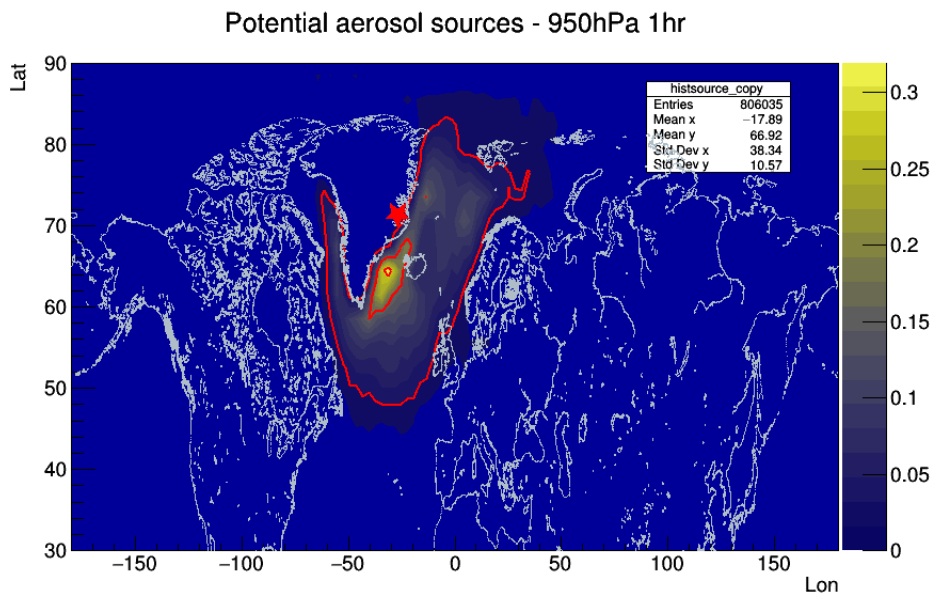


Figure 5.13: Potential aerosol areas from 2000 to 2016 along with contour lines corresponding to 10%, 50% and 90% of the maximum value.

The potential SSA areas for the Renland site range in latitude from 50° N to 80° N, extending from the North Atlantic to the Fram Strait, with very little contribution from the Arctic Ocean. A minor contribution is expected from the Baffin Bay and the sea of West Greenland. It is worth noticing that 50% of the signal is however localized close to the ice

core site.

A seasonality study has been carried out (Fig. 5.14): such investigation revealed that the most extended source area (90% envelope) is found in the winter months (DJF), progressively reducing in the spring months (MAM), with a minimum in summertime (JJA), before expanding in autumn (SON).

In their study [Maselli et al. 2017](#) concluded that source areas arriving at Summit station originate primarily from S-SE (Fig. 5a in [Maselli et al. 2017](#)). Their findings are similar to those reported here, although it should be noticed that the two methods are different. In particular the authors ran the calculations for 10 days and their aerosol selection criterion was based on a 500 m threshold. Moreover, Summit station is located ~ 400 km west of Renland, at the top of the Greenland ice sheet (see Fig. 6.1).

This method could be applied to investigate potential source areas of impurities of different types, from marine aerosol to dust and volcanic ash, by applying the filtering parameters that best suits the transport of the impurity of interest. As an example, [Sodemann et al. 2006](#) used this methodology to locate potential Saharan dust sources found in an alpine glacier. A more advanced filter could make use of the relative humidity, RH, of the air parcel, to differentiate wet from dry deposition. Trajectories could also be differentiated by constraining for the typology of surface the air masses travel over (sea ice, vegetation, etc.).

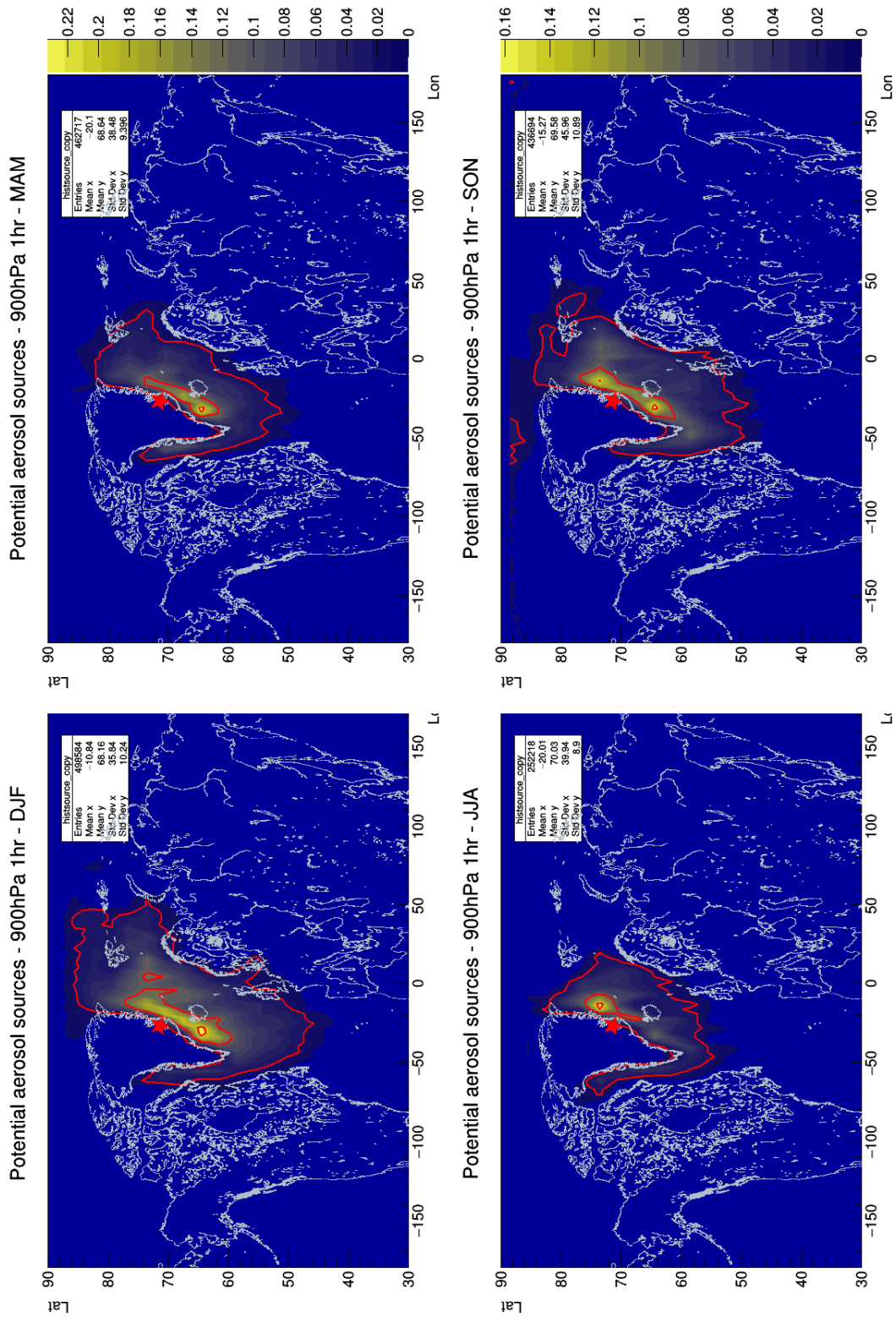


Figure 5.14: Seasonality study of the potential SSA source areas to Renland. 900hPa and 1hr filter parameters have been used here. From left to right, top to bottom: DJF, MAM, JJA, SON.

6

Sodium, Bromine and Iodine measurements in polar ice cores

This chapter aims at reviewing the measurements of bromine and iodine in polar ice cores. Relevant results from the extensive number of past sodium observations are also presented. Because of the large number of observations and plots, the reader is referred to the Figure number in the cited publication. The chapter is structured into the different timescales that are contained in ice core records: seasonal, decadal to centennial, and from millennial to glacial–interglacial timescales. Each timescale provides different insights on the mechanisms of production, transport and deposition of these impurities. Atmospheric chemistry studies (mostly BrO and IO) are also presented, when available, along with measurements in the snow/ice, to provide at seasonal timescales a complementary view of the mechanisms within the gas and liquid/ice phases of bromine and iodine.

The results of research activities are presented in this chapter, in the more general framework of Br, Na and I in polar ice cores, alongside other published records. Seasonal and decadal records by [Maffezzoli et al. 2017](#) (first author, see Appendix A) and [Vallelonga et al. 2017](#) (co-authored) are presented in section 6.1.2 and 6.2. Section 6.2.1 addresses the 1700-present iodine record in the Renland core (Cuevas et al., submitted, co-authored). The 120 kyr sodium and bromine NEEM record ([Spolaor et al. 2016b](#), co-authored) is displayed in section 6.5. The last section (Sec. 6.6) is dedicated to the 125 kyr record of bromine and sodium from the Renland core, for which a second first author manuscript is currently under preparation.

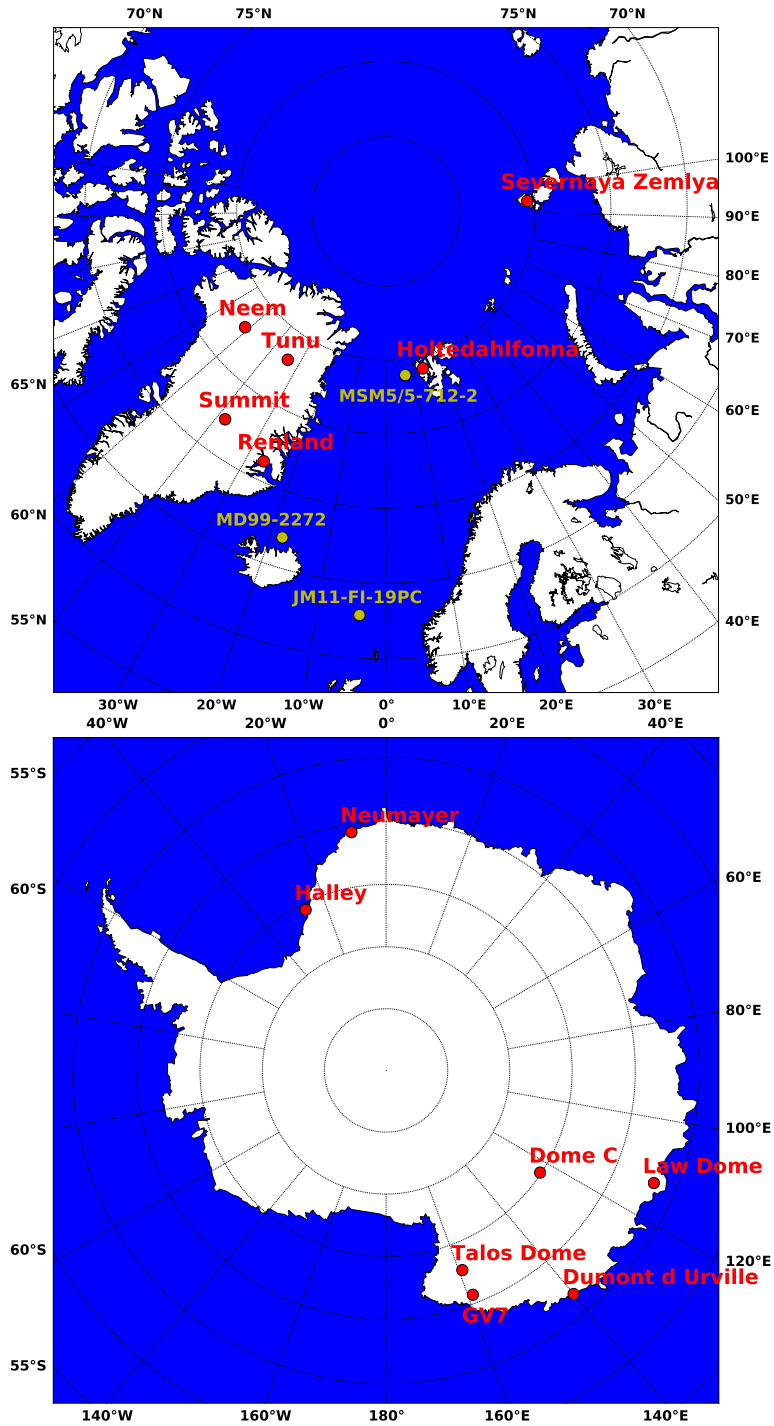


Figure 6.1: Ice core locations in the Arctic and Antarctica where sodium, bromine and iodine records are discussed. In yellow 3 marine cores are indicated. They are discussed in Sect. 6.6 along with the Renland ice core results.

Table 6.1: Published records of bromine and iodine in different Arctic (top) and Antarctic (bottom) sites. A selection of sodium records from the same locations is indicated. The accumulation rate A refers to a mean present value.

Color legend: bromine, sodium, iodine.

Type of record: S = seasonal, D = decadal/centennial, M = millennial or older.

Arctic site	Position	Elev (m A.S.L)	A ($\text{kg m}^{-2} \text{yr}^{-1}$)	Record	Reference
Holtedahlfonna and Svalbards	$\sim 79^{\circ}9' \text{N } 12^{\circ}23' \text{E}$	~ 1150	~ 500	S S S D D D	Heintzenberg and Leck 1994 Spolaor et al. 2014 Spolaor et al. 2013a Kekonen et al. 2005 Spolaor et al. 2016a
Severnaya Zemlya (Russian Arctic)	$80^{\circ}31' \text{N } 94^{\circ}49' \text{E}$	760	460	D D D	Spolaor et al. 2016a
Summit	$72^{\circ}20' \text{N } 38^{\circ}17' \text{W}$	3216	220	S S D	Maselli et al. 2017
Tunu	$78^{\circ}2' \text{N } 33^{\circ}52' \text{W}$	2113	110	S S D	Maselli et al. 2017
NEEM	$77^{\circ}45' \text{N } 51^{\circ}6' \text{W}$	2484	190	S M M	Gfeller et al. 2014 Spolaor et al. 2016b
Renland	$71^{\circ}18' \text{N } 26^{\circ}43' \text{W}$	2340	450	D M M	Hansson 1994 (D: Cuevas et al., in prep) (M M: Maffezzoli et al., in prep)
Antarctic site	Position	Elev (m A.S.L)	A ($\text{kg m}^{-2} \text{yr}^{-1}$)	Record	Reference
Neumayer	$70^{\circ}40' \text{S } 38^{\circ}16' \text{W}$	200	~ 1000	S S	Huang and Jaeglé 2017 Frieß et al. 2010
Northern Victoria Land (Talos Dome–GV7)	$\sim 72^{\circ}48' \text{S } 159^{\circ}6' \text{E}$	2315–1700	80–250	S S S	Maffezzoli et al. 2017
Talos Dome	$72^{\circ}49' \text{S } 159^{\circ}10' \text{E}$	2330	80	D M M M	Severi et al. 2017 Spolaor et al. 2013c Schüpbach et al. 2013
Law Dome	$66^{\circ}46' \text{S } 112^{\circ}48' \text{E}$	1370	600	S S S D D D	Spolaor et al. 2014 Vallelonga et al. 2017
Dumont d'Urville	$66^{\circ}40' \text{S } 140^{\circ}1' \text{E}$	0	800	S S	Legrand et al. 2016b
Dome C	$75^{\circ}6' \text{S } 123^{\circ}33' \text{E}$	3233	15	S S	Legrand et al. 2016b

6.1 SEASONAL TIMESCALES

6.1.1 SODIUM

Several seasonality studies on sodium profiles in ice cores have now been carried out for more than three decades. Most of them show seasonal cycles with winter maxima and summer minima. Originally, the results were attributed to enhanced advection of marine air masses over ice sheets in winter time (Herron 1982; Legrand and Delmas 1984; Fischer and Wagenbach 1996). Examples of published records of deposited sodium at Summit and South Pole can be seen in Legrand and Mayewski 1997 (Summit: Fig.2; South Pole: Fig. 3). Since increased wind strength and sea ice extent show a similar seasonality with winter maxima (see e.g. at Law Dome, Curran et al. 1998, Fig. 3a-3b), the original investigations, which did not account for a sea ice sodium source, concluded that the seasonality of such marine proxy was mainly wind driven, since a greater sea ice extent was thought to reduce sodium inputs from the ocean sources, located further away. At Law Dome, consistent with Curran et al. 1998 (Fig. 1), a similar seasonal pattern was recently found by Vallelonga et al. 2017 (Fig. 7). Wintertime enhanced concentrations of sea salt aerosol (Na^+) have also been detected at Neumayer (Huang and Jaeglé 2017, Fig. 1d). Sodium cycles in the Arctic environment also show winter maxima (e.g. at Svalbard: Heintzenberg and Leck 1994, Fig. 4; Maselli et al. 2017, Fig. 3b). Similarly, at NEEM, snowpit and firn core studies confirm sodium seasonality with winter/early spring maxima (Kuramoto et al. 2011, Fig. 4; Gfeller et al. 2014, Fig. 9).

The importance of winter time sodium inputs from sea ice at coastal Antarctic locations was recognized when sulphate depletion from precipitation of mirabilite was noticed in SSA at Neumayer (Wagenbach et al. 1998, Fig. 5a). Negative values of nssSO_4^{2-} were also found at Halley (Antarctica). Rankin and Wolff 2003 estimated 60% of the total sea salts arriving at Halley originate from brine and frost flowers on the sea ice surface, rather than from open water. Sea ice was therefore established as a significant source of SSA at both poles (Rankin et al. 2002; Yang et al. 2008). However, salty blowing snow is at present believed to be the most significant SSA source from sea ice surfaces (frost flowers playing a minor role) and roughly equally contributing as the ocean to the total sodium budget (e.g. Huang and Jaeglé 2017). Model studies coupled with ice core observations are now trying to quantify the relative magnitude of sea ice, open water sources to SSA, as well as to understand the importance of meteorology (wind direction, strength) to the observed seasonal variability.

In the Canadian Arctic, some studies have reported an inverse correlation between sodium and spring sea ice extent (Grumet et al. 2001). With an empirical orthogonal function (EOF) analysis, also Kinnard et al. 2006 found a negative correlation between Baffin Bay sea ice concentration and sea-salt aerosols in the Devon Ice Cap core (represented by the

dominant mode, much influenced by the major sea salt ionic species, which accounts for 55.1 % of the total variance). This finding suggests that, especially in areas where open water dominated, a reduced sea ice cover leads to greater emission of sea salt aerosols from open waters. With similar methods, [Kreutz et al. 2000](#), using the Siple Dome ice core (West Antarctica), show that the ice core sea salt record is a proxy for the strength and position of the Amundsen Sea low (ASL), and no relationship is found with sea ice extent. [Kaspari et al. 2005](#) using 16 International Trans-Antarctic Scientific Expedition (ITASE) cores investigated sources (sea spray and frost flowers) and transport pathways of marine aerosols into West Antarctica. Analysis of $\text{SO}_4^{2-}/\text{Na}^+$ ratios indicate that frost flowers contribute up to $\sim 40\%$ to the Na^+ budget. They found that significant positive correlations of sea ice extent and Na^+ time series exist in some regions of West Antarctica. At the same time, higher wind speeds in winter and higher Na^+ concentrations when sea level pressure is lower indicate that intensified atmospheric circulation enhances transport and production of marine aerosols. According to the model study by [Levine et al. 2014](#) it was shown that, subject to current climate conditions and on interannual timescales, meteorology, not sea ice extent, is the dominant control on the atmospheric concentration of sea salt, simulated at Antarctic sites - both coastal and continental.

Despite the number of observations which show a consistent sodium seasonality with wintertime maxima, it is clear that the main uncertainties regarding this tracer concern the relative importance of the contributing open water and sea ice sources (brine, frost flowers, blowing snow). A number of studies also indicate that wind strength is still a major control of sea-salt aerosols in both the Arctic and Antarctica, whether the aerosols are derived from sea ice or the open ocean surface.

6.1.2 BROMINE

Despite atmospheric studies of bromine compounds having been performed at polar latitudes since the 1990s, bromine in snow and ice samples has been detected only recently because of combination of low concentrations in the snow ($\approx 0.1\text{-}1$ ppb) and analytical difficulties (the limit of detection, LOD, defined as 3 times the standard deviation of blank samples, is on the order of 0.1 ppb, see Sect. 6.1.2). Bromide (Br^-) is detected through ion chromatography, while total bromine measurements are performed with ICP-MS instruments. Species other than Br^- are not expected to contribute much to the bromine budget ([Spolaor et al. 2013b](#)). For the atmospheric studies related to bromine compounds, the reader is referred to Sections 4.2.2 and 4.2.4. Unless specified, we refer to "bromine measurements" as total bromine.

The first Antarctic detection of bromine in polar snow dates back to 2009, when [Jones et al. 2009](#) were investigating a bromine explosion event that occurred in October on top of sea ice in the Weddel Sea, near the Halley station, in association with high wind speeds

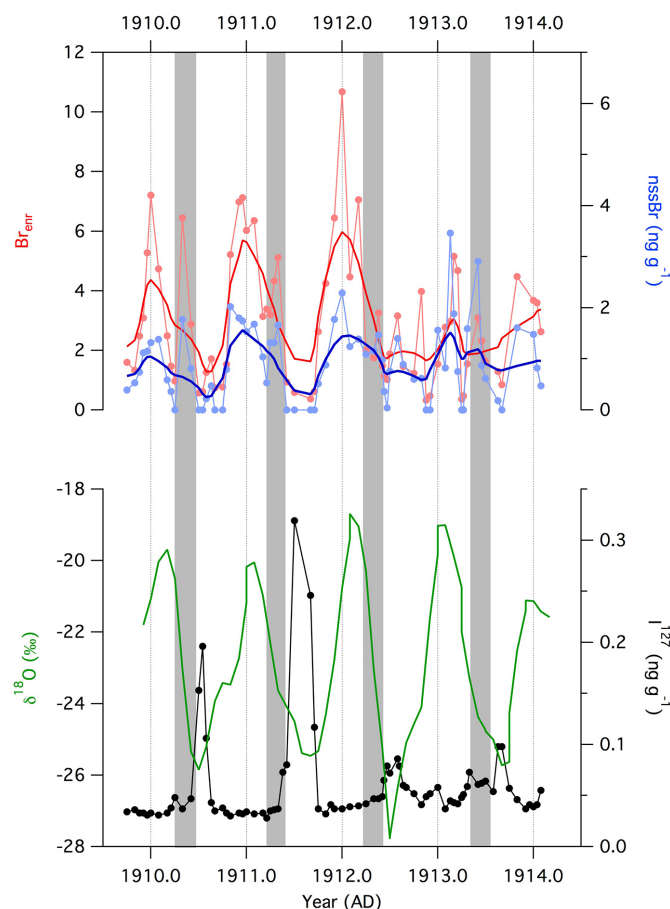


Figure 6.2: First reported seasonal variability in bromine enrichment (top: Br_{enr} and nssBr) and iodine (bottom) observed at Law Dome, coastal East Antarctica. Vertical grey bars highlight the presence of a late autumn peak in nssBr and Br_{enr} . From Spolaor et al. 2014.

and saline blowing snow. The authors related the event to a surface snow bromide concentration of 2 ppb (Fig. 5a). From a later snowpit, the layer was identified at 6 cm snow depth after 10 days (Fig. 5b). In a bromine (and iodine) speciation study (Spolaor et al. 2013b), bromine was found in interglacial Antarctic samples only as Br^- , at concentrations of 100–200 ppt. No bromate, BrO_3^- was found above the 38 ppt detection limit.

A few years later, seasonal signals of Br_{enr} and nssBr with spring/summer maxima and winter minima were reported at Law Dome, over a 4 year time period (Spolaor et al. 2014, Fig. 6.2). The seasonality is in overall agreement with BrO seasonality from satellite observations. The authors also report an additional Br_{enr} autumn peak, which is speculated to be related either to scavenging of bromine compounds at the end of the polar day or to

fresh sea ice creation in autumn with associated bromine activation. A recent study at Law Dome (Vallelonga et al. 2017, Fig. 7) is consistent with the previously observed seasonality: a 26 year firn record (1987-2012) of monthly deposition data indicates that the period of peak bromine enrichment is during austral spring-summer, from November to February, although such seasonality is mainly driven by sodium, which generally shows higher concentrations in winter months.

In a transect from Talos Dome to GV7 (East Antarctica), snowpit measurements covering a few years reveal a distinct seasonality in both bromine and bromine enrichment, occasionally sustained by higher sodium in the winter layers (Maffezzoli et al. 2017, Fig. 4-7). Br_{enr} maxima are found around October, possibly due to a combined effect of maximum sea ice extent and insolation driving bromine activation (Maffezzoli et al. 2017, Fig. 7b). At Dumont d'Urville (DDU) and Concordia (Dome C) a multi-year study on sea salt aerosols and bromine in both the aerosol and gas phases was carried out by Legrand et al. 2016b. Unlike other Antarctic coastal locations, the seasonal variability of sodium (in SSA) at DDU exhibits summer maxima (around January, Fig. 2b). This feature is unique to the DDU site, which suffers particularly strong sources of SSA in summer months from the nearby ocean. Model simulations run at DDU overestimate sodium concentrations by a factor of ~ 2 in summer and ~ 3 in winter, possibly because the model does not correctly reproduce winds from coastal glaciers and the Antarctic plateau. Despite this discrepancy, the predicted predominant winter sea ice source of sodium (Figs. 5a, 5e) agrees with crude estimates based on the observed sulfate-to-sodium ratios, which suggest that sea ice inputs account for $\sim 70\%$ of the sodium budget in winter months. At Concordia station, sodium concentrations are lower in summer ($\sim 5 \text{ ng m}^{-3}$) than in winter months $\sim 20 \text{ ng m}^{-3}$, the latter showing also a much larger variability (Fig. 5d). Overall, the model correctly reproduced the observed annual sodium variability (slightly overestimating concentrations during the first part of winter), suggesting that similar open water and sea ice inputs are to be expected in winter months, the open water source being stronger during summer (Fig. 5f). Sulphate-to-sodium ratio measurements (0.13) during a strong marine advection event in July are consistent with a significant ($\sim 66\%$) sea ice source. This study points out that at this site, year to year sodium variability in winter months is significant. The source of this variability has to be found in the meteorological conditions affecting the low sodium load at this remote site.

Bromide measurements in bulk aerosol at DDU show seasonal oscillations with maxima ($\sim 5 \text{ ng g}^{-1}$ in summer (January), similarly to sodium (Fig. 2a, 11a)). Bromine enrichment to seawater of sea salt aerosol in turn displays seasonal cycles, with summer minima and winter maxima. The values are consistently lower than 1 except in winter, with values $\gtrsim 1$ (Figs. 2c, 11c). Note that in the study the bromine departure from sea water concentration is calculated as $1000\text{Br}^-/\text{Na}^+$). Such result indicates that debromination from SSA takes place

throughout the year except in midwinter, consistent with previous observations (Sander et al. 2003; Peterson et al. 2017). The SSA debromination can also be quantified by the depletion factor, DF (see Jourdain and Legrand 2002 for more details), defined as:

$$DF = 1 - (\text{Br}^-/\text{Na}^+)_{\text{meas}}/(\text{Br}^-/\text{Na}^+)_{\text{ref}} \quad (6.1)$$

The variability of DF (values up to $\sim 40\%$ in late spring months, Table 3) closely follows the variability of SSA Br_{enr} (Fig. 11c). SSA dechlorination, on the other hand, takes place only in summertime, possibly due to greater acidity of SSA in this period. SSA acidity does not appear to be a strong requirement for bromine activation. The authors also addressed the issue of halogen-sodium fractionations at the sea ice source, due to precipitation of mirabilite at $\sim -8^\circ\text{C}$ (halites precipitate at -20°C). They calculated that the loss of sodium would account for an increase of $\sim 20\%$ of the Cl^-/Na^+ ratio. Since $\text{Na} \gg \text{Br}$, Br^-/Na^+ would not be much affected (e.g. Simpson et al. 2005, Table 1, columns Cl^-/Na^+ and Br^-/Na^+).

The dependence of SSA debromination on particle size was also investigated (Fig. 12). Consistent with Sander et al. 2003, Legrand et al. 2016b found that submicrometer particles are enriched in bromine (up to $\simeq 4$). Particles with diameter $\sim 1 \mu\text{m}$ are depleted in bromide ($\simeq 0.5$), while large (10-20 μm) particles almost retain seawater ratio. Unlike at Dumont d'Urville, the poor correlation between bromide and sodium found at Concordia prevents any robust conclusion at this inland site.

Bromine was detected in snowpit/firn core records, spanning 2009–2013 and collected at NEEM and Svalbard (Holtedahlfonna) (Spolaor et al. 2014, Fig. 5). In both studies, the profiles of Br_{enr} and nssBr show higher spring/summer values, with some seasonal features especially at NEEM. In an additional study at Svalbard, Br_{enr} was only detected in the upper portion of the core (Spolaor et al. 2013a, Fig. 6). In both studies the authors explained the partial absence of seasonal features at Svalbard with summertime percolation, smoothing the stratigraphy. Two 250+ year records were obtained from Summit and Tunu (Maselli et al. 2017). In both cores seasonal investigations revealed that bromine, sodium and Br_{enr} cycles show respectively midsummer, winter and mid-to-late summer maxima (Maselli et al. 2017, Fig. 3a-b-e). The authors attributed the late-summer bromine enrichment to submicrometer particles, with lifetimes up to ~ 5 -10 days, which often show enriched bromine (e.g. Legrand et al. 2016b, Sander et al. 2003). A change in the timing of maximum bromine concentration from a solely summer peak in the pre-industrial era towards a broad spring-summer peak by the 1970 is observed. The authors suggest that this shift could possibly be explained by additional springtime sources of bromine during the industrial era.

6.1.3 IODINE

Unlike the Arctic, concentrations of IO up to several ppt have been detected from ground-based (Frieß et al. 2001; Saiz-Lopez et al. 2007b; Frieß et al. 2010) and satellite-based (Saiz-Lopez et al. 2007a; Schönhardt et al. 2008; Schönhardt et al. 2012) DOAS spectrometers in Antarctica, over sea ice covered areas. The first IO measurements at Neumayer station from Frieß et al. 2001 were reported with higher IO mixing ratios (5–10 ppt) during summer than in winter: several possible explanations were given to explain the observed seasonality. At Halley, just 12 km from the sea edge, Saiz-Lopez et al. 2007b reported maximum IO and BrO concentrations in spring (October), with maximum IO of 20 ppt. The concentrations of both IO and BrO exhibited a diurnal cycle, essentially tracking the solar radiation, thus indicating that both species are produced photochemically (Saiz-Lopez et al. 2007b). The seasonal behavior of gas-phase IO, with regular springtime production over sea ice has now been confirmed by satellite observations.

Early iodine investigations in polar ice revealed that iodine in interglacial samples of the Talos Dome ice core was present in concentrations of 0.005–0.0032 ppb, as iodide (I^-). No iodate was detected above the 0.007 ppb detection limit (Spolaor et al. 2013b).

At Neumayer, a snowpit investigation revealed a seasonal cycle of iodine, with winter maxima (up to ~ 0.65 ppb) and summer minima (Frieß et al. 2010, Fig. 9). Since the maxima in the emission have been observed to occur in winter/summer, the authors concluded that iodine suffers a loss by photolysis during summer months, which is stopped at the start of the polar night. Maximum iodine concentrations up to 0.3 ppb were reported by seasonal investigations at Law Dome, a coastal site near the Casey station (Spolaor et al. 2014, Fig. 6.2). The authors reported a loss of iodine in summer layers, consistent with the previous study. Additional snowpit studies in the Arctic environment revealed (Spolaor et al. 2014, Fig. 5) some seasonality with maxima in summer at NEEM while no seasonality was observed at Svalbard (Holtedahlfonna). Absence of seasonal cycles at Svalbard was also reported in Spolaor et al. 2013a (Fig. 3). It is likely that summertime percolation strongly affects the seasonal cycles at Svalbard.

Snowpit measurements from a Talos Dome–GV7 traverse (East Antarctica), covering a few years show average annual iodine concentrations of ~ 0.04 ppb with an annual variability around 10–15 % (Maffezzoli et al. 2017, Table 3). The mean value is close to the background values found in Antarctic shallow/firn cores near the research stations of Neumayer (Frieß et al. 2010) and Casey (Law Dome, Spolaor et al. 2014). Unlike these measurements which reported clear winter maxima, no strong seasonal signal was found, except in one case with a high winter value. Some isolated iodine concentrations were also reported in winter. Overall, the low iodine concentrations reflect a low input of iodine in this area of Antarctica compared to the other locations. This picture is confirmed by satellite measurements (Fig. 4.7), which show average IO concentrations close to the detection limit over

the area of the transect compared to Law Dome, Neumayer or any other coastal location (Maffezzoli et al. 2017). Surface snow iodine measurements from GV7 (East Antarctica, 95 km from the Indian Ocean) show a diurnal cycle with minima at noon, again suggesting daytime photochemical reactivation (Spolaor, pers. comm.).

While photolytic loss of iodine in summertime has now been reported, the quantification of this loss has still to be determined. Moreover, further studies are needed to evaluate how the loss relates to the distance between the site under investigation and the source area (affecting the absolute iodine concentration in the snow), as well as with parameters such as temperature or annual accumulation. A greater loss at inland dry sites, like Dome C, is to be expected. If the rate of loss of iodine at a given site is constant in time, then any rate of change in the iodine variability in timeseries could reflect the variability of the source strength. However, this is unlikely at glacial-interglacial timescales, when the changes in accumulation rate (and insolation) could affect the amount of loss.

6.1.4 RELATIVE TRANSPORT OF SODIUM AND BROMINE

Since sodium is transported as SSA and bromine is transported both in the SSA and in the gas phase, it is to be expected that these two tracers undergo a relative fractionation during transport, because of their different depositional velocities. The picture is complicated by the fact that bromine gas phase species can be adsorbed back into the aerosol phase during the air mass transport. As explained in section 4.1, SSA exhibits a wide range of atmospheric lifetimes, depending primarily on particle size r_{30} . Gas-phase bromine species, the dominant ones being HOBr, HBr and BrO in summer and Br₂ in wintertime (absence of sunlight reduces photolysis reactions) in turn have different depositional velocities. Overall, if one wants to relate a $Br_{\text{enr}} \simeq Br/Na$ as record in ice cores as indicator of seasonal sea ice, as in 4.2.6, the effect on transport can mask the sea ice-driven processes which lead to a climatic Br_{enr} signature. In particular, the Br_{enr} variability can be related to a source variability only on the hypothesis that the transport of bromine and sodium does not change considerably at the time scale of the record.

In order to investigate such features of bromine and sodium, model and/or experimental studies can be performed. The latter are performed by sampling surface snow along a route from a location which is believed to be close to the source, towards the interior of the ice sheet. The relative decay of the bromine and sodium concentrations (and their ratio) gives a clue to their different transport processes. Few such studies have been performed both in the Arctic and Antarctic environment. Simpson et al. 2005 measured sodium and bromine concentrations in surface snow samples during a springtime (March to May) transect from the edges of leads on the sea ice near Barrow (Alaska) towards the Brooks range, for an overall distance of ~ 280 km (the elevation pattern is not specified but is here assumed not to play a role, i.e. sea level throughout). Although both chemicals show a concentration vari-

ability spanning different orders of magnitude, their results (Fig. 6.3) suggest that the decay of bromide concentration is more gradual than that of sodium, on a distance range of a few hundreds of kilometers. In particular, from a very crude calculation if such a linear fit in the logarithmic domain of the concentrations is representative, a starting value of $Br_{\text{enr}} \simeq 0.5$ ($Na^+ \simeq 100 \mu\text{M} \simeq 2300 \text{ ppb}$; $Br^- \simeq 0.1 \mu\text{M} \simeq 7.9 \text{ ppb}$; sea water Na^+/Br^- mass ratio = $6.2 \cdot 10^{-3}$; $M_{Na} \simeq 23 \text{ g/mol}$; $M_{Br} \simeq 79.9 \text{ g/mol}$) would increase to $Br_{\text{enr}} \simeq 45$ ($Na^+ \simeq 1 \mu\text{M} \simeq 23 \text{ ppb}$; $Br^- \simeq 0.08 \mu\text{M} \simeq 6 \text{ ppb}$) at 250 km. It is worth pointing out that such absolute values of Br_{enr} have never been observed after this original study.

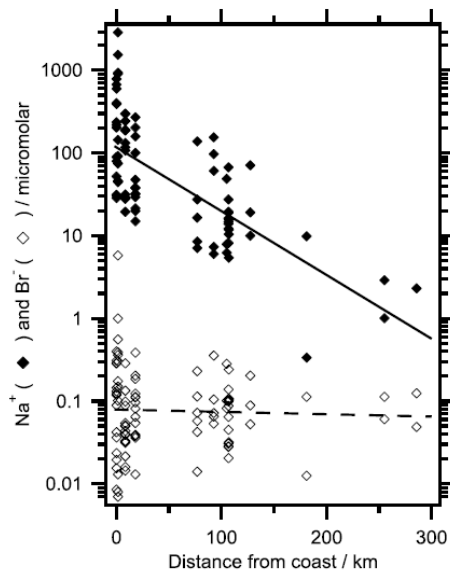


Figure 6.3: Sodium and bromide in the spring-time snow pack as a function of distance from the coast. From [Simpson et al. 2005](#).

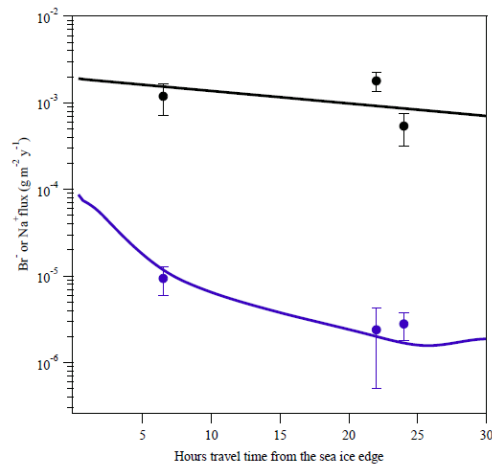


Figure 6.4: Comparison between the modelled deposition fluxes of sodium (black) and bromide (blue) with measurements at Talos Dome (circles, 7h from sea ice edge) and Dome C (circles, 22 and 24h from sea ice edge). From [Spolaor et al. 2013c](#).

In order to validate their interpretation on the observed Talos Dome 200 kyr bromine and sodium record, [Spolaor et al. 2013c](#) run the THAMO (Tropospheric HALogen chemistry MOdel) model to simulate the evolution of bromine and sodium in an air parcel from the sea ice edge to Talos Dome. The model predicted (for the model input parameters the reader is referred to [Spolaor et al. 2013c](#)) that within ~ 300 km from the sea ice edge bromine is enriched compared to sodium. The transition between enrichment and depletion of bromine, assumed by a larger deposition velocity (~ 3 times) of HBr than sea-salt aerosol, takes place at 8-9 h of travel time (~ 300 km assuming a wind speed of 9 m s^{-1} , see Fig. 7 in [Spolaor et al. 2013c](#)). The depletion of bromine in the Talos Dome record in glacial times (compared to the interglacial enrichment) is therefore explained by the greater dis-

tance (~ 700 - 800 km) that the air mass covers from a more distant sea ice edge to the ice core site. This transport mechanism is opposite to what is suggested by [Simpson et al. 2005](#) for a coastal Arctic site.

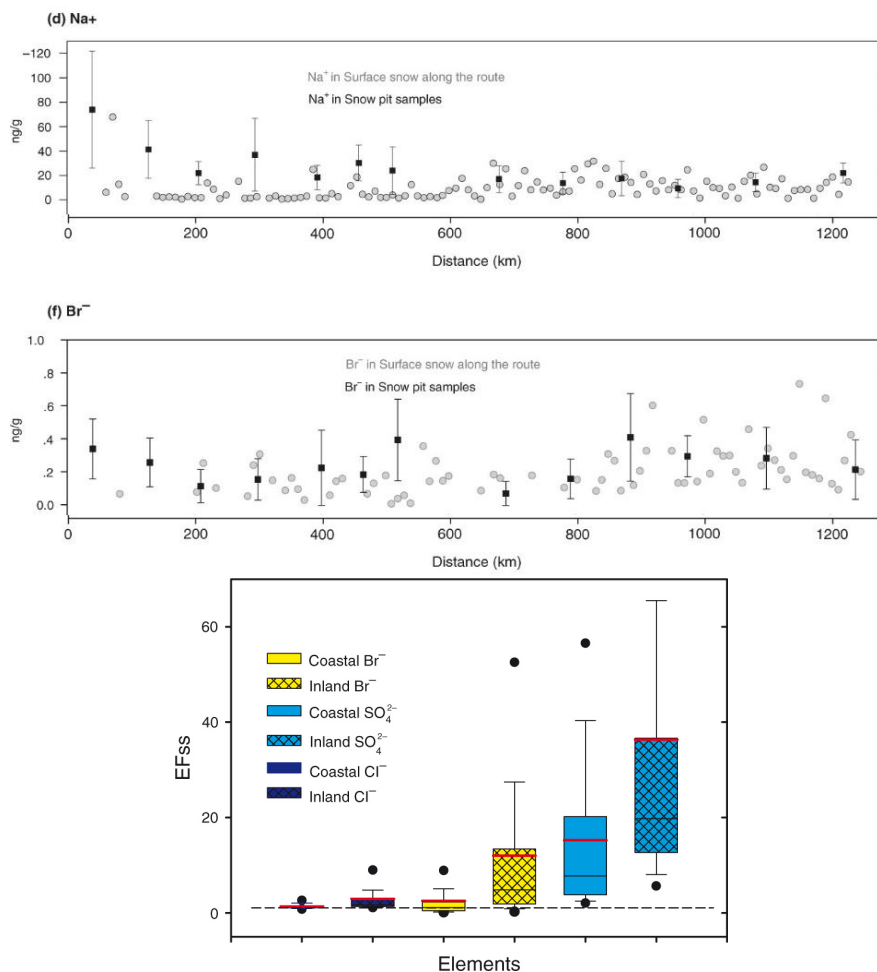


Figure 6.5: Top two panels: Na^+ and Br^- concentrations in surface snow and snow pit samples collected along the transect from Zhongshan Station to Dome A. Bottom panel: bromine enrichment factors clustered into the coastal (30-600 km) and inland (600-1248 km) sections of the transect. Adapted from [Li et al. 2014](#).

An Antarctic transect between Zhongshan Station (first sample collected 40 km from the coast, 832 m a.s.l., accumulation $260 \text{ kg m}^{-2} \text{ yr}^{-1}$) and Dome A (1250 km from the coast, 4093 m a.s.l., accumulation $23.5 \text{ kg m}^{-2} \text{ yr}^{-1}$) was performed between December 2012 and January 2013 (Antarctic summer) to investigate the deposition of mercury ([Li et al. 2014](#)). Among the different ionic species, Na^+ and Br^- were measured in surface snow samples and

snow pits (Fig. 6.5). The higher enrichment factors of bromine (i.e. Br_{enr} in inland snow compared to more coastal locations suggest indeed that the two species undergo a different transport mechanism, and that bromine species have a longer residence time than sodium, consistent with [Simpson et al. 2005](#), although with a much smoother gradient. It is also possible that the accumulation pattern along the transect (see Table 1) affects the absolute concentrations of Na^+ and Br^- (hence their ratio).

Measurements of bromine and other compounds in two Greenland ice cores (Summit and Tunu, [Maselli et al. 2017](#)) revealed higher enrichment values in the Summit core, located more inland (Fig. S3), compared to the more coastal Tunu core. The authors speculated that since micrometer particles, with longer residence times, are often enriched in bromine ([Sander et al. 2003](#); [Legrand et al. 2016b](#)), a transport effect acts to increase Br_{enr} values in the aerosols which travel further and are deposited further inland.

The THAMO model run ([Spolaor et al. 2016b](#)) showed an increase of total bromine (gas-phase + aerosol) in an air parcel travelling over FYSI and conversely, a decrease when such air parcels travel over MYSI or continental ice (Fig. 4.10). Unfortunately, no sea salt aerosol profile is shown as output, in order to perform a comparison between the two species. It is worth noticing that HBr deposition velocity which was set to 1 cm s^{-1} in [Spolaor et al. 2013c](#), was set to 2 cm s^{-1} in [Spolaor et al. 2016b](#) (see supplementary). An increased deposition velocity of HBr would have the effect of predicting an even stronger bromine removal from the atmosphere in [Spolaor et al. 2013c](#) model exercise.

Surface snow was sampled during a transect between Casey station and Law Dome summit (coastal Antarctica) ([Vallelonga et al. 2017](#)). Determination of bromine and sodium show that Br_{enr} does not vary considerably over the distance of the transect ($\sim 120 \text{ km}$). Increased values of both species are found at sites with increasing accumulation (up to $600 \text{ kg m}^{-2} \text{ yr}^{-1}$), suggesting that at such accumulation values, wet deposition is the dominant removal mechanisms (Fig. 8). A longer transect is needed to extend this dataset and make stronger conclusions.

Year-round measurements of SSA and gas-phase bromine were carried out at Dumont d'Urville and Concordia (Dome C) ([Legrand et al. 2016b](#)). The two stations are 1100 km apart. Using monthly averaged data from 2008 to 2013, the concentrations between the two sites are:

$$Br_{SSA,DDU} \simeq 2.4 \longrightarrow Br_{SSA,Concordia} \simeq 0.11 \text{ (Fig.11a, 3b)} \quad (6.2)$$

$$Br_{GAS,DDU} \simeq 9.7 \longrightarrow Br_{GAS,Concordia} \simeq 2.2 \text{ (Fig.4)} \quad (6.3)$$

$$Na_{SSA,DDU} \simeq 420 \longrightarrow Na_{SSA,Concordia} \simeq 8 \text{ (Fig.5c, d)} \quad (6.4)$$

where all concentrations are expressed in ng g^{-1} . From Eq. 6.2,6.3,6.4 the ratio of decrease Na_{SSA} is ~ 50 , while for bromine $Br_{SSA} \sim 20$ and $Br_{GAS} \sim 4$. Although measurements of

both species in the snow were not carried out at the two sites, and the above gradients cannot be translated in a straightforward way to Br_{enr} values in snow, a positive gradient of this quantity between Dumont d'Urville and Concordia is to be expected.

The spatial variability of sodium and bromine in snow pits was investigated in a transect performed in coastal East Antarctica from Talos Dome to GV7, from November 2013 to January 2014 (Maffezzoli et al. 2017). The deposited fluxes of both Na and Br show a similar rapid decrease after 100 km from the Indian Ocean (supposed to be the main source area). Moving away from the Indian Ocean and approaching the Ross Sea, the deposited fluxes of both elements appear constant (Fig. 9). It is however not possible to observe any fractionation (not even in the Br_{enr}) since the transect is oriented between two marine sources.

From the above studies (the spatial pattern of altitude and accumulation at the different locations certainly complicate the interpretation), it is not possible to make definitive conclusions on the relative fractionation of sodium and bromine during their transport, although some evidence regarding a longer atmospheric lifetime of bromine species, that would yield an increased Br_{enr} values at greater distances, are present. The quantification of this effect in a Br_{enr} signal variability, compared to a source (seasonal sea ice) effect, is yet to be determined. Further considerations concerning on this point are presented in section 6.4.

6.2 DECADAL TO CENTENNIAL TIMESCALES

The only existing halogen record in Antarctica at decadal timescales is from Law Dome, for which two ice cores provide a 1927-1989 AD record of iodine and a 1927-2013 record of sodium and bromine (Vallelonga et al. 2017). A significant correlation between Br_{enr} and 90-110°E sector FYSI was found ($\rho=0.357$, $p<0.001$, Table 2). A similar linear decreasing trend was observed in both Br_{enr} and MSA (Fig. 5), the latter linked to the opening of sea ice cover during the summer and autumn seasons by previous studies (Curran et al. 2003). Decadal running means show comparable results between the two species, with positive FYSI anomalies before 1985 and negative anomalies in the last decade (Fig. 5). A weak positive correlation between 11-year smoothed Br_{enr} and I_{enr} (calculated with respect to the I/Na mass ratio in sea water, $5.93 \cdot 10^{-6}$) suggests a common driver of halogen variability (Fig. 6). The observed high and low values of halogen enrichment are observed to be concurrent with the phases of the Interdecadal Pacific Oscillation (IPO), a low-frequency climate mode related to the El Niño-Southern Oscillation.

In a 25 year snow pit sodium record at Talos Dome, Severi et al. 2017 reported a positive correlation ($\rho=0.71$, $n=23$) during the satellite period (1979-2003) between sea salt sodium flux ($ssNa^+$) and the sum of September maxima Ross Sea + Western Pacific sea ice extents (Fig. 5). The authors used such a linear calibration to reconstruct the SIE as the sum of

the Ross Sea and Pacific sectors of the Southern Ocean between 1920 and 2003, using the TALDICE sodium dataset (Fig. 6), finding that since 1920 the maximum SIE has occurred in the last two decades.

Spolaor et al. 2013a presented the first comparison between halogens in surface snow and sea ice extension. An 11 m long firn core was drilled in 2012 from the summit of the Holtedahlfonna glacier (Svalbard) and measured for bromine and iodine concentrations. The ice core record covers the 2003-2012 time period. A statistically significant negative correlation between a combined March-May sea ice in three basins (Greenland, Kara and Barents Seas and Baffin Bay) and iodine was found (Fig. 5i, note that left axis is reversed). The authors point out that the iodine flux from sea ice algae is enhanced when the sea ice melts, otherwise a positive correlation would be found. This is consistent with IO measurements, which become detectable only in the presence of open sea water (Mahajan et al. 2010). The bromine record indicates that bromine is almost always enriched beyond sea water, up to 6 times (quantified as $\%Br_{\text{enr}} = [(Br/(Na \cdot 0.0062)) \cdot 100 - 100]$, Fig. 6). Consistent with an increase of atmospheric bromine above seasonal sea ice in spring, the authors compared the $\%Br_{\text{enr}}$ record with Arctic seasonal sea ice, calculated as the difference between March (maximum) and September (minimum of the previous year) sea ice areas. Back trajectory calculations were performed to establish the source areas: among them the Arctic Ocean and the Canadian Archipelago were identified (Fig. 4). Positive significant correlations were found between the $\%Br_{\text{enr}}$ record and such sea ice areas, although a significant correlation was also found for the Hudson Bay, which was not identified by the back trajectory study (Fig. 7).

Century scale records of sea salt ions concentrations (Na^+ , Cl^- , Mg_2^+ , and K^+) have been investigated by Kekonen et al. 2005 (Fig. 4). Na and Cl were found at maximum concentrations between the fifteenth and mid sixteenth centuries, the warmest period according the core $\delta^{18}O$ profile. The authors suggest that high sea salt inputs thus originate from a stronger open water source and a sea ice retreat in this period. In the most recent part of the core (since the 20th century), all sea salt and terrestrial tracers exhibits declining concentrations: melting and runoff at this site are believed to play a significant role at this site.

A 29 meter section of the Akademii Nauk ice core (Severnaya Zemlya Archipelago) provided an additional halogen record from the (Russian) Arctic, in the time period 1950–1999 (Spolaor et al. 2016a). The authors reported a connection between Br_{exc} (i.e. nssBr) and Laptev Sea spring sea ice ($\rho=0.44$, Fig. 7), both showing a decreasing trend since the 1980s. The evaluation of the sea ice source basin has been established with back trajectories. Moreover, the authors point out that $\approx 80\%$ of Laptev sea ice is seasonal, therefore well suited for bromine explosion cycles in springtime. Since Arctic sea ice is generally thicker and less permeable than Antarctic sea ice, it is likely that iodine compounds, biologically produced from sea ice algae colonies, can be released into the atmosphere only when the sea ice cover disappears. The Akademii Nauk ice core iodine signal is positively correlated with satellite

observations of Laptev Sea summer sea ice ($\rho=0.49$, Table 1 and Fig. 8a) and with spring sea ice ($\rho=0.50$). It should be noted that while in Spolaor et al. 2013a (Svalbard) iodine was negatively correlated with March-May sea ice, in Spolaor et al. 2016a the correlation with the Laptev summer sea ice extent is found to be positive (likely because 80% of Laptev Sea spring sea ice is seasonal, hence its presence is positively contributing to iodine emissions).

Bromine and MSA were measured in two ice cores from central and north-eastern Greenland, the Summit and Tunu ice cores: the records cover the time period 1750–2010 (Maselli et al. 2017). MSA has shown some potential as a sea ice proxy, especially in Antarctica, as some results suggest that it reflects biological activity in sea ice marginal zones (Curran and Jones 2000). So far in the Arctic only O’Dwyer et al. 2000 reported a significant correlation ($\rho=-0.66$) between an MSA record (at Svalbard) and Arctic sea ice extent (O’Dwyer et al. 2000). In central Greenland (Summit), MSA concentrations has been found negatively correlated to surface air temperatures, the latter is speculated to decrease biological emissions, but no clear correlation with sea ice extent has lead to univocal results, since ~ 1750 (Legrand 1997). In their study, Maselli et al. 2017 found a significant correlation between MSA and variability of marginal sea ice zone (OWIP - open water in ice pack, calculated as difference between sea ice area, derived from sea ice concentration over the area of the grid cell, and sea ice extent, calculated with a $>15\%$ constrain on the sea ice concentration), the latter identified by back trajectory studies. The comparison between MSA and bromine time series shows that in the pre-industrial era bromine was also likely linked to the local sea ice conditions. The authors speculate that the departure of correlation with MSA in the industrial era is linked to changes in acidity and NO_x pollution, enhancing bromine release from sea ice.

6.2.1 1700-PRESENT IODINE VARIABILITY IN THE RENLAND CORE

In the MBL, the main source ($\sim 75\%$) of atmospheric iodine is the ocean release of inorganic iodine (HOI , I_2) following the deposition of atmospheric ozone and the reaction with iodide at the sea surface (Carpenter et al. 2013; MacDonald et al. 2014). Organo-iodine compounds account for the remaining part (CH_3I , CH_2I_2). In the Antarctic PBL, the biological emissions of inorganic iodine from sub-ice algae is the main source of iodine to the polar atmosphere (Saiz-Lopez et al. 2015). A negative feedback mechanism between ozone and iodine was proposed since an anthropogenic ozone enhancement would increase iodine inputs, which in turn would accelerate ozone destruction (Prados-Roman et al. 2015).

The Renland ice core iodine record provides the opportunity to investigate the connection between ozone-induced iodine emissions and the following negative feedback between them. Iodine was measured in the Renland ice core in the same Venice-Perth ICP-MS measurement campaign that is described in section 6.6 in the context of bromine and sodium. For the description of the experimental setup, the reader is referred to section 6.6.2. The ac-

cumulation reconstruction for the last 4 kyr at Renland (Sec. 5.5) was used to calculate the air-to-snow fluxes of iodine.

Iodine concentrations were stable from the onset of the Industrial Period (1750 AD) to 1940 AD, followed by a drop to values of 0.01 ng g^{-1} during the 1940s (Fig. 6.6). Since the 1950s, iodine concentrations (fluxes) have risen nearly 4 (3) fold. The sharp increase in iodine concentrations since 1950 has occurred in a period when the tropospheric ozone levels have increased globally, e.g. the longest quantitative ozone record in Europe indicates that ozone doubled between 1950s and 2000, while several sites in Europe showed a lack of positive trend since 2000 (Cooper et al. 2014). A 33% increase of oceanic iodine fluxes over the North Atlantic (an area sampled by the Renland site, see Sec. 5.6) since the 1950s is indicated by the CAM-Chem chemistry-climate model, in response to a 30% ozone increase during this period (Cuevas et al., in prep). Over the same period, a baseline simulation, without the ozone-induced emission of iodine from the oceans, yields a constant and 10 times lower iodine emission flux. At the same time, with the ozone-induced inorganic iodine emissions implemented in the model simulation, an increase of ozone loss rates due to active iodine species is observed (not shown), consistent with the negative feedback mechanism suggested by Prados-Roman et al. 2015.

During the 1950-1989 period, iodine concentrations in the ice core increase significantly as well as ocean iodine emissions and tropospheric ozone in the North Atlantic ($\rho=0.392$, $p=0.017$ and $\rho=0.362$, $p=0.028$ respectively). Overall, this suggests that ozone-driven ocean emissions of iodine may have controlled the variability of atmospheric iodine levels during the 1950-1989 period. On the other hand, during the period 1990-2011 iodine concentrations increased despite stable atmospheric ozone concentrations (no significant correlation: $\rho=0.136$, $p=0.567$), indicating a different forcing mechanism for iodine emission during the last two decades. Since 1990, Arctic sea ice has experienced a simultaneous thinning and enhanced sub-ice biological productivity, under the forcing of recent Arctic warming. The correlations found between iodine concentration and mean late spring / early summer Arctic sea ice thickness and Arctic sub-ice biological productivity are $\rho=-0.68$ ($p=0.001$) and $\rho=0.65$ ($p=0.002$) respectively. Hence, we suggest that since the 1990s atmospheric iodine levels in this region might have been significantly influenced by the enhanced sub-ice biological production.

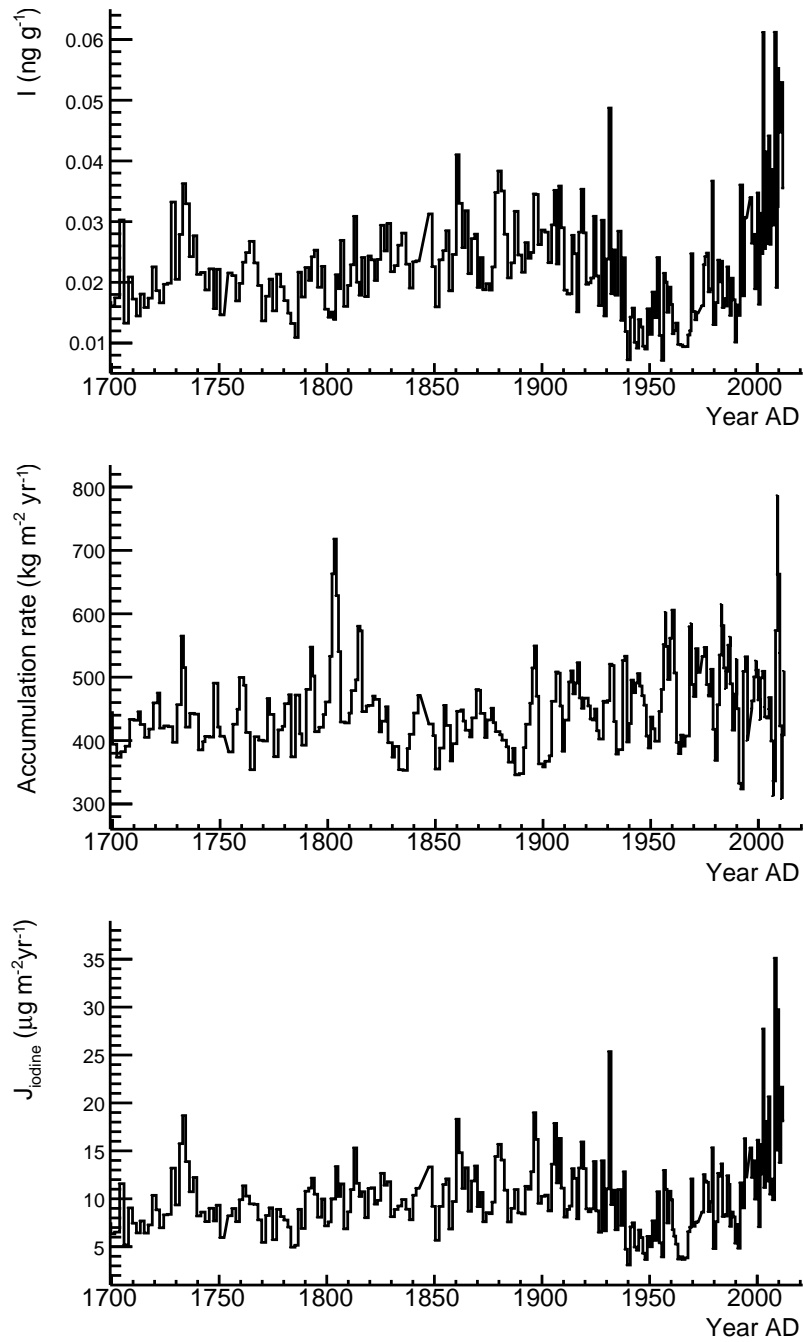


Figure 6.6: Iodine concentration (top), annual accumulation (middle, see Sect. 5.5) and flux (bottom) records from the Renland ice core since 1700 AD (Cuevas et al., submitted).

6.3 FROM MILLENNIAL TO GLACIAL – INTERGLACIAL TIMESCALES

Since the 1980s, satellite observations allow comparison between sea ice sodium records. Several attempts have been made but the studies have found that both in Greenland (Fischer 2001; Hutterli et al. 2007) and Antarctica (Abram et al. 2013 and references therein) sodium records are mostly related with atmospheric circulation patterns rather than sea ice extents. However, over centennial and longer time periods, the atmospheric circulation contribution to sodium time series may average out, increasing the sea ice signature. If so, sodium timeseries will reflect mainly sea ice extent trends. An additional evidence that led ice core scientists to deduce that sodium does indeed contain an often dominant sea ice signature is that higher sodium fluxes are found during the LGM (Last Glacial Maximum) and in general during the glacial periods. Indeed, in a qualitative way, Antarctic sodium records agree with marine sediments (see Abram et al. 2013). Yet, additional complication is represented by the fact that in Antarctica, sodium flux time series appear rather constant during cold periods, if compared to the degree of variability inferred from marine sediment sea ice proxies (Fig. 4 in Abram et al. 2013; Röthlisberger et al. 2010). This feature could be related to the fact that as the sea ice extent increases radially from the Antarctic continent, the transport time between new source areas and the ice core also increases; as a result sodium fluxes become less sensitive for very large sea ice areas (Abram et al. 2013; Röthlisberger et al. 2010; Fischer et al. 2007a). Overall, it is generally believed that sodium is a qualitative sea ice proxy at these timescales. In Antarctica, the only ice core that provides a combined bromine (and sodium) and iodine record is the Talos Dome ice core (Ross Sea sector, Spolaor et al. 2013c), spanning the last 215 kyr. Specific considerations concerning the ssNa flux variability for the last 150 kyr in connection to Ross Sea sea ice have been presented by Schüpbach et al. 2013.

In Greenland, the picture is complicated by the fact that a very different geometry exists. The Arctic is a partially closed basin surrounded by land and in glacial periods the presence of Laurentide and Eurasian ice sheets over nowadays water and/or sea ice-covered areas had likely profound implications on the Arctic circulation. At present, sea ice is formed in the Arctic basin and is then transported through the Fram and Davis strait into the North Atlantic. In situ formation of sea ice is therefore only of secondary importance in the southernmost regions of the Arctic. Open ocean is the primary sea salt source during modern conditions, and cyclonic activity over the northern Atlantic leads to transport of SSA onto the Greenland ice sheet (Fischer et al. 2007b). In Greenland, the use of Br_{enr} in the NEEM sodium-bromine record (Spolaor et al. 2016b) was discussed in relation to the fingerprint of Canadian Arctic sea ice (Sec. 6.5). Bromine and sodium were also recently measured in the 2015-drilled Renland ice core (Sec. 6.6, Maffezzoli et al., in prep.), spanning ~ 120 kyr. At present, no published iodine records exist in the Arctic. Iodine was measured in the Ren-

land ice core but it is not presented in this work. In particular, the stability of this impurity over glacial timescales is not yet established, and may be challenged by atmospheric dust loading (see Sec. 6.4).

6.4 ANTARCTICA: TALOS DOME

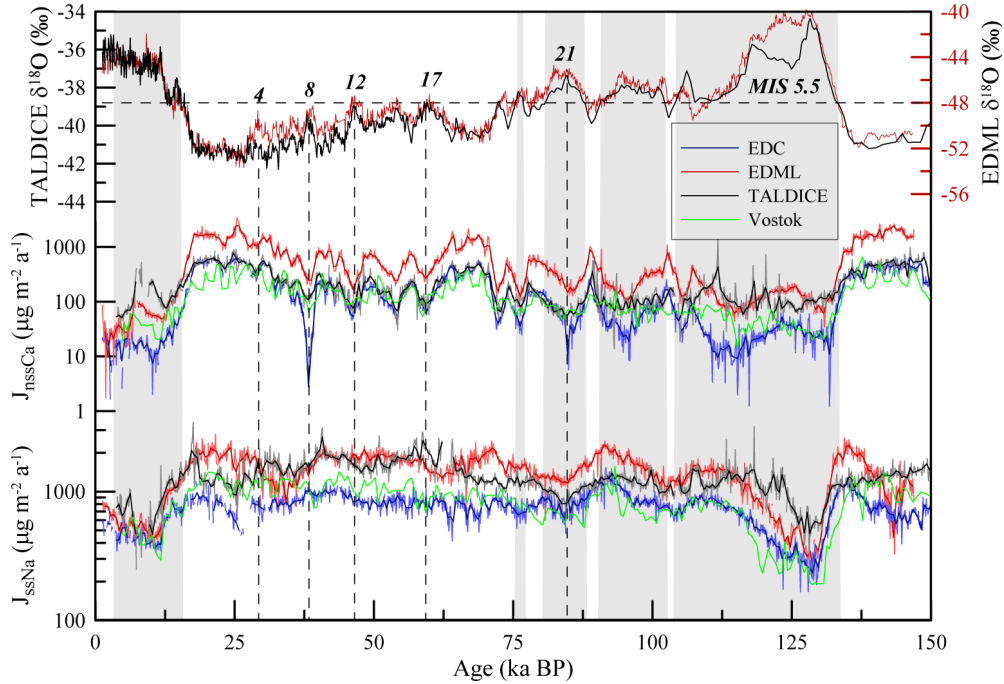


Figure 6.7: Bottom panel: the $ssNa^+$ flux (J_{ssNa}) of TALDICE (new data) is plotted in black along the one of EDC (blue), EDML (red, new CFA data), and Vostok (green). Light colours indicate 100 yr median values, dark colours 500 yr median values. All data are shown on the AICC2012 age scale. From Schüpbach et al. 2013.

The 150 kyr variability of $ssNa$ flux at Talos Dome is presented in Fig. 6.7 along with other ice cores in Antarctica (Schüpbach et al. 2013). If comparing Holocene and Eemian levels of J_{ssNa} , the Talos Dome ice core shows very similar levels, while EDC and EDML Eemian fluxes were only half (EDC) or even less (EDML) compared to the Holocene. At EDC, Wolff et al. 2006 point out that here J_{ssNa} reflects winter sea ice extent in the Indian Ocean sector of the Southern Ocean, due to very low summer sea ice extent in this area even during glacial periods (Fig. 6.8B, Gersonde et al. 2005). At EDML, Eemian J_{ssNa} is even more reduced than in EDC, possibly due to an even stronger decline in sea ice coverage in the Atlantic sector related to a reduction of both winter and summer sea extent in the Atlantic sector at that time (Gersonde et al. 2005; Fischer et al. 2007a). While the low J_{ssNa} are

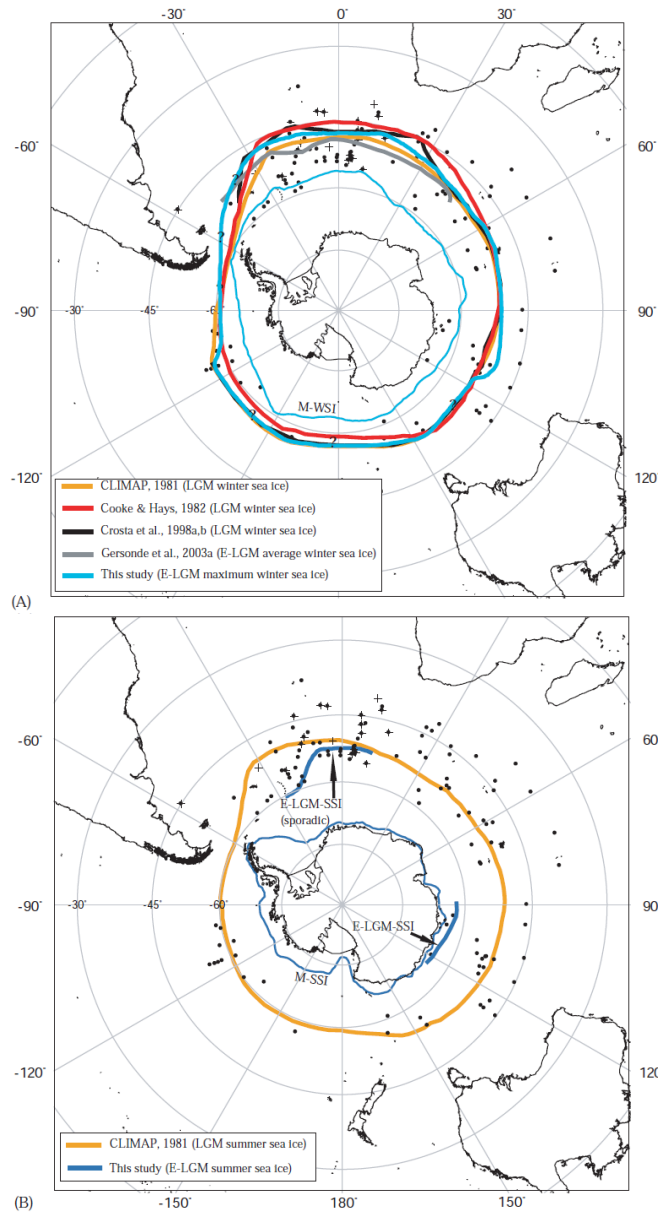


Figure 6.8: (A) Comparison of LGM WSI (winter sea ice) edge reconstructions presented by different studies. (B) Comparison of LGM summer sea ice edge reconstructions from CLIMAP (1981) and this study (Gersonde et al. 2005). From Gersonde et al. 2005.

in line with the warming in Antarctica during the Eemian (EPICA Community Members, 2004), the J_{ssNa} levels at Talos Dome suggest that a significant and present-like sea ice cover

in the Ross Sea was present during the last interglacial.

In their study at Talos Dome, [Schüpbach et al. 2013](#) notice that in the 115-20 kyr BP period, the Talos Dome J_{ssNa} is consistently lower than in EDML (Fig. 6.7), with only two exceptions: between 40-30 kyr BP and 65-55 kyr BP. In the former (40-30 kyr BP), higher $\delta^{18}O$ values at EDML compared to Talos Dome are observed (6.7, top panel). This would indicate a warming of the Atlantic Sector in this period, resulting in lower sea ice extent and sodium inputs. In the latter (65-55 kyr BP), [Schüpbach et al. 2013](#) point out that the inversion of the J_{ssNa} relationship marks the transition between from MIS 4 into MIS 3, with greater variability observed at Talos Dome (Ross Sea) compared to EDC or EDML, whose long term J_{ssNa} variations remain around the same mean. This suggests that the shift in sea ice coverage from MIS 5 to MIS 3 is less pronounced in the Indian (EDC) and Atlantic (EDML) sectors, if compared to the Ross Sea (Talos Dome).

[Spolaor et al. 2013c](#) presented a 215 kyr record of sodium and bromine/iodine species (Br^- , I^- , IO_3^-), measured by IC/ICP-QMS (halogens) and ICP-SFMS (sodium) (Fig. 6.9). Bromide and sodium concentrations are negatively correlated ($r = -0.54$). Additionally, Br^- is positively correlated with $\delta^{18}O$ ($r = 0.79$).

The authors quantified the bromine departure from sea water concentration by introducing the bromide fractionation index, $\%Br_{fi}$, defined as:

$$\%Br_{fi} = \frac{(ssBr - Br) \cdot 100}{ssBr}, \quad (6.5)$$

where $ssBr$ is bromine concentration expected from sea water (i.e. $ssBr = 0.006 Na$). Positive $\%Br_{fi}$ thus indicates bromine depletion, while negative values indicate enrichment.

Glacial ice is depleted in bromine (mean $\%Br_{fi} = 68\%$, up to 100%), while interglacial ice is enriched ($\%Br_{fi}$ up to -440%) (Fig. 6.10). The correlation between $\%Br_{fi}$ and sea ice presence (SIP, from [Crosta et al. 2004](#)) is $r = 0.55$ (the value increases to $r = 0.65$ if only bromide depletion periods are considered). As presented in section 6.1.4, the authors explained the observed $\%Br_{fi}$ variability as a difference in the transport between bromine and sodium. Their model simulation suggests that (unlike some measurements in snow, [Simpson et al. 2005](#), [Li et al. 2014](#)) bromide undergoes a faster deposition than sodium (Fig. 6.4). Based on this result, [Spolaor et al. 2013c](#) suggested a bromide-sodium deposition scheme (Fig. 5 in their paper). According to this mechanism, glacial snow would be depleted in bromide since seasonal sea ice would be further away from the ice core site, therefore the air parcel would experience more loss of bromine, compared to sodium. The situation is reversed during interglacial periods, where closer seasonal sea ice would reduce bromine loss. Overall, the Br^- enhancement observed during interglacial periods changes to a Br^- depletion in colder climates because of the reduced proximity to multi-year sea ice. Based on these considerations, [Spolaor et al. 2013c](#) estimated that glacial MYSI extended ~ 500 km north

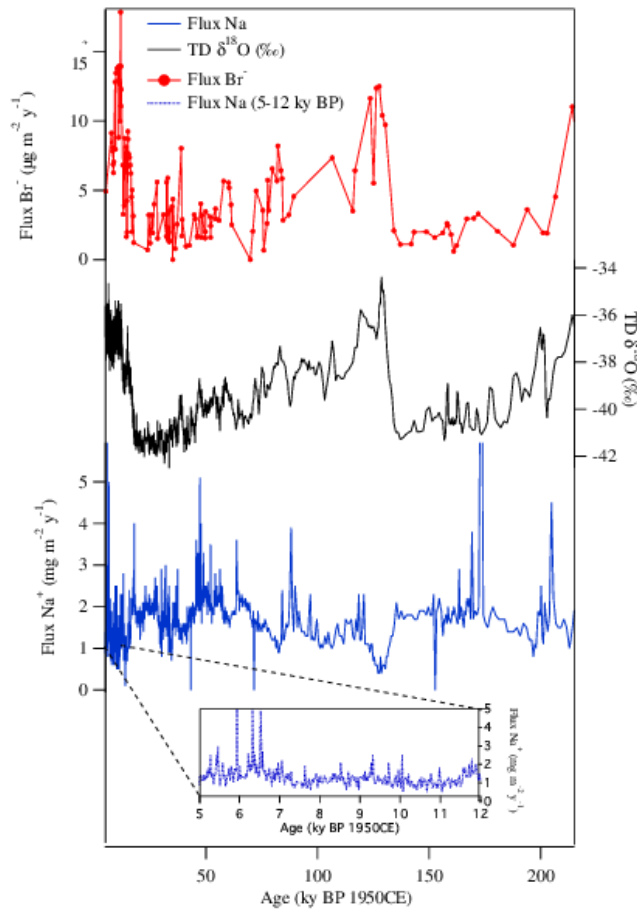


Figure 6.9: Plot of Br^- fluxes (red) in the TD ice core. Br^- fluxes correlate with $\delta^{18}\text{O}$ (black curve) and anti-correlate with Na fluxes (blue curve). The inset box represents the sodium flux between 6 and 12 kyr BP. Note that sodium and $\delta^{18}\text{O}$ were recorded as a high-resolution data set while bromide was measured at lower resolution. From Spolaor et al. 2013c.

of the Antarctic coast, with maximum extension from 16 to 80 kyr BP and 134 to 205 kyr BP. The authors report that the transport mechanism is consistent with observed bromine depletion in snow/ice samples at Dome C (Spolaor et al. 2013c). Results from a snow pit at Dome C, spanning 1880-present do actually show bromine depletion throughout most of the stratigraphy (Spolaor, pers. comm.). This result would be opposite that expected from surface measurements by Li et al. 2014, who showed a tendency towards bromine enrichment as one moves towards inland of Antarctica, and from SSA and gas-phase bromine results presented by Legrand et al. 2016b.

Schüpbach et al. 2013, using the J_{ssNa} record, suggested that the sea ice extent in the Ross

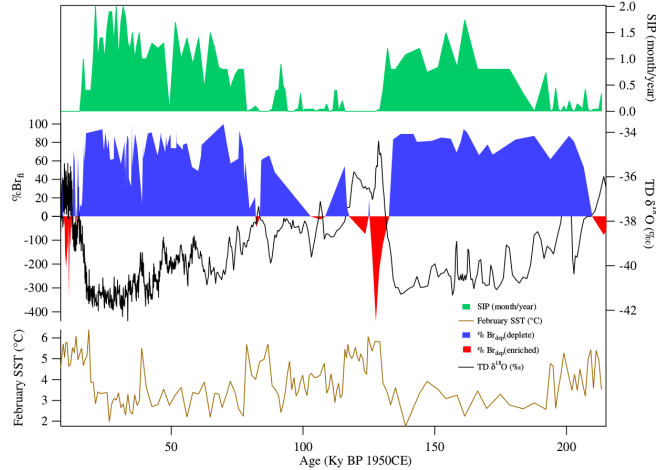


Figure 6.10: $\%Br_{fi}$ is plotted with sea ice presence (SIP, green area, expressed as month/year) and February sea-surface temperature (red line) (Crosta et al. 2004). Talos Dome $\delta^{18}O$ is also shown. The red areas indicate Br^- enrichment (i.e. negative $\%Br_{fi}$) while blue areas indicate bromide depletion. From Spolaor et al. 2013c.

Sea was similar in the Holocene and in the Eemian. Unfortunately, due to a coarse resolution in the bromide measurements (1 m resolution), a comparison between the J_{ssNa} (Schüpbach et al. 2013) and the $\%Br_{fi}$ (Spolaor et al. 2013c) records would not lead to robust conclusions (in Spolaor et al. 2013c only a few Eemian ice samples were analyzed).

Iodine speciation measurements were carried out on Talos Dome samples (Spolaor et al. 2013c). Total iodine ($I_{tot} = I^- + IO_3^-$) was higher during the glacial (mean of $3.2 \mu g m^{-2} yr^{-1}$) than during interglacial periods (mean of $1.1 \mu g m^{-2} yr^{-1}$), with a maximum of $11.2 \mu g m^{-2} yr^{-1}$ during the LGM (Fig. 6.11). The enhanced total iodine flux in the glacial is speculated to be related to the greater sea ice extent during the cold period, promoting biological emissions by sea ice algae. The picture of an extended glacial sea ice is roughly consistent to what was concluded from the bromine study, for the last glacial cycle (~ 80 kyr-present). The correlation between I_{tot} and sea ice presence (Crosta et al. 2004) is $r = 0.65$. Interestingly, there is a factor ~ 2 difference between the total iodine flux in the two glacial periods covered by the record. From MIS 2 to MIS 5, $I_{tot} \simeq 3.6 \mu g m^{-2} yr^{-1}$; from MIS 6 to MIS 7 $I_{tot} \simeq 1.6 \mu g m^{-2} yr^{-1}$. The correlation between I_{tot} and iron ($r = 0.25$) indicates that the effect of an increased ocean fertilization does not play a major role in the observed iodine variability, as the sea ice extent does. Unlike iodide, iodate (IO_3^-) is found above detection limit only during periods of maximum dust load (Fig. 6.11). The authors suggested that the increased amount of atmospheric dust (from $1-2 mg m^{-2} yr^{-1}$ during interglacials to $15-20 mg m^{-2} yr^{-1}$ during glacials, Lambert et al. 2008) leads to the formation of metal iodates by the interaction between gas-phase oxide molecules, such as I_2O_4 , and dust (correlation between

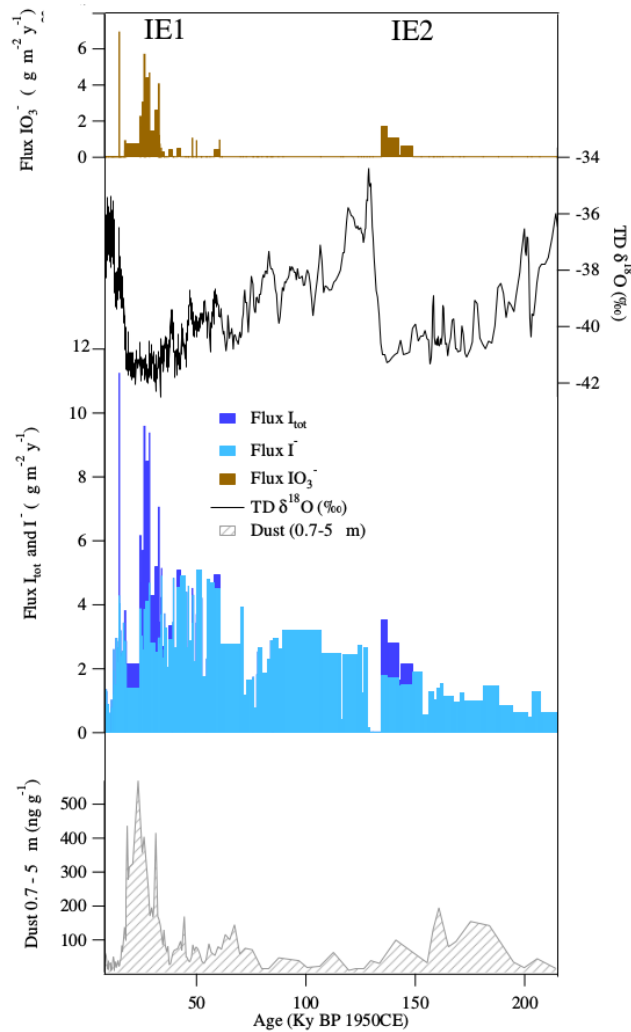


Figure 6.11: Iodate (IO_3^- , brown), iodide (I^- , light blue) and total iodine (I_{tot} , blue) in Talos Dome ice core samples. While I^- is present in all samples, IO_3^- is closely linked with the fine dust load (grey shaded area, [Delmonte et al. 2004](#)) and is present only from 16.8 to 33.8 kyr BP and 134.2 to 143.2 kyr BP. From [Spolaor et al. 2013c](#).

0.7-5 μm dust and IO_3^- , $r = 0.77$). This mechanism would provide a secondary effect in I_{tot} as a sea ice extent indicator, at locations characterized by a high dust load and significant IO_3^-/I^- ratios. The impact of atmospheric dust loading on iodine concentrations in polar snow/ice should be further investigated before any robust conclusions on iodine records at multimillennial timescales are drawn.

6.5 GREENLAND: NEEM

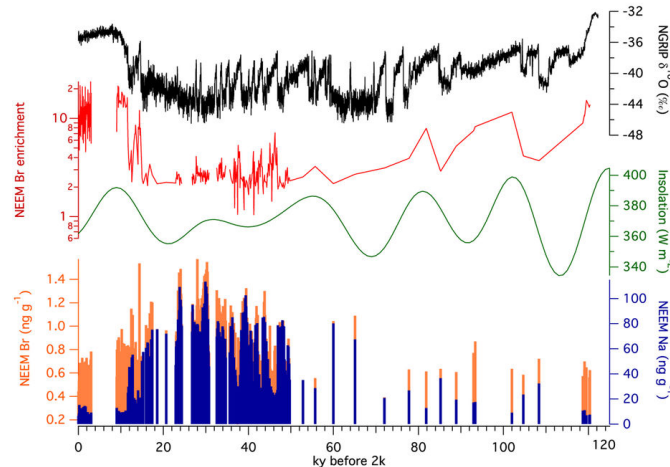


Figure 6.12: Bromine and sodium in the NEEM ice core over the past glacial cycle. Minimum Br_{enr} values are observed during the coldest phases of the glacial, while the maximum is observed during the Holocene climatic optimum. From [Spolaor et al. 2016b](#).

The only existing multi millennial Arctic bromine record was retrieved from the NEEM ice core ([Spolaor et al. 2016b](#)), covering the last 120 kyr (since the end of the Eemian). The dominant source areas of the marine aerosols arriving in northwest Greenland were estimated to be the Canadian Arctic and the Baffin Bay ([Barrie et al. 1992](#)). The variability of sodium and bromine are therefore considered indicators of such basins ([Spolaor et al. 2016b](#)).

Bromine and sodium concentrations show a similar variability, with the lowest concentrations during the late Holocene and the highest during the glacial period (Fig. 6.12, bottom). If comparing the sodium and bromine (concentration) variabilities at NEEM (Fig. 6.12) and fluxes at Talos Dome (Fig. 6.9), the striking difference is that, while at NEEM, sodium and bromine concentration trends are similar, at Talos Dome they appear anticorrelated. This suggests that a different mechanism is in play in the two sites. However, Br_{enr} at NEEM (Fig. 6.12, red) is positively correlated with $\delta^{18}\text{O}$ ($R^2=0.54$), supporting the connection between warm climate conditions, greater presence of FYSI and enhanced bromine photochemistry ([Spolaor et al. 2016b](#)). Similarly, at Talos Dome $\% \text{Br}_{\text{fi}}$ was negatively correlated with $\delta^{18}\text{O}$ ($\% \text{Br}_{\text{fi}}$ and Br_{enr} are defined such as a negative $\% \text{Br}_{\text{fi}}$ indicates a Br_{enr} enrichment, see Eq. 6.5 and Eq. 4.45). Overall, in both sites, enrichment (depletion) of bromine beyond the sea water value is systematically found in warmer (colder) periods.

Br_{enr} in the NEEM ice core is greatest during the early Holocene ($\text{Br}_{\text{enr}} = 15.6 \pm 3.2 (1\sigma)$

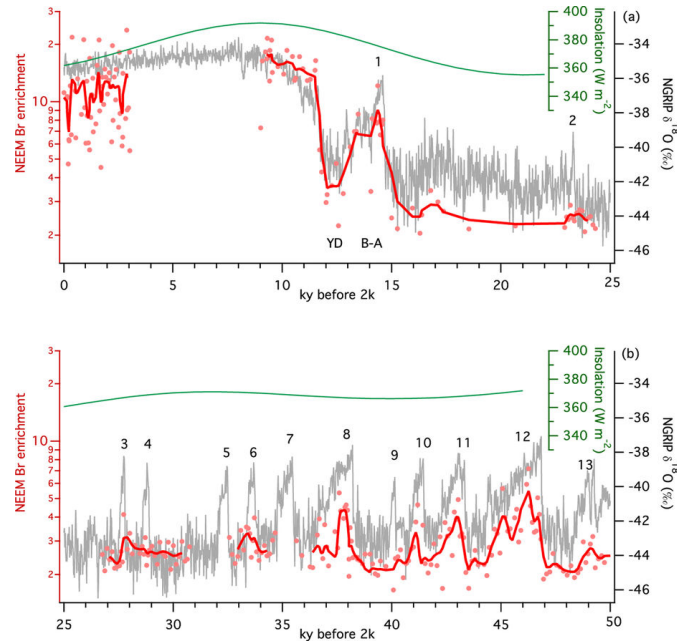


Figure 6.13: Variability in bromine enrichment occurs on stadial-interstadial scales. Bromine enrichment follows the NGRIP $\delta^{18}\text{O}$ profile during abrupt climate changes in the glacial. The greatest Br_{enr} values observed in the Holocene (panel a) occur during the Holocene Climate Optimum and not in the most recent samples. In the glacial (panel b), consistently lower Br_{enr} values are observed, corresponding to a greater extent of multi-year sea ice in the Canadian Arctic. From Spolaor et al. 2016b.

9.0-11.5 kyr b2k) and with values between 2-3 during the stadial periods of the glacial (Fig. 6.13). This difference reflects a variability between increased FYSI and correspondingly lower MYSI in the Canadian Arctic and Baffin Bay during warm periods, and viceversa during cold periods. During the last 3000 years, lower Br_{enr} values ($\text{Br}_{\text{enr}} = 10.6 \pm 4.9 (1\sigma)$ 0.03-3.03 kyr b2k) than the early Holocene suggest an expansion of MYSI in recent millennia. Both the reduction of MYSI during early Holocene and its expansion during recent millennia is supported by sea ice reconstructions based on marine sediments (references in Spolaor et al. 2016b).

From the above observations, the suggested mechanism of Br_{enr} response to sea ice at NEEM (a bimodal behaviour for low Br_{enr} was introduced in Sec. 4.2.6) is described by Fig. 6.14. In particular, at NEEM, the mode corresponding to open water conditions is not observed at any time throughout the record. During the faster climate oscillations (DO events, YD and BA), Br_{enr} follows the $\delta^{18}\text{O}$ variability, suggesting that during such climate periods, in the source basins sea ice varies from MYSI to FYSI as temperature increases (6.13). The authors used a linear calibration between Br_{enr} and FYSI area in three climate scenarios, late

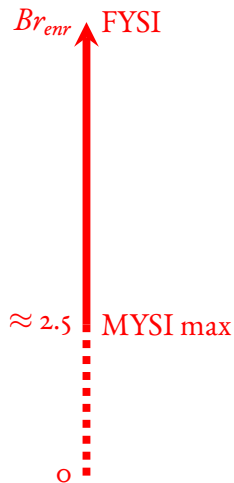


Figure 6.14: Br_{enr} as proxy for first-year sea ice (FYSI) in the NEEM ice core. Throughout the record, low values are associated to multi-year sea ice (MYSI) conditions in the Canadian Arctic and Baffin Bay basins.

Holocene (0.03-3.03 ky BP), early Holocene (9.0-11.5 ky BP) and glacial (20.6-30.7 ky BP) to estimate the FYSI area during the early Holocene (Fig. 4 in Spolaor et al. 2016b). The applied method assumes that 1) during the glacial $FYSI = 0$ and 2) that 1979-2013 satellite observations of FYSI are representative of late Holocene FYSI. The linear extrapolation predicts early Holocene FYSI to be $\sim 1 \text{ Mkm}^2$ more extended than present conditions. Given that present times MYSI area is $\sim 0.44 \text{ Mkm}^2$, an increase of 1 Mkm^2 of FYSI would lead to complete MYSI loss in the Canadian Arctic.

The NEEM ice core Br_{enr} interpretation relies on the hypothesis that any different transport fractionation that affects bromine and sodium (see Sec. 6.1.4) is constant in time (i.e. does not depend on the type of source, FYSI/MYSI/OW, on the source area, or in other words does not depend on the absolute concentrations of sodium and bromine), and can be therefore treated as a constant offset throughout. This seems a plausible hypothesis since the aerosol source areas for the NEEM ice cores are closed basins. On this hypothesis, the variability would be related to the source (i.e. sea ice) strength. It is also worth noticing that, while bromine enrichment in NEEM is interpreted as a sea ice source effect (higher values representing increased FYSI coverage), at Talos Dome negative Br_{enr} values (i.e. enrichment) was interpreted as a transport mechanism, but still based on the assumption that with greater MYSI, FYSI would be pushed further away.

6.6 GREENLAND: RENLAND

The Renland ice core site was described in Chapter 5 along with some glaciological parameters (timescale and annual layer thicknesses, density and strain profiles), as well as the accumulation reconstruction for the last 4000 years and the potential aerosol areas inferred from Hysplit back trajectory studies. This section will address the measurements of sodium and bromine in relation to a sea ice signal at Renland, for the last glacial-interglacial period (~ 125 kyr). All the time series will be presented on the V_4 timescale.

6.6.1 THE ICE CORE ICP-MS SAMPLES

The RECAP ice core sub-samples ($n=1205$) were decontaminated and collected from a continuous ice core melting system as part of the RECAP Continuous Flow Analysis (CFA) campaign conducted at the University of Copenhagen in autumn/winter 2015 (Fig. 3.3). The ice core was melted at a speed of approx. 3 cm min^{-1} on a gold coated pure copper melter head. The CFA melter and analytical setup have been described respectively by [Bigler et al. 2011](#) and [Kaufmann et al. 2008](#). Briefly, water was pumped and collected continuously from the melter head into pre-cleaned polyethylene vials (cleaned with ultrapure water, $> 18.2 \text{ M } \Omega\text{cm}^{-1}$) at two different depth resolutions. From the ice cap surface to a depth of 535.15 m, each sample incorporated ice meltwater corresponding to a depth interval of 55 cm. From a depth of 535.15 m to the ice cap bedrock each sample integrated ~ 18 cm of depth. The time resolution is annual to centennial in the holocene and centennial to millennial in the glacial and Eemian sections (Fig. 6.15). After collection, samples were immediately refrozen at -30°C and shipped to Cà Foscari University of Venice (Italy, $n=770$) and Curtin University of Technology (Perth, Western Australia, $n=435$) for determination of bromine (isotope ^{79}Br), sodium (isotope ^{23}Na) and iodine (isotope ^{127}I) by inductively coupled plasma mass spectrometry (Sec. 6.6.2). Samples were kept in the dark after collection until analysis to prevent bromine photolysis reactions. Different subsets of the samples were analyzed using two different types of inductively coupled plasma mass spectrometer instruments at the two laboratories. A laboratory intercomparison was performed on a common set of samples ($n=141$) to investigate the differences between the two setups. This comparison is discussed in Section 6.6.3.

6.6.2 ANALYTICAL DETERMINATION OF NA, BR AND I: ICP-QMS AND ICP-SFMS

Venice — Italy

Bromine and sodium (^{79}Br , ^{23}Na and ^{127}I) were determined by Inductively Collision Reaction Cell-Inductively Coupled Plasma-Mass Spectrometry (CRC-ICP-MS, Agilent 7500cx, Agilent, California, USA). The introduction system consisted of a ASX-520 autosampler

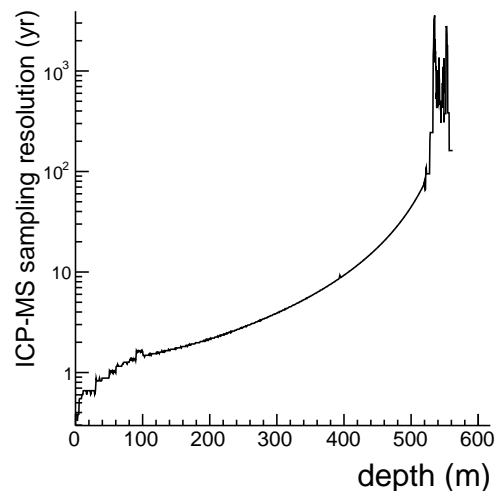


Figure 6.15: Time integrated within the ICP-MS sampling resolution: 55 cm from the surface to 535.15 m and ~ 18.3 cm from 535.15 m to bedrock (the V4 timescale has been used here).

(CETAC Technologies, Omaha, USA) and Scott spray chamber fitted with a MicroFlow PFA nebulizer. The sample flow was kept at $100 \mu\text{L min}^{-1}$. All reagents and standard solutions were prepared with ultrapure water (UPW, $18.2 \text{ M } \Omega\text{cm}^{-1}$). Nitric acid (5% v/v, trace metal grade, Romil, Cambridge, UK) and UPW washes (2 minutes each respectively) were used for background recovery after every sample. The experimental routine (standards and calibrations), as well as the overall instrument performance (detection limits and reproducibility) are the same as in [Spolaor et al. 2016b](#). The detection limits (calculated as three times the standard deviation of the blanks, 3σ) for sodium, bromine and iodine were respectively 1 ppb, 0.05 ppb and 0.005 ppb.

Perth — Australia

Curtin University analyses were performed by Sector Field Inductively Coupled Plasma Sector Field Mass Spectroscopy in reverse Nier-Johnson geometry (ICP-SFMS, Element XR, Thermo Fisher, Germany) inside a Class 100 clean room environment at Curtin University TRACE facility (Trace Research Advanced Clean Environment Facility). The ICP-SFMS introduction system consisted of an elemental scientific Inc. (ESI, Omaha, USA) syringe-pumped autosampler (Seafast II) connected by perfluoro-alkoxy (PFA) capillary tubing to a six port, two-way, high purity valve (ESI) with a one mL PFA capillary injection loop. The sample was pushed from the injection loop to the instrument using an ultrapure water carrier. A 1 ppb indium internal standard in 5% v/v nitric acid (HNO_3 , double PFA

distilled) flow rate was mixed inline at $25 \mu\text{L min}^{-1}$ with the sample water using a tee (final flow rate of $400 \mu\text{L min}^{-1}$, take-up time 1.5 min) just before nebulization. Nebulisation occurred in a peltier cooled (2°C) quartz cyclonic spray chamber (PC₃, ESI), fitted with a PFA micro-concentric nebulizer (PFA-ST, ESI). Bromine and sodium isotopes (^{79}Br and ^{23}Na) were detected in medium resolution (10% valley resolution of 4000 amu) and normalized to ^{115}In , while iodine (^{127}I) was detected in low resolution ($R = 300$) and normalized to ^{115}In . Introduction system memory effects were reduced by rinsing the system in between samples with high purity HNO_3 (3%) and UPW. One procedural blank and one quality controlled standard (QC) were analyzed every 5 samples to monitor the system stability. The detection limits for Br, Na and I were 0.18, 1.1 and 0.002 ppb respectively ($n=80$, calculated as 3σ the blank values). The majority of the sample concentrations were above the detection limits for both sodium and bromine (97%). Repeatability of measurements was systematically tested in each analytical run by measuring replicates of quality control standards throughout the analyses. The relative standard deviations of the QC concentrations were 9 % for Br, 4% for Na and 16% for I ($n=82$, analyzed over >100 hours). Calibration standards were prepared by sequential dilution (seven standards) of NIST traceable commercial standards (High-Purity Standards, (Charleston, USA)). All linear regressions showed $R^2 > 0.99$ ($n=8$, $p < 0.001$). All the materials used for the analytical preparations (flasks, vials, pipettes, ...) were systematically cleaned with UPW ($>18.2 \text{ M } \Omega\text{cm}^{-1}$) and double PFA distilled ultra-pure HNO_3 (3%, prepared from IQ grade HNO_3 , Choice Analytical Pty Ltd, Australia) throughout. All the chemical preparations took place inside an additional Class-10 module.

6.6.3 LABORATORY INTERCOMPARISON

Reproducibility of measurements between the two laboratories was tested by analyzing with both setups ~ 140 samples of a 6.2 m snowpit which was dug in June 2015. The snowpit was sampled in the field at ~ 4 cm resolution using polyethylene vials. The samples were kept frozen at -20°C and shipped to Venice (Italy). Here they were melted, measured by ICP-QMS, frozen again and shipped to Perth (Australia) for ICP-SFMS determinations. The samples arrived in Perth $\sim 70\%$ frozen and 30% melted.

Figure 6.16 shows the sodium and bromine comparison between the two setups. The linear X^2 -fit (constrained to zero) probability is extremely poor, reflecting a possible underestimation of the experimental errors, or some systematic uncertainty concentration-dependent. Yet, the slope of the fit is close to 1 ($m = 1.084 \pm 0.011$ for sodium; $m = 1.085 \pm 0.011$ for bromine). The distributions of the residuals show an average measurement offset of -1.4 ± 0.5 ppb (sodium) and -0.039 ± 0.016 ppb (bromine), with a standard deviation (RSD) of 6.1 ppb (sodium) and 0.19 ppb (bromine). If a few outliers are removed from the residual distribution (by applying Chauvenet's criterion at 3σ CL) and a gaussian fit is performed (see insets), $\text{RSD}=0.11$ ppb (bromine), $\text{RSD}=1.9$ ppb (sodium).

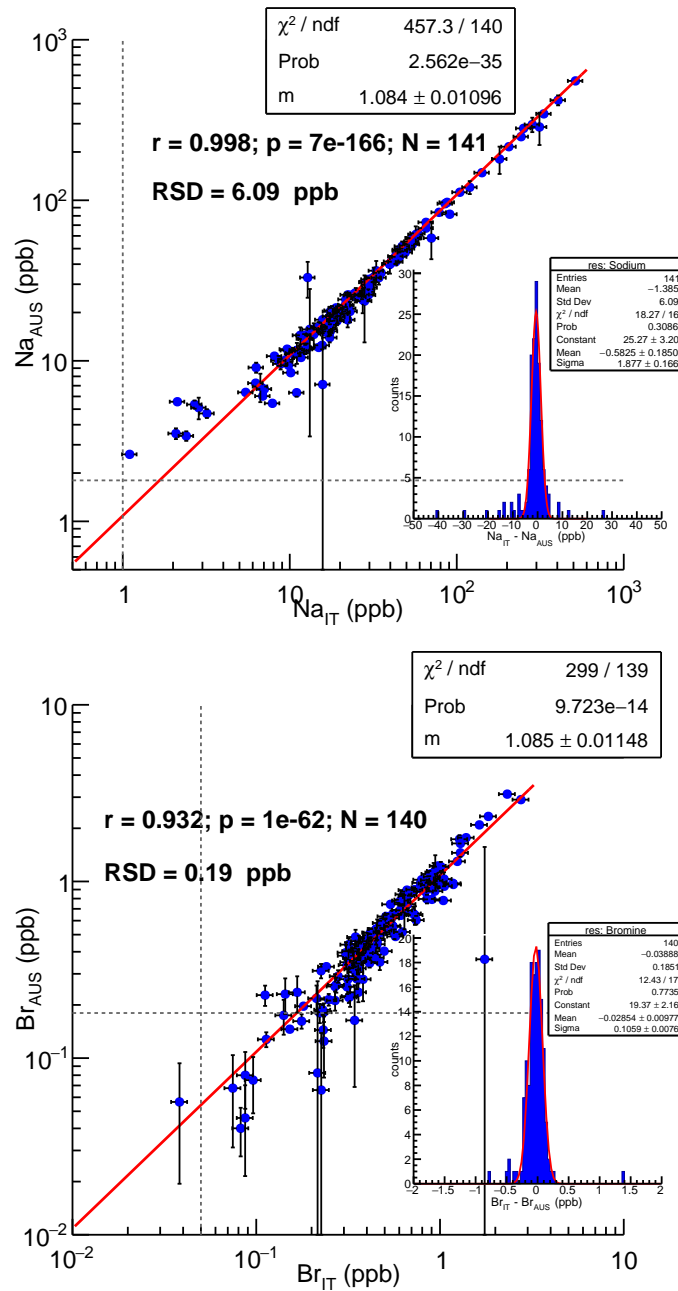


Figure 6.16: Sodium (top) and bromine (bottom) comparison between ICP-QMS (Venice) and ICP-SFMS (Perth). Red lines: χ^2 linear fit. Insets: distribution of residuals. Grey lines: detection limits.

It is worth noting that since the deviation from the slope to 1 is the same for both analytes, in the Br_{ent} values such error is canceled.

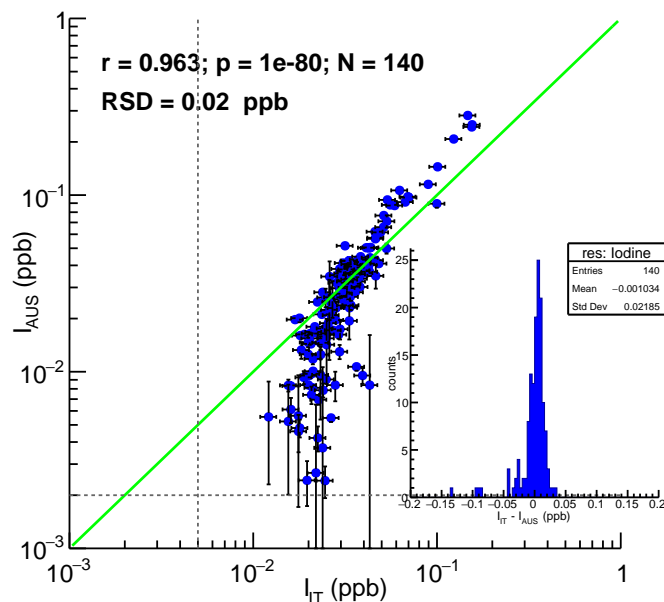


Figure 6.17: Iodine comparison between ICP-QMS (Venice) and ICP-SFMS (Perth). Inset: distribution of residuals. Green line is the $I_{\text{AUS}} = I_{\text{ITA}}$ line (not a fit).

The iodine comparison (Fig. 6.17) reveals that for $I_{\text{IT}} \gtrsim 0.05$ ppb, I_{AUS} are systematically higher (more than 3σ) than I_{IT} . Viceversa, at $I_{\text{IT}} \lesssim 0.03$ ppb, I_{AUS} are lower ($\approx 1-2\sigma$). The RSD is 0.02 ppb. This value is significant if compared to the mean iodine concentration in the core (≈ 0.02 ppb for the Holcene, Fig. 6.6). Since standard reference materials were not available, it is not possible to distinguish which of the two laboratory measurements are more accurate. The differences may be found in the intrinsic sample concentrations, which were not constant between the two campaigns. The samples were unfrozen, measured and frozen again in Venice. Afterwards, they were shipped to Perth, melted and measured again. It is likely that the low iodine concentrations were altered between the analytical phases. Additionally, the samples arrived in Perth not completely frozen and biological growth could have modified (likely increased) the iodine concentrations. Unlike these samples used to perform the laboratory comparison, the Renland ice core samples remained sealed until analyzed in the respective laboratory. A careful check on the Renland iodine concentration time series reveals a continuous trend between I_{IT} and I_{AUS} sections (not shown).

From this study, it appears that caution during sample handling and transport is more

essential for reliable measurements of iodine than it is for sodium and bromine.

6.6.4 TECHNIQUE COMPARISON: IC, CFA AND ICP-MS

Since sodium was discretely measured by ion chromatography in the Renland 1988 core (Hansson 1994, Fig. 3 third panel), continuously by absorption spectroscopy during the Copenhagen 2015 CFA campaign and in discrete samples by ICP-MS (ICP-QMS and ICP-SFMS), a preliminary compatibility analysis between these measurements is presented here (Fig. 6.18).

The $\delta^{18}\text{O}$ comparison shows that some time offset exists between the two cores in some time ranges. The Renland 1988 core was dated by ice flow model, using three time fixed points (YD, BA and the culmination of the Eemian at 130 kyr BP). A careful assessment of the new dating, using synchronizations with other cores and other dating techniques will provide more clues on the time offset. Additionally, some absolute $\delta^{18}\text{O}$ difference between the 2015 integrated values and the 1988 discrete profile, and some other differences especially during the DO events (e.g. DO 19, 20) are visible (even if a time offset is considered).

The sodium comparison (Fig. 6.18, middle panel) suggests that the 1988 IC measurements overestimate Na concentrations, especially in the time periods 10-20 kyr, 45-75 kyr and also > 90 kyr. In the 2015 core, the CFA (note that CFA measurements are more highly resolved) and the ICP-MS measurements are overall consistent with each other.

Similarly to sodium, the CFA and ICP-MS calcium measurements are consistent with each other within ≈ 10 ppb. The higher ICP-MS values might suggest that ICP-MS detects an additional insoluble dust fraction. The 1988 IC measurements differ greatly, with differences up to 100 ppb compared to the other two techniques.

This comparison suggests that the CFA and ICP-MS techniques are overall consistent, and the sodium consistency holds also during the Holocene part of the record (not shown; calcium was not measured by ICP-MS in the Holocene section). All the following considerations are based on the ICP-MS measurements. The 1988 IC measurements should be interpreted with care, although it is acknowledged that they were measured in a different core with different glaciological flow characteristics. In a future perspective, a quantitative comparison between CFA and ICP-MS could reveal some clues on the ICP-MS insoluble fraction recovery factors for the crustal elements.

6.6.5 THE CRUSTAL CONTRIBUTION TO THE SODIUM SIGNAL

Sodium signals could potentially have an additional contribution from crustal sources ($\text{Na}_2\text{O} \approx 2-4$ weight percent oxide, in the upper continental crust, UCC, Rudnick and Gao 2003, Table 1). The potential additional sodium input at Renland was estimated in two different ways: by looking at Cl/Na and Na/Mg ratios and from a combined sodium-calcium

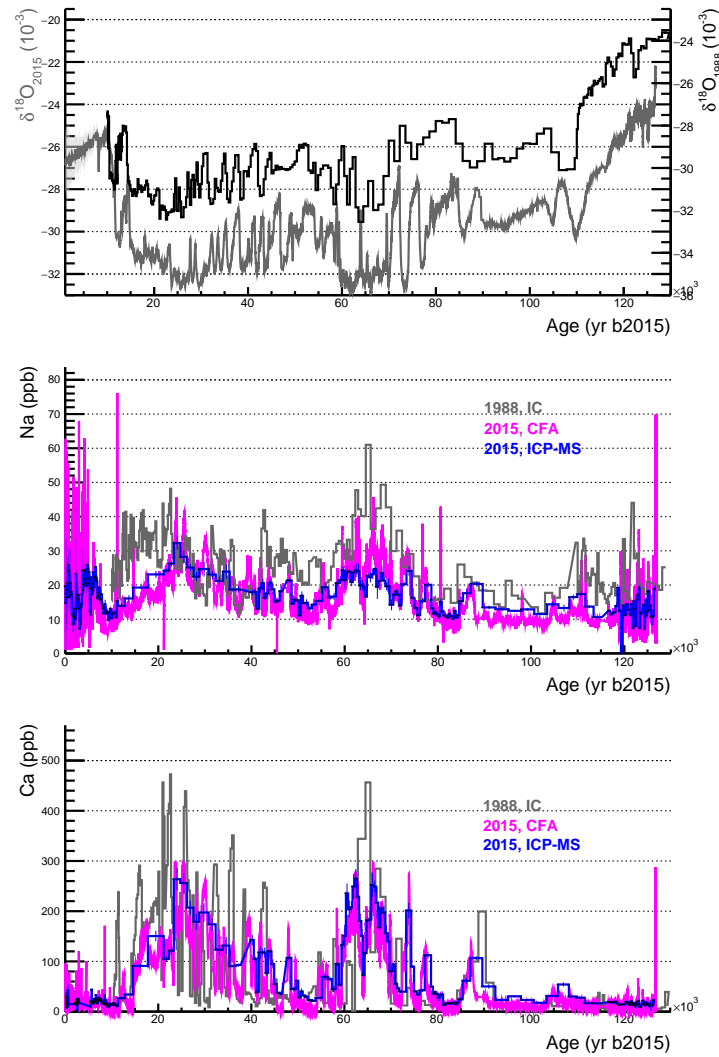


Figure 6.18: Comparison of $\delta^{18}\text{O}$, sodium and calcium between the Renland 1988 (from [Hansson 1994](#)) measurements, and Renland 2015 CFA and ICP-MS measurements. Top: $\delta^{18}\text{O}$ (black, right axis: 1988; grey, left axis: 2015), note the axes are shifted by 3‰. Middle: sodium (grey: IC 1988; magenta: CFA; blue: ICP-MS). Bottom: calcium (grey: IC 1988; magenta: 2015 CFA; blue: 2015 ICP-MS). Experimental errors on sodium and calcium ICP-MS profiles are indicated but too small to be clearly visible: $\sigma_{\text{Ca}} \approx 1\text{-}2$ (10-20) ppb in the Holocene (glacial); $\sigma_{\text{Na}} \approx 1\text{-}3$ uniformly in time. IC = ion chromatography. ICP-MS: combined Venice-Perth (sodium), Perth (calcium).

correction. Chloride, magnesium and calcium were all measured by ICP-SFMS throughout the glacial part and in some Holocene sections of the record.

Chlorine to sodium mass ratios higher than sea water (1.8) are observed in ice cores dur-

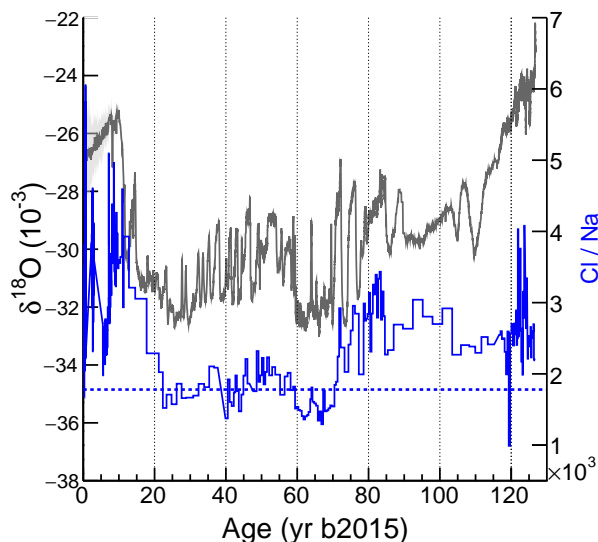


Figure 6.19: Variability of the chlorine to sodium mass ratio in the 2015 Renland core. The dotted line indicates the sea water value (1.8).

ing interglacial periods, due to the release of HCl from the SSA (HCl has a longer residence time), scavenged by acids (HNO_3 , H_2SO_4). During the glacial periods, when atmospheric dust loading increases, the Cl/Na decreases, possibly because acids are neutralized by dust (Röthlisberger et al. 2003). As a consequence, HCl release from SSA is reduced, and in turn the Cl/Na ratio. Additional post depositional effects can further modify the the Cl/Na ratio (Röthlisberger et al. 2003). From the observation of Cl^-/Na^+ ratios, Hansson 1994 (Fig. 3) suggested extra sodium sources, particularly during the glacial part of the record. Our sodium and chloride results (Fig. 6.19) show that during the glacial part, the Cl/Na value shows indeed depleted values in some parts of the record. The minimum (1.4) is found at ~ 66 kyr, suggesting an extra sodium contribution from crustal sources of around 29% at that time. At the LGM, the contribution is $\approx 15\%$.

In the UCC, the Na/Mg mass ratio is ≈ 1 (Rudnick and Gao 2003), while the seawater ratio is ≈ 8.3 . The observed Renland ratios are close to sea water values in the Holocene, and decrease in the glacial part of the record to a minimum of 2.5 at 66 kyr. At this point in time, Mg is ≈ 10 ppb and Na is ≈ 25 ppb. By assuming that Mg is purely of crustal origin, an upper limit of crustal contribution to sodium would be ≈ 10 ppb, i.e. $10/25 \approx 40\%$.

Alternatively, one could use the calcium-sodium ratios in sea water and in the UCC, to isolate the sea salt sodium (and the non-sea-salt calcium) contribution. This procedure is

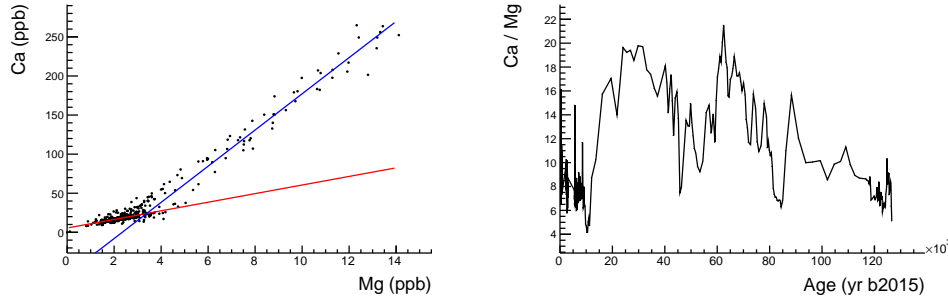


Figure 6.20: Ca/Mg scatter plot (left) and Ca/Mg ratio with respect to time (right).

sometimes adopted in ice core glaciochemistry literature (see for e.g. Severi et al. 2017). By assuming $R_c = \frac{Ca}{Na} = 1.78$ and $R_{sw} = 0.038$ the calcium to sodium mass ratios in the UCC and in sea water respectively, one can solve:

$$ssNa = Na - \frac{nsCa}{R_c} = \frac{R_c Na - Ca}{R_c - R_{sw}} \quad (6.6)$$

$$nsCa = \frac{R_c Ca - R_c R_{sw} Na}{R_c - R_{sw}} \quad (6.7)$$

The calculated $ssNa$ values (not shown) indicate that the marine contribution to the overall Na signal is 50-100% in the Holocene and negative in the glacial part. This surprising result leads to the following investigation. A scatter plot of calcium and magnesium reveals that Ca/Mg ratios oscillate between 5 - 23.5 (Fig. 6.20), while in the UCC, their mass ratio (Rudnick and Gao 2003) is between $\sim 2-3$. It appears therefore that R_c is not representative of the calcium dust arriving at Renland for the whole time period. Excess of carbonate dust in the glacial period is likely the reason of high Ca concentrations in this part of the record, possibly originated from gypsum minerals ($CaSO_4 \cdot 2 H_2O$, Legrand and Mayewski 1997). Further investigations are needed to establish to which extent the calcium correction can be used to extract the pure marine contribution to the sodium signal.

From crude Cl/Na and Na/Mg calculations we have shown that the maximum (at 66 kyr) crustal contribution to the sodium signal would be $\approx 29-40\%$. The sea salt sodium ($ssNa$) was calculated using the Cl/Na ratios (Mg is interfered by sea water contribution). Only in the samples in which $Cl/Na < 1.8$ (sea water mass ratio), the crustal component of sodium was calculated as:

$$ssNa = \frac{Cl}{[Cl/Na]_{sw}} \quad (6.8)$$

$$nsNa = Na - ssNa \quad (6.9)$$

where $[Cl/Na]_{sw}=1.78$. It was found that at the LGM, $\frac{nssNa}{Na} = 15\%$; at 66 kyr $\frac{nssNa}{Na} = 29\%$ (the maximum crustal input of the whole record). The sea salt sodium, $ssNa$, was used to calculate the Br_{enr} (Sect. 6.6.6).

6.6.6 THE 126 KYR RECORD OF SODIUM AND BROMINE

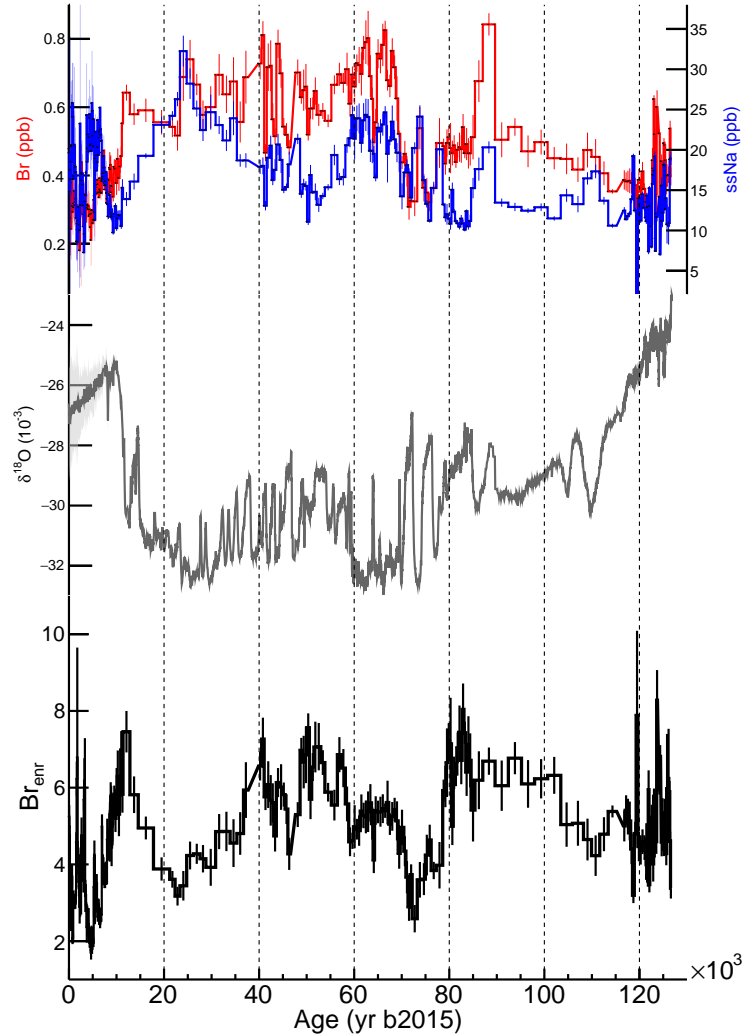


Figure 6.21: Renland bromine and sodium records of the last ~ 125 kyr. From top to bottom: sodium (blue) and bromine (red) concentrations, $\delta^{18}O$ and $Br_{enr} = \frac{Br}{0.0062 \cdot Na}$ (black).

In the Holocene (present - 11 kyr), sodium and bromine concentrations are on average

17.6 ppb ($\sigma=9.6$ ppb) and 0.34 ppb ($\sigma=0.12$ ppb) respectively. In the glacial (11 kyr-120 kyr), the average sodium concentrations slightly increase to 18.2 ppb ($\sigma=6.2$ ppb); bromine concentrations increase to 0.56 ppb ($\sigma=0.14$ ppb). In the Eemian part of the record (120 - 126 kyr), bromine values are similar (0.39 ppb, $\sigma=0.10$ ppb) to the Holocene, while sodium concentrations (13.2 ppb, $\sigma=3.4$ ppb) are slightly lower. The concentration trend of both tracers is roughly anticorrelated with $\delta^{18}\text{O}$, as it is observed for most elements (the concentration is inversely proportional to the accumulation). Bromine and sodium concentration trends at Renland are in general agreement with what was found in the NEEM core (Fig. 6.12). It is worth mentioning again that this finding is opposite to Talos Dome (Fig. 6.9), where bromine fluxes were found to be positively correlated to $\delta^{18}\text{O}$.

The bromine enrichment curve (Fig. 6.21, bottom) displays values greater than the sea water ratio throughout the record. Periods of minimum Br_{enr} values ($\lesssim 3$) are found in the Holocene, at ~ 22 kyr, ~ 72 kyr and during the late Eemian. The Br_{enr} trend is positively correlated to $\delta^{18}\text{O}$ during the glacial period ($\rho \simeq 0.6-0.7$). No correlation is found during the interglacial periods, when low Br_{enr} values are found. This finding seems opposite to what was found in the NEEM core (Fig. 6.13) where maximum Br_{enr} values were found in the Holocene. At NEEM, Br_{enr} was interpreted throughout the record as a proxy for seasonal sea ice (FYSI), and assuming that low values were indicating larger MYSI extents in the Canadian Arctic and Baffin Bay (Fig. 6.14).

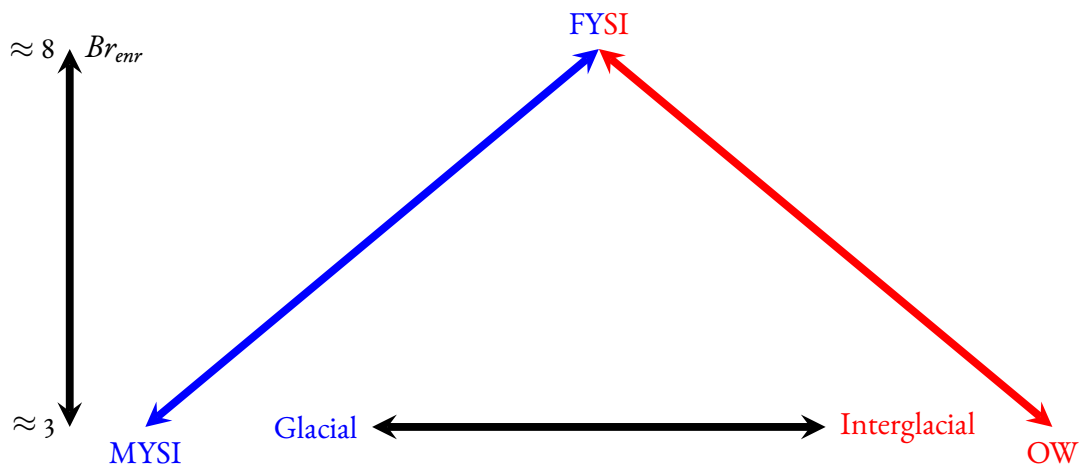


Figure 6.22: Br_{enr} interpretation at Renland. Br_{enr} as proxy for FYSI with respect to MYSI (blue, glacial conditions) and for FYSI with respect to open water, OW (red, interglacial conditions).

The behavior of Br_{enr} at Renland can be explained by the location of the core with respect to the seasonal sea ice signature of this proxy (Fig. 6.22). In modern times, the potential aerosol sources at Renland (Fig. 5.10) are dominated by open water conditions.

Consistently, low Br_{enr} values are observed during the Holocene. It is to be expected that a similar scenario occurred during the Eemian, when low Br_{enr} values are also found. The behavior of the proxy during interglacial conditions suggests therefore a variability between OW and FYSI (represented as a red arrow in Fig. 6.22). Conversely, during the glacial period, the proxy is indicating FYSI in a generally "iced" world. In this scenario, therefore, low values identify more extensive MYSI (represented as a blue arrow in Fig. 6.22). The "iced" world Br_{enr} behavior is the only one found at NEEM, since here the source basins are filled with FYSI in modern conditions and were filled with MYSI during the glacial. No low Br_{enr} values associated to open water signature are found at NEEM.

On the other hand, Br_{enr} at Renland displays a bimodal behavior between glacial and interglacial periods. A "tipping" point between the two modes is expected to occur when transitioning from a "warm" into a "iced" world. The possibility of a transition between the two modes during a warm glacial period is not ruled out. This is investigated in the following sections.

6.6.7 THE LGM, THE DEGLACIATION AND INTO THE HOLOCENE

The Br_{enr} values at the LGM (~ 22 - 24 kyr ago) are some of the lowest (≈ 2.5 - 3) of the entire RECAP record (Fig. 6.23). Such low values are to be interpreted as maximum extent of MYSI in the sampling area of the core (Fig. 6.22, blue arrow). This condition is consistent with marine sediment cores from the Svalbard margin (Fig. 6.23), green) and the Norwegian sea (Fig. 6.23) and Fig. 6.21, brown), where $PIP_{25} \approx 1$ values during MIS2 (30 to 17 kyr ago), and therefore maximum MYSI cover, were reported during this period (Müller and Stein 2014 and Hoff et al. 2016).

Two effects could play a role during the deglaciation: a net sea ice area loss (MYSI + FYSI) in favor of open water, and the replacement of MYSI by FYSI. The present shift from primarily MYSI to mainly seasonal ice has been widely reported in the Arctic (e.g. in Rigor and Wallace 2004). Such shift into a seasonal dominated Arctic sea ice is expected to be more enhanced during the deglaciation. Overall, sea ice loss and transformation of MYSI in FYSI would increase Br_{enr} values. The observed consistent increase of Br_{enr} throughout the deglaciation until ~ 12 kyr therefore suggests that the maximum FYSI was reached at this latter point in time. The increasing trend is not observed to change significantly during the Bølling-Allerød (BA) nor at the onset of the Younger Dryas (YD). Hoff et al. 2016 and Müller and Stein 2014 find that PIP_{25} values have decreased to ≈ 0.4 - 0.5 during the BA and YD. Both marine and ice core results suggest that MYSI was transforming into FYSI from the LGM to the YD.

To better constrain the timing of the tipping point around 12 kyr, replicate measurements were performed on a parallel RECAP ice core piece, sampled at centennial resolution (≈ 3 cm vs ≈ 18 cm). The measurements were performed by ICP-SFMS at Venice (Italy).

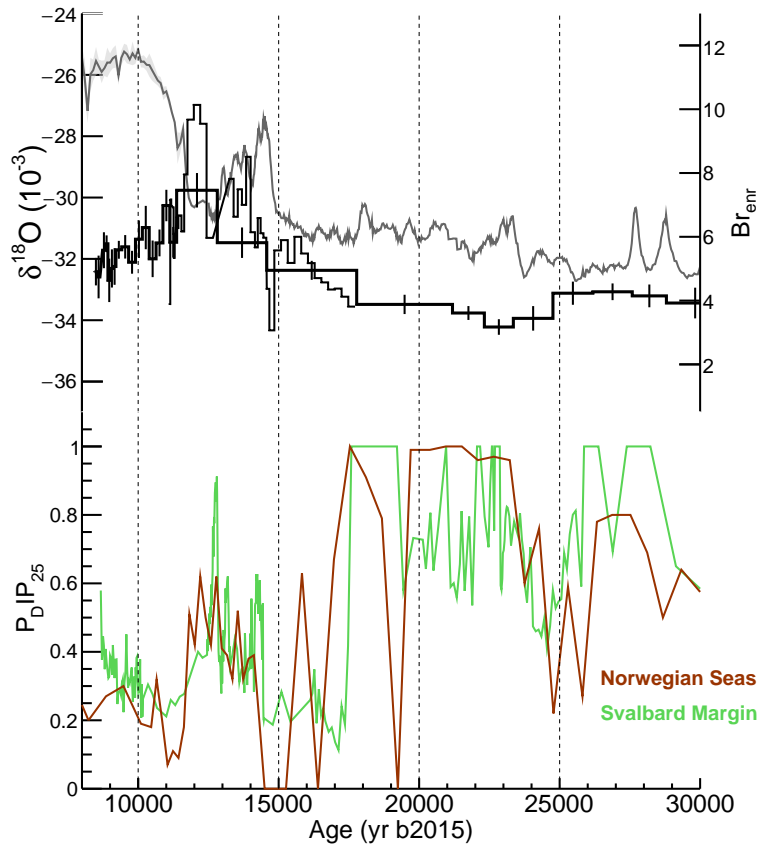


Figure 6.23: Centennial resolution measurements of Br_{enr} over the deglaciation and comparison with P_DIP_{25} from marine cores. Top: $\delta^{18}O$, Br_{enr} : the thin (thick) line corresponds to the high (low) resolution measurements. Bottom: P_DIP_{25} from the Norwegian Seas (brown, Hoff et al. 2016) and the Svalbard Margin (green, Müller and Stein 2014). Br_{enr} starts declining to Holocene levels from 12.2 ± 0.2 kyr.

The increase in Br_{enr} values abruptly stops and changes direction at 12.2 kyr ago, during the Younger Dryas (Fig. 6.23): a decrease in the values is observed at 12.2 kyr as sea ice is transitioning into the Holocene conditions (6.22, red arrow).

The transition into open water conditions in the Holocene (low PIP_{25}) is also observed in Hoff et al. 2016 and Müller and Stein 2014, with a timing of ~ 12.2 - 12.8 kyr and ~ 12.8 kyr respectively (Fig. 6.23). A PIP_{25} record from the North Icelandic Shelf (Fig. 6.1) also shows very similar results (Fig. 6.24), with maximum P_BIP_{25} found at ~ 12.1 kyr. After this point-in-time, at Renland and in all the marine cores, the sea ice proxy (Br_{enr} and PIP_{25}) values start to decrease.

The 14-18 kyr period shows a difference between the marine core records: while in the

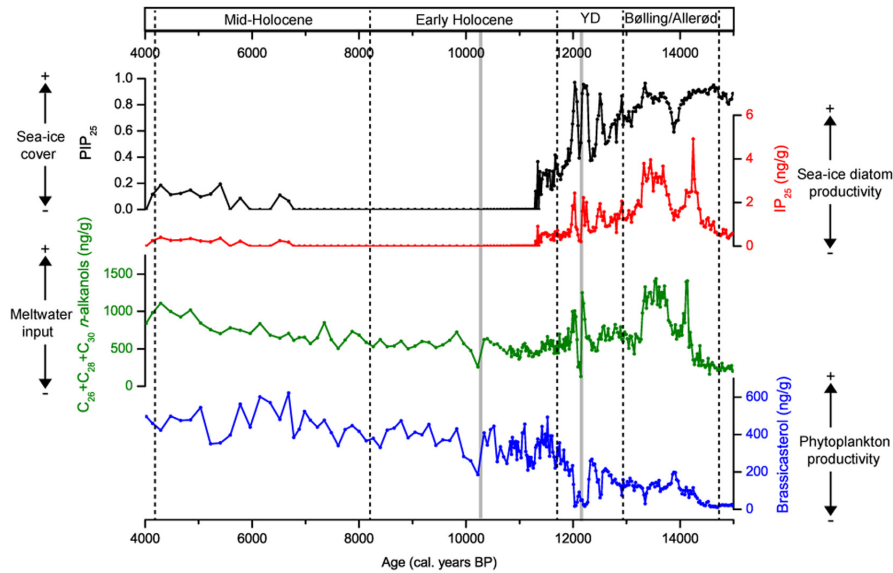


Figure 6.24: Biomarker concentrations and $P_{IP_{25}}$ index (top panel) from the Icelandic MD99-2272 core. Light gray bars indicate the Saksunarvatn ash (10.3 kyr) and Vedde Ash (12.1 kyr). From [Xiao et al. 2017](#).

Norwegian Sea and Svalbard Margin the PIP_{25} values indicate open water conditions (Fig. 6.23), the Icelandic core suggests that extensive sea ice cover was present from the YD to 15 kyr (Fig. 6.24, top panel). [Xiao et al. 2017](#) points out that inflow of warm Atlantic water may be responsible for sea ice melt in the Norwegian Sea and in the Svalbard Margin during the Bølling-Allerød (Fig. 6 in [Xiao et al. 2017](#)) but does not seem to affect the sea ice north of Iceland. Consistent with [Xiao et al. 2017](#), the steady increase of Br_{enr} values in the Renland core from the LGM to the YD suggests that FYSI was continuously replacing MYSI and any early spatially localized open water signature did not contribute much to the integrated sea ice area sampled by the ice core. Since the Icelandic record dates back only 15 kyr, this conclusion cannot be extrapolated further back to 18 kyr.

Br_{enr} values suggest that MYSI was at maximum extent during 30 - 17 kyr in the Renland source area. Similar conditions are found in the Norwegian Sea and in the Svalbard margin, where perennial sea ice cover is indicated by $PIP_{25} \approx 1$. Increasing Br_{enr} suggests a shift from MYSI to FYSI during the deglaciation (blue arrow in Fig. 6.22), which stopped at ~ 12.2 during the Younger Dryas. The tipping point is also observed within a few hundred year difference in all three marine cores, suggesting again that Arctic sea ice conditions from north of Iceland to the Fram Strait were similar. These combined findings indicate that the large-scale collapse of sea ice in the Greenland Sea occurred between 12.2 and 12.8 kyr, during the YD. Since 12.2 kyr, the trend towards generally low Br_{enr} (2-4) and low PIP_{25} values indicates persistent open water conditions throughout the Holocene (Fig. 6.27).

6.6.8 \overline{Br}_{ENR}^* : A SEA ICE INDICATOR FROM Br_{ENR}

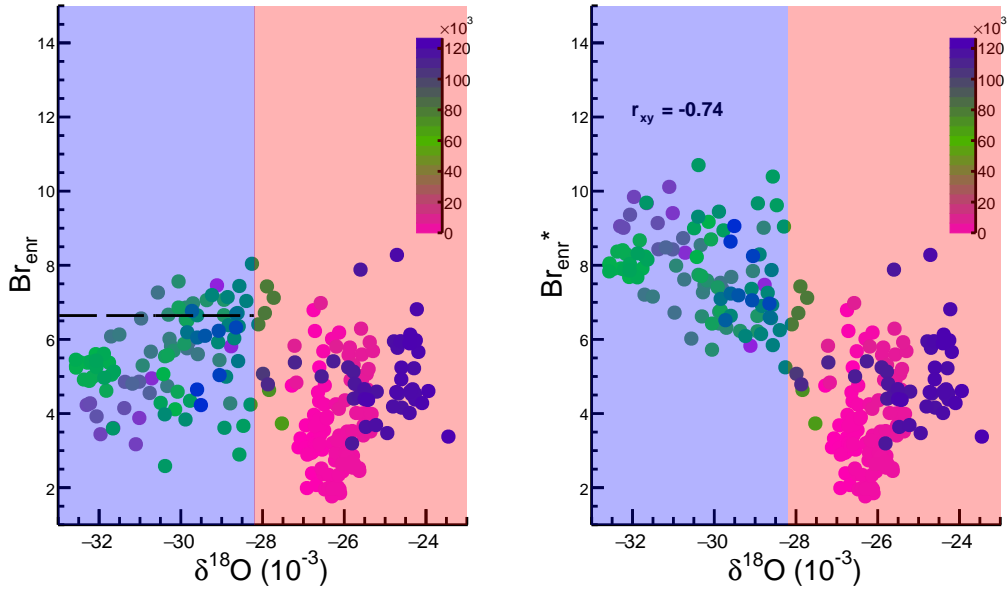


Figure 6.25: Scatter plot of Br_{enr} and $\delta^{18}\text{O}$ and linearization of the sea ice proxy. The Br_{enr} values of the points lying in the blue region ("iced world") were modified by Eq. 6.10. No transformation (Eq. 6.11) is applied to the points in the red region ("open water"). The \overline{Br}_{enr} is indicated (6.6). The colors of the points (top right color bar) reflect the age of the samples.

If we assume the same linear dependence of Br_{enr} with $\delta^{18}\text{O}$ in both the two modes represented in Fig. 6.22, it is possible to linearize the Br_{enr} response with respect to the two types of sea ice. The following possibility was investigated by choosing the $\delta^{18}\text{O}$ value at the observed transition (12.2 kyr) as the threshold above which Br_{enr} switches to the "open ocean" response (Fig. 6.22, red arrow). The "linearizing" approach consists of the following steps:

- The $\delta^{18}\text{O}$ threshold at the 12.2 kyr transition is chosen as the variable leading the transition between the two possible Br_{enr} modes. It is defined as $\overline{\delta^{18}\text{O}}$. The Br_{enr} value at that 12.2 kyr transition is considered the maximum value below which MYSI and OW start to dominate respectively in the "iced" and "open ocean" world, based on the $\delta^{18}\text{O}$ value. It is defined as \overline{Br}_{enr} .
- All the ice samples were checked for their $\delta^{18}\text{O}$ value, and the following transforma-

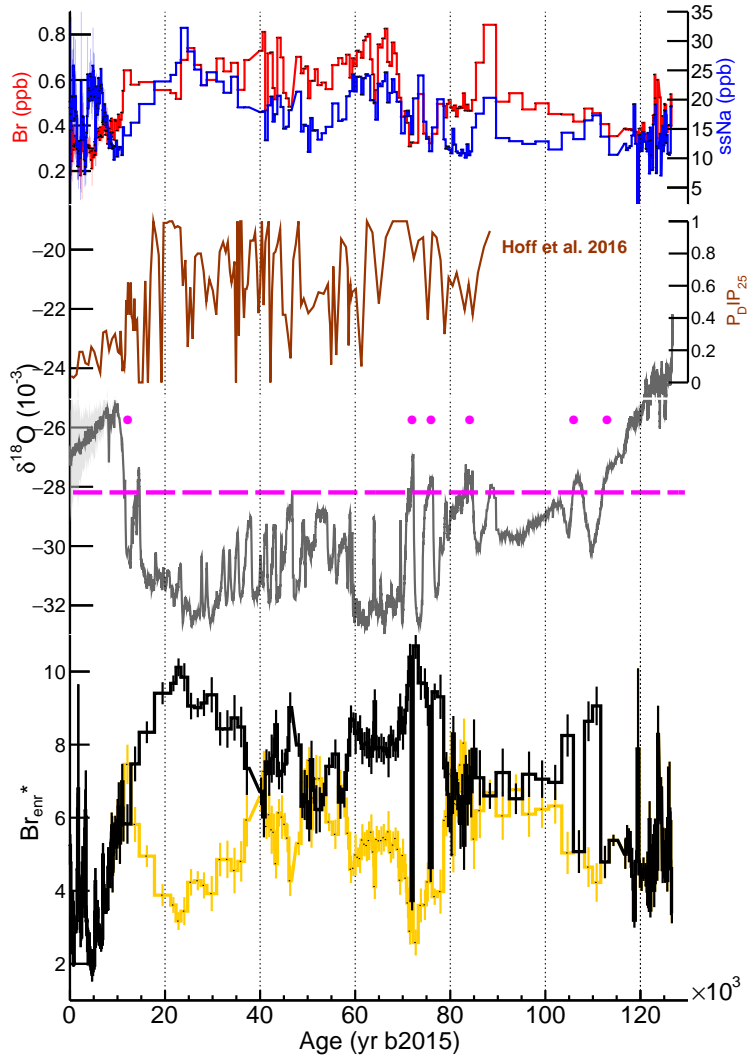


Figure 6.26: Sodium (blue) and bromine (red) concentrations. $P_{DIP_{25}}$ index (brown) from the Norwegian Sea (Hoff et al. 2016). $\delta^{18}\text{O}$ profile (grey) and $\delta^{18}\text{O}$ threshold (magenta line: -28.2‰). Bottom panel: Br_{enr}^* (black) and Br_{enr} (orange).

tion is applied:

$$\delta^{18}\text{O} < \overline{\delta^{18}\text{O}}(\text{"iced" scenario}), \text{Br}_{\text{enr}} \rightarrow \overline{\text{Br}_{\text{enr}}} + (\overline{\text{Br}_{\text{enr}}} - \text{Br}_{\text{enr}}) \quad (6.10)$$

$$\delta^{18}\text{O} > \overline{\delta^{18}\text{O}}(\text{"water" scenario}), \text{Br}_{\text{enr}} \rightarrow \text{Br}_{\text{enr}} \quad (6.11)$$

The decrease in Br_{enr} value due to increasing MYSI in cold periods is accounted for by adding an extra contribution (Eq. 6.10).

It was found that $\overline{\delta^{18}\text{O}} = -28.2\text{‰}$ and $\overline{Br_{\text{enr}}} = 6.6$. The $\overline{\delta^{18}\text{O}}$ threshold intercepts the $\delta^{18}\text{O}$ curve in 6 points in time (Fig. 6.26): at 12.2 kyr (by construction), at DO events 19 (72 kyr), DO 20 (76 kyr), DO 21 (83-84 kyr), DO 24 (107 kyr) and from DO 25 into the Eemian (> 112 kyr).

The modified Br_{enr} scale (indicated as Br_{enr}^*) does not have any physical meaning, although it can now be interpreted as a linear indicator of total sea ice (analogous to the PIP_{25} index). The new linear sea ice proxy Br_{enr}^* is now inversely correlated with $\delta^{18}\text{O}$ ($\rho = -0.74$, Fig. 6.25 and 6.26). A Br_{enr}^* maximum is found at 23 kyr. As previously mentioned, this finding is consistent with what is found in the Svalbard margin (Müller and Stein 2014) and the Norwegian sea (Hoff et al. 2016, Fig. 6.21) (maximum sea ice cover during MIS 2: 30 to 17 kyr ago). Extended sea ice cover is found between 60 and 80 kyr (except during DO 19 and 20, which the Br_{enr} transformation predicts Br_{enr}^* values $\approx 3.5-4.5$ for), with maximum at 73 kyr. Similar Br_{enr}^* values ($\approx 10.6-10.7$), suggest that similar sea ice extents were present at 22 kyr and at 73 kyr. Sea ice declines at ~ 59 kyr (synchronous within 1 kyr from the end of GS-18) and progressively increases from this point in time to 22 kyr. Low Br_{enr}^* values (≈ 6) at ~ 52 kyr are consistent with intermediate PIP_{25} values in this period. Ice older than 80 kyr towards GI-25 and the Eemian interglacial displays a general decrease in Br_{enr}^* .

Despite the similarity between Br_{enr}^* and PIP_{25} records, a few points have been recognized in this linearization exercise that will need to be addressed:

- What is the physical cause associated to $\overline{\delta^{18}\text{O}}$? It is here naively assumed that temperature should be the main forcing driving the oscillation between the "iced" and "water" scenarios. Similarly, $\overline{Br_{\text{enr}}}$ is here treated empirically.
- An uncertainty on $\overline{\delta^{18}\text{O}}$ would have a great impact on Br_{enr}^* values in periods having a high isotopic values, i.e. warm DO events: DO 19, 20, 21, 24 and 25.
- $\overline{Br_{\text{enr}}}$ depends on the sampling resolution at 12.2 kyr (Fig. 6.23), but the transformation is applied to the whole record. Particularly, in the glacial section, the ice compression leads to an uneven time resolution (Fig. 6.15), which ranges from some hundreds of years to a few millennia.

6.6.9 THE HOLOCENE

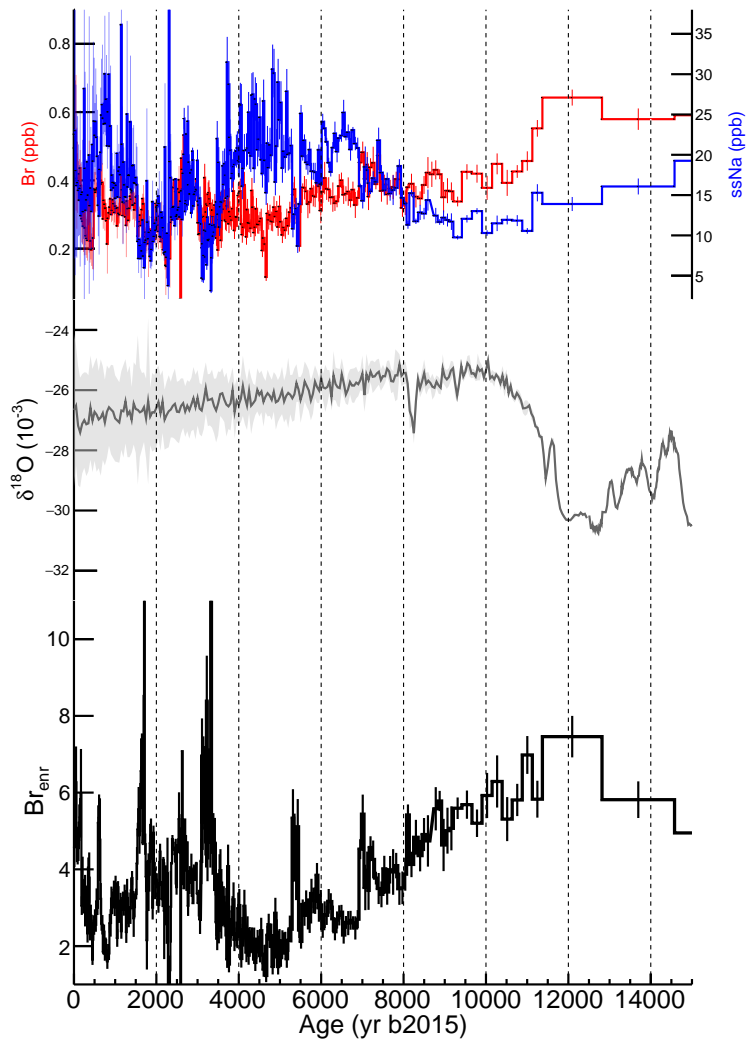


Figure 6.27: Sodium (blue) and bromine (red) concentrations, $\delta^{18}\text{O}$ (grey) and Br_{enr} (black). Na, Br and Br_{enr} are 20 yr averages (thick lines) up to ~ 2.8 kyr. The original sampling resolution was kept for older ice. $\delta^{18}\text{O}$ values are 100 yr averages. The shaded areas correspond to 1 standard deviation within the averaging window.

The Holocene covers 530 m of the entire 584 m long RECAP core. The 55 cm sampling resolution corresponds to centennial resolution in the early Holocene and increases to annual resolution at the surface. Such resolution allows a more detailed insight into any cli-

matic signature left in the core. It is worth keeping in mind that as resolution increases, more effects would be visible and hence the variability is also expected to increase; such noise being automatically smoothed out by the ice compression in the deeper layers. While allowing a deeper investigation, the interpretation becomes more challenging, for a wide combination of effects becomes visible. At the moment of writing, the time series presented in this Holocene section have been dated using the V₄ timescale, which shows, at 370 m, a difference of ~ 450 years with the annual layer counted timescale. Clearly, the V₄ chronology needs to be refined before robust conclusions are drawn.

Since in the Holocene $\delta^{18}\text{O} > \overline{\delta^{18}\text{O}}$, the Br_{enr} variable is to be interpreted as a sea ice indicator without any transformation (Eq. 6.11). The Holocene part of the record (Fig. 6.27) shows steadily decreasing Br_{enr} values from 12 kyr up ~ 4.8 -5 kyr. As mentioned in Sec. 6.6.7, since the YD, the Renland core source area is characterized by a steady increase of open water. Point-in-time high values of Br_{enr} are observed at 7 and 5.4 kyr and reflect fast sea ice pulses. Almost zero PIP_{25} values are found in the marine core north of Iceland at the onset of the Holocene (11.7-11.3 kyr) indicating that open water was already dominating at this latitude (Xiao et al. 2017) and remained ice free until the mid-Holocene (~ 6.8 kyr). Minimum PIP_{25} values are found between 8200 and 7800 yr ago in the Fram Strait (Müller et al. 2012, Fig. 8).

Since the Holocene Br_{enr} absolute minimum at 4.8-5 kyr, generally increasing Br_{enr} values are observed up to the present time. Some relative minima (6.5 kyr, 800 yr ago) and maxima (3.3 and 1.7 kyr) are found superimposed on the lower frequency trend, reflecting minima and maxima in sea ice extents respectively. Generally, a greater variability in the Br_{enr} record is observed in this part of the record. A similar picture is found on the North Icelandic shelf, with increasing PIP_{25} after 6.8 kyr (Fig. 6.24) (Xiao et al. 2017), and in the Fram Strait and the Eastern Greenland shelf, showing $\text{PIP}_{25} \approx 0.4$ -0.8 during the last 7 kyr (Fig. 8 in Müller et al. 2012).

Overall, both the Renland and the marine core results suggest that during the Holocene, open water conditions dominated from Iceland to the Fram Strait until ≈ 5 -8 kyr, followed by a sea ice increase towards present times.

7

Conclusions and outlook

Measurements of iodine in surface snow have been carried out in coastal East Antarctica during a traverse from Talos Dome to GV7 (Maffezzoli et al. 2017). Average annual concentrations of 0.04 ppb are similar to background values observed in the Antarctic coastal locations of Law Dome and Neumayer. Unlike those locations, low iodine annual variability ($\approx 10\text{--}15\%$) and no seasonality of the signal are observed in the traverse samples, indicating, consistent with satellite measurements of IO, a lower biological production in this area compared to the other locations. Iodine loss from the snowpack has been reported in other Antarctic sites, from the observation of higher concentrations in winter layers, and greater atmospheric IO mixing ratios during spring/summertime, when maximum biological production is expected. The extent to which annual iodine loss can affect longer records is yet to be quantified. Similar bromine-iodine timeseries are observed in the 1930–1990 Law Dome record (Vallelonga et al. 2017), suggesting a common driver of halogen variability. Iodine concentrations from the Renland core have tripled from 1950 to the present. Chemistry model simulations suggest that such a trend reflects the anthropogenic ozone increase until the 1990, after which enhanced sub-ice biological production caused by the recent Arctic sea ice thinning explains the trend (Cuevas et al., submitted). Atmospheric dust loading has been reported to affect the deposited iodine fluxes during glacial periods at Talos Dome (Spolaor et al. 2013c). Additional investigations are thus needed to interpret iodine records at glacial–interglacial timescales. The 125 kyr iodine record from Renland, the first millennial iodine record from the northern hemisphere, will provide clearer indications.

Sodium is generally considered a qualitative sea ice indicator; marine aerosols and dependence on meteorology have been shown to be the dominant limitations to a purely sea ice signature. An increasing body of evidence is pointing to bromine enrichment beyond

sea water level, $Br_{\text{enr}} = Br / (0.0062 \cdot Na)$, as an indicator of seasonal sea ice. The seasonality of bromine was investigated in the traverse samples (Maffezzoli et al. 2017) and confirm the previous findings from ice cores, atmospheric measurements and chemistry models. In both the polar regions, fresh sea ice surfaces are the primary sources of bromine, the release mechanisms being bromine explosion cycles, which enhance its concentrations in the snow beyond sea water values, pointing to Br_{enr} as a promising sea ice indicator. Uncertainties related to the different transport fractionations of bromine and sodium still remain the major unknown and can challenge its deploy. Combined surface snow measurements and model efforts are needed to quantify its effect on the observed Br_{enr} values. Bromine photolysis and loss from the snowpack, first suggested, has not been further observed. Yet, this feature should still be addressed.

The Br_{enr} record in the NEEM ice core provides a history of sea ice in the Canadian Archipelago, Hudson Bay and Baffin Bay, covering the last 120 kyr. The record shows that the maximum extension of first year sea ice (FYSI) and corresponding minimum multi-year sea ice (MYSI) occurred 9000 years ago during the Holocene climate optimum, while lowest FYSI conditions were present during glacial stadials. A correspondence between Br_{enr} and $\delta^{18}\text{O}$ during Dansgaard–Oeschger events, Bølling–Allerød and Younger Dryas indicates a sea ice response to temperature oscillations also at such timescales.

The 125 kyr Br_{enr} record in the Renland ice core reflects a different combination of FYSI, MYSI and open water (OW) in different climate phases. Consistent with reduced bromine recycling over FYSI in either OW or MYSI conditions, the low Br_{enr} values observed during interglacials and glacial stadials reflect respectively predominant OW and MYSI within the aerosol source area, identified with the Greenland Sea by back trajectory analyses. Thus, Br_{enr} displays at Renland a bimodal behaviour, low values pointing respectively to either MYSI and OW conditions during "cold" and "warm" periods, a tipping point marking the transition between the two modes.

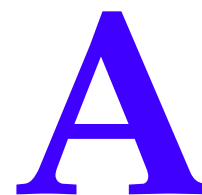
Maximum extent of MYSI occurred at ~ 22 kyr and ~ 72 kyr, consistent within a few kyr with a marine record from the Norwegian Sea (Hoff et al. 2016). Similar variability between Br_{enr} and $\delta^{18}\text{O}$ timeseries during the glacial part of the record indicate that warmer conditions were characterized by increased FYSI.

The increasing Br_{enr} trend from the LGM towards the onset of the Holocene indicates that FYSI was replacing MYSI during the deglaciation. This is consistent with sea ice proxies from marine sediment cores recovered from the Fram Strait and the Norwegian Sea. Such trend abruptly stops and changes direction during the Younger Dryas at 12.2 ± 0.2 kyr, suggesting that a tipping point occurs at this point-in-time. Within 12.1 - 12.8 kyr, such a shift from marginal sea ice to open water conditions is observed from sediment cores retrieved North of Iceland (Xiao et al. 2017) in the Norwegian Sea (Hoff et al. 2016) and in the Fram Strait (Müller and Stein 2014). All records show dominant open water conditions

during the Holocene, with some indications of a slight sea ice recovery since ≈ 6.8 -5 kyr.

A linearization approach is presented, to linearly relate Br_{enr} to $\delta^{18}\text{O}$ over the 125 kyr. A constant $\delta^{18}\text{O}$ threshold is suggested to be, on first approximation, the variable responsible for the tipping point mechanism. Some uncertainties behind this method are acknowledged and should be further addressed.

Altogether, the following points can be summarized from this research. Sodium remains a qualitative sea ice indicator at annual and decadal timescales, while being more promising at glacial–interglacial timescales, despite some evidence of a decreased sensitivity reported in Antarctica. Some unknowns regarding the relative transfer of bromine and sodium persist, although their ratio Br_{enr} appears to explain sea ice variability. Yet, quantitative sea ice reconstructions are still limited. Additional surface snow measurements along with chemistry model studies are needed to achieve a more complete understanding. Overall, the interpretation of iodine records is still complex and their sea ice signature still exploratory. The uncertainties are related to either the different emission sources at the two poles, the influence of other species and the postdepositional effects that have been shown to affect iodine absolute concentrations in surface snow.



Bromine, iodine and sodium in surface snow along the 2013 Talos dome–Gv7 traverse (northern Victoria Land, East Antarctica)

The chapter reports [Maffezzoli et al. 2017](#) in its original form.

Halogen chemistry in the polar regions occurs through the release of halogen elements from different sources. Bromine is primarily emitted from sea salt aerosols and other saline condensed phases associated with sea ice surfaces, while iodine is affected by the release of organic compounds from algae colonies living within the sea ice environment. Measurements of halogen species in polar snow samples are limited to a few sites although there is some evidence that they are related to sea ice extent. We examine here total bromine, iodine and sodium concentrations in a series of 2 m cores collected during a traverse from Talos Dome (72° 48' S, 159° 06' E) to GV7 (70° 41' S, 158° 51' E) analyzed by inductively coupled plasma-sector field mass spectrometry (ICP-SFMS) at a resolution of 5 cm.

We find a distinct seasonality of the bromine enrichment signal in most of the cores, with maxima during the austral spring. Iodine shows average concentrations of 0.04 ppb with little variability. No distinct seasonality is found for iodine and sodium. The transect reveals homogeneous air-to-snow fluxes for the three chemical species along the transect due to competing effects of air masses originating from the Ross Sea and the Southern Ocean.

A.1 INTRODUCTION

Halogen elements play an important role in polar boundary layer chemistry. The release of reactive halogen species from sea ice substrates has been demonstrated to be crucial in the destruction of tropospheric ozone at polar latitudes (so-called Ozone Depletion Events) during springtime ([Barrie et al. 1988](#); [Simpson et al. 2007b](#); [Abbatt et al. 2012](#)).

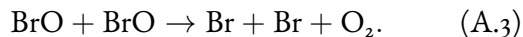
Although the ocean is the main reservoir of sea salts, various condensed phases of high salinity are found on young sea ice surfaces. During seawater freezing, brine is separated from the frozen water matrix and expulsion processes lead to both upward and

downward movement as temperature decreases ([Abbatt et al. 2012](#)).

Therefore, high salinity brine, frost flowers and salty blowing snow make newly formed sea ice surfaces a highly efficient substrate for inorganic halides and for their activation and release in the atmosphere ([Saiz-Lopez and von Glasow 2012](#); [Yang et al. 2008](#)). Some studies have also pointed out the role of open water sea salts as a significant bromine source ([Yang et al. 2005](#); [Sander et al. 2003](#)).

Reactive halogen species are involved in cyclic reactions between halogen radicals, their oxides and ozone. Reactions (A1)–(A3) show the main cycles for bromine.

Atomic bromine radicals result from photolysis of molecular bromine, leading to formation of bromine monoxide, BrO, through the reaction with ozone:



Self-reaction of BrO may form two bromine atoms (85 %) or a Br₂ molecule (15 %) which is readily photolyzed. The mechanism has a catalytic behavior that destroys ozone.

High concentrations of vertical columns of BrO and IO have been confirmed by SCIAMACHY (SCanning Imaging Absorption spectroMeter for Atmospheric CHartographY) satellite observations over Antarctic sea ice (Schönhardt et al. 2012).

Bromine can then be recycled and re-emitted from halogen-rich condensed phases (such as sea salt aerosol or other saline solutions) or from sea ice surfaces (Pratt et al. 2013), leading to an exponential increase of bromine in the gas phase (Vogt et al. 1996). Such reactions, known as bromine explosions, lead to enhanced bromine in the atmosphere. A recent 1-D chemistry model simulation predicted an increase of bromine deposition on surface snowpack after 24 to 48 h of recycling over first-year sea ice (Spolaor et al. 2013c).

The stability of bromine in the snowpack was investigated at Summit station, Greenland (Thomas et al. 2011), to explain the observed mixing ratios of BrO. Measurements in East Antarctica (Legrand et al. 2016b) revealed that snowpack cannot account for the observed gas-phase inorganic bromine in the atmosphere.

Bromine enrichment in snow (compared to sodium, relative to seawater) has therefore been recently used to reconstruct sea ice variability from ice cores both in the Antarctic and Arctic regions (Spolaor et al. 2013a, Spolaor et al. 2016b).

Iodine is emitted by ocean biological colonies and sea ice algae (Saiz-Lopez et al. 2011; Atkinson et al. 2012) mainly in the form of organic alkyl iodide (R-I) and possibly other compounds. These can be released by wind-forced sea spray generation or percolation up to the sea ice surface through brine channels and are subsequently photolyzed to inorganic species.

Plumes of enhanced IO concentrations from satellites and ground-based measurements were observed over Antarctic coasts, suggesting a link with biological and chemical sea ice related processes (Schönhardt et al. 2008). Grilli et al. 2013 have shown that ground-based IO concentrations in Dumont d'Urville (Indian sector) were more than one order of magnitude lower than in the Atlantic sector (Halley station, Saiz-Lopez et al. 2007b), consistent with greater sea ice in the latter. On the other hand, only sporadic events with IO concentrations above detection limits have been observed in the Arctic regions, possibly due to the greater thickness and lower porosity of Arctic sea ice which prevents an efficient release of iodine species in the atmosphere (Mahajan et al. 2010).

Measurements of sea ice related species such as bromine and iodine could therefore allow a sea ice signature to be obtained from ice core records. Until recently, only sodium has been used to qualitatively reconstruct sea ice at glacial–interglacial timescales (e.g., Wolff et al. 2006), but this proxy has limitations at annual and decadal scales, because of the noise input caused by meteorology and open water sources (Abram et al. 2013). Methane sulfonic acid (MSA) is an end product of the oxidation of dimethylsulfide (DMS), which is produced by phytoplankton synthesis of DMSP (dimethylsulfonium propionate). MSA deposition has been successfully linked to Antarctic winter sea ice extent (Curran et al. 2003; Abram et al. 2010) and Arctic sea ice conditions (Maselli et al. 2017) on decadal to centennial scales, although some studies reported that the correlation with satellite sea ice observations is strongly site dependent (Abram et al. 2013). Several atmospheric studies reported no evidence of such link (Preunkert et al. 2007; Weller et al. 2011). Postdepositional processes causing loss and migration in the ice layers have also been widely reported to affect MSA, especially at low accumulation sites (Mulvaney et al. 1992; Pasteur and Mulvaney 2000; Delmas et al. 2003; Weller et al. 2004; Isaksson et al. 2005; Abram et al. 2008).

Victoria Land has been intensively studied for the past two decades. The Taylor Dome (Grootes et al. 2001) and Talos Dome (Stenni et al. 2011) deep ice cores respectively provide 150 and 300 kyr climatic records directly influenced by marine air masses. Sala et al. 2008 pointed out the presence of marine com-

pounds (ikaite) at Talos Dome, typically formed at the early stages of sea ice formation. Their back trajectory calculations also showed that favorable events for air mass advection from the sea ice surface to Talos Dome are rare but likely to occur. An extensive study by Scarchilli et al. 2011 on provenance of air masses has shown that Talos Dome receives 50 % of its total precipitation from the west (Indian Ocean), 30 % from the east (Ross Sea and Pacific Ocean) and approximately 15 % from the interior. Within the framework of the ITASE program (International Trans-Antarctic Scientific Expedition, Mayewski et al. 2005), several traverses were carried out to evaluate the spatial patterns of isotopic values and chemical species linked to marine influence (Magand et al. 2004; Proposito et al. 2002; Becagli et al. 2004b; Becagli et al. 2005; Benassai et al. 2005).

We present here bromine, iodine and sodium deposition in coastal East Antarctica by investigating their total concentrations within a series of shallow firn cores, covering the 2010–2013 time period. The cores were drilled during a traverse performed in late December 2013 in Victoria Land (East Antarctica) from Talos Dome (72° 48' S, 159° 06' E) to GV7 (70° 41' S, 158° 51' E). The variability of these species at sub-annual timescales will inform on timing and seasonality as well as spatial patterns of their deposition and possible depositional or postdepositional effects. Such information is necessary for the interpretation at longer timescales of these elements. These sub-annual resolution investigations are still limited to the Indian Ocean sector (Law Dome, Spolaor et al. 2014) of Antarctica. The only data available on iodine in the Atlantic sector (Neumayer station) have been reported from a snow pit study by Frieß et al. 2010. This study will test the regional variability of these tracers, providing measurements from the Ross Sea to the Indian Ocean sector that remains otherwise unstudied.

A.2 SAMPLING AND ANALYSES

A.2.1 TRAVERSE SAMPLING

The traverse was performed in the northern Victoria Land region of East Antarctica (Fig. A.1) from 20 November 2013 to 8 January 2014. The starting and ending locations were Talos Dome (72° 48' S, 159°

12' E) and location "6" (A.1), close to GV7 (70° 41' S, 158° 51' E), for a total distance of about 300 km. Talos Dome (275 km WNW from Mario Zucchelli station) is located approximately 250 km from the Ross Sea and 290 km from the Indian Ocean. GV7 is a peripheral site on the ice divide coming from Talos Dome, located just 95 km from the Indian Ocean.

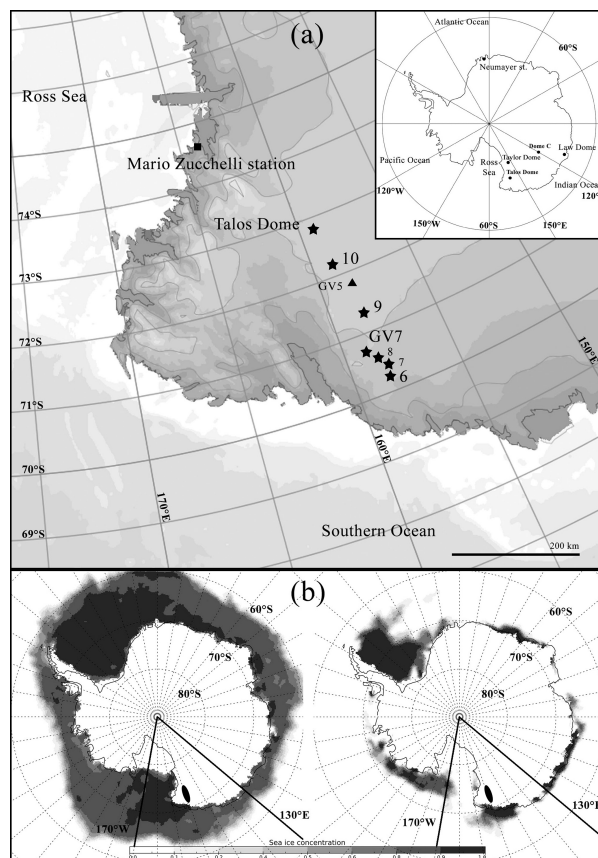


Figure A.1: (a) Schematic map of the traverse area and coring sites marked with stars. The cores were drilled between 20 November 2013 and 8 January 2014 (early austral summer). (b) Maximum (left, August 2011) and minimum (right, January 2010) sea ice concentrations in the 130° E–170° W sector for the 2010–2013 time interval covered by the core records (NSIDC data Meier et al. 2013). The traverse location is marked with an ellipse.

During the transect, seven shallow cores, labeled hereafter TD (Talos Dome), 10, 9, GV7, 8, 7 and 6 were hand drilled to 2 m depth (except for GV7 which was 2.5 m). The main characteristics of the coring sites are reported in Table 1. Density profiles were obtained from each core immediately after drilling.

The hand auger had a diameter of 10 cm and consisted of an aluminum barrel equipped with fiberglass extensions.

Table A.1: Core drilling site information.

Core site	Core depth (cm)	Lat. (S)	Long. (E)	Elevation (m a.s.l.)	Distance from Ross Sea (km)	Distance from Indian Ocean (km)	Distance to next core (km)
TD	200	72° 48'	159° 06'	2315	250	290	71
10	200	72° 12'	158° 41'	2200	310	240	94
9	200	71° 21'	158° 23'	2151	380	180	78
GV7	250	70° 41'	158° 51'	1957	430	95	13
8	200	70° 36'	158° 35'	1934	440	90	11
7	200	70° 31'	158° 25'	1894	460	90	18
6	200	70° 21'	158° 24'	1781	470	85	–

The cores were sampled in the cold laboratory at the Cà Foscari University of Venice under a class 100 laminar flow hood. Each core was cut with a commercial hand saw and decontaminated through mechanical chiseling by removing approximately 1 cm of the external layer. Every tool was cleaned each time a piece of sample was decontaminated into three serial baths of ultra-pure water (UPW), which was changed every 10 washes. The cores were then subsampled at 5 m resolution (3 cm for the GV7 core) into polyethylene vials previously cleaned with UPW and then kept frozen at -20 °C until analysis.

A.2.2 ANALYTICAL MEASUREMENTS

Total sodium (Na), bromine (Br) and iodine (I) concentrations were determined by inductively coupled plasma-sector field mass spectrometry (ICP-SFMS Element2, ThermoFischer, Bremen, Germany) at the Cà Foscari University of Venice following the methodology described in [Spolaor et al. 2014](#).

The samples were melted one hour before measurements. During this time, exposure from direct light was reduced by covering them with aluminum foils, minimizing bromine and iodine photolysis reactions.

The introduction system consisted of a cyclonic Peltier-cooled spray chamber (ESI, Omaha, USA). The operational flow rate was kept at 0.4 mL min⁻¹, for an overall sample volume of 5.0 mL. Each sample determination consisted of five instrumental detections (less than 2 % variation between them). The five values were then averaged to provide the final quantification. Each analytical run (10 samples) ended with a HNO₃

(5 %) and UPW cleaning session of 3 min to ensure a stable background level throughout the analysis.

The external standards that were used to calibrate the analytes were prepared by gravimetric method by diluting the separate stock 1000 ppm IC (Ion Chromatography) solution (TraceCERT® purity grade, Sigma-Aldrich, MO, USA) of the three analytes into a primary solution which was further diluted into six bromine and iodine standards (0.01, 0.05, 0.1, 0.5, 1 and 4 ppb) and 6 sodium standards (0.5, 1, 5, 10, 50 and 100 ppb).

The calibration regression lines showed correlation coefficients $R^2 > 0.99$ ($N = 6$, $p = 0.05$). The detection limits, calculated as three times the standard deviation of the blanks, were 50 and 5 ppt for bromine and iodine respectively and 0.8 ppb for sodium. The reproducibility of the measurements was carried out by repeated measurements of standard samples within the calibration range. The residual standard deviations (RSDs) were respectively 5 % (bromine), 3 % (sodium) and 2 % (iodine).

Procedural UPW blanks were analyzed periodically to test the cleanliness of the instrument lines.

Stable isotopes of water (¹⁸O and D) measurements were conducted on subsample aliquots, which were immediately refrozen and shipped to the Center for Ice and Climate (Copenhagen, Denmark). Analyses were carried out using a cavity ring-down spectrometer (Picarro, Santa Clara, USA) using the method described by [Gkinis et al. 2010](#). Septum-sealed glass vials were used for these measurements to prevent any sample evaporation during the experimental phases.

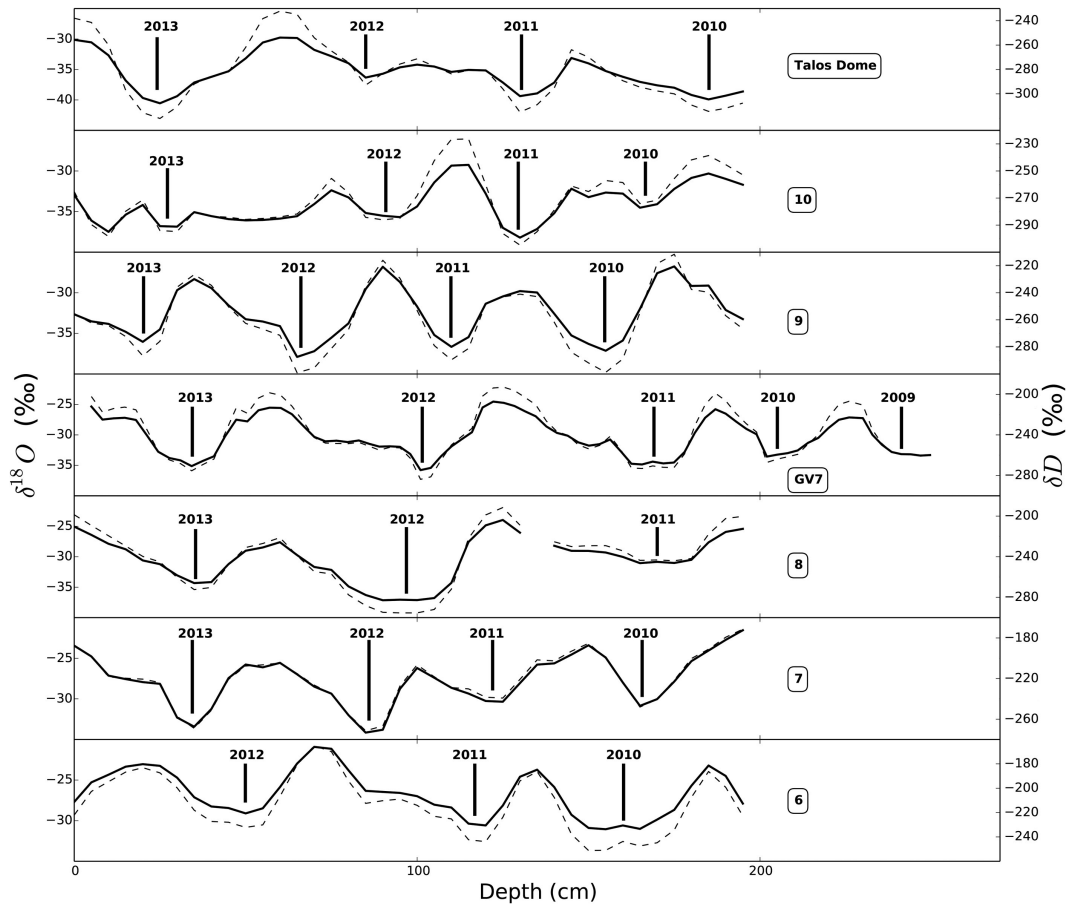


Figure A.2: $\delta^{18}\text{O}$ (thick line) and δD (dashed line) profiles of the cores. Resolution of sampling is 5 cm. The winter of each year is indicated with lines in correspondence with the water isotope minima. For core 10, the 2013 winter layer is uncertain.

Table A.2: Summary of accumulation rate data from northern Victoria Land. All uncertainties (shown in parentheses) are 1σ errors.

Core	Accumulation rates ($\text{kg m}^{-2} \text{yr}^{-1}$)							
	2013 traverse ^a					2001–2002 ^b	1965–2001 ^c	2001–2012 ^d
	2013	2012	2011	2010	Average			
TD	223	144	187	–	185 (31)	104 (37)	86.6 ^e	71 (4)
	–	66 ^d	107 ^d	78 ^d	81 (17) ^d			
10	260 ^f	140	140	120	133 (9)	GV ₅ 156 (27)	GV ₅ 129 (6)	
9	180	180	180	180	180 (0)			
GV7	228	261	260	156	232 (32)	261 (50)	241 (12)	
8	240	260	280	–	260 (16)			
7	220	180	200	180	195 (18)			
6	–	200	260	200	220 (29)			

^a This work. ^b Becagli et al. 2004b. ^c Frezzotti et al. 2007. ^d From stake farm ($n = 41$) (C. Scarchilli, personal communication, 2016). ^e 1966–1996, Stenni et al. 2002. ^f Uncertain due to smoothed isotopic signal.

A.3 RESULTS AND DISCUSSION

A.3.1 STABLE WATER ISOTOPES AND SNOW ACCUMULATION

The cores were dated based on the seasonal variations identified in the stable water isotopes (both $\delta^{18}\text{O}$ and δD). Midwinters were associated with the relative minima of the isotopic curves (Fig. A.2). In case a winter isotopic plateau was found, the center of the plateau was associated to midwinter depth (2011 in core GV7; 2012 and 2011 in core 8; 2010 in core 6). Almost all of the cores cover the period between 2010 and late 2013, providing four years of snow deposition. The only exception is represented by core 6, whose upper layer is missing.

The annual deposition signal looks less clear in the two cores that were drilled at the sites with the highest elevation and the closest to the Ross Sea, cores TD and 10, and especially for 2013 in core 10. The two sites are probably the most affected by surface remobilization and isotopic diffusion due to low accumulation. Indeed, nonuniformities in the shallow snow layers such as sastrugi, dunes, wind crusts and other features have been identified as an important aspect of the surface morphology around the Talos Dome area (Frezzotti et al. 2004; Frezzotti et al. 2007).

The annual accumulation rates were calculated by selecting the depth intervals included within consecutive maximum or minimum $\delta^{18}\text{O}$ values (Table A.2). Each snow layer within this interval (i.e., sampling resolution, 5 cm) was multiplied by the density of the snow at that depth, with the density curves having the same resolution. The contributions were summed over the annual thickness. Table 2 also includes accumulation rates in Victoria Land reported from previous studies. The GV5 site is located between sites 10 and 9 (Fig A.1).

The accumulation rates found during the traverse are in general agreement with the previous works (Becagli et al. 2004b; Frezzotti et al. 2007), except for Talos Dome. The accumulation values calculated from the isotopic profile in Talos Dome are well above those measured by the stake farm ($n = 41$, C. Scarchilli, personal communication, 2016) for the same years. The inconsistency between the accumulation rates derived from the core and those derived from the stake farm and previous measurements suggests that the isotopic

assignments of the years may be incorrect at this site and that the profile contains more years than have been assigned. This core is therefore not used in further calculations. The fluxes of deposition of sodium, bromine and iodine in the other cores along the transect are calculated using the accumulation rates from this work.

The accumulation pattern along the transect increases from Talos Dome to the Southern Ocean (GV7, 8, 7 and 6), as the previous works have also found (Magand et al. 2004; Frezzotti et al. 2007). Scarchilli et al. 2011 already pointed out how Talos Dome receives 50 % of its total precipitation from the north–west (Indian Ocean), 30 % from the east (Ross Sea and Pacific Ocean) and approximately 15 % from the interior of the plateau. In this picture, our accumulation data show a decrease from the Indian Ocean to Talos Dome.

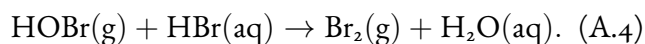
The sites are located at decreasing altitudes moving from the Talos Dome site (highest point) towards the coast facing the Indian sector (site 6). The minimum $\delta^{18}\text{O}$ value found in each core shows a decreasing trend with altitude, with an elevation gradient of $-1.35 \text{ ‰ } 100 \text{ m}^{-1}$. This super-adiabatic lapse rate is confirmed by the surface snow samples collected during the 2001/02 ITASE traverse (Magand et al., 2004).

A.3.2 SODIUM, BROMINE AND IODINE

Sodium shows a mean concentration of 34 ppb, in agreement with published values in this area (Becagli et al. 2004a; Becagli et al. 2004b; Bertler et al. 2005; Severi et al. 2009). Among the three elements, sodium shows the highest standard deviation (21 ppb) because of the high variability of sea spray inputs at coastal sites. Singularities of up to 200 ppb are probably associated with sea-salt-rich marine storms. Iodine has an average concentration of 43 ppt, associated with a lower variability (23 %) compared to bromine (42 %) and sodium (61 %).

The bromine enrichment has been calculated as the bromine excess with respect to seawater concentrations, $\text{Br}_{\text{enr}} = [\text{Br}] / (0.0062 \cdot [\text{Na}])$, where $[\text{Br}]$ and $[\text{Na}]$ are the bromine and sodium concentrations in the sample and 0.0062 is the bromine-to-sodium concentration ratio in seawater (Millero et al. 2008). Similarly, non-sea-salt bromine $[\text{nssBr}] = [\text{Br}] - 0.0062 \cdot [\text{Na}]$. Benassai et al. 2005 have concluded that sea-salt

sodium is the dominant fraction (more than 80 %) of the total sodium budget in this area. No correction to sodium was therefore applied for this calculation. Despite bromine being a sea salt marker like sodium, it is activated when gas-phase HOBr oxidizes bromide over halogen-rich sea ice surfaces (i.e., first-year sea ice, FYSI) and suspended sea salt aerosol and is exponentially released as Br₂ (Reaction A4):



Following photolysis, atomic bromine radicals can be converted back to HBr. Therefore, sea ice presence should lead to bromine enrichment or depletion, depending on whether deposition is dominated by the depleted sea salt aerosol or by the enriched gas-phase HBr. Bromine enrichment has already been linked to sea ice presence in both Arctic and Antarctic coastal sites (Simpson et al. 2005; Spolaor et al. 2013c; Spolaor et al. 2014; Spolaor et al. 2016b; Vallelonga et al. 2017).

The distributions of bromine enrichment values are reported in Fig. A.3, divided into the cores closest to the Ross Sea (TD, 10 and 9; blue distribution) and to the Indian Ocean (GV, 8, 7 and 6; red distribution). The first set of cores show on average higher values (5.7 ± 0.3) than the second (4.2 ± 0.2). The variability (root mean square, RMS) is also higher (3.5 ± 0.2) in the first set compared to the "Indian Ocean" set (2.5 ± 0.1) because of greater distance covered by the sampling (165 km compared to 40 km). Overall, the values extend from a minimum of 0.5–17 with more than 98 % of the samples showing values greater than 1 (i.e., seawater enriched values). A detailed insight into the few < 1 values revealed that these samples were associated with very high contributions of sodium inputs (> 120 ppb) and therefore likely associated with strong marine events. Such distribution of enrichment supports the theory that this parameter is, in these coastal sites, affected by sea ice signature.

The measurements of the chemical species for the different coring sites along the traverse are reported in Figs.A.4–A.6 on an age scale (with the exception of Talos Dome which is reported on a depth scale in the supplementary material). Sodium time series show great variability: peaks are often found in summer, although they are also observed in winter, e.g., in core 8.

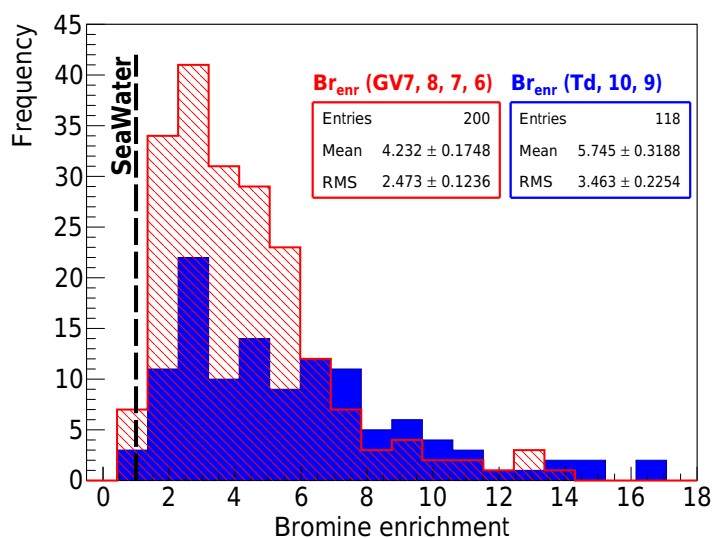


Figure A.3: Distribution of bromine enrichment values within cores TD, 10 and 9 (blue) and GV7, 8, 7 and 6 (red). The dashed line indicates the seawater value ($\text{Br}_{\text{enr}} = 1$).

These findings confirm that, as previous works pointed out (Curran et al. 1998), in coastal sites, storm events carrying open ocean sea salts are more important than sea ice as a sea salt source, although the high level of variability also suggests that meteorology and natural variability play a role (Wagenbach et al. 1998). Bromine and both Br_{enr} and nssBr show annual variations, with maximum values in late spring–summer, confirming ice core measurements by Spolaor et al. 2014, Vallelonga et al. 2017 and aerosol measurements by Legrand et al. 2016b. Iodine shows a more stable signal throughout the year, although a high winter singularity and a more extended peak are observed in the GV7 and 8 cores respectively.

The timing of the bromine enrichment signal in ice cores relies on the combined effect of sea ice and sunlight responsible for the photochemical production and release of molecular bromine, Br₂ (Pratt et al. 2013). Sea ice area in the 130° E–170° W sector was calculated for the 2010–2013 period using publicly available NSIDC passive microwave sea ice concentration data (Meier et al. 2013) by multiplying the sea concentration in each grid pixel by the area of the pixel (25 x 25 km²) and integrating over the domain. The longitude sector was decided on the basis of Scarchilli et al. 2011, who concluded that air masses arriving in this area originate from the Ross Sea and from the Indian Ocean sector by analyzing 5-day back trajectories from 1980 to 2001.

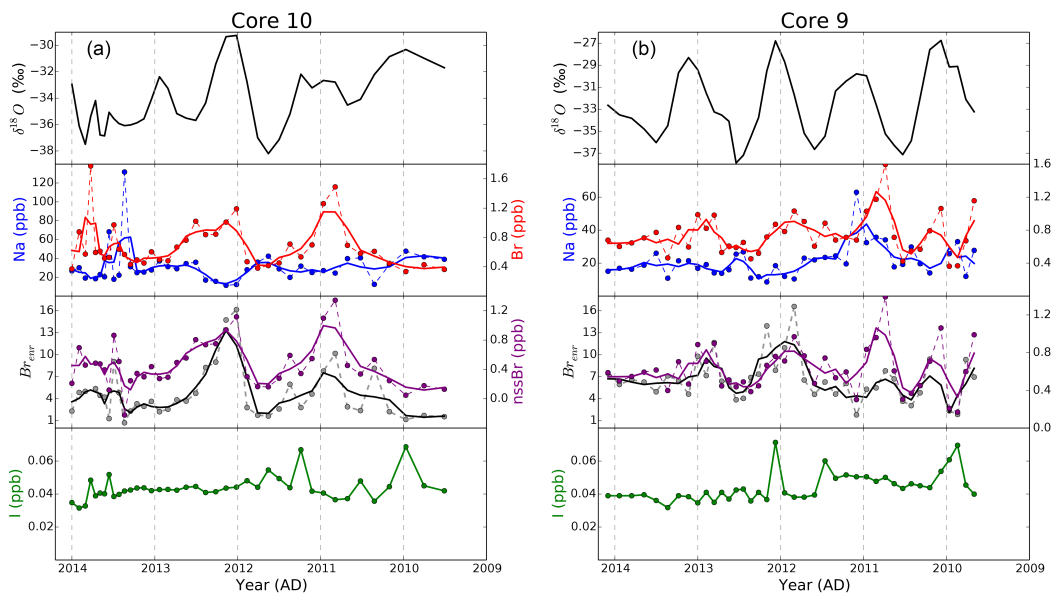


Figure A.4: Variability of $\delta^{18}\text{O}$ (upper panel), Na (middle top panel, left axis), Br (middle top panel, right axis), Brenr (middle bottom panel, left axis), nssBr (middle bottom panel, right axis) and I (bottom panel) in cores 10 (left) and 9 (right). Thick lines represent 3-month running means of the raw data (circles).

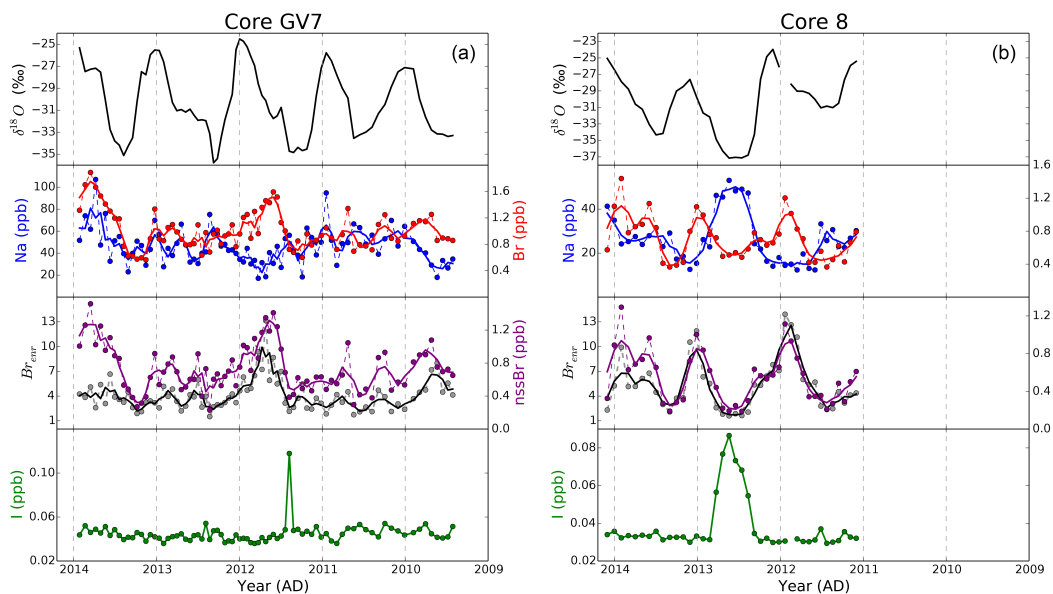


Figure A.5: Variability of $\delta^{18}\text{O}$ (upper panel), Na (middle top panel, left axis), Br (middle top panel, right axis), Brenr (middle bottom panel, left axis), nssBr (middle bottom panel, right axis) and I (bottom panel) in cores GV7 (left) and 8 (right). Thick lines represent 3-month running means of the raw data (circles).

Figure A.1 shows the minimum and maximum found in January 2010 and August 2011, respectively. The monthly sea ice areas from 2010 to 2013 were calculated for such sector and plotted in Fig.A.7a (blue); each monthly value was normalized to the total annual sea ice area. The minimum sea ice is found in February, while a longer-lasting maximum throughout win-

ter and spring is observed, before a rapid decrease in November. Solar radiation values Fig.A.7a (red points) were calculated at 71°S , 158°E using the tropospheric ultraviolet and visible (TUV) radiation model within the [300, 500] nm wavelength interval. Each point represents a daily average of the 15th day of each

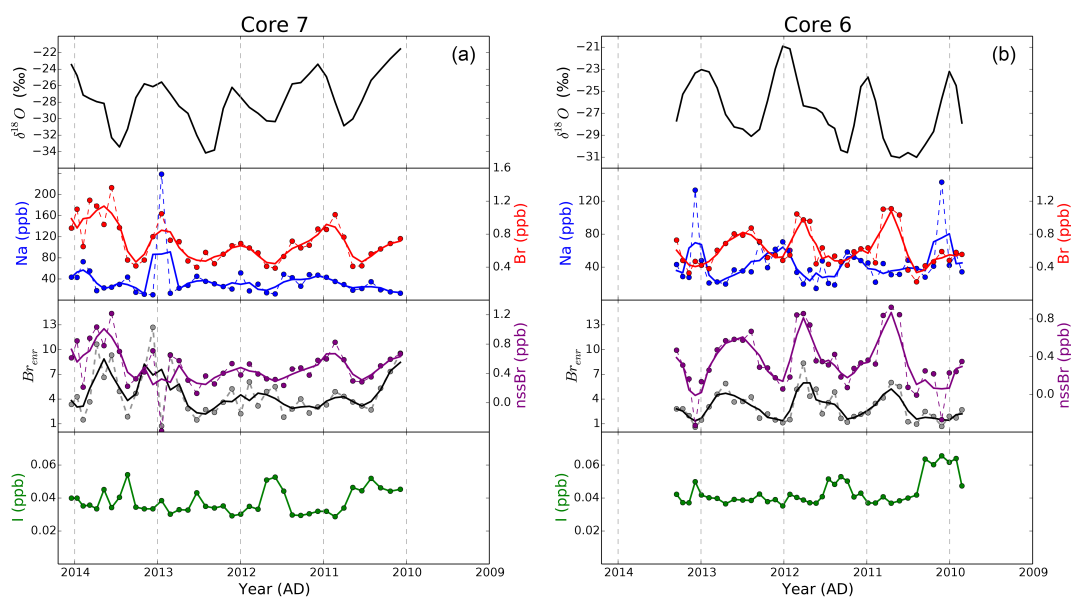


Figure A.6: Variability of $\delta^{18}\text{O}$ (upper panel), Na (middle top panel, left axis), Br (middle top panel, right axis), Br_{enr} (middle bottom panel, left axis), nssBr (middle bottom panel, right axis) and I (bottom panel) in cores 7 (left) and 6 (right). Thick lines represent 3-month running means of the raw data (circles).

Table A.3: Iodine average concentrations and variability during the 2013–2010 time period. All values are expressed in ppb.

Core	2013		2012		2011		2010	
	I	SD	I	SD	I	SD	I	SD
10	0.041	0.005	0.043	0.001	0.049	0.008	0.040	0.005
9	0.038	0.003	0.041	0.010	0.046	0.008	0.047	0.003
GV7	0.044	0.004	0.042	0.004	0.043	0.004	0.047	0.005
8	0.033	0.002	0.049	0.021	0.032	0.002	–	–
7	0.038	0.006	0.034	0.004	0.037	0.009	0.041	0.008
6	–	–	0.039	0.002	0.044	0.006	0.041	0.008

month of 2012 and is considered a monthly representation.

The sub-annual distribution of bromine enrichment along the transect is shown in Fig.A.7b (blue). Each bin contains the cumulative monthly value for every year in every core normalized by the total value of each year (which may change according to year and location). The histogram is then normalized by the overall sum measured in the transect. The distribution shows a clear sub-annual oscillation with lowest and highest annual contribution in May (autumn) and October–November (late spring), respectively. The combined effect of sea ice and insolation (Fig.A.7b, magenta product distribution) shows similar features, with the maximum in November, albeit with a much more pronounced springtime increase

than is seen in the bromine enrichment. Such comparison suggests that the combined effect of sea ice and insolation is related to the seasonality of bromine enrichment. Monthly sea ice area values are reported in Fig.A.7c (blue) together with annual averaged values of bromine enrichment (black) and first-year sea ice (red), calculated as the difference of maximum and minimum sea ice areas. A longer record would be needed to evaluate the correlation between bromine enrichment values and FYSI area and investigate a quantitative link.

Table A.3 shows the average annual iodine concentrations for each location together with its standard deviation. The mean value (0.043 ppb) is close to the background values found in Antarctic shallow firn cores near the research stations of

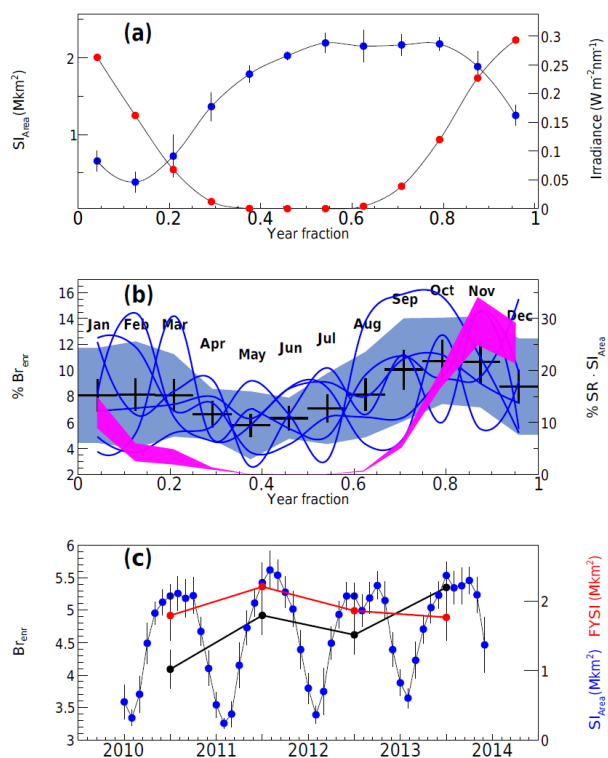


Figure A.7: (a) Monthly values of sea ice area (blue) within the 130° E– 170° W sector from 2010 to 2013 ($\pm 1\sigma$, month variability) and daily average (24 h) total downwelling spectral irradiance (red) calculated using the TUV model at 71° S, 158° E. Each irradiance calculation was set on the 15th day of each month in 2012. (b) Seasonality of annual bromine enrichment along the traverse: the monthly trend shows a seasonal feature with the maximum in spring. Each line refers to a core of the transect ($\pm 1\sigma$, shaded blue area). The month averages are displayed in black. The systematic uncertainties associated with the dating are shown as vertical error bars. The magenta band represents the product distribution of normalized sea ice area and insolation expressed in annual percentage. (c) Monthly sea ice area values (blue) from 2010 to 2013 with annual values of FYSI (red) and averaged bromine enrichment (black).

Neumayer (Frieß et al. 2010) and Casey (Law Dome, Spolaor et al. 2014). Unlike previous observations of a clear winter peak of iodine with concentrations up to 0.6 ppb (Neumayer) and 0.3 ppb (Law Dome), no clear seasonality is observed in the transect records, with annual variability around 10–15%. Core 7 (Fig. A.6) shows some variability which corresponds to winter peaks. High iodine concentrations are observed in core 8 during the 2012 winter, in association with a strong sea salt (sodium) input, although similar strong winter peaks are observed in 2011 at GV7.

The low background level and low variability of iodine found along the transect reflect a low input of iodine in this area of Antarctica compared to other loca-

tions. This picture is confirmed by satellite measurements, which show average IO concentrations close to the detection limit over the area of the transect compared to Law Dome, Neumayer or any other coastal location (Fig. A.8, right panel). The high elevation of the traverse area, compared to the others, is likely to play a role in preventing efficient iodine transport from the source areas.

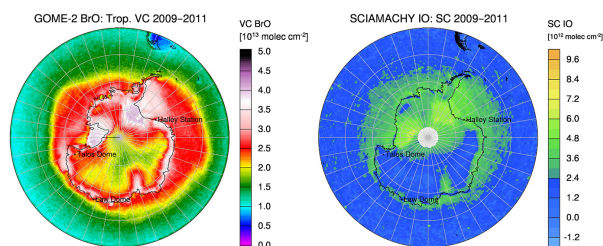


Figure A.8: Average atmospheric column concentrations of BrO and IO in Antarctica between 2009 and 2011 from Spolaor et al. 2014

Frieß et al. 2010 and Spolaor et al. 2014 have attributed iodine seasonal signal patterns to summertime photochemical recycling of IO from the snowpack, leading to depletion in the summer layers and higher concentrations in winter when absence of sunlight inhibits photoactivation. The lower variability found across the northern Victoria Land traverse cores could result from a reduced summer recycling due to low iodine concentrations available in the snow.

A.3.3 SPATIAL FLUX VARIABILITY

Glaciochemistry around Antarctica is very strongly influenced by, among several properties, the distance from the sea and the pathways of the air mass trajectories (Bertler et al. 2005). Atmospheric circulation patterns around the Talos Dome area have been investigated by Scarchilli et al. 2011, who have shown that the main input is represented by the Southern Ocean (Indian sector) with a lower contribution from the Ross Sea.

The spatial variability of sodium, bromine, bromine enrichment and iodine is investigated in Fig. A.9. The twelve panels display the annual fluxes of Na, Br, I and integrated annual values of bromine enrichment for each core in relation to its distance from the Indian Ocean. Sodium fluxes show the highest values and variability around the closest locations

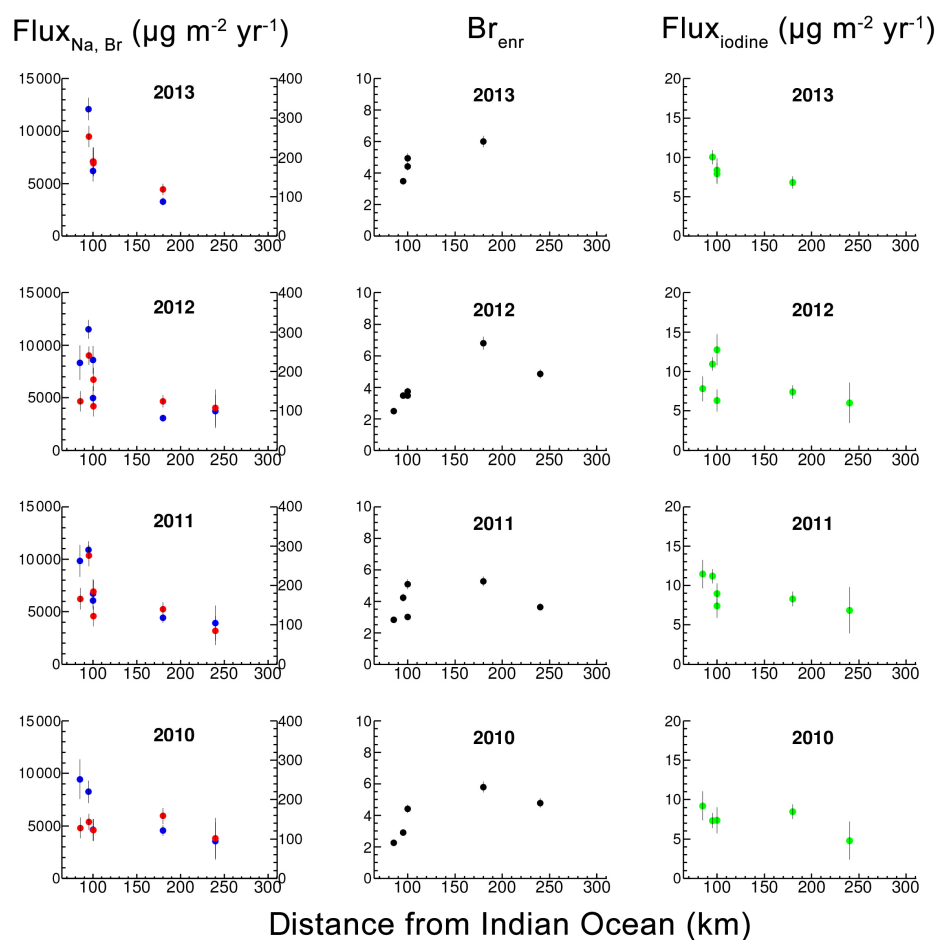


Figure A.9: Mean annual fluxes of sodium (blue, left axes), bromine (red, right axes), iodine (green) and bromine enrichment values (black) as a function of distance from the Indian Ocean. Each dot represents a location along the traverse.

to the Southern Ocean (GV7, 8, 7 and 6), where the accumulation increases. After rapidly decreasing within the first 100 km, the sodium flux becomes stable as the input from the SO decreases but the one from the Ross Sea gradually increases. Bromine exhibits a similar behavior to sodium with a homogeneous flux within cores 10 and 9 and an increase (up to 3 times) in the last 100 km from the SO. Elevation could partly account for the fractionation of sodium and bromine, having 180 m of height difference separating GV7, 8, 7 and 6, and 240 m from GV7 to core 10. The effect of elevation is combined with the influence of the distance from the source to resolve the two effects. The pattern of bromine enrichment is linked among other things to the different bromine fractionations during transport in the gas phase and the aerosol phase compared to sodium. Unlike sodium and bromine, no decrease is observed for bromine enrichment from our data (Fig.A.9, second column), although no clear trend

can be inferred. This can be due to the multiple origins of air advection (Ross Sea/Indian Ocean) to their uneven strength or because the distances are not large enough for any difference to be observed.

A slightly lower fractionation after 100 km from the SO is observed for iodine, consistent with the homogeneous satellite measurements of IO (Fig.A.9, right).

A.4 CONCLUSIONS

The 2013/14 Talos Dome – GV7 traverse provided an opportunity to expand the existing sodium dataset in Victoria Land and investigate important features of bromine and iodine temporal and spatial variabilities so far only available in Antarctica at Law Dome and Neumayer station.

The accumulation rates agree with previous studies, with increasing values from the Ross Sea to the

Southern Ocean. Accumulation rates calculated at Talos Dome are higher than previously reported, likely caused by isotopic diffusion and remobilization. Further studies are required at this site in order to access the reproducibility of the climate signal. The locations near the Southern Ocean exhibit high variability due to the higher accumulation.

Sodium and bromine concentrations in the snow samples result in a positive bromine enrichment compared to seawater, confirming the sea ice influence in the area for the extra bromine deposition. While sodium does not capture clear sub-annual variations associated with sea ice, bromine enrichment shows consistent seasonal variabilities with late spring maxima. There is some evidence that the seasonality is linked to the combined effect of sea ice growth and sunlight, which trigger photochemistry above fresh sea ice. The timing of deposition is coherent among Victoria Land, Law Dome, Dumont d'Urville (Indian sector) and Neumayer (Atlantic sector). Iodine shows an average value of 0.04 ppb, similar to background values observed in the Antarctic coastal locations of Law Dome and Neumayer. Unlike those locations, low iodine annual variability and no consistent seasonality of the signal are observed in the traverse samples.

The spatial variability study reveals homogeneous fluxes of Na, Br and I over the transect length, with an increase in absolute values and variability at the sites close to the Indian Ocean due to high accumulation and proximity to the coasts. Uniform satellite values of BrO and IO over Victoria Land are consistent with the snow measurements. A fractionation due to distance of these potential proxies is probably not found due to the combined double input of air masses from the Ross Sea and the Indian Ocean.

A transect covering larger distances and directed towards the interior of the plateau would give an insight into this feature, especially clarifying the spatial pattern of bromine enrichment with respect to the differences in gas-phase and aerosol depositions.

References

- Abbatt, J. and Molina, M. (1992). The heterogeneous reaction of $\text{HOCl} + \text{HCl} \rightarrow \text{Cl}_2 + \text{H}_2\text{O}$ on ice and nitric acid trihydrate: Reaction probabilities and stratospheric implications. *Geophysical Research Letters*, 19(5):461–464.
- Abbatt, J., Thomas, J. L., Abrahamsson, K., Boxe, C., Granfors, A., Jones, A., King, M., Saiz-Lopez, A., Shepson, P., Sodeau, J., et al. (2012). Halogen activation via interactions with environmental ice and snow in the polar lower troposphere and other regions. *Atmospheric Chemistry and Physics*, 12(14):6237–6271.
- Abbatt, J. P. (1994). Heterogeneous reaction of HOBr with HBr and HCl on ice surfaces at 228 K. *Geophysical Research Letters*, 21(8):665–668.
- Abram, N. J., Curran, M. A., Mulvaney, R., and Vance, T. (2008). The preservation of methanesulphonic acid in frozen ice-core samples. *Journal of Glaciology*, 54(187):680–684.
- Abram, N. J., Thomas, E. R., McConnell, J. R., Mulvaney, R., Bracegirdle, T. J., Sime, L. C., and Aristarain, A. J. (2010). Ice core evidence for a 20th century decline of sea ice in the Bellingshausen Sea, Antarctica. *Journal of Geophysical Research: Atmospheres*, 115(D23).
- Abram, N. J., Wolff, E. W., and Curran, M. A. (2013). A review of sea ice proxy information from polar ice cores. *Quaternary Science Reviews*, 79:168–183.
- Adams, J., Holmes, N., and Crowley, J. (2002). Uptake and reaction of HOBr on frozen and dry NaCl/NaBr surfaces between 253 and 233 K. *Atmospheric Chemistry and Physics*, 2(1):79–91.
- Alley, R., Finkel, R., Nishiizumi, K., Anandakrishnan, S., Shuman, C., Mershon, G., Zielinski, G., and Mayewski, P. A. (1995). Changes in continental and sea-salt atmospheric loadings in central Greenland during the most recent deglaciation: model-based estimates. *Journal of Glaciology*, 41(139):503–514.

- Andreas, E. L. (1992). Sea spray and the turbulent air-sea heat fluxes. *Journal of Geophysical Research: Oceans*, 97(C7):11429–11441.
- Atkinson, H. M., Huang, R.-J., Chance, R., Roscoe, H. K., Hughes, C., Davison, B., Schönhardt, A., Mahajan, A. S., Saiz-Lopez, A., Hoffmann, T., et al. (2012). Iodine emissions from the sea ice of the weddell sea. *Atmospheric Chemistry and Physics*, 12(22):11229–11244.
- Atkinson, R., Baulch, D., Cox, R., Crowley, J., Hampson, R., Hynes, R., Jenkin, M., Rossi, M., Troe, J., and Wallington, T. (2008). Evaluated kinetic and photochemical data for atmospheric chemistry: Volume iv—gas phase reactions of organic halogen species. *Atmospheric Chemistry and Physics*, 8(15):4141–4496.
- Ayash, T., Gong, S., and Jia, C. Q. (2008). Direct and indirect shortwave radiative effects of sea salt aerosols. *Journal of Climate*, 21(13):3207–3220.
- Barrie, L., Bottenheim, J., Schnell, R., Crutzen, P., and Rasmussen, R. (1988). Ozone destruction and photochemical reactions at polar sunrise in the lower arctic atmosphere. *Nature*, 334(6178):138–141.
- Barrie, L. A., Gregor, D., Hargrave, B., Lake, R., Muir, D., Shearer, R., Tracey, B., and Bidleman, T. (1992). Arctic contaminants: sources, occurrence and pathways. *Science of the Total Environment*, 122(1-2):1–74.
- Becagli, S., Benassai, S., Castellano, E., Largiuni, O., Migliori, A., Traversi, R., Flora, O., and Udisti, R. (2004a). Chemical characterization of the last 250 years of snow deposition at talos dome (east antarctica). *International Journal of Environmental Analytical Chemistry*, 84(6-7):523–536.
- Becagli, S., Proposito, M., Benassai, S., Flora, O., Genoni, L., Gragnani, R., Largiuni, O., Pili, S. L., Severi, M., Stenni, B., et al. (2004b). Chemical and isotopic snow variability in east antarctica along the 2001/02 itase traverse. *Annals of Glaciology*, 39(1):473–482.
- Becagli, S., Proposito, M., Benassai, S., Gragnani, R., Magand, O., Traversi, R., and Udisti, R. (2005). Spatial distribution of biogenic sulphur compounds (msa, nssso42-) in the

- northern victoria land–dome c–wilkes land area, east antarctica. *Annals of Glaciology*, 41(1):23–31.
- Begoin, M., Richter, A., Weber, M., Kaleschke, L., Tian-Kunze, X., Stohl, A., Theys, N., and Burrows, J. P. (2010). Satellite observations of long range transport of a large bro plume in the arctic. *Atmospheric Chemistry and Physics*, 10(14):6515–6526.
- Belt, S. T., Massé, G., Rowland, S. J., Poulin, M., Michel, C., and LeBlanc, B. (2007). A novel chemical fossil of palaeo sea ice: Ip 25. *Organic Geochemistry*, 38(1):16–27.
- Belt, S. T. and Müller, J. (2013). The arctic sea ice biomarker ip 25: a review of current understanding, recommendations for future research and applications in palaeo sea ice reconstructions. *Quaternary Science Reviews*, 79:9–25.
- Benassai, S., Becagli, S., Gragnani, R., Magand, O., Proposito, M., Fattori, I., Traversi, R., and Udisti, R. (2005). Sea-spray deposition in antarctic coastal and plateau areas from itase traverses. *Annals of Glaciology*, 41(1):32–40.
- Bertler, N., Mayewski, P. A., Aristarain, A., Barrett, P., Becagli, S., Bernardo, R., Bo, S., Xiao, C., Curran, M., Qin, D., et al. (2005). Snow chemistry across antarctica. *Annals of Glaciology*, 41(1):167–179.
- Bigler, M., Svensson, A., Kettner, E., Vallelonga, P., Nielsen, M. E., and Steffensen, J. P. (2011). Optimization of high-resolution continuous flow analysis for transient climate signals in ice cores. *Environmental Science & Technology*, 45(10):4483–4489.
- Biscaye, P., Grousset, F., Revel, M., Van der Gaast, S., Zielinski, G., Vaars, A., and Kukla, G. (1997). Asian provenance of glacial dust (stage 2) in the greenland ice sheet project 2 ice core, summit, greenland. *Journal of Geophysical Research: Oceans*, 102(C12):26765–26781.
- Boetius, A., Anesio, A. M., Deming, J. W., Mikucki, J. A., and Rapp, J. Z. (2015). Microbial ecology of the cryosphere: sea ice and glacial habitats. *Nature reviews Microbiology*.
- Bory, A. J.-M., Biscaye, P. E., and Grousset, F. E. (2003). Two distinct seasonal asian source regions for mineral dust deposited in greenland (northgrip). *Geophysical Research Letters*, 30(4).

- Brent, R. P. (1971). An algorithm with guaranteed convergence for finding a zero of a function. *The Computer Journal*, 14(4):422–425.
- Brown, T. A., Belt, S. T., Philippe, B., Mundy, C. J., Massé, G., Poulin, M., and Goselin, M. (2011). Temporal and vertical variations of lipid biomarkers during a bottom ice diatom bloom in the canadian beaufort sea: further evidence for the use of the ip25 biomarker as a proxy for spring arctic sea ice. *Polar Biology*, 34(12):1857–1868.
- Carpenter, L., Liss, P., and Penkett, S. (2003). Marine organohalogenes in the atmosphere over the atlantic and southern oceans. *Journal of Geophysical Research: Atmospheres*, 108(D9).
- Carpenter, L. J., MacDonald, S. M., Shaw, M. D., Kumar, R., Saunders, R. W., Parthipan, R., Wilson, J., and Plane, J. M. (2013). Atmospheric iodine levels influenced by sea surface emissions of inorganic iodine. *Nature Geoscience*, 6(2):108.
- Cavitte, M. G. P., Parrenin, F., Ritz, C., Young, D. A., Blankenship, D. D., Frezzotti, M., and Roberts, J. L. (2017). Stable accumulation patterns around dome c, east antarctica, over the last glacial cycle. *The Cryosphere Discussions*, 2017:1–26.
- Chance, K. (1998). Analysis of bro measurements from the global ozone monitoring experiment. *Geophysical Research Letters*, 25(17):3335–3338.
- Choi, S., Wang, Y., Salawitch, R., Canty, T., Joiner, J., Zeng, T., Kurosu, T., Chance, K., Richter, A., Huey, L. G., et al. (2012). Analysis of satellite-derived arctic tropospheric bro columns in conjunction with aircraft measurements during arctas and arcpac. *Atmospheric Chemistry and Physics*.
- Cicerone, R. J. (1981). Halogens in the atmosphere. *Reviews of Geophysics*, 19(1):123–139.
- Cole-Dai, J., Budner, D. M., and Ferris, D. G. (2006). High speed, high resolution, and continuous chemical analysis of ice cores using a melter and ion chromatography. *Environmental science & technology*, 40(21):6764–6769.
- Comiso, J. C. (2012). Large decadal decline of the arctic multiyear ice cover. *Journal of Climate*, 25(4):1176–1193.

Cooper, O. R., Parrish, D., Ziemke, J., Balashov, N., Cupeiro, M., Galbally, I., Gilge, S., Horowitz, L., Jensen, N., Lamarque, J.-F., et al. (2014). Global distribution and trends of tropospheric ozone: An observation-based review. *Elem Sci Anth*, 2.

Coulter, W. and Hogg, W. (1971). Apparatus and method for measuring a dividing particle size of a particulate system. US Patent 3,557,352.

Covert, D. S., Kapustin, V. N., Quinn, P. K., and Bates, T. S. (1992). New particle formation in the marine boundary layer. *Journal of Geophysical Research: Atmospheres*, 97(D18):20581–20589.

Cox, G. F. and Weeks, W. F. (1974). Salinity variations in sea ice. *Journal of Glaciology*, 13(67):109–120.

Crosta, X., Sturm, A., Armand, L., and Pichon, J.-J. (2004). Late quaternary sea ice history in the indian sector of the southern ocean as recorded by diatom assemblages. *Marine Micropaleontology*, 50(3):209–223.

Cunningham, J. and Waddington, E. (1993). Air flow and dry deposition of non-sea salt sulfate in polar firn: paleoclimatic implications. *Atmospheric Environment. Part A. General Topics*, 27(17-18):2943–2956.

Curran, M. A. and Jones, G. B. (2000). Dimethyl sulfide in the southern ocean: Seasonality and flux. *Journal of Geophysical Research: Atmospheres*, 105(D16):20451–20459.

Curran, M. A., Palmer, A. S., Van Ommen, T. D., Morgan, V. I., Phillips, K. L., McMorrow, A. J., and Mayewski, P. A. (2002). Post-depositional movement of methanesulphonic acid at law dome, antarctica, and the influence of accumulation rate. *Annals of Glaciology*, 35(1):333–339.

Curran, M. A., Van Ommen, T. D., and Morgan, V. (1998). Seasonal characteristics of the major ions in the high-accumulation dome summit south ice core, Law Dome, Antarctica. *Annals of Glaciology*, 27(1):385–390.

Curran, M. A., van Ommen, T. D., Morgan, V. I., Phillips, K. L., and Palmer, A. S. (2003). Ice core evidence for antarctic sea ice decline since the 1950s. *Science*, 302(5648):1203–1206.

- Dansgaard, W. (1973). *Stable isotope glaciology*. Meddelelser om Grønland. C. A. Reitzel.
- Dansgaard, W. and Johnsen, S. (1969). A flow model and a time scale for the ice core from camp century, greenland. *Journal of Glaciology*, 8(53):215–223.
- De Angelis, M., Steffensen, J. P., Legrand, M., Clausen, H., and Hammer, C. (1997). Primary aerosol (sea salt and soil dust) deposited in greenland ice during the last climatic cycle: Comparison with east antarctic records. *Journal of Geophysical Research: Oceans*, 102(C12):26681–26698.
- De Leeuw, G., Andreas, E. L., Anguelova, M. D., Fairall, C., Lewis, E. R., O’Dowd, C., Schulz, M., and Schwartz, S. E. (2011). Production flux of sea spray aerosol. *Reviews of Geophysics*, 49(2).
- Delmas, R., Wagnon, P., GOTO-AZUMA, K., Kamiyama, K., and Watanabe, O. (2003). Evidence for the loss of snow-deposited msa to the interstitial gaseous phase in central antarctic firn. *Tellus B*, 55(1):71–79.
- Delmonte, B., Baroni, C., Andersson, P. S., Schoberg, H., Hansson, M., Aciego, S., Petit, J.-R., Albani, S., Mazzola, C., Maggi, V., et al. (2010). Aeolian dust in the talos dome ice core (east antarctica, pacific/ross sea sector): Victoria land versus remote sources over the last two climate cycles. *Journal of Quaternary Science*, 25(8):1327–1337.
- Delmonte, B., Basile-Doelsch, I., Petit, J.-R., Maggi, V., Revel-Rolland, M., Michard, A., Jagoutz, E., and Grousset, F. (2004). Comparing the epica and vostok dust records during the last 220,000 years: stratigraphical correlation and provenance in glacial periods. *Earth-Science Reviews*, 66(1):63–87.
- Dibb, J. E., Ziemba, L. D., Luxford, J., and Beckman, P. (2010). Bromide and other ions in the snow, firn air, and atmospheric boundary layer at summit during gshox. *Atmospheric Chemistry and Physics*, 10(20):9931–9942.
- Dickson, R., Lazier, J., Meincke, J., Rhines, P., and Swift, J. (1996). Long-term coordinated changes in the convective activity of the north atlantic. *Progress in Oceanography*, 38(3):241–295. n/a.

- Dokken, T. M. and Jansen, E. (1999). Rapid changes in the mechanism of ocean convection during the last glacial period. *Nature*, 401(6752):458–461.
- Domine, F., Taillandier, A. S., Simpson, W. R., and Severin, K. (2005). Specific surface area, density and microstructure of frost flowers. *Geophysical Research Letters*, 32(13).
- Draxler, R. and Hess, G. (1997). Description of the Hysplit 4 modeling system noaa tech. *NOAA Tech Memo ERL ARL-224*, 24.
- Draxler, R. R. and Hess, G. (1998). An overview of the hysplit_4 modelling system for trajectories. *Australian meteorological magazine*, 47(4):295–308.
- Draxler, R. R., Stunder, B., Rolph, G., and Taylor, A. (1999). *HYSPLIT4_Users's Guide*. US Department of Commerce, National Oceanic and Atmospheric Administration, Environmental Research Laboratories, Air Resources Laboratory.
- EPICA Community Members, . (2004). Eight glacial cycles from an antarctic ice core. *Nature*, 429(6992):623–628.
- Fan, S.-M. and Jacob, D. J. (1992). Surface ozone depletion in arctic spring sustained by bromine. *Nature*, 359:8.
- Farman, J. C., Gardiner, B. G., and Shanklin, J. D. (1985). Large losses of total ozone in antarctica reveal seasonal clox/nox interaction. *Nature*, 315(6016):207–210.
- Fischer, H. (2001). Imprint of large-scale atmospheric transport patterns on sea-salt records in northern greenland ice cores. *Journal of Geophysical Research: Atmospheres*, 106(D20):23977–23984.
- Fischer, H., Fundel, F., Ruth, U., Twarloh, B., Wegner, A., Udisti, R., Becagli, S., Castellano, E., Morganti, A., Severi, M., et al. (2007a). Reconstruction of millennial changes in dust emission, transport and regional sea ice coverage using the deep epica ice cores from the atlantic and indian ocean sector of antarctica. *Earth and Planetary Science Letters*, 260(1):340–354.

- Fischer, H., Siggaard-Andersen, M.-L., Ruth, U., Röhlisberger, R., and Wolff, E. (2007b). Glacial/interglacial changes in mineral dust and sea-salt records in polar ice cores: Sources, transport, and deposition. *Reviews of Geophysics*, 45(1).
- Fischer, H. and Wagenbach, D. (1996). Large-scale spatial trends in recent firn chemistry along an east-west transect through central greenland. *Atmospheric Environment*, 30(19):3227–3238.
- Foster, K. L., Plastringe, R. A., Bottenheim, J. W., Shepson, P. B., Finlayson-Pitts, B. J., and Spicer, C. W. (2001). The role of br2 and brcl in surface ozone destruction at polar sunrise. *Science*, 291(5503):471–474.
- Frezzotti, M., Bitelli, G., de Michelis, P., Deponti, A., Forieri, A., Gandolfi, S., Maggi, V., Mancini, F., Remy, F., Tabacco, I. E., et al. (2004). Geophysical survey at talos dome, east antarctica: the search for a new deep-drilling site. *Annals of Glaciology*, 39(1):423–432.
- Frezzotti, M., Urbini, S., Proposito, M., Scarchilli, C., and Gandolfi, S. (2007). Spatial and temporal variability of surface mass balance near talos dome, east antarctica. *Journal of Geophysical Research: Earth Surface*, 112(F2).
- Frieß, U., Deutschmann, T., Gilfedder, B., Weller, R., and Platt, U. (2010). Iodine monoxide in the antarctic snowpack. *Atmospheric Chemistry and Physics*, 10(5):2439–2456.
- Frieß, U., Sihler, H., Sander, R., Pöhler, D., Yilmaz, S., and Platt, U. (2011). The vertical distribution of bro and aerosols in the arctic: Measurements by active and passive differential optical absorption spectroscopy. *Journal of Geophysical Research: Atmospheres*, 116(D14).
- Frieß, U., Wagner, T., Pundt, I., Pfeilsticker, K., and Platt, U. (2001). Spectroscopic measurements of tropospheric iodine oxide at neumayer station, antarctica. *Geophysical Research Letters*, 28(10):1941–1944.
- Funder, S., Goosse, H., Jepsen, H., Kaas, E., Kjær, K. H., Korsgaard, N. J., Larsen, N. K., Linderson, H., Lyså, A., Möller, P., et al. (2011). A 10,000-year record of arctic ocean sea-ice variability—view from the beach. *Science*, 333(6043):747–750.

- Gálvez, Ó., Baeza-Romero, M. T., Sanz, M., and Saiz-Lopez, A. (2016). Photolysis of frozen iodate salts as a source of active iodine in the polar environment. *Atmospheric Chemistry & Physics*, 16(19).
- Gersonde, R., Crosta, X., Abelmann, A., and Armand, L. (2005). Sea-surface temperature and sea ice distribution of the southern ocean at the epilog last glacial maximum—a circum-antarctic view based on siliceous microfossil records. *Quaternary Science Reviews*, 24(7):869–896.
- Gfeller, G., Fischer, H., Bigler, M., Schüpbach, S., Leuenberger, D., and Mini, O. (2014). Representativeness and seasonality of major ion records derived from neem firn cores. *The Cryosphere*, 8(5):1855–1870.
- Gkinis, V., Popp, T. J., Johnsen, S. J., and Blunier, T. (2010). A continuous stream flash evaporator for the calibration of an ir cavity ring-down spectrometer for the isotopic analysis of water. *Isotopes in environmental and health studies*, 46(4):463–475.
- Grilli, R., Legrand, M., Kukui, A., Méjean, G., Preunkert, S., and Romanini, D. (2013). First investigations of io, bro, and no₂ summer atmospheric levels at a coastal east antarctic site using mode-locked cavity enhanced absorption spectroscopy. *Geophysical Research Letters*, 40(4):791–796.
- Grilli, R., Méjean, G., Kassi, S., Ventrillard, I., Abd-Alrahman, C., and Romanini, D. (2012). Frequency comb based spectrometer for in situ and real time measurements of io, bro, no₂, and h₂co at pptv and ppqv levels. *Environmental science & technology*, 46(19):10704–10710.
- Grootes, P. M., Steig, E. J., Stuiver, M., Waddington, E. D., Morse, D. L., and Nadeau, M.-J. (2001). The taylor dome antarctic 18 o record and globally synchronous changes in climate. *Quaternary Research*, 56(3):289–298.
- Grumet, N. S., Wake, C. P., Mayewski, P. A., Zielinski, G. A., Whitlow, S. I., Koerner, R. M., Fisher, D. A., and Woollett, J. M. (2001). Variability of sea-ice extent in baffin bay over the last millennium. *Climatic Change*, 49(1):129–145.

- Hägglom, A. (1982). Driftwood in svalbard as an indicator of sea ice conditions. *Geografiska Annaler. Series A. Physical Geography*, pages 81–94.
- Hammer, C. U. (1980). Acidity of polar ice cores in relation to absolute dating, past volcanism, and radio-echoes. *Journal of Glaciology*, 25(93):359–372.
- Hansson, M. E. (1994). The renland ice core. a northern hemisphere record of aerosol composition over 120,000 years. *Tellus B*, 46(5):390–418.
- Hara, K., Osada, K., Kido, M., Hayashi, M., Matsunaga, K., Iwasaka, Y., Yamanouchi, T., Hashida, G., and Fukatsu, T. (2004). Chemistry of sea-salt particles and inorganic halogen species in antarctic regions: Compositional differences between coastal and inland stations. *Journal of Geophysical Research: Atmospheres*, 109(D20).
- Hausmann, M. and Platt, U. (1994). Spectroscopic measurement of bromine oxide and ozone in the high arctic during polar sunrise experiment 1992. *Journal of Geophysical Research: Atmospheres*, 99(D12):25399–25413.
- Haywood, J., Ramaswamy, V., and Soden, B. (1999). Tropospheric aerosol climate forcing in clear-sky satellite observations over the oceans. *Science*, 283(5406):1299–1303.
- Heintzenberg, J. and Leck, C. (1994). Seasonal variation of the atmospheric aerosol near the top of the marine boundary layer over spitsbergen related to the arctic sulphur cycle. *Tellus B: Chemical and Physical Meteorology*, 46(1):52–67.
- Herron, M. M. (1982). Impurity sources of f-, cl-, no₃- and so₄ 2- in greenland and antarctic precipitation. *Journal of Geophysical Research: Oceans*, 87(C4):3052–3060.
- Herron, M. M. and Langway, C. C. (1980). Firn densification: An empirical model. *Journal of Glaciology*, 25(93):373–385.
- Hoff, U., Rasmussen, T. L., Stein, R., Ezat, M. M., and Fahl, K. (2016). Sea ice and millennial-scale climate variability in the nordic seas 90 [thinsp] kyr ago to present. *Nature Communications*, 7.

- Hönninger, G., Leser, H., Sebastian, O., and Platt, U. (2004). Ground-based measurements of halogen oxides at the hudson bay by active longpath doas and passive max-doas. *Geophysical Research Letters*, 31(4).
- Hönninger, G. and Platt, U. (2002). Observations of bro and its vertical distribution during surface ozone depletion at alert. *Atmospheric Environment*, 36(15):2481–2489.
- Honrath, R., Guo, S., Peterson, M. C., Dziobak, M., Dibb, J. E., and Arsenault, M. (2000). Photochemical production of gas phase no_x from ice crystal no₃-. *Journal of Geophysical Research: Atmospheres*, 105(D19):24183–24190.
- Howe, J. N., Piotrowski, A. M., Noble, T. L., Mulitza, S., Chiessi, C. M., and Bayon, G. (2016). North atlantic deep water production during the last glacial maximum. *Nature Communications*, 7.
- Huang, J. and Jaeglé, L. (2017). Wintertime enhancements of sea salt aerosol in polar regions consistent with a sea ice source from blowing snow. *Atmospheric Chemistry and Physics*, 17(5):3699–3712.
- Huff, A. K. and Abbatt, J. P. (2002). Kinetics and product yields in the heterogeneous reactions of hobr with ice surfaces containing nabr and nacl. *The Journal of Physical Chemistry A*, 106(21):5279–5287.
- Hunke, E. C., Notz, D., Turner, A. K., and Vancoppenolle, M. (2011). The multiphase physics of sea ice: A review for model developers. *Cryosphere*, 5(4):989–1009.
- Hutterli, M. A., Crueger, T., Fischer, H., Andersen, K. K., Raible, C., Stocker, T. F., Siggaard-Andersen, M.-L., McConnell, J., Bales, R., and Burkhart, J. (2007). The influence of regional circulation patterns on wet and dry mineral dust and sea salt deposition over greenland. *Climate Dynamics*, 28(6):635–647.
- Isaksson, E., Kekonen, T., Moore, J., and Mulvaney, R. (2005). The methanesulfonic acid (msa) record in a svalbard ice core. *Annals of Glaciology*, 42(1):345–351.
- Jobson, B., Niki, H., Yokouchi, Y., Bottenheim, J., Hopper, F., and Leitch, R. (1994). Measurements of c₂-c₆ hydrocarbons during the polar sunrise1992 experiment: Evi-

dence for cl atom and br atom chemistry. *Journal of Geophysical Research: Atmospheres*, 99(D12):25355–25368.

Johnsen, S., Dansgaard, W., Clausen, H., and Langway, C. C. (1972). Oxygen isotope profiles through the antarctic and greenland ice sheets. *Nature*, 235(5339):429–434.

Johnsen, S., Dansgaard, W., and White, J. (1989). The origin of arctic precipitation under present and glacial conditions. *Tellus B*, 41(4):452–468.

Jones, A. E., Anderson, P. S., Begoin, M., Brough, N., Hutterli, M. A., Marshall, G. J., Richter, A., Roscoe, H. K., and Wolff, E. W. (2009). Bro, blizzards, and drivers of polar tropospheric ozone depletion events. *Atmospheric Chemistry and Physics*, 9(14):4639–4652.

Jourdain, B. and Legrand, M. (2002). Year-round records of bulk and size-segregated aerosol composition and hcl and hno₃ levels in the dumont d’urville (coastal antarctica) atmosphere: Implications for sea-salt aerosol fractionation in the winter and summer. *Journal of Geophysical Research: Atmospheres*, 107(D22).

Justwan, A. and Koç, N. (2008). A diatom based transfer function for reconstructing sea ice concentrations in the north atlantic. *Marine Micropaleontology*, 66(3):264–278.

Kaleschke, L., Richter, A., Burrows, J., Afe, O., Heygster, G., Notholt, J., Rankin, A., Roscoe, H., Hollwedel, J., Wagner, T., et al. (2004). Frost flowers on sea ice as a source of sea salt and their influence on tropospheric halogen chemistry. *Geophysical Research Letters*, 31(16).

Kalnay, E., Kanamitsu, M., Kistler, R., Collins, W., Deaven, D., Gandin, L., Iredell, M., Saha, S., White, G., Woollen, J., et al. (1996). The ncep/ncar 40-year reanalysis project. *Bulletin of the American meteorological Society*, 77(3):437–471.

Kanaya, Y., Kajii, Y., and Akimoto, H. (2003). Solar actinic flux and photolysis frequency determinations by radiometers and a radiative transfer model at rishiri island: comparisons, cloud effects, and detection of an aerosol plume from russian forest fires. *Atmospheric Environment*, 37(18):2463–2475.

- Kaspari, S., Dixon, D., Sneed, S., and Handley, M. (2005). Sources and transport pathways of marine aerosol species into west antarctica. *Annals of Glaciology*, 41(1):1–9.
- Kaufmann, P. R., Federer, U., Hutterli, M. A., Bigler, M., Schüpbach, S., Ruth, U., Schmitt, J., and Stocker, T. F. (2008). An improved continuous flow analysis system for high-resolution field measurements on ice cores. *Environmental science & technology*, 42(21):8044–8050.
- Keene, W. C., Sander, R., Pszenny, A. A., Vogt, R., Crutzen, P. J., and Galloway, J. N. (1998). Aerosol ph in the marine boundary layer: A review and model evaluation. *Journal of Aerosol Science*, 29(3):339–356.
- Kekonen, T., Moore, J., Perämäki, P., Mulvaney, R., Isaksson, E., Pohjola, V., and van de Wal, R. S. (2005). The 800 year long ion record from the lomonosovfonna (svalbard) ice core. *Journal of Geophysical Research: Atmospheres*, 110(D7).
- Kim, K., Yabushita, A., Okumura, M., Saiz-Lopez, A., Cuevas, C. A., Blaszcak-Boxe, C. S., Min, D. W., Yoon, H.-I., and Choi, W. (2016). Production of molecular iodine and tri-iodide in the frozen solution of iodide: implication for polar atmosphere. *Environmental Science & Technology*, 50(3):1280–1287.
- Kinnard, C., Zdanowicz, C. M., Fisher, D. A., and Wake, C. P. (2006). Calibration of an ice-core glaciochemical (sea-salt) record with sea-ice variability in the canadian arctic. *Annals of Glaciology*, 44(1):383–390.
- Knüsel, S., Piguet, D. E., Schwikowski, M., and Gäggeler, H. W. (2003). Accuracy of continuous ice-core trace-element analysis by inductively coupled plasma sector field mass spectrometry. *Environmental science & technology*, 37(10):2267–2273.
- Koo, J.-H., Wang, Y., Kurosu, T., Chance, K., Rozanov, A., Richter, A., Oltmans, S., Thompson, A., Hair, J., Fenn, M., et al. (2012). Characteristics of tropospheric ozone depletion events in the arctic spring: analysis of the arctas, arcpac, and arcions measurements and satellite bro observations. *Atmospheric Chemistry and Physics*, 12(20):9909–9922.
- Košler, J. and Sylvester, P. J. (2003). Present trends and the future of zircon in geochronology: laser ablation icpms. *Reviews in mineralogy and geochemistry*, 53(1):243–275.

- Kreher, K., Johnston, P., Wood, S., Nardi, B., and Platt, U. (1997). Ground-based measurements of tropospheric and stratospheric bro at arrival heights, antarctica. *Geophysical Research Letters*, 24(23):3021–3024.
- Kreutz, K., Mayewski, P. A., Pittalwala, I., Meeker, L., Twickler, M., and Whitlow, S. (2000). Sea level pressure variability in the amundsen sea region inferred from a west antarctic glaciochemical record. *Journal of Geophysical Research: Atmospheres*, 105(D3):4047–4059.
- Kuramoto, T., Goto-Azuma, K., Hirabayashi, M., Miyake, T., Motoyama, H., Dahl-Jensen, D., and Steffensen, J. P. (2011). Seasonal variations of snow chemistry at neem, greenland. *Annals of Glaciology*, 52(58):193–200.
- Kwok, R., Panzer, B., Leuschen, C., Pang, S., Markus, T., Holt, B., and Gogineni, S. (2011). Airborne surveys of snow depth over arctic sea ice. *Journal of Geophysical Research: Oceans*, 116(C11).
- Lambert, F., Delmonte, B., Petit, J.-R., Bigler, M., Kaufmann, P. R., Hutterli, M. A., Stocker, T. F., Ruth, U., Steffensen, J. P., and Maggi, V. (2008). Dust-climate couplings over the past 800,000 years from the epica dome c ice core. *Nature*, 452(7187):616.
- Landais, A., Barkan, E., and Luz, B. (2008). Record of $\delta^{18}O$ and $17O$ -excess in ice from vostok antarctica during the last 150,000 years. *Geophysical Research Letters*, 35(2).
- Law, K., Sturges, W., Blake, D., Blake, N., Burkholder, J., Butler, J., Cox, R., Haynes, P., Ko, M., Kreher, K., et al. (2007). Halogenated very short-lived substances, chapter 2 in: Scientific assessment of ozone depletion: 2006, global ozone research and monitoring project–report no. 50. *World Meteorological Organization, Geneva, Switzerland*, 572.
- Le Bras, G. and Platt, U. (1995). A possible mechanism for combined chlorine and bromine catalyzed destruction of tropospheric ozone in the arctic. *Geophysical Research Letters*, 22(5):599–602.
- Legrand, M. (1987). Chemistry of antarctic snow and ice. *Le Journal de Physique Colloques*, 48(C1):C1–77.

- Legrand, M. (1997). Ice-core records of atmospheric sulphur. *Philosophical Transactions of the Royal Society of London B: Biological Sciences*, 352(1350):241–250.
- Legrand, M., de Angelis, M., Cachier, H., and Gaudichet, A. (1995). Boreal biomass burning over the last 80 years recorded in a summit-greenland ice core. In *Ice core studies of global biogeochemical cycles*, pages 347–360. Springer.
- Legrand, M., De Angelis, M., Staffelbach, T., Neftel, A., and Stauffer, B. (1992). Large perturbations of ammonium and organic acids content in the summit-greenland ice core. fingerprint from forest fires? *Geophysical Research Letters*, 19(5):473–475.
- Legrand, M. and Delmas, R. (1984). The ionic balance of antarctic snow: a 10-year detailed record. *Atmospheric Environment (1967)*, 18(9):1867–1874.
- Legrand, M., Feniet-Saigne, C., Sattzman, E., Germain, C., Barkov, N., and Petrov, V. (1991). Ice-core record of oceanic emissions of dimethylsulphide during the last climate cycle. *Nature*, 350(6314):144–146.
- Legrand, M., Hammer, C., De Angelis, M., Savarino, J., Delmas, R., Clausen, H., and Johnsen, S. J. (1997a). Sulfur-containing species (methanesulfonate and SO_4) over the last climatic cycle in the greenland ice core project (central greenland) ice core. *Journal of Geophysical Research: Oceans*, 102(C12):26663–26679.
- Legrand, M., Hammer, C., De Angelis, M., Savarino, J., Delmas, R., Clausen, H., and Johnson, S. (1997b). Sulphur containing species (MSA and SO_4) over the last climatic cycle in the grip (central greenland) ice core. *J. Geophys. Res.*, 102:26663–26679.
- Legrand, M., Lorius, C., Barkov, N., and Petrov, V. (1988). Vostok (antarctica) ice core: atmospheric chemistry changes over the last climatic cycle (160,000 years). *Atmospheric Environment (1967)*, 22(2):317–331.
- Legrand, M. and Mayewski, P. (1997). Glaciochemistry of polar ice cores: a review. *Reviews of Geophysics*, 35(3):219–243.
- Legrand, M., McConnell, J., Fischer, H., Wolff, E. W., Preunkert, S., Arienzo, M., Chellman, N., Leuenberger, D., Maselli, O., Place, P., et al. (2016a). Boreal fire records in northern hemisphere ice cores: a review. *Climate of the Past*, 12(10):2033.

- Legrand, M., Yang, X., Preunkert, S., and Theys, N. (2016b). Year-round records of sea salt, gaseous, and particulate inorganic bromine in the atmospheric boundary layer at coastal (dumont d'urville) and central (concordia) east antarctic sites. *Journal of Geophysical Research: Atmospheres*, 121(2):997–1023.
- Levine, J., Yang, X., Jones, A., and Wolff, E. (2014). Sea salt as an ice core proxy for past sea ice extent: A process-based model study. *Journal of Geophysical Research: Atmospheres*, 119(9):5737–5756.
- Lewis, E. R. and Schwartz, S. E. (2004). *Sea salt aerosol production: mechanisms, methods, measurements, and models-A critical review*, volume 152. American Geophysical Union.
- Li, C., Kang, S., Shi, G., Huang, J., Ding, M., Zhang, Q., Zhang, L., Guo, J., Xiao, C., Hou, S., Sun, B., Qin, D., and Ren, J. (2014). Spatial and temporal variations of total mercury in antarctic snow along the transect from zhongshan station to dome a. *Tellus B: Chemical and Physical Meteorology*, 66(1):25152.
- Liao, W., Case, A., Mastromarino, J., Tan, D., and Dibb, J. E. (2006). Observations of hono by laser-induced fluorescence at the south pole during antci 2003. *Geophysical Research Letters*, 33(9).
- Lieb-Lappen, R. and Obbard, R. (2015). The role of blowing snow in the activation of bromine over first-year antarctic sea ice. *Atmospheric Chemistry and Physics*, 15(13):7537–7545.
- Lorius, C. and Merlivat, L. (1975). Distribution of mean surface stable isotopes values in east antarctica; observed changes with depth in coastal area. Technical report, CEA Centre d'Etudes Nucleaires de Saclay.
- Lupker, M., Aciego, S., Bourdon, B., Schwander, J., and Stocker, T. (2010). Isotopic tracing (sr, nd, u and hf) of continental and marine aerosols in an 18th century section of the dye-3 ice core (greenland). *Earth and Planetary Science Letters*, 295(1):277–286.
- Ma, X., Von Salzen, K., and Li, J. (2008). Modelling sea salt aerosol and its direct and indirect effects on climate. *Atmospheric Chemistry and Physics*, 8(5):1311–1327.

- Macdonald, R. and Bowers, J. (1996). Contaminants in the arctic marine environment: priorities for protection. *ICES Journal of Marine Science*, 53(3):537–563.
- MacDonald, S., Gómez Martín, J., Chance, R., Warriner, S., Saiz-Lopez, A., Carpenter, L., and Plane, J. (2014). A laboratory characterisation of inorganic iodine emissions from the sea surface: dependence on oceanic variables and parameterisation for global modelling. *Atmospheric Chemistry and Physics*, 14(11):5841–5852.
- Maffezzoli, N., Spolaor, A., Barbante, C., Bertò, M., Frezzotti, M., and Vallelonga, P. (2017). Bromine, iodine and sodium in surface snow along the 2013 talos dome–gv7 traverse (northern victoria land, east antarctica). *The Cryosphere*, 11(2):693–705.
- Magand, O., Frezzotti, M., Pourchet, M., Stenni, B., Genoni, L., and Fily, M. (2004). Climate variability along latitudinal and longitudinal transects in east antarctica. *Annals of Glaciology*, 39(1):351–358.
- Mahajan, A. S., Shaw, M., Oetjen, H., Hornsby, K. E., Carpenter, L. J., Kaleschke, L., Tian-Kunze, X., Lee, J. D., Moller, S. J., Edwards, P., et al. (2010). Evidence of reactive iodine chemistry in the arctic boundary layer. *Journal of Geophysical Research: Atmospheres*, 115(D20).
- Mahowald, N. M., Lamarque, J.-F., Tie, X. X., and Wolff, E. (2006). Sea-salt aerosol response to climate change: Last glacial maximum, preindustrial, and doubled carbon dioxide climates. *Journal of Geophysical Research: Atmospheres*, 111(D5).
- Malmgren, F. and Institut., G. (1927). *On the properties of sea-ice*. A.S. John Griegs Boktrykkeri.
- Martin, J. H., Gordon, R. M., and Fitzwater, S. E. (1990). Iron in antarctic waters. *Nature*, 345(6271):156–158.
- Maselli, O. J., Chellman, N. J., Grieman, M., Layman, L., McConnell, J. R., Pasteris, D., Rhodes, R. H., Saltzman, E., and Sigl, M. (2017). Sea ice and pollution-modulated changes in greenland ice core methanesulfonate and bromine. *Climate of the Past*, 13(1):39.

- Mayewski, P., Lyons, W., Spencer, M., Twickler, M., Buck, C., and Whitlow, S. (1990). An ice-core record of atmospheric response to anthropogenic sulphate and nitrate. *Nature*, 346(6284):554–556.
- Mayewski, P. A., Frezzotti, M., Bertler, N., Van Ommen, T., Hamilton, G., Jacka, T. H., Welch, B., Frey, M., Dahe, Q., Jiawen, R., et al. (2005). The international trans-antarctic scientific expedition (itase): an overview. *Annals of Glaciology*, 41(1):180–185.
- McConnell, J., Henderson, G., et al. (1992). Photochemical bromine production implicated in arctic boundary-layer ozone depletion. *Nature*, 355(6356):150.
- McConnell, J. R., Lamorey, G. W., Lambert, S. W., and Taylor, K. C. (2002). Continuous ice-core chemical analyses using inductively coupled plasma mass spectrometry. *Environmental science & technology*, 36(1):7–11.
- McElroy, C., McLinden, C., and McConnell, J. (1999). Evidence for bromine monoxide in the free troposphere during the arctic polar sunrise. *Nature*, 397(6717):338.
- Meier, W., Fetterer, F., Savoie, M., Mallory, S., Duerr, R., and Stroeve, J. (2013). Noaa/nsidc climate data record of passive microwave sea ice concentration, version 2, natl. snow and ice data cent., boulder, colo.
- Millero, F. J., Feistel, R., Wright, D. G., and McDougall, T. J. (2008). The composition of Standard Seawater and the definition of the Reference-Composition Salinity Scale. *Deep Sea Research Part I: Oceanographic Research Papers*, 55(1):50–72.
- Molina, M. J. and Rowland, F. S. (1974). Stratospheric sink for chlorofluoromethanes: chlorine atom-catalysed destruction of ozone. *Nature*, 249(5460):810–812.
- Monahan, E. C., Fairall, C. W., Davidson, K. L., and Boyle, P. J. (1983). Observed interrelations between 10m winds, ocean whitecaps and marine aerosols. *Quarterly Journal of the Royal Meteorological Society*, 109(460):379–392.
- Mook, W. and Rozanski, K. (2000). Environmental isotopes in the hydrological cycle. *IAEA Publish*, 39.

- Moore, R., Webb, M., Tokarczyk, R., and Wever, R. (1996). Bromoperoxidase and iodoperoxidase enzymes and production of halogenated methanes in marine diatom cultures. *Journal of Geophysical Research: Oceans*, 101(C9):20899–20908.
- Moore, R. M. and Groszko, W. (1999). Methyl iodide distribution in the ocean and fluxes to the atmosphere. *Journal of Geophysical Research: Oceans*, 104(C5):11163–11171.
- Mozurkewich, M. (1995). Mechanisms for the release of halogens from sea-salt particles by free radical reactions. *Journal of Geophysical Research: Atmospheres*, 100(D7):14199–14207.
- Müller, J., Massé, G., Stein, R., and Belt, S. T. (2009). Variability of sea-ice conditions in the fram strait over the past 30,000 years. *Nature Geoscience*, 2(11):772–776.
- Müller, J. and Stein, R. (2014). High-resolution record of late glacial and deglacial sea ice changes in fram strait corroborates ice–ocean interactions during abrupt climate shifts. *Earth and Planetary Science Letters*, 403:446–455.
- Müller, J., Werner, K., Stein, R., Fahl, K., Moros, M., and Jansen, E. (2012). Holocene cooling culminates in sea ice oscillations in fram strait. *Quaternary Science Reviews*, 47:1–14.
- Mulvaney, R., Pasteur, E. C., Peel, D. A., Saltzman, E. S., and WHUNG, P.-Y. (1992). The ratio of msa to non-sea-salt sulphate in antarctic peninsula ice cores. *Tellus B*, 44(4):295–303.
- Neftel, A., Beer, J., Oeschger, H., Zürcher, F., and Finkel, R. (1985). Sulphate and nitrate concentrations in snow from south greenland 1895–1978. *Nature*, 314(6012):611–613.
- Nghiem, S., Rigor, I., Clemente-Colón, P., Neumann, G., and Li, P. (2016). Geophysical constraints on the antarctic sea ice cover. *Remote Sensing of Environment*, 181:281–292.
- North Greenland Ice Core Project members, . (2004). High-resolution record of northern hemisphere climate extending into the last interglacial period. *Nature*, 431(7005):147–151.

- Obbard, R. W., Roscoe, H. K., Wolff, E. W., and Atkinson, H. M. (2009). Frost flower surface area and chemistry as a function of salinity and temperature. *Journal of Geophysical Research: Atmospheres*, 114(D20).
- O'Dwyer, J., Isaksson, E., Vinje, T., Jauhiainen, T., Moore, J., Pohjola, V., Vaikmäe, R., and van de Wal, R. S. (2000). Methanesulfonic acid in a svalbard ice core as an indicator of ocean climate. *Geophysical Research Letters*, 27(8):1159–1162.
- Papanastasiou, D. K., McKeen, S. A., and Burkholder, J. B. (2014). The very short-lived ozone depleting substance chbr 3 (bromoform): revised uv absorption spectrum, atmospheric lifetime and ozone depletion potential. *Atmospheric Chemistry & Physics*, 14(6).
- Pasteur, E. C. and Mulvaney, R. (2000). Migration of methane sulphonate in antarctic firn and ice. *Journal of Geophysical Research: Atmospheres*, 105(D9):11525–11534.
- Peterson, P. K., Pöhler, D., Sihler, H., Zielcke, J., General, S., Frieß, U., Platt, U., Simpson, W. R., Nghiem, S. V., Shepson, P. B., Stirm, B. H., Dhaniyala, S., Wagner, T., Caulton, D. R., Fuentes, J. D., and Pratt, K. A. (2017). Observations of bromine monoxide transport in the arctic sustained on aerosol particles. *Atmospheric Chemistry and Physics*, 17(12):7567–7579.
- Petit, J.-R., Jouzel, J., Raynaud, D., Barkov, N. I., Barnola, J.-M., Basile, I., Bender, M., Chappellaz, J., Davis, M., Delaygue, G., et al. (1999). Climate and atmospheric history of the past 420,000 years from the vostok ice core, antarctica. *Nature*, 399(6735):429–436.
- Platt, U. and Hönninger, G. (2003). The role of halogen species in the troposphere. *Chemosphere*, 52(2):325–338.
- Platt, U. and Janssen, C. (1995). Observation and role of the free radicals no 3, clo, bro and io in the troposphere. *Faraday Discussions*, 100:175–198.
- Platt, U. and Stutz, J. (2008). Differential absorption spectroscopy. *Differential Optical Absorption Spectroscopy*, pages 135–174.
- Pöhler, D., Vogel, L., Frieß, U., and Platt, U. (2010). Observation of halogen species in the amundsen gulf, arctic, by active long-path differential optical absorption spectroscopy. *Proceedings of the National Academy of Sciences*, 107(15):6582–6587.

- Prados-Roman, C., Cuevas, C., Fernandez, R. P., Kinnison, D. E., Lamarque, J.-F., and Saiz-Lopez, A. (2015). A negative feedback between anthropogenic ozone pollution and enhanced ocean emissions of iodine. *Atmospheric Chemistry and Physics*, 15(4):2215–2224.
- Pratt, K. A., Custard, K. D., Shepson, P. B., Douglas, T. A., Pöhler, D., General, S., Zielcke, J., Simpson, W. R., Platt, U., Tanner, D. J., et al. (2013). Photochemical production of molecular bromine in arctic surface snowpacks. *Nature Geoscience*, 6(5):351–356.
- Preunkert, S., Legrand, M., Jourdain, B., Moulin, C., Belviso, S., Kasamatsu, N., Fukuchi, M., and Hirawake, T. (2007). Interannual variability of dimethylsulfide in air and seawater and its atmospheric oxidation by-products (methanesulfonate and sulfate) at dumont d'urville, coastal antarctica (1999–2003). *Journal of Geophysical Research: Atmospheres*, 112(D6).
- Preunkert, S., Legrand, M., and Wagenbach, D. (2001). Sulfate trends in a col du dome (french alps) ice core: A record of anthropogenic sulfate levels in the european midtroposphere over the twentieth century. *Journal of Geophysical Research: Atmospheres*, 106(D23):31991–32004.
- Proposito, M., Becagli, S., Castellano, E., Flora, O., Genoni, L., Gragnani, R., Stenni, B., Traversi, R., Udisti, R., and Frezzotti, M. (2002). Chemical and isotopic snow variability along the 1998 itase traverse from terra nova bay to dome c, east antarctica. *Annals of Glaciology*, 35(1):187–194.
- Przybylak, R., Sadourny, R., and Mysak, L. A. (2003). *The climate of the Arctic*. Springer.
- Rankin, A. M. and Wolff, E. W. (2003). A year-long record of size-segregated aerosol composition at halley, antarctica. *Journal of Geophysical Research: Atmospheres*, 108(D24).
- Rankin, A. M., Wolff, E. W., and Martin, S. (2002). Frost flowers: Implications for tropospheric chemistry and ice core interpretation. *Journal of Geophysical Research: Atmospheres*, 107(D23).
- Read, K., Lewis, A., Bauguitte, S., Rankin, A. M., Salmon, R., Wolff, E. W., Saiz-Lopez, A., Bloss, W., Heard, D., Lee, J., et al. (2008). Dms and msa measurements in the antarctic

boundary layer: impact of bro on msa production. *Atmospheric Chemistry and Physics*, 8(11):2985–2997.

Reeh, N., Fisher, D. A., Koerner, R. M., and Clausen, H. B. (2005). An empirical firn-densification model comprising ice lenses. *Annals of Glaciology*, 42(1):101–106.

Rhodes, R. H., Yang, X., Wolff, E. W., McConnell, J. R., and Frey, M. M. (2017). Sea ice as a source of sea salt aerosol to greenland ice cores: a model-based study. *Atmospheric Chemistry and Physics*, 17(15):9417–9433.

Richter, A., Wittrock, F., Eisinger, M., and Burrows, J. P. (1998). Some observations of tropospheric bro in northern hemispheric spring and summer 1997. *Geophysical Research Letters*, 25(14):2683–2686.

Rigor, I. G. and Wallace, J. M. (2004). Variations in the age of arctic sea-ice and summer sea-ice extent. *Geophysical Research Letters*, 31(9).

Roberts, J., Plummer, C., Vance, T., van Ommen, T., Moy, A., Poynter, S., Treverrow, A., Curran, M., and George, S. (2015). A 2000-year annual record of snow accumulation rates for law dome, east antarctica. *Climate of the Past*, 11(5):697–707.

Roscoe, H., Brough, N., Jones, A., Wittrock, F., Richter, A., Van Roozendaal, M., and Hendrick, F. (2014). Characterisation of vertical bro distribution during events of enhanced tropospheric bro in antarctica, from combined remote and in-situ measurements. *Journal of Quantitative Spectroscopy and Radiative Transfer*, 138:70–81.

Röthlisberger, R., Bigler, M., Hutterli, M., Sommer, S., Stauffer, B., Junghans, H. G., and Wagenbach, D. (2000a). Technique for continuous high-resolution analysis of trace substances in firn and ice cores. *Environmental Science & Technology*, 34(2):338–342.

Röthlisberger, R., Crosta, X., Abram, N. J., Armand, L., and Wolff, E. W. (2010). Potential and limitations of marine and ice core sea ice proxies: an example from the indian ocean sector. *Quaternary Science Reviews*, 29(1):296–302.

Röthlisberger, R., Hutterli, M. A., Sommer, S., Wolff, E. W., and Mulvaney, R. (2000b). Factors controlling nitrate in ice cores: Evidence from the dome c deep ice core. *Journal of Geophysical Research: Atmospheres*, 105(D16):20565–20572.

- Röthlisberger, R., Mulvaney, R., Wolff, E. W., Hutterli, M. A., Bigler, M., De Angelis, M., Hansson, M. E., Steffensen, J. P., and Udisti, R. (2003). Limited dechlorination of sea-salt aerosols during the last glacial period: Evidence from the european project for ice coring in antarctica (epica) dome c ice core. *Journal of Geophysical Research: Atmospheres*, 108(D16).
- Rudnick, R. and Gao, S. (2003). Composition of the continental crust. *Treatise on geochemistry*, 3:659.
- Saiz-Lopez, A., Blaszcak-Boxe, C., and Carpenter, L. (2015). A mechanism for biologically induced iodine emissions from sea ice. *Atmospheric Chemistry and Physics*, 15(17):9731–9746.
- Saiz-Lopez, A., Chance, K., Liu, X., Kurosu, T. P., and Sander, S. P. (2007a). First observations of iodine oxide from space. *Geophysical Research Letters*, 34(12).
- Saiz-Lopez, A., Fernandez, R., Ordóñez, C., Kinnison, D., Gómez Martín, J., Lamarque, J., and Tilmes, S. (2014). Iodine chemistry in the troposphere and its effect on ozone. *Atmospheric Chemistry and Physics*, 14(23):13119–13143.
- Saiz-Lopez, A., Mahajan, A. S., Salmon, R. A., Bauguitte, S. J.-B., Jones, A. E., Roscoe, H. K., and Plane, J. M. (2007b). Boundary layer halogens in coastal antarctica. *Science*, 317(5836):348–351.
- Saiz-Lopez, A., Plane, J. M., Baker, A. R., Carpenter, L. J., von Glasow, R., Gómez Martín, J. C., McFiggans, G., and Saunders, R. W. (2011). Atmospheric chemistry of iodine. *Chemical reviews*, 112(3):1773–1804.
- Saiz-Lopez, A. and von Glasow, R. (2012). Reactive halogen chemistry in the troposphere. *Chemical Society Reviews*, 41(19):6448–6472.
- Sala, M., Delmonte, B., Frezzotti, M., Proposito, M., Scarchilli, C., Maggi, V., Artioli, G., Dapiaggi, M., Marino, F., Ricci, P., et al. (2008). Evidence of calcium carbonates in coastal (talos dome and ross sea area) east antarctica snow and firn: environmental and climatic implications. *Earth and Planetary Science Letters*, 271(1):43–52.

- Salawitch, R., Canty, T., Kurosu, T., Chance, K., Liang, Q., da Silva, A., Pawson, S., Nielsen, J., Rodriguez, J., Bhartia, P., et al. (2010). A new interpretation of total column bro during arctic spring. *Geophysical Research Letters*, 37(21).
- Salawitch, R. J. (2006). Atmospheric chemistry: Biogenic bromine. *Nature*, 439(7074):275–277.
- Sander, R., Keene, W., Pszenny, A., Arimoto, R., Ayers, G., Baboukas, E., Caine, J., Crutzen, P., Duce, R., Hönninger, G., et al. (2003). Inorganic bromine in the marine boundary layer: a critical review. *Atmospheric Chemistry and Physics*, 3(5):1301–1336.
- Scarchilli, C., Frezzotti, M., and Ruti, P. M. (2011). Snow precipitation at four ice core sites in east antarctica: provenance, seasonality and blocking factors. *Climate Dynamics*, 37(9):2107–2125.
- Schönhardt, A., Begoin, M., Richter, A., Wittrock, F., Kaleschke, L., Gómez Martín, J., and Burrows, J. (2012). Simultaneous satellite observations of io and bro over antarctica. *Atmospheric Chemistry and Physics*, 12(14):6565–6580.
- Schönhardt, A., Richter, A., Wittrock, F., Kirk, H., Oetjen, H., Roscoe, H. K., and Burrows, J. (2008). Observations of iodine monoxide columns from satellite. *Atmospheric Chemistry and Physics*, 8(3):637–653.
- Schroeder, W., Anlauf, K., Barrie, L., Lu, J., Steffen, A., Schneeberger, D., and Berg, T. (1998). Arctic springtime depletion of mercury. *Nature*, 394(6691):331.
- Schüpbach, S., Federer, U., Kaufmann, P., Albani, S., Barbante, C., Stocker, T., and Fischer, H. (2013). High-resolution mineral dust and sea ice proxy records from the talos dome ice core. *Climate of the Past*, 9(6):2789–2807.
- Scott, D. B., Schell, T., St-Onge, G., Rochon, A., and Blasco, S. (2009). Foraminiferal assemblage changes over the last 15,000 years on the mackenzie-beaufort sea slope and amundsen gulf, canada: Implications for past sea ice conditions. *Paleoceanography*, 24(2).
- Seidenkrantz, M.-S. (2013). Benthic foraminifera as palaeo sea-ice indicators in the subarctic realm—examples from the labrador sea—baffin bay region. *Quaternary Science Reviews*, 79:135–144.

- Severi, M., Becagli, S., Caiazzo, L., Ciardini, V., Colizza, E., Giardi, F., Mezgec, K., Scarchilli, C., Stenni, B., Thomas, E., et al. (2017). Sea salt sodium record from talos dome (east antarctica) as a potential proxy of the antarctic past sea ice extent. *Chemosphere*, 177:266–274.
- Severi, M., Becagli, S., Castellano, E., Morganti, A., Traversi, R., and Udisti, R. (2009). Thirty years of snow deposition at talos dome (northern victoria land, east antarctica): Chemical profiles and climatic implications. *Microchemical Journal*, 92(1):15–20.
- Severi, M., Becagli, S., Traversi, R., and Udisti, R. (2015). Recovering paleo-records from antarctic ice-cores by coupling a continuous melting device and fast ion chromatography. *Analytical chemistry*, 87(22):11441–11447.
- Sigg, A., Fuhrer, K., Anklin, M., Staffelbach, T., and Zurmuehle, D. (1994). A continuous analysis technique for trace species in ice cores. *Environmental science & technology*, 28(2):204–209.
- Simpson, W., Carlson, D., Hönninger, G., Douglas, T., Sturm, M., Perovich, D., and Platt, U. (2007a). First-year sea-ice contact predicts bromine monoxide (bro) levels at barrow, alaska better than potential frost flower contact. *Atmospheric Chemistry and Physics*, 7(3):621–627.
- Simpson, W., Glasow, R. v., Riedel, K., Anderson, P., Ariya, P., Bottenheim, J., Burrows, J., Carpenter, L., Frieß, U., Goodsite, M. E., et al. (2007b). Halogens and their role in polar boundary-layer ozone depletion. *Atmospheric Chemistry and Physics*, 7(16):4375–4418.
- Simpson, W. R., Alvarez-Aviles, L., Douglas, T. A., Sturm, M., and Domine, F. (2005). Halogens in the coastal snow pack near barrow, alaska: Evidence for active bromine air-snow chemistry during springtime. *Geophysical Research Letters*, 32(4).
- Simpson, W. R., King, M. D., Beine, H. J., Honrath, R. E., and Peterson, M. C. (2002). Atmospheric photolysis rate coefficients during the polar sunrise experiment alert2000. *Atmospheric Environment*, 36(15):2471–2480.

Slinn, W., Hasse, L., Hicks, B., Hogan, A., Lal, D., Liss, P., Munnich, K., Sehmel, G., and Vittori, O. (1978). Some aspects of the transfer of atmospheric trace constituents past the air-sea interface. *Atmospheric Environment (1967)*, 12(11):2055–2087.

Slinn, W. G. N. (1983). Air-to-sea transfer of particles. In *Air-sea exchange of gases and particles*, pages 299–405. Springer.

Sodemann, H., Palmer, A., Schwierz, C., Schwikowski, M., and Wernli, H. (2006). The transport history of two saharan dust events archived in an alpine ice core. *Atmospheric Chemistry and Physics*, 6(3):667–688.

Solomon, S., Garcia, R. R., and Ravishankara, A. (1994). On the role of iodine in ozone depletion. *Journal of Geophysical Research: Atmospheres*, 99(D10):20491–20499.

Sommer, S., Wagenbach, D., Mulvaney, R., and Fischer, H. (2000). Glacio-chemical study spanning the past 2 kyr on three ice cores from dronning maud land, antarctica: 2. seasonally resolved chemical records. *Journal of Geophysical Research: Atmospheres*, 105(D24):29423–29433.

Spolaor, A., Gabrieli, J., Martma, T., Kohler, J., Björkman, M., Isaksson, E., Varin, C., Vallelonga, P., Plane, J., and Barbante, C. (2013a). Sea ice dynamics influence halogen deposition to svalbard. *The Cryosphere*, 7(5):1645–1658.

Spolaor, A., Opel, T., McConnell, J. R., Maselli, O. J., Spreen, G., Varin, C., Kirchgeorg, T., Fritzsche, D., Saiz-Lopez, A., and Vallelonga, P. (2016a). Halogen-based reconstruction of russian arctic sea ice area from the akademii nauk ice core (severnaya zemlya). *The Cryosphere*, 10(1):245–256.

Spolaor, A., Vallelonga, P., Gabrieli, J., Kehrwald, N., Turetta, C., Cozzi, G., Poto, L., Plane, J. M., Boutron, C., and Barbante, C. (2013b). Speciation analysis of iodine and bromine at picogram-per-gram levels in polar ice. *Analytical and Bioanalytical Chemistry*, 405(2-3):647–654.

Spolaor, A., Vallelonga, P., Gabrieli, J., Martma, T., Björkman, M., Isaksson, E., Cozzi, G., Turetta, C., Kjær, H., Curran, M., et al. (2014). Seasonality of halogen deposition in polar snow and ice. *Atmospheric Chemistry and Physics*, 14(18):9613–9622.

- Spolaor, A., Vallelonga, P., Plane, J., Kehrwald, N., Gabrieli, J., Varin, C., Turetta, C., Cozzi, G., Kumar, R., Boutron, C., et al. (2013c). Halogen species record antarctic sea ice extent over glacial–interglacial periods. *Atmospheric Chemistry and Physics*, 13(13):6623–6635.
- Spolaor, A., Vallelonga, P., Turetta, C., Maffezzoli, N., Cozzi, G., Gabrieli, J., Barbante, C., Goto-Azuma, K., Saiz-Lopez, A., Cuevas, C. A., and Dahl-Jensen, D. (2016b). Canadian Arctic sea ice reconstructed from bromine in the Greenland NEEM ice core. *Scientific Reports*, 6:33925.
- St-Hilaire-Gravel, D., Bell, T. J., and Forbes, D. L. (2010). Raised gravel beaches as proxy indicators of past sea-ice and wave conditions, lowther island, canadian arctic archipelago. *Arctic*, pages 213–226.
- Steffensen, J. (1988). Analysis of the seasonal variation in dust, cl-, no3-, and so4 2- in two central greenland firn cores. *Annals of Glaciology*, 10(1):171–177.
- Stein, A., Draxler, R. R., Rolph, G. D., Stunder, B. J., Cohen, M., and Ngan, F. (2015). Noaa’s hypsplit atmospheric transport and dispersion modeling system. *Bulletin of the American Meteorological Society*, 96(12):2059–2077.
- Stenni, B., Buiron, D., Frezzotti, M., Albani, S., Barbante, C., Bard, E., Barnola, J., Baroni, M., Baumgartner, M., Bonazza, M., et al. (2011). Expression of the bipolar see-saw in antarctic climate records during the last deglaciation. *Nature Geoscience*, 4(1):46–49.
- Stenni, B., Proposito, M., Gragnani, R., Flora, O., Jouzel, J., Falourd, S., and Frezzotti, M. (2002). Eight centuries of volcanic signal and climate change at talos dome (east antarctica). *Journal of Geophysical Research: Atmospheres*, 107(D9).
- Sturm, M. and Massom, R. A. (2009). Snow and sea ice. *Sea ice. Oxford, Wiley-Blackwell*, pages 153–204.
- Stutz, J., Thomas, J. L., Hurlock, S., Schneider, M., Glasow, R. v., Piot, M., Gorham, K., Burkhardt, J. F., Ziemba, L., Dibb, J. E., et al. (2011). Longpath doas observations of surface bro at summit, greenland. *Atmospheric Chemistry and Physics*, 11(18):9899–9910.

- Tang, T. and McConnell, J. (1996). Autocatalytic release of bromine from arctic snow pack during polar sunrise. *Geophysical Research Letters*, 23(19):2633–2636.
- Tarasick, D. and Bottenheim, J. (2002). Surface ozone depletion episodes in the arctic and antarctic from historical ozonesonde records. *Atmospheric Chemistry and Physics*, 2(3):197–205.
- Taylor, K., Alley, R., Fiacco, J., Grootes, P., Lamorey, G., Mayewski, P., and Spencer, M. J. (1992). Ice-core dating and chemistry by direct-current electrical conductivity. *Journal of Glaciology*, 38(130):325–332.
- Textor, C., Schulz, M., Guibert, S., Kinne, S., Balkanski, Y., Bauer, S., Bernsten, T., Berglen, T., Boucher, O., Chin, M., et al. (2006). Analysis and quantification of the diversities of aerosol life cycles within aerocom. *Atmospheric Chemistry and Physics*, 6(7):1777–1813.
- Theys, N., Van Roozendael, M., Hendrick, F., Yang, X., De Smedt, I., Richter, A., Begoin, M., Errera, Q., Johnston, P., Kreher, K., et al. (2011). Global observations of tropospheric bromine columns using gome-2 satellite data. *Atmospheric Chemistry and Physics*, 11(4):1791.
- Thomas, J. L., Stutz, J., Lefer, B., Huey, L. G., Toyota, K., Dibb, J. E., and Glasow, R. v. (2011). Modeling chemistry in and above snow at summit, greenland—part 1: Model description and results. *Atmospheric Chemistry and Physics*, 11(10):4899–4914.
- Thomas, R. (2013). *Practical guide to ICP-MS: a tutorial for beginners*. CRC press.
- Thorpe, S. (1992). Bubble clouds and the dynamics of the upper ocean. *Quarterly Journal of the Royal Meteorological Society*, 118(503):1–22.
- Toyota, T., Massom, R., Tateyama, K., Tamura, T., and Fraser, A. (2011). Properties of snow overlying the sea ice off east antarctica in late winter, 2007. *Deep Sea Research Part II: Topical Studies in Oceanography*, 58(9):1137–1148.
- Traversi, R., Becagli, S., Castellano, E., Migliori, A., Severi, M., and Udisti, R. (2002). High-resolution fast ion chromatography (fic) measurements of chloride, nitrate and sulphate along the epica dome c ice core. *Annals of Glaciology*, 35(1):291–298.

- Tucker, W., Perovich, D. K., Gow, A. J., Weeks, W. F., and Drinkwater, M. R. (1992). Physical properties of sea ice relevant to remote sensing. *Microwave remote sensing of sea ice*, pages 9–28.
- Tuckermann, M., Ackermann, R., Götz, C., Lorenzen-Schmidt, H., Senne, T., Stutz, J., Trost, B., Unold, W., and Platt, U. (1997). Doas-observation of halogen radical-catalysed arctic boundary layer ozone destruction during the arctic-campaigns 1995 and 1996 in ny-ålesund, spitsbergen. *Tellus B: Chemical and Physical Meteorology*, 49(5):533–555.
- Vallelonga, P., Maffezzoli, N., Moy, A. D., Curran, M. A., Vance, T. R., Edwards, R., Hughes, G., Barker, E., Spreen, G., Saiz-Lopez, A., et al. (2017). Sea-ice-related halogen enrichment at law dome, coastal east antarctica. *Climate of the Past*, 13(2):171.
- Van den Broeke, M. R., Bamber, J., Lenaerts, J., and Rignot, E. (2011). Ice sheets and sea level: thinking outside the box. *Surveys in Geophysics*, 32(4-5):495–505.
- Vogt, R., Crutzen, P. J., and Sander, R. (1996). A mechanism for halogen release from sea-salt aerosol in the remote marine boundary layer. *Nature*, 383(6598):327–330.
- Volkman, J. K., Barrett, S. M., and Dunstan, G. A. (1994). C₂₅ and c₃₀ highly branched isoprenoid alkenes in laboratory cultures of two marine diatoms. *Organic Geochemistry*, 21(3-4):407–414.
- Wagenbach, D., Ducroz, F., Mulvaney, R., Keck, L., Minikin, A., Legrand, M., Hall, J., and Wolff, E. (1998). Sea-salt aerosol in coastal antarctic regions. *Journal of Geophysical Research: Atmospheres*, 103(D9):10961–10974.
- Wagner, T. and Platt, U. (1998). Satellite mapping of enhanced bro concentrations in the troposphere. *Nature*, 395(6701):486.
- Warneck, P. (1999). *Chemistry of the natural atmosphere*, volume 71. Academic press.
- Weller, R., Traufetter, F., Fischer, H., Oerter, H., Piel, C., and Miller, H. (2004). Postdepositional losses of methane sulfonate, nitrate, and chloride at the european project for ice coring in antarctica deep-drilling site in dronning maud land, antarctica. *Journal of Geophysical Research: Atmospheres*, 109(D7).

- Weller, R., Wagenbach, D., Legrand, M., Elsässer, C., TIAN-KUNZE, X., and KÖNIG-LANGLO, G. (2011). Continuous 25-yr aerosol records at coastal antarctica–i: inter-annual variability of ionic compounds and links to climate indices. *Tellus B*, 63(5):901–919.
- Wennberg, P. (1999). Atmospheric chemistry: Bromine explosion. *Nature*, 397(6717):299–301.
- Wettlaufer, J. and Worster, M. (1995). Dynamics of premelted films: frost heave in a capillary. *Physical Review E*, 51(5):4679.
- Whitlow, S., Mayewski, P., Dibb, J., Holdsworth, G., and Twickler, M. (1994). An ice-core-based record of biomass burning in the arctic and subarctic, 1750–1980. *Tellus B*, 46(3):234–242.
- Whitlow, S., Mayewski, P. A., and Dibb, J. E. (1992). A comparison of major chemical species seasonal concentration and accumulation at the south pole and summit, greenland. *Atmospheric Environment. Part A. General Topics*, 26(11):2045–2054.
- Winstrup, M., Svensson, A. M., Rasmussen, S. O., Winther, O., Steig, E. J., and Axelrod, A. E. (2012). An automated approach for annual layer counting in ice cores. *Climate of the Past*, 8(6):1881–1895.
- Wittrock, F., Oetjen, H., Richter, A., Fietkau, S., Medeke, T., Rozanov, A., and Burrows, J. (2004). Max-does measurements of atmospheric trace gases in ny-ålesund-radiative transfer studies and their application. *Atmospheric Chemistry and Physics*, 4(4):955–966.
- Wolff, E., Bigler, M., Curran, M., Dibb, J. E., Frey, M., Legrand, M., and McConnell, J. (2012). The carrington event not observed in most ice core nitrate records. *Geophysical Research Letters*, 39(8).
- Wolff, E. W. (1995). Nitrate in polar ice. In Delmas, R. J., editor, *Ice Core Studies of Global Biogeochemical Cycles*, number 30 in NATO ASI series, pages 195–224. Springer-Verlag, Berlin.
- Wolff, E. W., Chappellaz, J., Blunier, T., Rasmussen, S. O., and Svensson, A. (2010). Millennial-scale variability during the last glacial: The ice core record. *Quaternary Science Reviews*, 29(21):2828–2838.

- Wolff, E. W., Fischer, H., Fundel, F., Ruth, U., Twarloh, B., Littot, G. C., Mulvaney, R., Röthlisberger, R., De Angelis, M., Boutron, C. F., et al. (2006). Southern ocean sea-ice extent, productivity and iron flux over the past eight glacial cycles. *Nature*, 440(7083):491–496.
- Wolff, E. W., Rankin, A. M., and Röthlisberger, R. (2003). An ice core indicator of antarctic sea ice production? *Geophysical Research Letters*, 30(22).
- Wren, S. N., Donaldson, D., and Abbatt, J. (2013). Photochemical chlorine and bromine activation from artificial saline snow. *Atmospheric Chemistry and Physics*, 13(19):9789–9800.
- Xiao, X., Zhao, M., Knudsen, K. L., Sha, L., Eiríksson, J., Gudmundsdóttir, E., Jiang, H., and Guo, Z. (2017). Deglacial and holocene sea-ice variability north of iceland and response to ocean circulation changes. *Earth and Planetary Science Letters*, 472:14–24.
- Xu, L., Russell, L. M., and Burrows, S. M. (2016). Potential sea salt aerosol sources from frost flowers in the pan-arctic region. *Journal of Geophysical Research: Atmospheres*, 121(18).
- Yamanouchi, T. and Charlock, T. (1995). Radiative effects of clouds, ice sheet and sea ice in the antarctic. *Oceanographic Literature Review*, 7(42):529.
- Yang, X., Cox, R. A., Warwick, N. J., Pyle, J. A., Carver, G. D., O’Connor, F. M., and Savage, N. H. (2005). Tropospheric bromine chemistry and its impacts on ozone: A model study. *Journal of Geophysical Research: Atmospheres*, 110(D23).
- Yang, X., Pyle, J., Cox, R., Theys, N., and Roozendaal, M. V. (2010). Snow-sourced bromine and its implications for polar tropospheric ozone. *Atmospheric Chemistry and Physics*, 10(16):7763–7773.
- Yang, X., Pyle, J. A., and Cox, R. A. (2008). Sea salt aerosol production and bromine release: Role of snow on sea ice. *Geophysical Research Letters*, 35(16).
- Zhao, X., Strong, K., Adams, C., Schofield, R., Yang, X., Richter, A., Friess, U., Blechschmidt, A.-M., and Koo, J.-H. (2016). A case study of a transported bromine explo-

sion event in the canadian high arctic. *Journal of Geophysical Research: Atmospheres*,
121(1):457-477.